Advanced geophysical studies of accretion of oceanic lithosphere in Mid-Ocean Ridges characterized by contrasting tectono-magmatic settings

By
Min Xu

MSci. University of Science and Technology of China, 2006

Submitted in partial fulfillment of the requirements for the degree of
Doctor of Philosophy
at the
MASSACHUSETTS INSTITUTE OF TECHNOLOGY
and the
WOODS HOLE OCEANOGRAPHIC INSTITUTION

February 2012

© 2012 Min Xu
All rights reserved.

The author hereby grants to MIT and WHOI permission to reproduce and to distribute publicly paper and electronic copies of this thesis document in whole or in part in any medium now known or hereafter created.

ARCHIVES
MASSACHUSETTS INSTITUTE OF TECHNOLOGY
MAR 14 2012
LIBRARIES

Signature of Author

Joint Program in Oceanography, Massachusetts Institute of Technology and
Woods Hole Oceanographic Institution
January 26, 2012

Certified by

Juan Pablo Canales
Thesis Supervisor, WHOI

Accepted by

Rob. L. Evans
Chair, Joint Committee for Marine Geology and Geophysics
Massachusetts Institute of Technology and Woods Hole Oceanographic Institution

Advanced geophysical studies of accretion of oceanic lithosphere in Mid-Ocean Ridges characterized by contrasting tectono-magmatic settings

By
Min Xu

Submitted to the department of Marine Geology and Geophysics,
MIT/WHOI Joint Program in Oceanography/Applied Ocean Science and Engineering
On Jan 26, 2012 in partial fulfillment of the requirements
for the degree of Doctor of Philosophy

Abstract

The structure of the oceanic lithosphere results from magmatic and extensional processes taking place at mid-ocean ridges (MORs). The temporal and spatial scales of the variability of these two processes control the degree of heterogeneity of the oceanic lithosphere, represented by two end-member models: the classical Penrose Model exemplified by layered magmatic crust formed along fast-spreading MORs, e.g., East Pacific Rise (EPR); and the recently defined Chapman Model describing heterogeneous mafic and ultramafic lithosphere formed in settings of oceanic detachment faulting common along slow-spreading MORs, e.g., Mid-Atlantic Ridge (MAR). This thesis is using advanced marine geophysical methods (including finite-difference wave propagation modeling, 3D multi-channel seismic reflection imaging, waveform inversion, streamer tomography, and near-bottom magnetics) to study lithospheric accretion processes in MORs characterized by contrasting tectono-magmatic settings: the magmatically dominated EPR axis between 9°30'-10°00'N, and the Kane Oceanic Core Complex (KOCC), a section of MAR lithosphere (23°20'-23°38'N) formed by detachment faulting. At the EPR study area, I found that the axial magma chamber (AMC) melt sill is segmented into four prominent 2-4-km-long sections spaced every ~5-10 km along the ridge axis characterized by high melt content (>95%). In contrast, within the intervening sections, the AMC sill has a lower melt content (41-46%). The total magma volume extracted from the AMC sill was estimated of ~46 $\times$ 10^6 m^3, with ~24 $\times$ 10^6 m^3 left unerupted in the upper crust as dikes after 2005-06 eruption. At the KOCC, I used streamer tomography to constrain the shallow seismic velocity structure. Lithological interpretation of the seismic tomographic models provides insights into the temporal and spatial evolution of the melt supply at the spreading axis as the KOCC formed and evolved. Investigation of a magnetic polarity reversal boundary in cross-section at the northern boundary of KOCC suggests that the boundary (representing both a frozen isotherm and an isochron) dips away from the ridge axis along the Kane transform fault scarp, with a west-dipping angle of ~45° in the shallow (<1 km) crust and <20° in the deeper crust.

THESIS SUPERVISOR:

Dr. Juan Pablo Canales, Associate Scientist, WHOI

DEFENSE CHAIR:

Dr. Daniel Lizarralde, Associate Scientist, WHOI

THESIS COMMITTEE:

Dr. Ralph Stephen, Senior Scientist, WHOI

Dr. Adam Soule, Associate Scientist, WHOI

Professor Stephane Rondenay, MIT and University of Bergen

Dr. Suzanne Carbotte, Heezen/Lamont Research Professor, LDEO

ACKNOWLEDGMENTS

There is a saying, "It takes a whole community to raise a child." The MIT-WHOI Joint Program has certainly done this for me, as there have been so many great people who have affected my career. I have been lucky enough and always feel honored doing my Ph.D. here.

This thesis could not have been completed without significant support and encouragement from my advisors, colleagues, friends and family. First, I would like to thank my supervisor, Pablo Canales, who led me into the world of ocean science. It has been an honor and a pleasure to be Pablo's first graduate student. I am extremely grateful for his patience and generosity when teaching me so much knowledge about marine seismology. Pablo's advices have been extremely critical for the development and execution of my thesis, and I really appreciate his stamina and tireless enthusiasms for reading and correcting my papers. I am also very thankful to my thesis committee members, Daniel Lizarralde, Adam Soule, Ralph Stephen, Stephane Rondenay, and Suzanne Carbotte, who have provided countless insightful suggestions that keep me on the right track finishing my thesis.

Many thanks to my project advisors and cooperators, Brian Tucholke, Ralph Stephen, and Maurice Tivey, who have worked with me during the past five and a half years. These research experiences have greatly broadened my horizons on marine geology and geophysics, synthetic seismology, and geomagnetism. Brian introduced me into the geological world of detachment fault system, and his patience and insightful comments on our scientific paper on Kane oceanic core complex are greatly appreciated. I am very thankful for Ralph who introduced me to the world of time-domain finite difference (TDFD) synthetic seismology and Tom Bolmer for setting up the workstation for my TDFD calculations. Ralph's encouragement, enthusiasm, and interactions with me have inspired me to dig out more interesting studies. I got to work with Maurice after

taking his wonderful class – marine geophysics (geomagnetism part), and it has been a pleasure to work with him to incorporate geomagnetic study to my seismic work on Kane oceanic core complex.

I am very grateful for the hospitality of Jian Lin, not only in our many individual and group scientific discussions, but also for hosting dozens of meals (special thanks to Kelan for making those wonderful meals!) and parties I have attended over these years at WHOI. Jian's enthusiasm and love for science is contagious, and it was Jian's talk given at University of Science and Technology of China (USTC) seven years ago that inspired me to pursue my Ph.D in marine geology and geophysics at WHOI.

The WHOI scientific community were always helpful, enthusiastic, and informative. They have played a significant role in my scientific growth over the past five and a half years. Many thanks to the WHOI geophysics and geochemistry seminar group, including but not limited to – Mark Behn, Jurek Blusztajn, John Collins, Henry Dick, Rob Evans, Dan Fornari, Chris German, Greg Hirth, Mark Kurz, Daniel McCorkle, Jeff McGuire, Jerry McManus, Laurent Montési, Hans Schouten, Alison Shaw, Nobu Shumizu, Ken Sims, Debbie Smith, Rob Sohn, Jack Whitehead.

Thanks for the continuous support of the MIT/WHOI Joint Program Academic Program Office - Valarie Caron, Christine Charette, Christina Cuellar, Rob Evans, Tricia Gebbie, Marsha Gomes, Michelle McCafferty, Daniel McCorkle, Delia Oppo and Julia Westwater. Thanks also go to Ms. Carol Sprague and Ronni Schwartz in the MIT EAPS Department Education Office.

My appreciation also goes to many colleagues and friends at MIT and WHOI who helped me a lot in both academia and everyday matter. I would especially like to thank Yajing Liu, Camilo Ponton, Youshun Sun, Hongfeng Yang, and Huajian Yao for their kindly and numerous help in the past, which made my life easier and happier even in a

foreign country. I appreciate the friendship and help from many students and postdocs at MIT and WHOI, including Maya Bhatia, Andrea Burke, Qin Cao, Chin-Wu Chen, Min Ding, Jimmy Elsenbeck, Fern Gibbons, Trish Gregg, Hui Huang, Mike Krawczynski, Karin Lemkau, Einat Lev, Chang Li, Junlun Li, Andrea Llenos, Yawei Luo, Shane McGary, Evelyn Mervine, Nathan Miller, Jean-Arthur Olive, Claire Pontbriand, Emily Roland, Casey Saenger, Xuefeng Shang, Fuxian Song, Mengmeng Tong, Ping Wang, Jingbo Wang, Zengrong Wang, Chris Waters, Matt Wei, Zao Xu, Ping Zhai. I would like to give a special thanks to Jie Quan for her persistent encouragement and support.

I am indebted to all participants of the cruises MGL0808 and MGL0812. The two cruises provided me unique and exciting experiences to learn conducting ocean bottom seismometer and multi-channel seismic experiments out of sea. I am especially thankful to the chief scientists and the science party: Jeff McGuire, John Mutter, Suzanne Carbotte, Pablo Canales, Mladen Nedimovic, Nathan Miller, Emily Roland, Helene Carton, Milena Marjanovic, Kori Newman, Omid Aghaei, and Lucy Stowe. Thank so much for their friendship and generously sharing knowledge with me during the cruises.

Finally, my family has been a constant support for me. My parents have always supported and encouraged me to pursue my career and fly freely since I was even a child. My grandmother, aunt, uncle, and sister offered me tremendous encouragements even they do not know what I am really working on. Without their love and continuing supports, it would have been impossible for me to finish this thesis work.

This thesis was funded by National Science Foundation grants OCE-9987004, OCE-0621660 and OCE-0327885, WHOI Academic Program Office and WHOI Deep Ocean Exploration Institute.

CONTENTS

Chapter 1

Introduction

1.1. GENERAL INTRODUCTION: ACCRETION OF OCEANIC LITHOSPHERE IN MID-OCEAN RIDGES

The structure of the oceanic lithosphere and seafloor morphology are the results of magmatic accretion (i.e., dike injection, gabbroic intrusions) and extensional processes (i.e., brittle faulting, ductile deformation) taking place at mid-ocean ridges (MORs). Away from mantle melting anomalies (e.g., hotspots), the relative importance of magmatic accretion appears to increase with increasing spreading rate, and the relative importance of tectonic extension appears to increase with decreasing spreading rate. The fast-spreading East Pacific Rise (EPR) and the slow-spreading Mid-Atlantic Ridge (MAR) are the best examples of these two kinds of seafloor spreading. The complex array of magmatic and tectonic processes, both of which vary spatially and through time, gives rise to a heterogeneous crustal section [*Carbotte and Scheirer*, 2004].

There are two fundamental end-member classes of oceanic crust: (1) along fast-spreading ridges, the ambient melt supply is able to keep up with the extension of the lithosphere and generate a regular, layered, fully igneous crust; and (2) along slow-spreading ridges, the melt supply is insufficient to keep up with extension, and is supplemented by tectonic extension. At an idealized fast-spreading ridge, the igneous structure of the oceanic crust is generated by magmatic processes operating within a zone

as narrow as a few kilometers, often resulting in a layered crust comprising, from top to bottom, extrusive basalts, sheeted dikes, and layered and massive gabbroic rocks, i.e., the so-called Penrose Model [*Penrose Conference Participants*, 1972]. At an idealized slow-spreading ridge, tectonic extension in places uplifts and exposes deep sections of the oceanic lithosphere on the seafloor through detachment faulting and forms oceanic core complexes (OCCs) (Chapman Model, [*Escartín and Canales*, 2011]).

Newly created oceanic crust is modified by brittle failure that occurs over a wider zone, extending a few tens of kilometers from the spreading axis. These volcanic and tectonic processes at MORs give rise to the undulating abyssal hill-and-trough terrain that characterizes the world's ocean floor. The rate of crustal formation and the pattern of melt delivery to the ridge axis play fundamental roles in determining the physical properties and structure of oceanic lithosphere created at MORs.

1.2. EAST PACIFIC RISE 9°50'N: MAGMATIC ACCRETION

During the last three decades there have been a number of detailed geophysical studies aimed at determining the distribution of melt within the crust beneath fast-spreading ridge axes [e.g., *Detrick et al.*, 1987; *Dunn and Forsyth*, 2003; *Hooft et al.*, 1997; *Kent et al.*, 1993a, 1993b; *Mutter et al.*, 1988; *Mutter et al.*, 1995; *Singh et al.*, 1998]. The EPR 9°N has been intensively studied following the discovery of a bright seismic reflector beneath the ridge axis which was interpreted as the roof of an axial magma chamber (AMC) [*Herron et al.*, 1980]. The EPR 9°N is also a RIDGE2000

Integrated Study Site (http://www.ridge2000.org/science/iss/) where scientists are investigating the linkages between mantle flow, crustal accretion, volcanic, hydrothermal, and biological processes that result in chemical and physical exchanges of energy and matter between the Earth's mantle and oceans [*Mutter et al.*, 2008]. Although the presence of an AMC along most of this section of the EPR was established in the 1990's, the technology at that time precluded acquiring data at high enough resolution to accurately assess the distribution of crustal melt bodies and their fine-scale physical properties. This is a key piece of information that is currently missing from our knowledge of the EPR mantle-to-microbe system.

In Summer 2008, the first multi-streamer 3D seismic reflection experiment (cruise MGL0812) was conducted using the new national academic seismic imaging facility, the R/V *Marcus G. Langseth*, focused on the EPR at 9°50' N. The primary goals of expedition MGL0812 were to use this multi-streamer capability to create an accurate 3D seismic reflection image of the magmatic-hydrothermal system within the EPR 9°50'N site by imaging the structure of AMC lid and shallow oceanic crust at a resolution, geometric accuracy, and scale comparable to seafloor observations of hydrothermal, biological, and volcanic activity (http://www.ldeo.columbia.edu/3DMCS).

Chapter 2 presents time-domain finite difference (TDFD) calculations of 2D laterally homogeneous and heterogeneous models to study the effect of melt distribution geometry and the physical properties of the sub-axis structure in controlling waveform polarities at

near-offset and in amplitude versus offset (AVO) behaviors of the AMC reflections. This information provides a context in which to frame the interpretations made in the following Chapter 3 regarding the nature and physical properties of the AMC melt lens obtained from 1D waveform inversions [e.g., *Collier and Singh*, 1997], and their along-axis variability inferred from partial-offset stacks [e.g., *Singh et al.*, 1998].

Chapter 3 presents the 3D seismic imaging of the AMC using partial-offset stacks of the AMC reflected compressional and shear waves detected in this 3D multi-channel seismic (MCS) dataset. These stacks give us a qualitative estimate of spatial variations in AMC properties (e.g., crystallinity), and allow detailed investigations of the relationships between AMC properties and other features such as seafloor hydrothermal fields [e.g, *Haymon et al.*, 1991], and seafloor volcanic eruptions [e.g, *Soule et al.*, 2007]. Furthermore, the detailed 1D seismic structures of the AMC melt lens are analyzed at two selected locations with contrasting melt contents by using waveform modeling in the time intercept-slowness domain.

1.3. KANE OCEANIC CORE COMPLEX 23°30'N: TECTONIC EXTENSION

"The scientific community present at the 2010 Chapman Conference on Detachments in Oceanic Lithosphere affirmed that oceanic detachments should be recognized as a fundamentally distinct mode of seafloor spreading that does not conform with the classical Penrose-model of oceanic crustal structure. This type of spreading is characterized by: formation of oceanic core complexes, heterogeneous lithosphere,

extensive exposure of serpentinized mantle at the seafloor, some of the largest hydrogen-rich, deep-sea hydrothermal systems and mineral deposits, and a large diversity of deep-sea and subsurface biosphere. We would like to emphasize that the recognition of this mode of spreading is one of the major advances in understanding plate tectonics in the last three decades." - From community statement on oceanic detachments by *Escartín and Canales* [2011].

Footwalls of 'detachment' faults at MORs uplift and expose deep sections of the oceanic lithosphere on the seafloor along slow- and intermediate-spreading ridges [*Cann et al.*, 1997; *MacLeod et al.*, 2002; *Tucholke et al.*, 1996, 1998], forming oceanic core complexes (OCCs). Numerous OCCs have been identified [*Cann et al.*, 1997; *Cannat et al.*, 2006; *Ohara et al.*, 2001; *Okino et al.*, 2004; *Reston et al.*, 2002; *Searle et al.*, 2003; *Smith et al.*, 2006; *Smith et al.*, 2008; *Tucholke et al.*, 2008; *Tucholke et al.*, 2001; *Tucholke et al.*, 1998], suggesting that exhumation of OCCs is a fundamental process in seafloor formation at MORs where melt supply is limited or intermittent [*Escartín et al.*, 2008; *Smith et al.*, 2006; *Tucholke et al.*, 2008]. Detailed *in situ* geological studies and high-resolution geophysical studies are required to understand the scales of lithological heterogeneity of the lithosphere in these settings and their implications for the origin and evolution of OCCs in particular, and of slow-spread lithosphere in general.

Kane is a large OCC (~23 km by ~40 km in dip and strike directions, respectively) formed between ~3.3 and 2.1 Ma by detachment faulting at the MAR adjacent to Kane

fracture zone. The Kane OCC and surrounding areas have been intensively studied by several geophysical and geological investigations [e.g., *Auzende et al.*, 1994; *Canales et al.*, 2008; *Cannat et al.*, 1995a; *Dick et al.*, 2008; *Kong et al.*, 1988].

The MCS data used in chapter 4 of this thesis were acquired in 2001 aboard R/V *Maurice Ewing* (cruise EW0102). The objectives of this cruise were to establish the upper seismic velocity structure of these OCCs both laterally and vertically, to gain insight into the deep nature of the oceanic crust and upper mantle now exposed in these OCCs, and to gain a better understanding of how and why OCCs form [*Tucholke and Collins*, 2001]. Chapter 4 presents high-resolution shallow seismic velocity models of the Kane OCC by using a first-arrival traveltime seismic tomography method.

In Chapter 5, we analyze a series of magnetic profiles collected by submersible *Nautile* during the 1992 *Kanaut Expedition* vertically up the southern wall of Kane fracture zone and present the calculated magnetization structure to determine the geometry of a magnetic polarity reversal boundary exposed in cross-section on the northern boundary of Kane OCC on the flanks of the MAR near 23°40'N.

1.4. THESIS OVERVIEW

The focus of this thesis is on the advanced geophysical studies of accretion of oceanic lithosphere in MORs characterized by contrasting tectono-magmatic settings:

EPR 9°50'N and MAR Kane OCC 23°30'N. The variability of the lithosphere structure is related both to spreading rate and to temporal and spatial changes in magma delivery from the mantle. A brief description and primary conclusions of each chapter are presented below.

The Chapters 2 and 3 focus on a fast-spreading MOR segment (EPR 9°50'N). The data used in the two chapters were acquired during a 3D MCS survey of the magmatic-hydrothermal system at the EPR 9°50'N using four 6-km-long hydrophone streamers (Cruise MGL0812). Specifically, in Chapter 2 I use a 2D time domain finite-difference solution to the full wave equation to test the feasibility of modeling seismic propagation through 2D representations of along-axis and cross-axis AMCs, and forward modeling the origin of crustal reflectivity observed at EPR 9°50'N (particularly sub-AMC events). These forward model synthetics will also be used as guide tools to assess the polarity and amplitude versus offset (AVO) behaviors of the AMC reflections, e.g., $P_{AMC}P$ and $P_{AMC}S$ waves, in the 3D MCS dataset. The seismic phases identified from the synthetic modeling of a realistic model suggest that the sub-AMC reflections are unlikely to arise from peg-leg multiples of the AMC reflections, *P*-to-*S* converted phases, or scattering due to rough topography, but could potentially arise from deeper multiple magma sills.

In Chapter 3, I use partial-offset $P_{AMC}P$ and $P_{AMC}S$ waves stacking to qualitatively estimate melt-rich and melt-poor sections of the AMC, and relate these results with hydrothermal system present on the seafloor and recent 2005-06 eruption processes. I

found four prominent melt-rich sections along northern EPR ~9°30'-10°N. The melt-rich sections are ~2-4 km long and spaced every ~5-10 km along the ridge axis, and interestingly, none of the melt-rich sections are located immediately beneath the most abundant hydrothermal vent fields. Furthermore, 1D waveform modeling in the time intercept-slowness (τ-p) domain was employed to investigate the physical properties of the AMC melt lens at two locations with contrasting melt content. The AMC melt lens is located ~1.4 km beneath the seafloor, and it is best modeled with a low Vp (2.98 km/s) and Vs ($\leq$ 0.5 km/s) structure in the melt-rich section, while with a higher Vp (4.67 km/s) and Vs (1.5-2.0 km/s) in the melt-poor section. The thickness of the AMC melt lens is ~16-40 m. These results indicate that the melt fraction in the AMC melt lens in the melt-rich sections can be as high as 95-100%, while in the melt-poor sections, the AMC melt lens has lower percentage of melt (41-46%). Over this 60-km-long section (9°30'-10°00'N), the presence of melt-poor sections occupies >75% of the length. This means that at a given time, only ~25% of the ridge axis is capable of producing diking and seafloor eruptions, with the remaining ~75% of the AMC is temporarily playing a passive role in the crustal accretion and primarily contributing to the accretion of the lower crust. Based on the melt-mush segmentation, two scenarios regarding the relationships between the 2005-06 eruption, the physical state of the AMC melt lens before and after this event, and hydrothermal activity are proposed: (1) The source of the 2005-06 eruption was a 10-km-long melt-rich lens, which has been driving hydrothermal circulation in this area. The eruption drained most of the melt in the 5-km-long central part, leaving behind a large fraction of connected crystals separating the distal ends of the lens from which melt was

not fully drained; (2) Prior to the eruption, intense hydrothermal activity cools the section of the AMC immediately beneath hydrothermal vents and prevents the formation of a melt-rich lens. The eruption was therefore fed from melt accumulated northern and/or south of the hydrothermal field where the hydrothermal cooling was less effective.

If the first scenario is correct, the volume of the 2005-06 eruption from the 5-km-long section has been estimated with the mean values of AMC melt lens dimensions (600 m × 28 m), and 55% melt fraction decrease within the AMC melt lens. Our calculation suggests a volume of magma extracted from the AMC melt lens of ~46×10^6 m^3, with ~24×10^6 m^3 left unerupted in the upper crust as dikes. The width of the dike is 3.4 m if the dike feeding the eruption extended over the 5-km-long central section, or 0.95 m if the dike fed the eruption over the 18-km-long section where the seafloor eruption has been documented. No obvious correlations were found between the melt-mush segmentation, axial summit trough (AST) width, axial depth and MgO wt.%. This may be explained by the time scale difference of morphological (AST width and axial depth) and geochemical (MgO wt.%) features (~10^2-10^3 years) and the melt-mush segmentation (decades).

The Chapters 4 and 5 focus on a slow-spreading MOR segment (MAR Kane OCC 23°30'N). In Chapter 4, I use refracted arrivals recorded along a 6-km-long hydrophone streamer during a MCS survey (cruise EW0102) to constrain the shallow seismic velocity structure of the Kane OCC. Results are presented in high-resolution traveltime seismic

tomographic models along six lines that cover all of the main morphological features of the Kane OCC, and based on the lithological interpretation of the velocity models I interpreted the temporal and spatial evolution of melt supply at this MAR segment during the formation of the Kane OCC. The results show that magmatism initially affected the northern and southern parts of the segment, while peridotites were exhumed in the central section. Within about 1 Myr after detachment faulting initiated, extensive gabbros were exhumed in the central to northern part of the Kane OCC, with the southern part apparently affected by an intermediate level of magmatism. Within the last ~0.2 Myr of OCC formation, gabbros probably continued to be exhumed in the northern section up to the Kane transform wall, but peridotites probably were again exhumed in the central section; composition of basement in the southern part of the OCC at this time is uncertain.

Finally, in Chapter 5, I analyze a series of magnetic profiles collected by submersible *Nautile* vertically up the southern wall of the Kane fracture zone and used the calculated magnetization structure to determine the geometry of a magnetic polarity reversal boundary exposed in cross-section on the northern boundary of Kane OCC on the flanks of the MAR near 23°40'N. In general, the polarity boundary dips away from the ridge axis along the Kane transform fault scarp, with a west-dipping angle of ~45° in the shallow crust (<1 km) and <20° in the deeper crust. The existence of the magnetic polarity boundary (C2r.2r/C2An.1n, ~2.581 Ma) indicates that lower crust (gabbros) and upper mantle (peridotites) are able to record a coherent magnetic signal. There is no

convincing correlation between the magnetization structures and lithological distribution, thus we rule out the possibility that the magnetic reversal boundary is exclusively caused by lithological changes. The result supports the conclusion of *Williams* [2007] that lower crust (gabbros) cool through their Curie temperature to become magnetic, with the polarity boundary representing both a frozen isotherm and an isochron.

References

Auzende, J.-M., M. Cannat, P. Gente, J.-P. Henriet, T. Juteau, J. A. Karson, Y. Lagabrielle, C. Mével, and M. A. Tivey (1994), Observation of sections of oceanic crust and mantle cropping out on the southern wall of Kane FZ (N. Atlantic), *Terra Nova*, *6*, 143-148, doi:10.1111/j.1365-3121.1994.tb00647.x.

Canales, J. P., B. E. Tucholke, M. Xu, J. A. Collins, and D. L. Dubois (2008), Seismic evidence for large-scale compositional heterogeneity of oceanic core complexes, *Geochem. Geophys. Geosyst.*, *9*(Q08002), doi:10.1029/2008GC002009.

Cann, J. R., D. K. Blackman, D. K. Smith, E. McAllister, B. Janssen, S. Mello, E. Avgerinos, A. R. Pascoe, and J. Escartín (1997), Corrugated slip surfaces formed at ridge-transform intersections on the Mid-Atlantic Ridge, *Nature*, *385*, 329-332, doi:10.1038/385329a0.

Cannat, M., et al. (1995a), Thin crust, ultramafic exposures, and rugged faulting patterns at the Mid-Atlantic Ridge (22°-24°N), *Geology*, *23*, 49-52, doi:10.1130/0091-7613(1995)023<0049:TCUEAR>2.3.CO;2.

Cannat, M., V. Mendel, E. Ruellan, K. Okino, J. Escartín, V. Combier, and M. Baala (2006), Modes of seafloor generation at a melt-poor ultraslow-spreading ridge, *Geology*, *34*(7), 605-608, doi:10.1130/G22486.1.

Carbotte, S. M., and D. S. Scheirer (2004), Variability of ocean crustal structure created along the global mid-ocean ridge, in Davis, E., and Elderfield, H., eds.,

Hydrogeology of the oceanic lithosphere: Cambridge, U.K., Cambridge University Press, 59-107.

Detrick, R. S., P. Buhl, E. E. Vera, J. C. Mutter, J. A. Orcutt, J. A. Madsen, and T. M. Brocher (1987), Multi-channel seismic imaging of a crustal magma chamber along the East Pacific Rise, *Nature*, *326*, 35-41.

Dick, H. J. B., M. A. Tivey, and B. E. Tucholke (2008), Plutonic foundation of a slow-spread ridge segment: The oceanic core complex at Kane Megamullion, 23°30'N, 45°20'W, *Geochem. Geophys. Geosyst.*, *9*, Q05014, doi:10.1029/2007GC001645.

Dunn, R. A., and D. W. Forsyth (2003), Imaging the transition between the region of mantle melt generation and the crustal magma chamber beneath the southern East Pacific Rise with short-period Love waves, *J. Geophys. Res.*, *108*(B7), 2352, doi:10.1029/2002JB002217.

Escartín, J., D. K. Smith, J. Cann, H. Schouten, C. H. Langmuir, and S. Escrig (2008), Central role of detachment faults in accretion of slow-spreading oceanic lithosphere, *Nature*, *455*, 790-794, doi:10.1038/nature07333.

Escartín, J., and J. P. Canales (2011), Detachments in Oceanic Lithosphere: Deformation, Magmatism, Fluid Flow, and Ecosystems, *Eos Trans. AGU*, *92*(4), doi:10.1029/2011EO040003.

Haymon, R. M., D. J. Fornari, M. H. Edwards, S. M. Carbotte, D. J. Wright, and K. C. Macdonald (1991), Hydrothermal vent distribution along the East Pacific Rise crest (9°09'-54'N) and its relationship to magmatic and tectonic processes on fast-spreading mid-ocean ridges, *Earth and Planet. Sci. Lett.*, *104*, 513-534.

Herron, T. J., P. L. Stoffa, and P. Buhl (1980), Magma chamber and mantle reflections - East Pacific Rise, *Geophys. Res. Lett.*, *7*, 989-992.

Hooft, E. E. E., R. S. Detrick, and G. Kent (1997), Seismic structure and indicators of magma budget along the southern East Pacific Rise, *J. Geophys. Res.*, *102*(B12), 27319-27340.

Kent, G. M., A. J. Harding, and J. A. Orcutt (1993a), Distribution of magma beneath the East Pacific Rise between the Clipperton transform and the 9°17'N deval from forward modeling of common depth point data, *J. Geophys. Res.*, *98*, 13,945-13,969.

Kent, G. M., A. J. Harding, and J. A. Orcutt (1993b), Distribution of magma beneath the East Pacific Rise near the 9°03'N overlapping spreading center from forward modeling of common depth point data, *J. Geophys. Res.*, *98*, 13,971-13,995.

Kong, L. S., R. S. Detrick, P. J. Fox, L. A. Mayer, and W. B. F. Bryan (1988), The morphology and tectonics of the MAR area from Sea Beam and Sea MARC I observations (Mid-Atlantic Ridge 23°N), *Mar. Geophys. Res.*, *10*, 59-90.

MacLeod, C. J., et al. (2002), Direct geological evidence for oceanic detachment faulting: the Mid-Atlantic Ridge, 15°45'N, *Geology*, *30*(10), 879-882.

Mutter, J. C., G. A. Barth, P. Buhl, R. S. Detrick, J. A. Orcutt, and A. J. Harding (1988), Magma distribution across ridge-axis discontinuities on the East Pacific Rise from multichannel seismic images, *Nature*, *336*, 156-158.

Mutter, J. C., S. M. Carbotte, W. Su, L. Xu, P. Buhl, R. S. Detrick, G. M. Kent, J. A. Orcutt, and A. J. Harding (1995), Seismic Images of Active Magma Systems Beneath the East Pacific Rise Between 17°05' and 17°35'S, *Science*, *268*, 391-395.

Mutter, J. C., S. M. Carbotte, J. P. Canales, and M. R. Nedimovic (2008), MGL0812 Cruise Report: A 3D MCS investigation of the magmatic-hydrothermal system at the East Pacific Rise 9°50'N.

Ohara, Y., T. Yoshida, and S. Kasuga (2001), Giant megamullion in the Parece Vela Backarc basin, *Marine Geophysical Researches*, *22*, 47-61.

Okino, K., K. Matsuda, D. M. Christie, Y. Nogi, and K. Koizumi (2004), Development of oceanic detachment and asymmetric spreading at the Australian-Antarctic Discordance, *Geochemistry, Geophysics, Geosystems*, *5*(12), Q12012, doi:10.1029/2004GC000793.

Penrose Conference Participants (1972), Penrose field conference on ophiolites, *Geotimes*, *17*, 24-25.

Reston, T. J., W. Weinrebe, I. Grevemeyer, E. R. Flueh, N. C. Mitchell, L. Kirstein, C. Kopp, H. Kopp, and et al. (2002), A rifted inside corner massif on the Mid-Atlantic Ridge at 5°S, *Earth and Planetary Science Letters*, *200*, 255-269.

Searle, R. C., M. Cannat, K. Fujioka, C. Mével, H. Fujimoto, A. Bralee, and L. M. Parson (2003), FUJI Dome: A large detachment fault near 64 E on the very slow-spreading southwest Indian Ridge, *Geochemistry, Geophysics, Geosystems*, *4*(8), 9105, doi:10.1029/2003GC000519.

Singh, S. C., G. M. Kent, J. S. Collier, A. J. Harding, and J. A. Orcutt (1998), Melt to mush variations in crustal magma properties along the ridge crest at the southern East Pacific Rise, *Nature*, *394*, 874-878.

Smith, D. K., J. R. Cann, and J. Escartín (2006), Widespread active detachment faulting and core complex formation near 13°N on the Mid-Atlantic Ridge, *Nature*, *442*, doi:10.1038/nature04950.

Smith, D. K., J. Escartín, H. Schouten, and J. R. Cann (2008), Fault rotation and core complex formation: Significant processes in seafloor formation at slow-spreading mid-ocean ridges (Mid-Atlantic Ridge, 13°-15°N), *Geochemistry, Geophysics, Geosystems*, in press.

Soule, S. A., D. J. Fornari, M. R. Perfit, and K. H. Rubin (2007), New insights into mid-ocean ridge volcanic processes from the 2005-2006 eruption of the East Pacific Rise, 9°46'N-9°56'N, *Geology*, *35*(12), 1079-1082.

Tucholke, B., and J. Collins (2001), Cruise Report R/V Ewing 01-02: Multichannel seismic reflection study of megamullions on the Mid-Atlantic Ridge.

Tucholke, B. E., J. Lin, and M. C. Kleinrock (1996), Mullions, megamullions, and metamorphic core complexes on the Mid-Atlantic Ridge, *Eos Transactions American Geophysical Union*, *77*, F724.

Tucholke, B. E., J. Lin, and M. C. Kleinrock (1998), Megamullions and mullion structure defining oceanic metamorphic core complexes on the Mid-Atlantic Ridge, *Journal of Geophysical Research*, *103*, 9857-9866.

Tucholke, B. E., K. Fujioka, T. Ishihara, G. Hirth, and M. Kinoshita (2001), Submersible study of an oceanic megamullion in the central North Atlantic, *Journal of Geophysical Research*, *106*(B8), 16,145-16,161.

Tucholke, B. E., M. D. Behn, R. Buck, and J. Lin (2008), The role of melt supply in detachment faulting and the formation of oceanic core complexes, *Geology*, *36*(6), 455-458; doi:10.1130/G24639A.

Williams, C. M. (2007), Oceanic lithosphere magnetization: marine magnetic investigations of crustal accretion and tectonic processes in mid-ocean ridge environments, Ph.D. thesis, 254 pp, Woods Hole Oceanographic Institution, Woods Hole.

Chapter 2

Waveform modeling of the seismic response of a mid-ocean ridge axial melt sill

Abstract

Seismic reflections from axial magma chambers (AMCs) are commonly observed along many mid-ocean ridges, and are thought to arise from the negative impedance contrast between a solid, high-velocity lid and the underlying low-velocity, partially molten sill. The polarity of the AMC reflection ($P_{AMC}P$) at vertical incidence is often used as a diagnostic tool for the nature of such low-velocity sill, and the contrasting amplitude versus offset (AVO) behaviors of the AMC reflections, e.g., $P_{AMC}P$ and S-converted $P_{AMC}S$ waves, for the melt and mush cases are exploited to investigate the physical property of the AMC. Here we use time-domain finite difference calculations of the 2D laterally homogeneous models to study the effect of structure features in controlling waveform polarities at near-offset and in AVO behaviors of the AMC reflections. For a thin AMC (thickness depends on frequency content of the signal), the waveform polarity of the top $P_{AMC}P$ reflection may be a poor indicator for the nature of the AMC sill because of the interference of the bottom $P_{AMC}P$ reflection, and the AVO behaviors of the top $P_{AMC}P$ and $P_{AMC}S$ reflections are also disrupted by the bottom AMC reflections. For a thick AMC, the bottom $P_{AMC}P$ reflection disrupts the AVO behavior of the $P_{AMC}S$ reflection. Any of these two scenarios would make the qualitative analysis of melt content from partial-offset stacks of P- and S-waves less clear and more difficult to interpret. Laterally heterogeneous models are calculated to investigate the effects of flat/rough seafloor topography and the finite-width of the AMC. The finite-width AMC causes diffractions at its edges, reducing the amplitude of the AMC reflections. Rough seafloor and/or rough AMC surface can also greatly reduce the amplitude of peg-leg multiples because of the scattering and destructive interference. Sub-AMC events are observed in the 3D multi-channel seismic dataset acquired over the RIDGE-2000 Integrated Study Site at East Pacific Rise (cruise MGL0812). The seismic phases identified from the synthetic modeling of a realistic model suggest that the sub-AMC reflections are unlikely to arise from peg-leg multiples of the AMC reflections, P-to-S converted phases, or scattering due to rough topography, but could potentially arise from deeper multiple magma sills.

2.1. INTRODUCTION

During the last few decades there have been a number of geophysical studies aimed at determining the distribution of melt within the crust beneath fast-spreading ridge axes [e.g., *Detrick et al.*, 1987]. The East Pacific Rise (EPR) 9°N was chosen as one of the sites of study following an earlier discovery of a bright seismic reflector beneath the ridge axis which was interpreted as the roof of an axial magma chamber (AMC) [*Herron et al.*, 1980]. The EPR 9-10°N is also a RIDGE-2000 Integrated Study Site (ISS) because of its abundance of hydrothermal sites where scientists are investigating the linkages between mantle flow, crustal accretion, volcanic, hydrothermal, and biological processes that result in chemical and physical exchanges of energy and matter between the Earth's mantle and oceans. In Summer 2008, the first academic multi-streamer 3D seismic reflection experiment of the new national seismic imaging facility, the R/V *Marcus G. Langseth* was conducted, focusing on the EPR 9°50'N. The primary goals of expedition MGL0812 were to use this multi-streamer capability to create an accurate 3D seismic reflection image of the magmatic-hydrothermal system within the EPR 9°50'N site by imaging the structure of the AMC lid and shallow oceanic crust at a resolution, geometric accuracy, and scale comparable to seafloor observations of hydrothermal, biological, and volcanic activity [*Mutter et al.*, 2008].

The preliminary inspection of along-axis seismic data shows clear AMC reflections at two-way traveltime (TWTT) ~4.0 s and prominent reflections at and near the ridge axis at traveltimes corresponding to middle and lower crustal levels ("sub-AMC event" in

Figure 2-1). If these events remain a robust feature after 3D imaging and migration of the 3D dataset, one would be tempted to interpret them as deep sills, which would have important implications for models regarding the formation of the lower oceanic crust. Currently two end-member models have been proposed: The "gabbro glacier" model, in which the lower crust is created by plastic deformation of minerals deposited at the bottom of a single, shallow melt lens [*Quick and Delinger*, 1993]. And the "multiple melt sill" model, in which the entire lower crust is created from melt rising upward from the mantle, in the form of episodic injections, melt sills at multiple levels, and/or continuous melt percolation [*Korenaga and Kelemen*, 1997].

However, interpretations of deep reflectors should be done carefully because it is known that apparent deep reflections can arise from a variety of reasons. For example, (1) multiples or reverberations within layer 2A or within the AMC sill, (2) *P* to *S* conversions at the seafloor, base of layer 2A, or top of the AMC, or (3) reflections from the bottom of the AMC sill are all potential scenarios that can produce significant energy that could be misinterpreted as deep lower crustal sills. Therefore careful identification of these potential scenarios will be critical to correctly interpret 3D seismic volumes arising from the MGL0812 experiment.

In this study, we employ a time-domain finite difference (TDFD) method to image wave propagation in complex, seafloor/sub-seafloor fluid-solid geometries [e.g., *Dougherty and Stephen*, 1991], which has been successfully used to model seismic

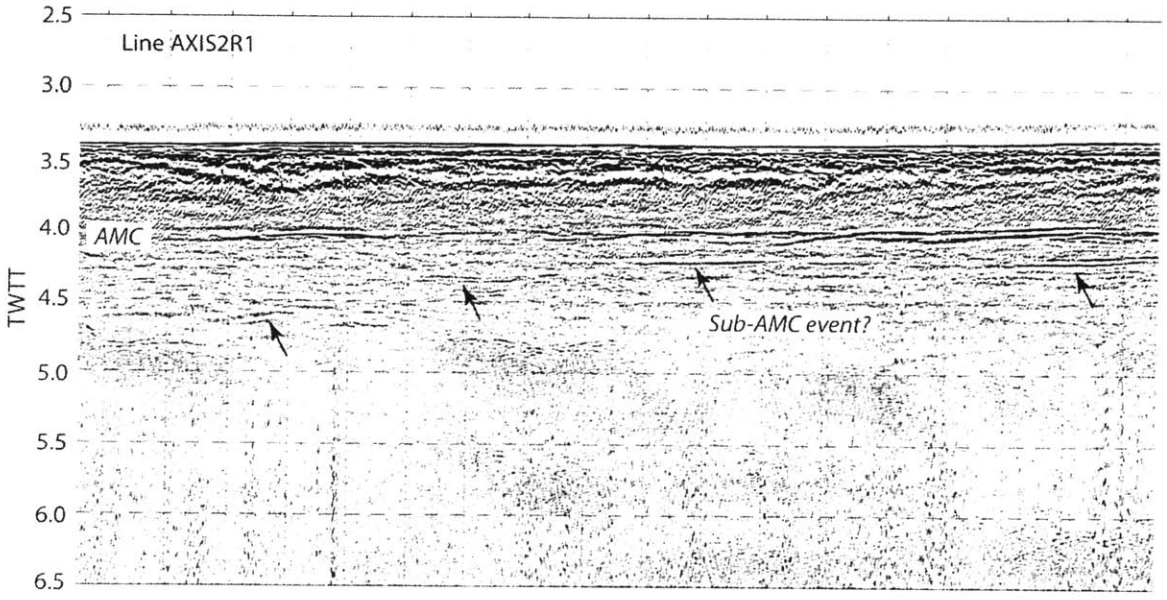

Figure 2-1. A brute stack example of an along-axis line AXIS2R1 acquired from the 3D multi-channel seismic dataset (cruise MGL0812). The clear axial magma chamber (AMC) reflection is labeled at two-way traveltime (TWTT) ~4.0 s. The arrows indicate clear observed sub-AMC reflection events.

propagation at ~10 Hz through a 2D representation of an AMC with a thin, liquid lid [*Swift et al.*, 1990]. Ideally, features in the reflection survey observations could be numerically modeled to confirm the interpretation of the melt distribution geometry (e.g., thickness and width of AMC, and melt sills layering) and the physical properties (e.g., compressional wave velocity *Vp* and shear wave velocity *Vs* within AMC) of the sub-axis structure. We use synthetic forward models to evaluate how different model parameters affect the polarity and the amplitude versus offset (AVO) behavior of waves reflected off the AMC. This information provides a context in which to frame the interpretations made in the following thesis Chapter 3 regarding the nature and physical properties of the AMC obtained from 1D waveform inversions [e.g., *Collier and Singh*, 1997], and their along-axis variability inferred from partial-offset stacking of *P* and *S*-converted waves [e.g., *Singh et al.*, 1998]. We also use the results of the TDFD calculations to provide insights into the plausible origins and nature of the observed sub-AMC reflectivity (Figure 2-1).

2.2. MODEL SETUP

The full wave equation in 2D is modeled using the TDFD method (see Appendix 2-A), which has been benchmarked for range-dependent problems and complex models, including velocity gradients and strong lateral heterogeneities [*Stephen*, 1990]. The model input is given by compressional (*Vp*) and shear (*Vs*) wave velocities and density (ρ) at all grid points. Attenuation is not considered in this study. A free surface on the top of the model is simulated with two grid layers set to *Vp* = 1e-8 km/s, *Vs* = 0 km/s, and ρ = 1000 kg/m^3. Absorbing boundaries based on the formulations of *Reynolds* [1978],

Higdon [1986] and *Clayton and Engquist* [1977] are used to reduce reflections from the grid boundaries.

We first considered two kinds of laterally homogeneous models: simple, constant-velocity-layer models consisting of 4 layers (hereinafter referred to as simple layered models, Figure 2-2) were used to investigate the polarities and AVO behaviors of the AMC reflections. A second set of laterally homogeneous model incorporating realistic crustal structures based on previous seismic observations and interpretations, hereinafter referred to as a realistic model (ESP05, Figure 2-3), was used to identify synthetic seismic phases.

Next we explored the effects of lateral heterogeneity by limiting the width of the AMC, and introducing seafloor topography by hanging two composites of laterally homogeneous structures below a rough seafloor interface (Figure 2-4).

2.2.1. Laterally Homogeneous Models

2.2.1.1. Simple Layered Models

The simple layered model includes 4 homogeneous layers: water, upper crust, AMC, lower crust (Figure 2-2). Because our study is focused on the seismic phases reflected off the AMC, we did not include a mantle layer in the model. Model parameters are listed in Table 2-1. Two kinds of AMC are considered in the simple layered model: melt case with Vs = 0 km/s and mush case with Vs = 2.0 km/s within the AMC. Model parameters such

as AMC thickness and the velocity structure immediately above the AMC can be modified to investigate their effects on the polarities and AVO behaviors of waveforms reflected off the AMC.

2.2.1.2. Realistic Model ESP05

Model ESP05 (Figure 2-3a) was adapted from the velocity and density structures of zero-age oceanic crust at 9°30'N on the EPR from an expanded spread profile (ESP) [*Vera et al.*, 1990]. The water depth is 2536 m in the model. In this model, an 80-m-thick high *Vp* (6.25 km/s) layer over a 300-m-thick layer with negative velocity gradient (*Vp* decreases from 6.25 to 4.5 km/s, and *Vs* from 3.38 to 2.9 km/s) overlay the AMC (Figure 2-3b). The AMC sill has a thickness of 180 m and is located 1.6 km below the seafloor.

2.2.2. Laterally Heterogeneous Models

A laterally heterogeneous model was created by laying the homogeneous model ESP05 (Figure 2-3) below the seafloor following flat/rough seafloor topography, and by limiting the width of the AMC (Figure 2-4). The seafloor topography is taken from a ridge-axis-perpendicular cross-section profile EPR3D1772P (cruise MGL0812). The AMC is located horizontally in the middle of the model with a width of 0.5 (not shown in Figure 2-4) or 2.0 km (shown in Figure 2-4). For the on-axis section, the velocity and density structures are the same as model ESP05; while for the off-axis section, we eliminated the low velocity AMC layer. The horizontal and vertical model dimensions used for the TDFD synthetic CMP gather calculations are 7 and 12 km, respectively.

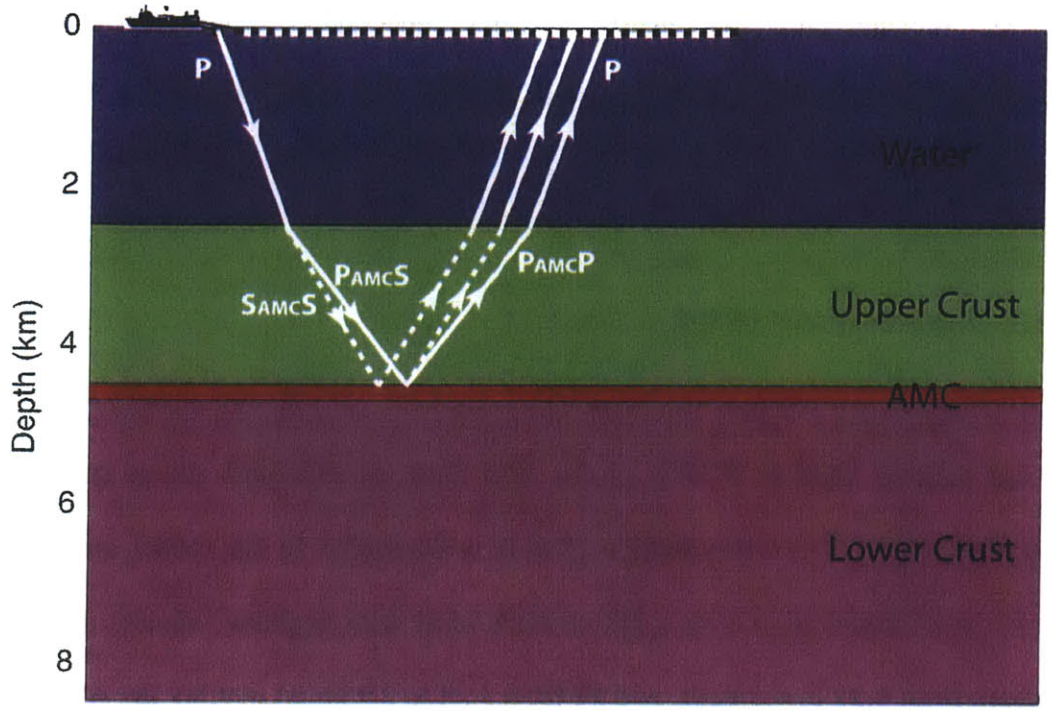

Figure 2-2. Simplified oceanic crust structure model and schematic ray paths for the AMC reflections *P*AMC*P*, *P*AMC*S* and *S*AMC*S*. Two cases of the AMC layer are investigated in this study: the melt case with Vs = 0 km/s, while the much case with Vs = 2.0 km/s within the AMC. The *P*- and *S*-wave propagation paths are indicated by the solid white lines and dashed white lines, respectively. Model parameters are listed in Table 2-1.

Table 2-1. Simple Layered Model Parameters (see Figure 2-2)

Layer		Layer Thickness (km)	Vp (km/s)	Vs (km/s)	ρ (kg/m^3)
Water		2.5	1.5	0	1000
Upper Crust		2.0	6.25	3.65	2700
AMC	Melt Case	0.2	3.0	0	2700
	Mush Case	0.2	3.0	2.0	2700
Lower Crust		3.8	7.4	4.25	3200

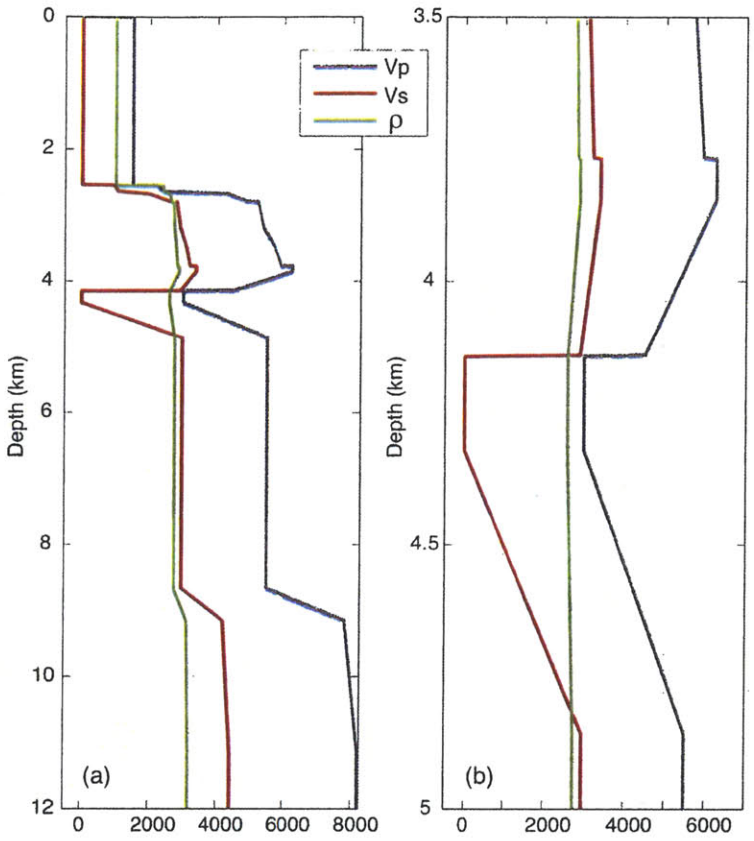

Figure 2-3. (**a**) A representative "realistic" model ESP05 used for time-domain finite difference (TDFD) calculations. (**b**) Expanded view of the ESP05 structure around the AMC. The water depth is 2,536 m, with 0 km depth representing the sea surface. The compressional- (*Vp*, blue lines) and shear- (*Vs*, red lines) wave velocities are measured in m/s, and density (ρ, green lines) is measured in kg/m^3.

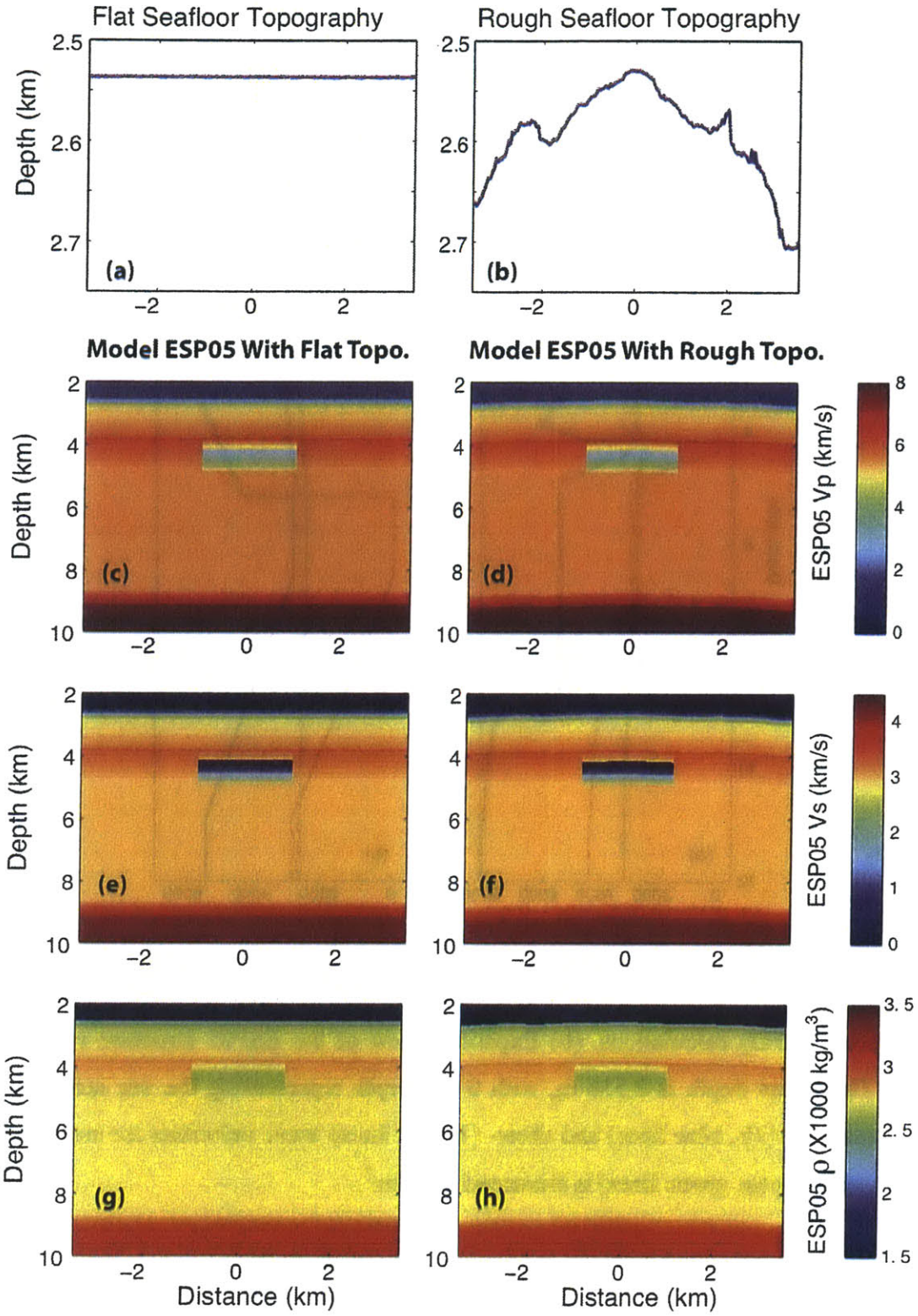
Flat Seafloor Topography
Rough Seafloor Topography
Depth (km)
(a)
(b)
Model ESP05 With Flat Topo.
Model ESP05 With Rough Topo.
(c)
(d)
(e)
(f)
(g)
(h)
ESP05 Vp (km/s)
ESP05 Vs (km/s)
ESP05 ρ (X1000 kg/m3)
Distance (km)

Figure 2-4. Two representative laterally heterogeneous models used for TDFD calculations to study the effects of a finite-width AMC and actual topography on cross-axis common-midpoint (CMP) gathers. **(a)** A flat seafloor topography with a water depth of 2,536 m. **(b)** A rough seafloor topography taken from a ridge-axis-perpendicular cross-section profile EPR3D1772P (cruise MGL0812). (**c**, **e**, **g**) Compressional wave velocity (Vp), shear wave velocity (Vs), and density (ρ) structures with a flat topography. (**d**, **f**, **h**) Compressional wave velocity (Vp), shear wave velocity (Vs), and density (ρ) structures with a rough topography. For the on-axis section, the velocity and density structures are the same as model ESP05 (Figure 2-3), while for the off-axis section, the low velocity AMC layer is eliminated. The AMC is located horizontally in the middle of the model with a width of 2.0 km (shown) and 0.5 km (not shown here). The horizontal and vertical model dimensions are 7 km × 12 km. The compressional and shear wave velocities are measured in km/s, and the density is measured in kg/m^3.

2.3. TIME-DOMAIN FINITE DIFFERENCE MODELING

The synthetic seismograms from TDFD calculations are expressed as time series of pressure. For the laterally homogeneous models, the synthetic seismograms are recorded in common-shotpoint (shot) gathers. For laterally heterogeneous models, the synthetic seismograms are recorded in common-midpoint (CMP) gathers. The source-receiver geometry for calculating synthetic shot and CMP gathers can be found in Appendix 2-B. Computing synthetic CMP gathers for laterally heterogeneous models is very computationally intensive because individual runs must be carried out for every source position with respect to the structure (i.e., a 78-fold synthetic CMP gather requires 78 different individual TDFD runs).

2.3.1. Benchmark Study: Comparison to Theoretically Computed Displacement Reflection Coefficients of AMC Reflection Waveforms

To test the feasibility of using the TDFD method to model seismic reflections off the AMC, we first consider the two simple layered models for the melt and mush cases. The predicted AVO behavior of the AMC reflections are compared with theoretically computed displacement reflection coefficients. The melt and mush cases only differ from each other in the *Vs* structure within the AMC layer: melt case indicates *Vs* = 0 km/s, while mush case indicates *Vs* = 2.0 km/s in the benchmark study. The simplified crustal model and schematic ray paths for AMC reflections are shown in Figure 2-2.

The theoretical calculations of the displacement reflection/transmission coefficients

of solid/solid, solid/liquid, and liquid/solid boundaries follow the equations of *Aki and Richards* [2002], *Nafe* [1957], and *Ergin* [1952]. The source and receivers are located at the sea surface. The theoretically computed reflection coefficients of AMC reflected waves, $P_{AMC}P$, $P_{AMC}S$, and $S_{AMC}S$ are plotted versus horizontal slowness and source-receiver offsets for a *P*-wave incident at seafloor (Figure 2-5). These reflection coefficients are much smaller than similar calculations by *Singh et al.* [1998] because our calculation includes wave propagation both in the water layer and the upper crust. From the comparison of the theoretically computed reflection coefficients of melt and mush cases, we expect to see that (1) a phase reversal occurs for $P_{AMC}P$ reflection in the case of melt, (2) a phase reversal occurs for $S_{AMC}S$ reflection in the case of mush, (3) the difference of the $P_{AMC}P$ reflection coefficient at the near- and far-offset is much larger for the melt case than for the mush case, and (4) $P_{AMC}S$ reflection has a much higher reflection coefficient for the melt case than for the mush case. Although $S_{AMC}S$ waves are theoretically possible, their presence is hard to detect in MCS field data because of the higher attenuation for shear wave propagation. The contrasting AVO behaviors of $P_{AMC}P$ and $P_{AMC}S$ reflections at 2-4 km offset for the melt case compared with the mush case can be used in a partial-offset stacking approach to identify the presence of melt-rich and melt-poor sections of the AMC [*Singh et al.*, 1998], as we do in the following thesis Chapter 3.

The geometry of the source-receiver pattern for the TDFD synthetic shot gather calculation is the same as a single-streamer MCS survey (see Appendix 2-B). The

synthetic seismograms of the two AMC cases are shown in Figure 2-6. All the principal phases, including the seafloor reflection, *P*- and *S*-head waves propagating along the seafloor interface, and both the top and bottom AMC reflections are identified based on the traveltime calculated using ray theory. The synthetic seismograms also clearly demonstrate the existence of phases that are theoretically possible but rarely seen in marine seismic data, such as *P*- and *S*-head waves, and *S*-converted phase $S_{AMC}S$.

Here we focus on a discussion of AVO behaviors of waves reflected off the AMC, i.e., $P_{AMC}P$, $P_{AMC}S$, and $S_{AMC}S$, and compare them to the theoretical calculations (the AVO behaviors of seafloor reflection, and *P*- and *S*-head waves only depends on the contrast between the water and upper crustal layer, which is the same for both models). For the melt case, the synthetic shot gather (Figure 2-6a) shows that: (1) the amplitude of $P_{AMC}P$ wave reflected from the top of the AMC first decreases with offset to zero amplitude at ~3.5 km, and then increases with polarity reversed with respect to the near-offset; (2) the amplitude of $P_{AMC}P$ wave reflected from the bottom of the AMC basically decreases in the whole offset range; (3) the amplitude of $P_{AMC}S$ wave sharply increases with offset to ~3.0 km, and then decreases slowly before it becomes contaminated with sea floor reflections, making the AVO behavior analysis in the far-offset difficult; and (4) the amplitude of $S_{AMC}S$ wave increases in the near offset and then decreases in the far-offset, and the maximum amplitude is at ~2.5 km offset. For the mush case, the synthetic shot gather (Figure 2-6b) shows that: (1) the amplitude of $P_{AMC}P$ wave reflected from the top of the AMC slowly decreases with offset, and the phase does not show any polarity

change; (2) similar to the melt case, the amplitude of $P_{AMC}P$ wave reflected from the bottom of the AMC basically decreases in the whole offset range; (3) the amplitude of the $P_{AMC}S$ wave increases with offset to the maximum amplitude at ~2.5 km and then decreases in the far offset, and the amplitude is much smaller when compared to the melt case in the far offset; and (4) the amplitude of $S_{AMC}S$ wave is very small in the near offset and sharply increases in the far offset. Although the discussion is somewhat affected by the interference of the AMC reflections with the seafloor reflection in the far offset, the AVO behaviors of the AMC reflected waves summarized from the synthetic shot gathers for both the melt and mush cases are totally consistent with the theoretical calculations (Figure 2-5).

The comparison of the synthetic shot gathers between the melt and mush case indicates that: (1) a phase reversal occurs for $P_{AMC}P$ wave in the melt case; (2) the melt case has smaller amplitude of $P_{AMC}P$ wave at offset from 2.0 to 4.0 km than the mush case; and (3) $P_{AMC}S$ wave has much higher amplitude for the melt case than for the mush case in the far offset. These differences between the two AMC cases have been exploited for qualitatively imaging melt and mush distributions along ridge axes [*Canales et al.*, 2006; *Singh et al.*, 1998]. More details about the *P*- and *S*-wave partial-offset stacking can be found in the following thesis Chapter 3. The agreement of the AVO behaviors of the waves reflected off the AMC between the TDFD synthetic calculations and the theoretical computed reflection coefficients demonstrates the ability of the TDFD method to model range-dependent seafloor and AMC features.

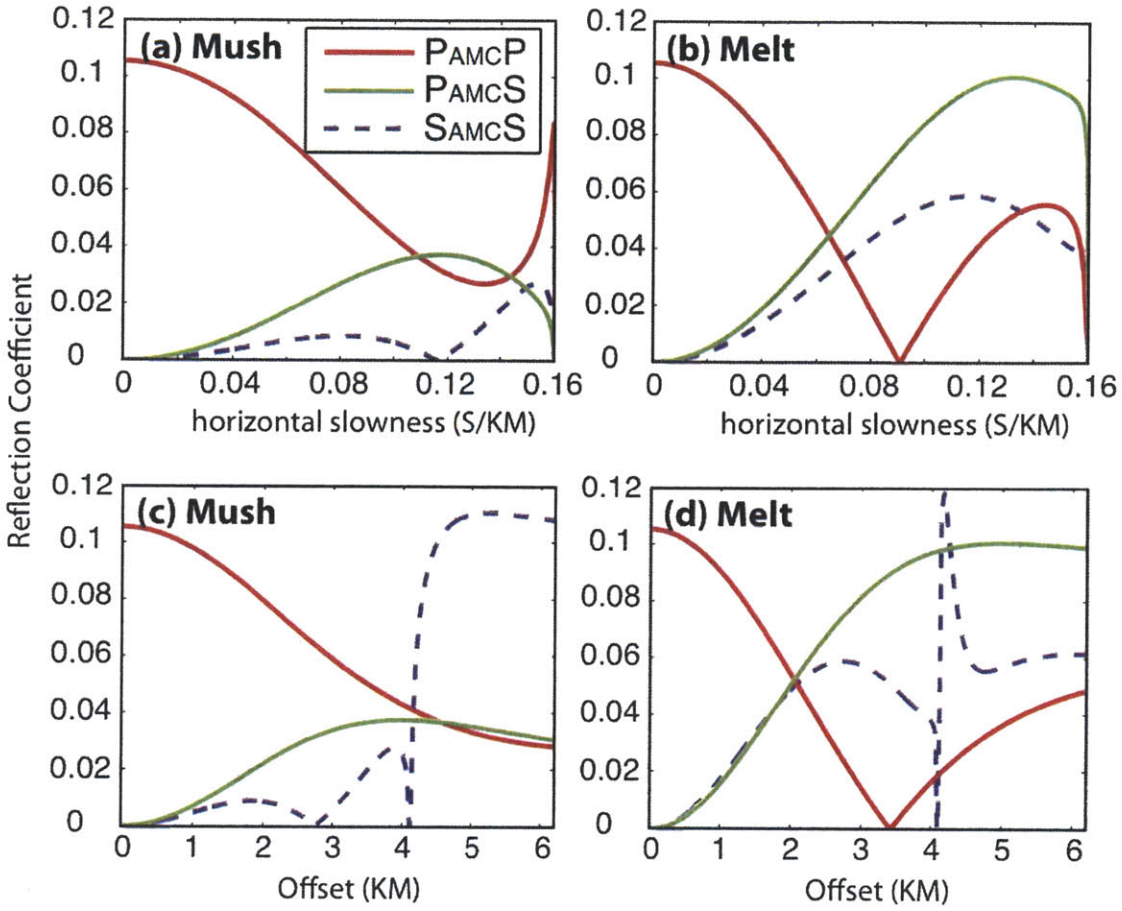

Figure 2-5. (**a**, **b**) Theoretically computed reflection coefficients (displacement) for *P*AMC*P* (solid red), *P*AMC*S* (solid green), and *S*AMC*S* (dashed blue) waves plotted versus horizontal slowness for a *P*-wave incident at seafloor. Two AMC cases are shown: (**a**) the mush case with Vs = 2.0 km/s within the AMC, and (**b**) the melt case with Vs = 0 km/s within the AMC. (**c**, **d**) Reflection coefficients plotted versus source-receiver offsets. The source and receivers are located at sea surface. The simplified oceanic crustal model and schematic ray paths for the AMC reflections *P*AMC*P*, *P*AMC*S* and *S*AMC*S*, are shown in Figure 2-2, and the model parameters used in these calculations are shown in Table 2-1.

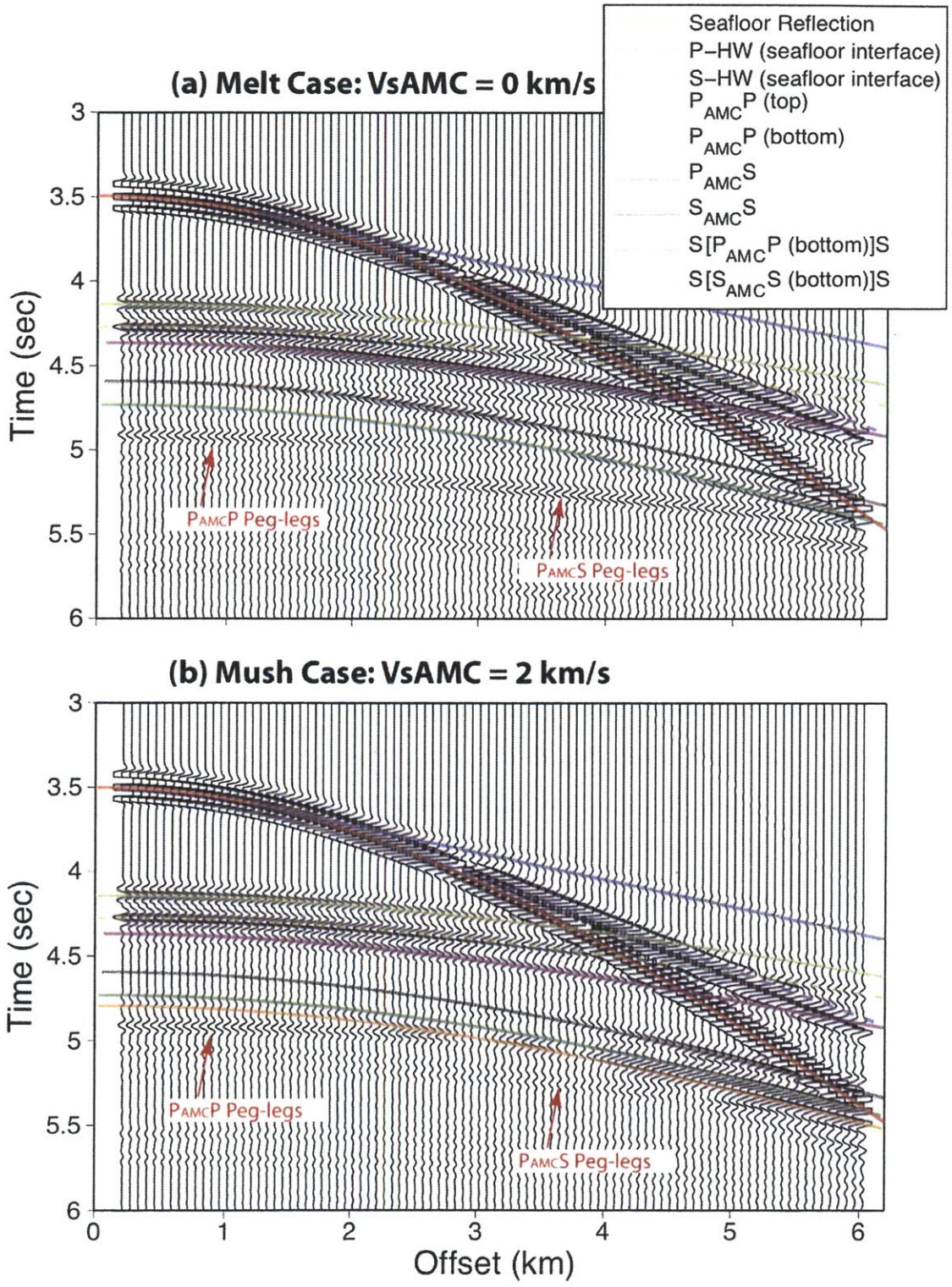
(a) Melt Case: VsAMC = 0 km/s
(b) Mush Case: VsAMC = 2 km/s
Seafloor Reflection
P–HW (seafloor interface)
S–HW (seafloor interface)
P_AMC P (top)
P_AMC P (bottom)
P_AMC S
S_AMC S
S[P_AMC P (bottom)]S
S[S_AMC S (bottom)]S
PAMCP Peg-legs
PAMCS Peg-legs
Time (sec)
Offset (km)
3
3.5
4
4.5
5
5.5
6
0
1
2
3
4
5
6

Figure 2-6. Synthetic seismograms (expressed as time series of pressure) plotted as a function of offset for (**a**) the melt case and (**b**) the mush case. The schematic oceanic crustal model used for the TDFD calculation is shown in Figure 2-2, and the model parameters are listed in Table 2-1. The AMC thickness is 200 m. The compressional point source and receivers are located at 7.5 m below the sea surface, and the source-receiver offset ranges from 200 to 6037.5 m at an interval of 12.5 m, i.e., 468 channels. Every fifth trace is shown. Colored lines indicate all the principal seismic phases, including seafloor reflection, pure *P*- and *S*-head waves (generated at the seafloor interface), top AMC reflections ($P_{AMC}P$, $P_{AMC}S$ and $S_{AMC}S$), and bottom AMC reflections ($S[P_{AMC}P(bottom)]S$ and $S[S_{AMC}S(bottom)]S$) based on the calculated traveltime using ray theory (Note that the traveltime curves do not represent the time of the arrivals' first break; they have been delayed to match the maximum peak of the arrivals to facilitate the phase identification). The $P_{AMC}P$ and $P_{AMC}S$ peg-leg multiples are also indicated.

2.3.2. Simple Layered Model Studies

2.3.2.1. Polarity Analyses of AMC Reflection Waveforms

Seismic reflections from the AMC arise from the large impedance contrast between a solid, high-velocity sheeted dike section and an underlying sill, presumably a partially molten, low-velocity feature [e.g., *Karson et al.*, 2002]. The polarity of the $P_{AMC}P$ wave at near-vertical incidence is often used as a diagnostic tool for the nature of the AMC sill, with a reversed polarity (with respect to the polarity of the positive-impedance seafloor reflection) commonly interpreted as indicating the presence of a low-velocity, partially molten sill [e.g., *Singh et al.*, 2006]. However, crustal architecture is complex; other crustal features can affect the polarity of the AMC reflection in a way that absence of observed reversed polarity in MCS data should not necessarily be interpreted as absence of a molten sill.

Here we investigate the effects of free-surface interference, AMC thickness, and velocity gradient above the AMC on the polarity of $P_{AMC}P$ waves reflected off the AMC by using the TDFD calculations. The discussion here will focus on the synthetic seismograms recorded at 200 m offset.

2.3.2.1.1. Effect of Free-Surface Interference

In a typical single-streamer marine seismic experiment, a hydrophone streamer is towed behind a survey vessel. Acoustic signals, commonly referred to as "shots", are produced by the seismic source. Seismic waves travel down through the water column

into the sub-seafloor, where they are reflected from the various geologic strata and travel back to the sea surface. Sources and receivers are usually located a few meters below the sea surface, which results in interference between waves reflected at the sea surface (which have inverted polarity because of the air/water interface) and the downgoing and upgoing waves. The sea surface reflected signals are known as "ghosts". We take the melt case model (Figure 2-2) for example to examine how the "ghost" affects the polarity of recorded waves. The direct arrival, seafloor reflection and $P_{AMC}P$ waves reflected from both the top and bottom of the AMC layer are recorded at 200 m offset, while the seafloor incident wave is recorded on a deeper receiver (i.e., ~80 m offset and ~2000 m below sea surface) located on the seafloor reflection propagation path. Figure 2-7 shows the waveform amplitudes scaled to the emitted source in a half-second time window. We assume that the positive peak of the recorded source waveform represents the zero-time and the polarity of the source waveform. We then use traveltimes calculated using ray theory to identify changes in waveform and polarity as the waves propagate through the model. We note that: (1) interference with free-surface reflections changes the waveform shapes, making waveforms more complicated and anti-symmetric, e.g., compare the emitted source waveform with the direct arrival or the seafloor incident waveforms; (2) the seafloor reflection and AMC reflected $P_{AMC}P$ waveforms are approximately symmetric; (3) the polarity of the top AMC reflected $P_{AMC}P$ waveform is reversed with respect to that of the seafloor reflection, and this reversal is not masked *a posteriori* by free-surface interferences with the upgoing wave. This exercise demonstrates that free-

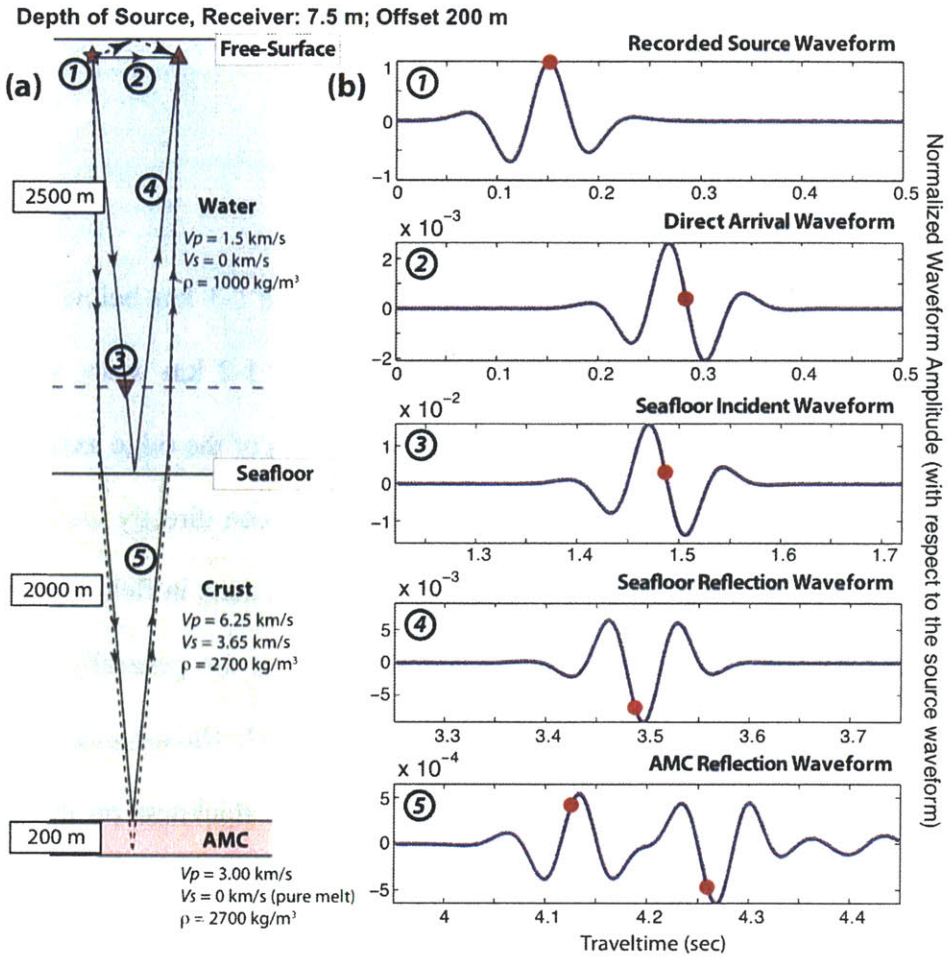

Figure 2-7. Effect of free-surface interference on polarity behavior of AMC reflected waveforms. (**a**) Schematic oceanic crustal model and ray paths for the 200 m source-receiver offset. The model parameters and source-receiver geometry pattern are indicted. The red star represents the seismic source, the triangle represents the receiver for recording the direct arrival, seafloor reflection, and AMC reflection waveforms, and the inverted triangle represents the receiver for recording the seafloor incident waveform. (**b**) The normalized waveforms (with respect to the recorded source waveform) shown in a half second window are (1) recorded source waveform, (2) direct arrival waveform, (3) seafloor incident waveform, (4) seafloor reflection waveform, and (5) top and bottom $P_{AMC}P$ reflection waveforms. Red dots are theoretically computed arrival times delayed by 0.152 s so that the peak of the recorded source waveform corresponds to zero-time.

surface interference does not have a detectable impact on the polarity of the waveforms reflected off the AMC.

2.3.2.1.2. Effect of the AMC Thickness

The AMCs along active spreading centers are located 1-3 km below the seafloor based on seismic imaging of their roof. They are usually 1-2 km wide, with extreme values between 0.25 km and 4.15 km beneath different parts of the ridge axis [*Kent et al.*, 1990, 1993a, 1993b]. The thickness of the AMC has not been directly well constrained because of the lack of robust evidence for basal AMC reflections in field data. However, investigations through waveform modeling suggest that they are generally about 100 m thick [*Canales et al.*, 2006] or less [*Collier and Singh*, 1997; *Hussenoeder et al.*, 1996; *Singh et al.*, 1998]. Here we investigate the effect of AMC thickness on the polarity of $P_{AMC}P$ waveforms reflected from the top and bottom of the AMC in the frequency band of our TDFD calculations (Figure 2-A). We change the AMC thickness in the melt case model, from 50 to 500 m with an interval of 50 m. The polarities of the top and bottom $P_{AMC}P$ reflections are identified by the peak amplitude positions (Figure 2-8). We note that for the AMC thicker than 150 m, $P_{AMC}P$ reflections from the top and bottom of the AMC do not interfere with each other, allowing comparison between the waveforms of the seafloor reflection and the top AMC reflection. For a thinner AMC, however, $P_{AMC}P$ reflections from the top (phase reversed) and bottom (phase not reversed) of the AMC interfere with each other, making them indistinguishable or difficult to identify their polarities (e.g., AMC thickness of 100 m in Figure 2-8). Therefore, for a thin AMC

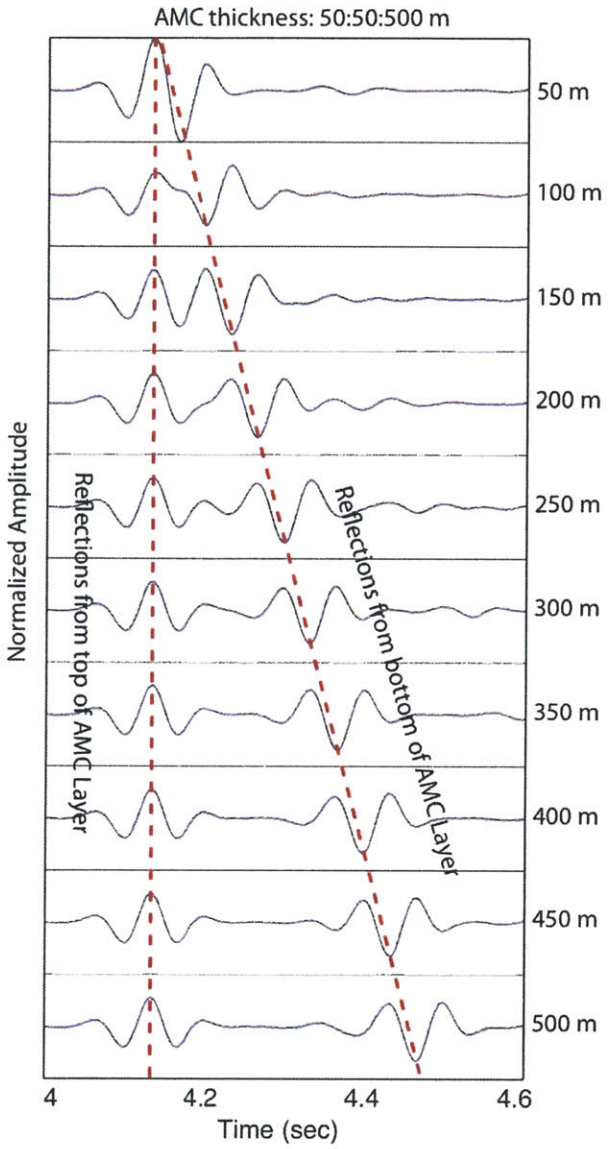

Figure 2-8. Effect of AMC thickness on polarity behavior of AMC reflected $P_{AMC}P$ waveforms. The synthetic seismograms are recorded at 200 m offset. The model is based on the melt case model (Figure 2-2) by varying the AMC thickness from 50 to 500 m at an interval of 50 m. Top (phase reversed with respect to the seafloor reflection) and bottom (phase not reversed) AMC reflections $P_{AMC}P$ are identified and plotted aligned with peak amplitude position of the top reflections.

(thickness depends on frequency content of the signal), the waveform polarity of the top AMC reflection $P_{AMC}P$ may be a poor indicator for the nature of the axial sill.

2.3.2.1.3. Effect of Velocity Gradient Layer above the AMC

Previous studies based on modeling of refraction data showed that immediately above the AMC, there is a zone of large negative velocity gradient where compressional wave velocity decreases from ~6.3 km/s to 3 km/s over a depth of approximately 300 m [*Vera et al.*, 1990] (see model ESP05 in Figure 2-3). The waveform inversion of long-offset reflection data provides a much better constraint on the detailed *P*- and *S*-wave velocity structures of the roof and floor of the AMC. *Singh et al.* [1999] observed that the AMC at southern EPR is overlain by a 50-60 m thick, high-velocity (6.0-6.2 km/s) roof layer and is underlain by at least a 150-200 m thick high-velocity floor, i.e., the AMC is bounded by a solid roof and a solid floor. Here we investigate the effect of this negative velocity gradient (solid roof) on the polarity of $P_{AMC}P$ waveforms reflected from the top and bottom of the AMC at 200 m offset. The models are modified from the melt case model (Figure 2-2) by adding a negative gradient layer above the AMC, and the gradient is controlled by the thickness of this new layer (e.g., 0-200 m, see Figure 2-9). To demonstrate the gradient cases both with and without interference between the top and bottom AMC reflections, we also change the thickness of the AMC from 50 to 200 m with an interval of 50 m. The 0 m thickness of the gradient layer, i.e., no gradient layer added above the AMC is also calculated and used as a reference for comparison. We note that the top $P_{AMC}P$ reflection decreases in amplitude as the thickness of the gradient layer

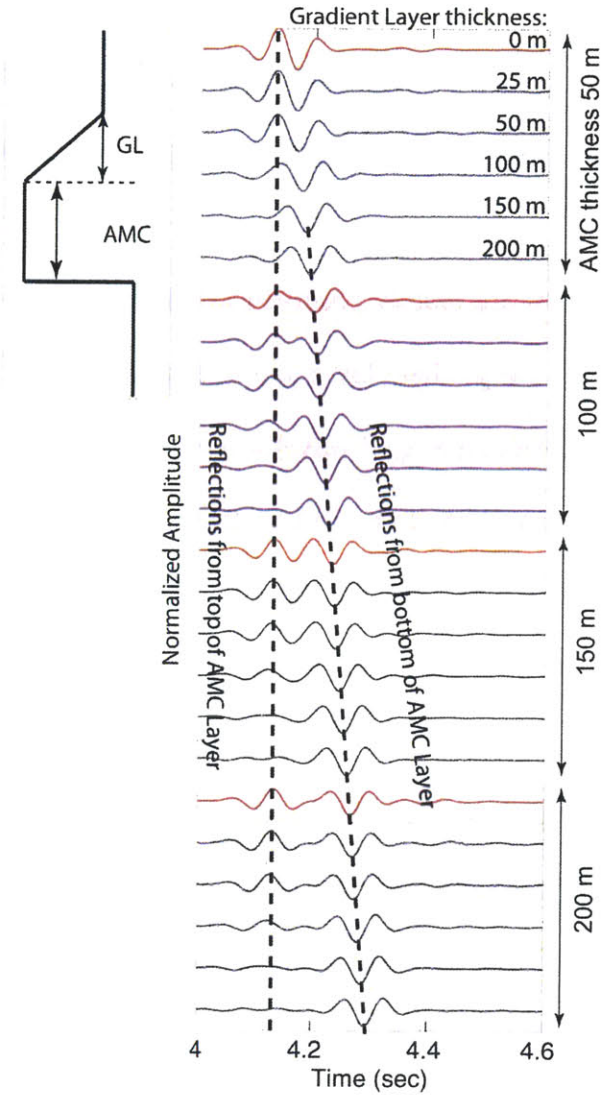

Figure 2-9. Effect of the velocity gradient layer (above the AMC) on the polarity behavior of AMC reflected $P_{AMC}P$ waveforms. The AMC thickness varies from 50 to 200 m at an interval of 50 m, and the corresponding AMC reflected $P_{AMC}P$ waveforms are indicated by different background colors. The gradient layer thickness ranges from 0 to 200 m. The synthetic seismograms are recorded at 200-m offset. The seismograms shown in red color are the calculations without gradient layer, and used as references for comparisons. The insert shows the schematic model of the gradient layer (GL) above the AMC. The gradient is controlled by the thickness of this layer.

increases, and eventually disappears. For the very thin AMC cases, e.g., 50-m-thick, the amplitude of the top $P_{AMC}P$ reflection decreases slower than thick AMC cases, e.g., 200-m-thick, because of its interference with the bottom $P_{AMC}P$ reflection (Figure 2-9).

Two important effects are readily observed in this exercise. First, for a thin AMC, the combined effect of a top gradient layer and interference of the bottom reflection can produce the top AMC reflection $P_{AMC}P$ waveform with polarity not reversed with respect to seafloor reflection waveform (e.g., AMC thickness of 50 m and gradient layer thickness of 200 m, Figure 2-9). And second, for a thicker AMC where reflections from the top and bottom of the AMC are well separated from each other, a thick top gradient layer can make the top $P_{AMC}P$ reflection effectively inexistent (e.g., AMC thickness thicker than 100 m and gradient layer thickness thicker than 150 m, Figure 2-9). In such cases, reflections from the bottom of the AMC could be misinterpreted as reflections from the top of the AMC. This exercise indicates that the observed polarity of the $P_{AMC}P$ could be an unreliable indicator of the nature of the AMC sill if there is a gradient zone above the AMC.

2.3.2.2. AVO Analyses of AMC Reflection Waveforms

The effect of the AMC thickness on the polarity of $P_{AMC}P$ reflections has been investigated focusing on the synthetic seismograms recorded at 200-m offset (see section 2.3.2.1.2). Here we investigate its effect on the AVO behavior of the AMC reflections, including $P_{AMC}P$ (from both the top and bottom of the AMC), $P_{AMC}S$, and $S_{AMC}S$ waves,

for the whole offset range. The models used for the TDFD calculations are based on the simple layered melt/mush case model by changing the AMC thickness to 50 and 340 m. The geometry of the source-receiver pattern for the TDFD synthetic shot gather calculation corresponds to that of a single-streamer MCS survey with receivers located from 200 to 6037.5 m at an interval of 12.5 m (see Appendix 2-B).

Synthetic seismograms were calculated for 50- and 340-m-thick AMC sills (Figures 2-10 and 2-11, respectively) for both the melt and mush cases. For the 50-m-thick AMC cases, the synthetic shot gathers (Figure 2-10) show that the interference between the top and bottom $P_{AMC}P$ reflections persists throughout the whole offset range. The interference disrupts the AVO behavior of the top $P_{AMC}P$ reflection, making the apparent amplitude of the top $P_{AMC}P$ reflection strong for both the melt and mush cases. The main consequence is that the $P_{AMC}P$ reflection does not show the contrasting amplitude behavior at near and far offset for the melt case, as was shown in the 200-m-thick AMC case (Figure 2-6). In addition, the bottom AMC reflections, e.g., $P[P_{AMC}P(bottom)]S$ and $P[S_{AMC}S(bottom)]S$ (they are too close to the $P_{AMC}S$ reflection, therefore we did not indicate them in the Figure 2-10), disrupt the AVO behavior of the $P_{AMC}S$ reflection, making the apparent amplitude of the $P_{AMC}S$ reflection in the mush case stronger than for the 200-m-thick AMC case (Figure 2-6).

For the 340-m-thick AMC cases, the bottom $P_{AMC}P$ reflection arrives at essentially the same time as the $P_{AMC}S$ reflection, disrupting its AVO behavior. The interference

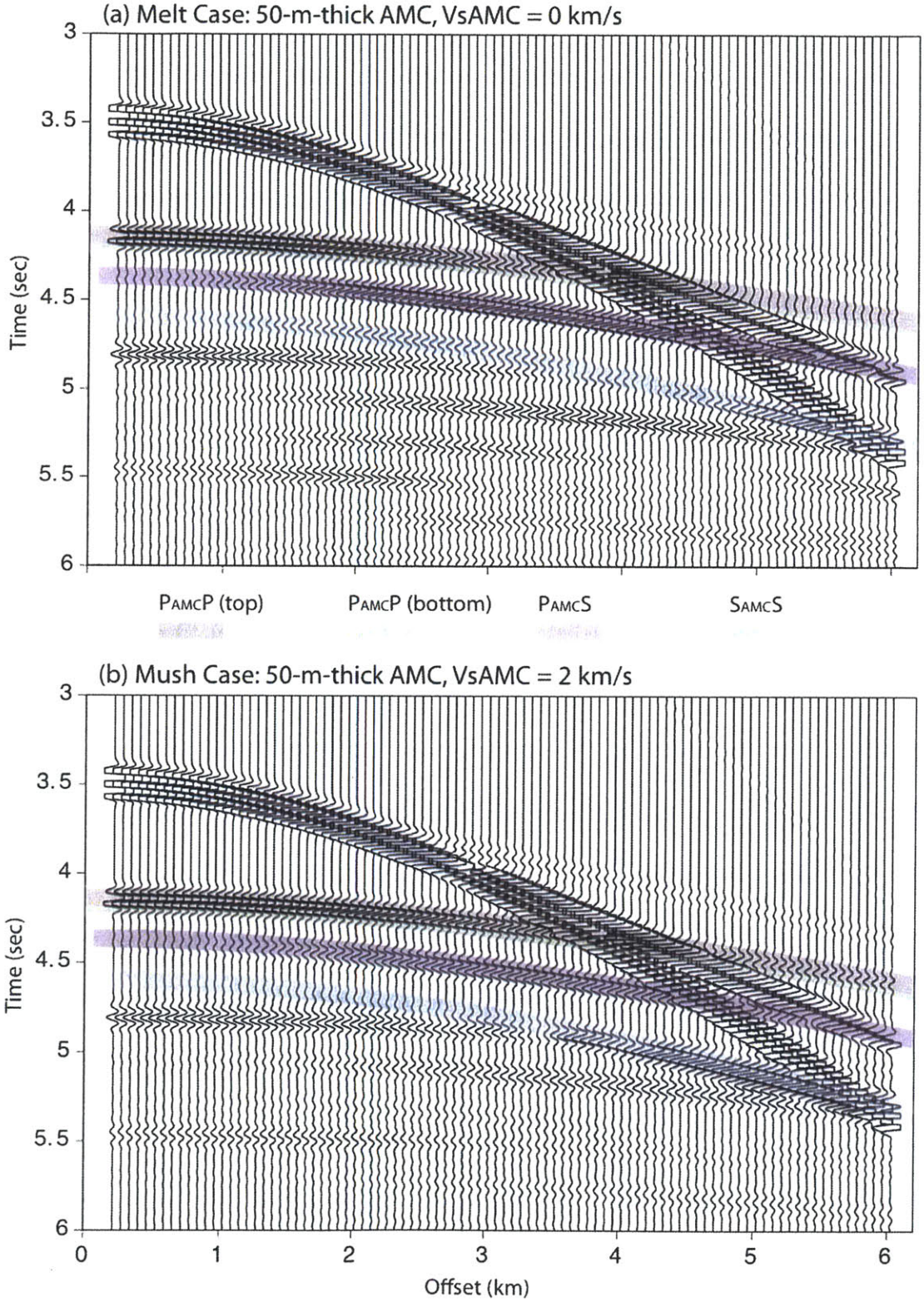
(a) Melt Case: 50-m-thick AMC, VsAMC = 0 km/s
Time (sec)
3
3.5
4
4.5
5
5.5
6
PAMCP (top)
PAMCP (bottom)
PAMCS
SAMCS
(b) Mush Case: 50-m-thick AMC, VsAMC = 2 km/s
Time (sec)
3
3.5
4
4.5
5
5.5
6
0
1
2
3
4
5
6
Offset (km)

Figure 2-10. Synthetic seismograms plotted as a function of offset for (**a**) the melt case and (**b**) the mush case. The AMC thickness is 50 m. Colored lines indicate the AMC reflections, including top AMC reflections ($P_{AMC}P$, $P_{AMC}S$ and $S_{AMC}S$), and bottom AMC reflections based on the calculated traveltime using ray theory (Note that the traveltime curves do not represent the time of the arrivals' first break; they have been delayed to match the maximum peak of the arrivals to facilitate the phase identification). Other features are the same as in Figure 2-6.

Figure 2-11. Synthetic seismograms plotted as a function of offset for (**a**) the melt case and (**b**) the mush case. The AMC thickness is 340 m. Colored lines indicate the AMC reflections, including top AMC reflections ($P_{AMC}P$, $P_{AMC}S$ and $S_{AMC}S$), and bottom AMC reflections based on the calculated traveltime using ray theory (Note that the traveltime curves do not represent the time of the arrivals' first break; they have been delayed to match the maximum peak of the arrivals to facilitate the phase identification). Other features are the same as in Figure 2-6.

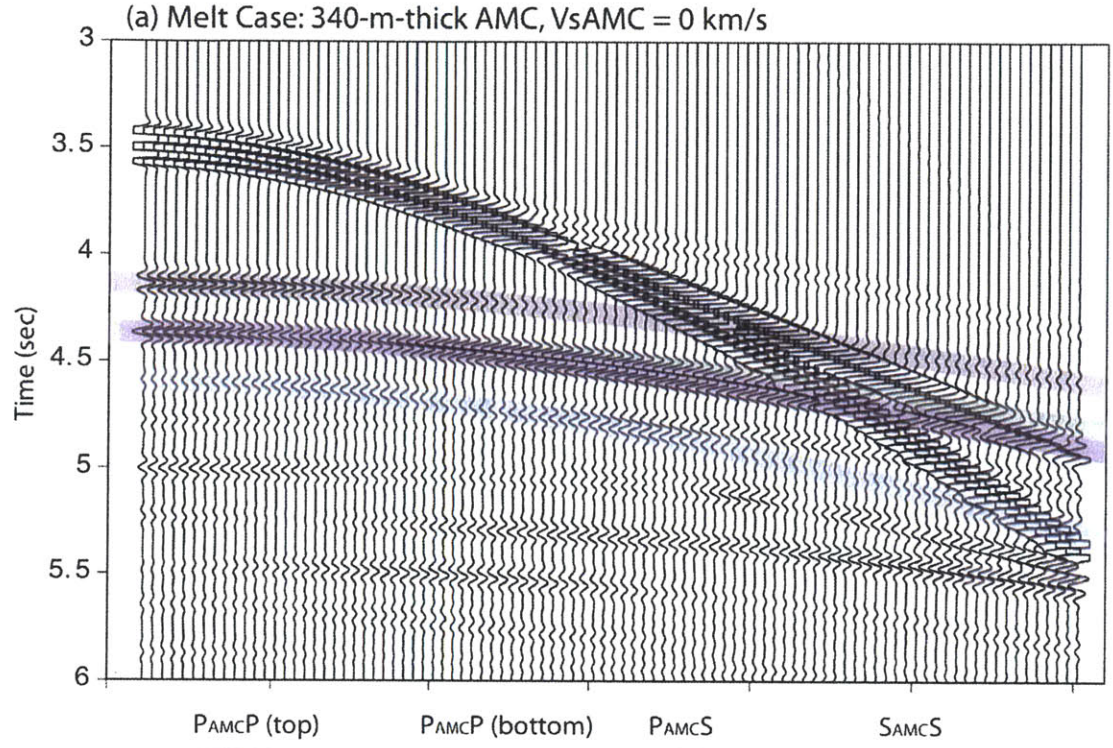
(a) Melt Case: 340-m-thick AMC, VsAMC = 0 km/s
Time (sec)
3
3.5
4
4.5
5
5.5
6
PAMCP (top)
PAMCP (bottom)
PAMCS
SAMCS

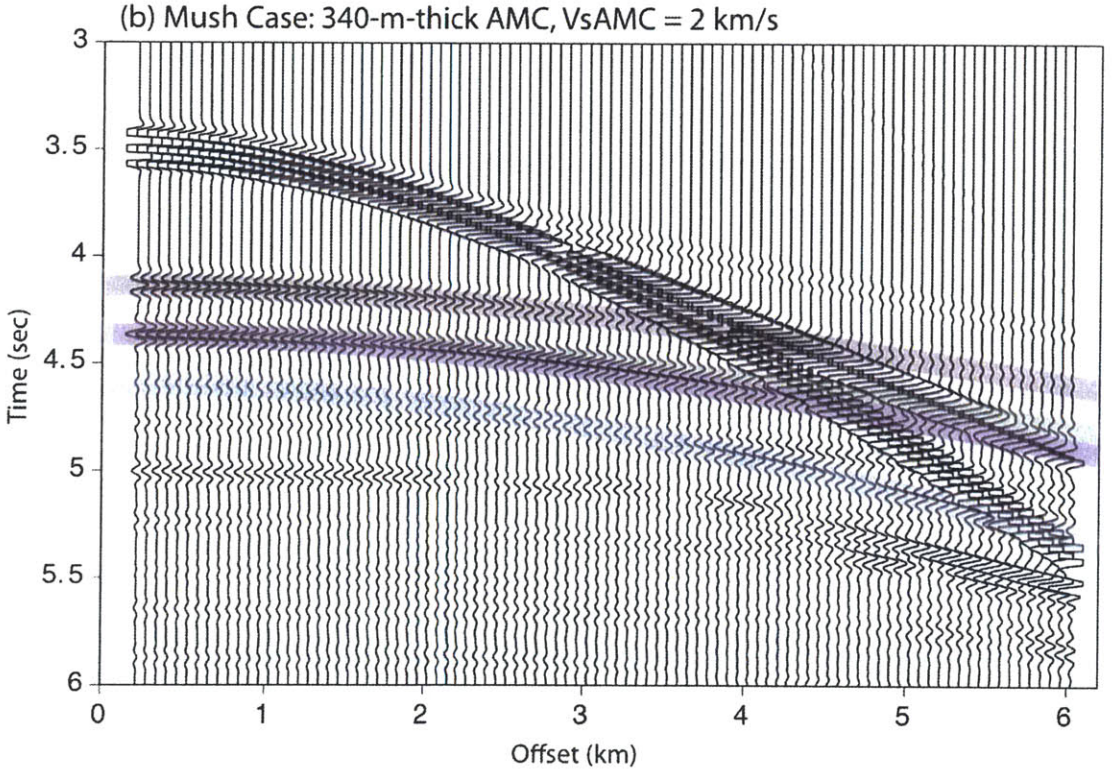
(b) Mush Case: 340-m-thick AMC, VsAMC = 2 km/s
Time (sec)
3
3.5
4
4.5
5
5.5
6
0
1
2
3
4
5
6
Offset (km)

between the bottom $P_{AMC}P$ and $P_{AMC}S$ reflections makes the apparent AVO behavior of $P_{AMC}S$ reflection for the melt and mush cases very similar to each other. The main consequence is that the $P_{AMC}S$ reflection does not show the contrasting behavior between the far and near offset as shown in the 200-m-thick AMC cases (Figure 2-6).

Thus, the effect of the AMC thickness on the AVO behavior of the AMC reflections is shown in two ways: (1) for a thin AMC (e.g., 50-m-thick, Figure 2-10), the bottom $P_{AMC}P$ reflection disrupts the AVO behavior of the top $P_{AMC}P$ reflection, and the bottom reflections, e.g., $P[P_{AMC}P(bottom)]S$ and $P[S_{AMC}S(bottom)]S$ disrupt the AVO behavior of the $P_{AMC}S$ reflection; and (2) for a thick AMC (e.g., 340-m-thick, Figure 2-11), the bottom $P_{AMC}P$ reflection disrupts the $P_{AMC}S$ reflection. Therefore any of these two scenarios would make the comparison of partial-offset stacks of near and far offset top $P_{AMC}P$ and $P_{AMC}S$ reflections less clear and more difficult to interpret. This will be taken into consideration in the following thesis Chapter 3 when we interpret the *P*- and *S*-wave partial-offset stacks derived from the 2008 MGL0812 3D MCS dataset from the EPR.

2.3.3. Realistic Model ESP05 Study: Identify Seismic Phases

Figure 2-12 shows the calculated synthetic seismograms of the "realistic" model ESP05. The geometry of the source-receiver pattern for the TDFD synthetic shot gather calculation is the same as a single-streamer MCS survey (see Appendix 2-B). Seismic phases shown in Figure 2-12 are identified based on three different methods: (1) Comparison with traveltimes predicted by a 2D ray tracing method based on ray theory

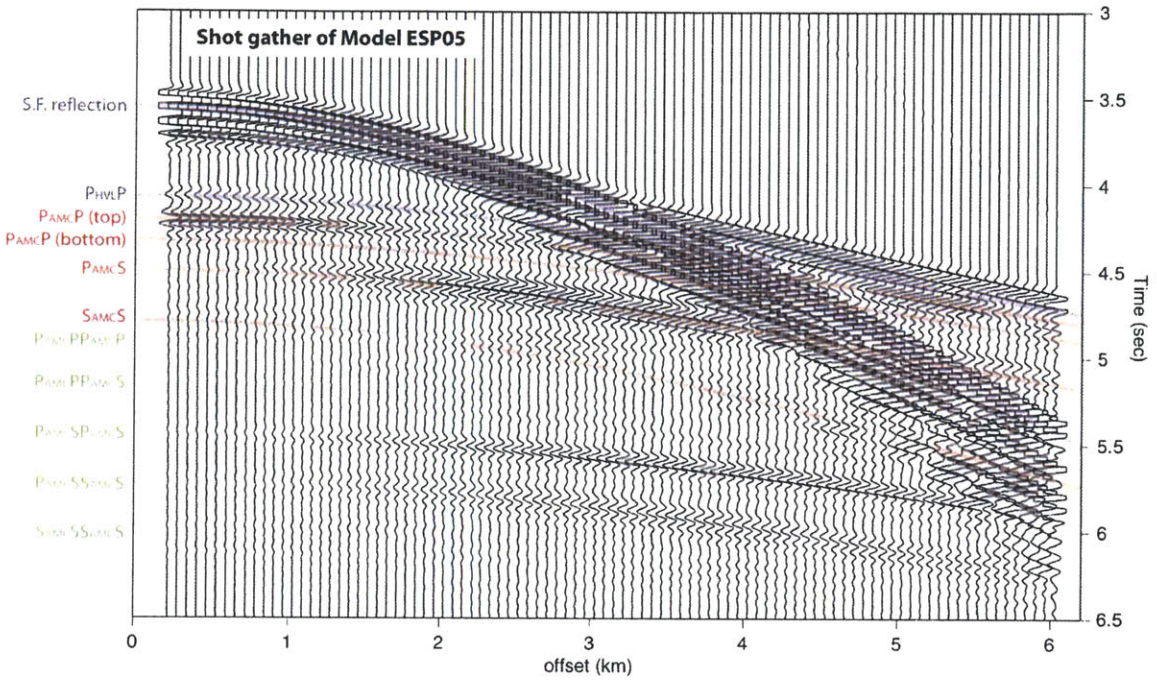

Figure 2-12. Synthetic seismograms plotted as a function of offset for "realistic" model ESP05. The ESP05 model is shown in Figure 2-3. Colored lines indicate the principal phases, including the seafloor reflection, AMC reflections and peg-leg multiples, based on the calculated traveltime using ray theory (Note that the traveltime curves do not represent the time of the arrivals' first break; they have been delayed to match the maximum peak of the arrivals to facilitate the phase identification). $P_{HVL}P$ represents the *P*-wave reflection from the high velocity lid (HVL) above the AMC in model ESP05 (Figure 2-3). Other features are the same as in Figure 2-6.

[e.g., *Zelt and Smith*, 1992]; (2) Comparison with the synthetic seismograms calculated with a corresponding no-shear model (Figure 2-13); (3) Compressional and shear energy density snapshots (Figure 2-14).

The traveltimes predicted by ray theory (shifted to match the waveform amplitude peak rather than the first break) are shown in Figures 2-12 and 2-13, and are used as the first reference to identify seismic phases. We computed traveltime curves for the following phases: Seafloor reflection, compressional wave $P_{HVL}P$ reflected from the high-velocity lid above the AMC (Figure 2-3), compressional waves $P_{AMC}P$ reflected from the top and bottom of the AMC, *P*-to-*S* converted shear wave [$P_{AMC}S$] reflected from the top of the AMC propagating as downgoing *P*-wave and upgoing *S*-wave in the upper crust (it is coincident with [$S_{AMC}P$] wave propagating as downgoing *S*-wave and upgoing *P*-wave in the upper crust), shear wave [$S_{AMC}S$] reflected from the top of the AMC propagating as both downgoing and upgoing *S*-waves in the upper crust, and peg-leg multiples which reflected from the top of the AMC twice and bounced back from the seafloor.

The synthetic seismograms of the corresponding no-shear ESP05 model are calculated by setting the shear wave velocity to 0 km/s everywhere in the model. Under the case of no-shear model, shear waves will not be generated during the synthetic simulations. Thus the comparison between full wave (Figure 2-12) and no-shear (Figure

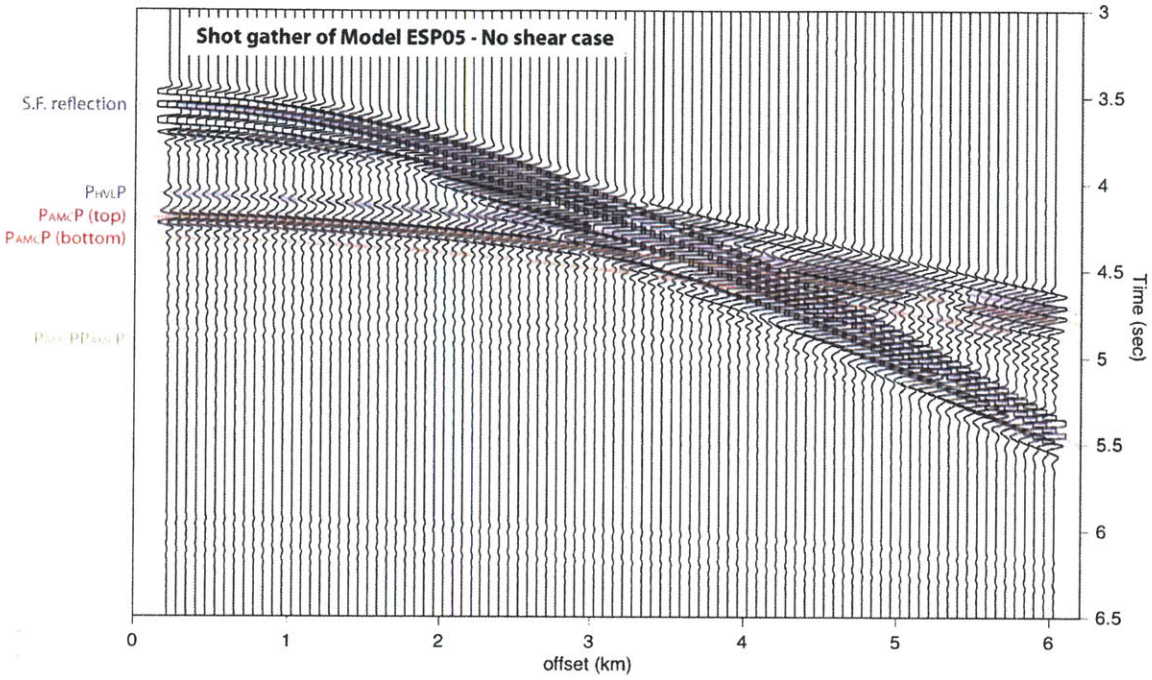

Figure 2-13. Synthetic seismograms plotted as a function of offset for corresponding no-shear model ESP05. No shear waves are generated. Colored lines indicate the principal compressional phases, including the seafloor reflection, AMC reflections and peg-leg multiples, based on the calculated traveltime using ray theory (Note that the traveltime curves do not represent the time of the arrivals' first break; they have been delayed to match the maximum peak of the arrivals to facilitate the phase identification). Other features are the same as in Figure 2-12. This no-shear synthetic calculation can be used to confirm *S*-converted seismic phases, e.g., $P_{AMC}S$ and $S_{AMC}S$, in the with-shear synthetic seismograms (Figure 2-12).

2-13) model calculations is used to identify *S*-converted seismic phases such as $P_{AMC}S$ and $S_{AMC}S$.

A series of snapshots of compressional and shear energy density, proportional to the squares of divergence and curl of displacement, respectively, obtained for model ESP05 are shown in Figure 2-14. The snapshots can be considered as representations of compressional and shear wave energy traveling across the model grid, and the different seismic phases and partitioning of energy can be seen in the snapshots. This view of consecutive snapshots is very useful for identifying seismic phases and gaining insight into the mechanisms of scattering and phase conversions.

All of the seismic phases generated in the synthetic seismograms (Figure 2-12) can be seen in Figure 2-14. The nomenclature indicated in brackets is after *Brekhovskikh* [1960] which is appropriate for the phases present in the case of a sharp interface between two media of constant velocities. Although model ESP05 is defined by velocity gradients rather than sharp interfaces, we prefer to use *Brekhovskikh*'s nomenclature in this study because it closely approximates the system of waves that exists in media with velocity gradients below/above a sharp interface (e.g., the seafloor and the AMC).

In the 2.0-s snapshots (Figure 2-14a, b), the direct water wave [P_1] emitted from the seismic source has reached the seafloor and partitioned into transmitted [P_1P_2] and seafloor reflected [P_1P_1] compressional waves and a transmitted converted shear wave

[P_1S_2]. In the 2.2-s snapshots (Figure 2-14c, d), the transmitted *P*-wave [P_1P_2] has reached the high velocity layer above the AMC and partitioned into a reflected [$P_{HVL}P$] compressional wave from the lid, a reflected [$P_{AMC}P$] compressional wave from the AMC and a reflected converted shear wave [$P_{AMC}S$] from the AMC. In the 2.4-s snapshots (Figure 2-14e, f), if the lower medium of model ESP05 was a uniform half-space, the transmitted waves [P_1P_2] and [P_1S_2] would propagate out the bottom of the model. However, in the presence of the velocity gradients, portions of these waves are refracted in the upper crustal velocity gradients and impinge on the seafloor from below. These are referred to as *P*- and *S*-diving waves. In the upper layer, they are kinematically similar to the pure head waves described in *Brekhovskikh* [1960], and we have labeled them the same symbols, [$P_1P_2P_1$] and [$P_1S_2P_1$]. The pure head waves do not exist in model ESP05 because they are only defined for a homogeneous lower layer. Where there is a velocity gradient in the lower layer, the pure head wave becomes an interference wave [*Červený and Ravindra*, 1971]. Thus strictly speaking, the head waves, [$P_1P_2P_1$] and [$P_1S_2P_1$], shown in Figure 2-14 are interference head waves. The *P*-diving wave [$P_1P_2P_1$] can be seen in the water column as it propagates in front of the direct water wave [P_1] after 2.4 s, and the *S*-diving wave [$P_1S_2P_1$] can be seen after 2.8 s. When the *P*-diving wave [$P_1P_2P_1$] is incident on the seafloor from below, it also partitions into a reflected converted shear wave [$P_1P_2S_2$] (compressional wave through the water, P_1; *P*-diving through the upper crust, P_2; and converted shear reflection at the seafloor, S_2). This converted shear wave [$P_1P_2S_2$] is coupled to the *P*-diving wave [$P_1P_2P_1$] at the seafloor, and is also tangential to the transmitted shear wave [P_1S_2] at depth.

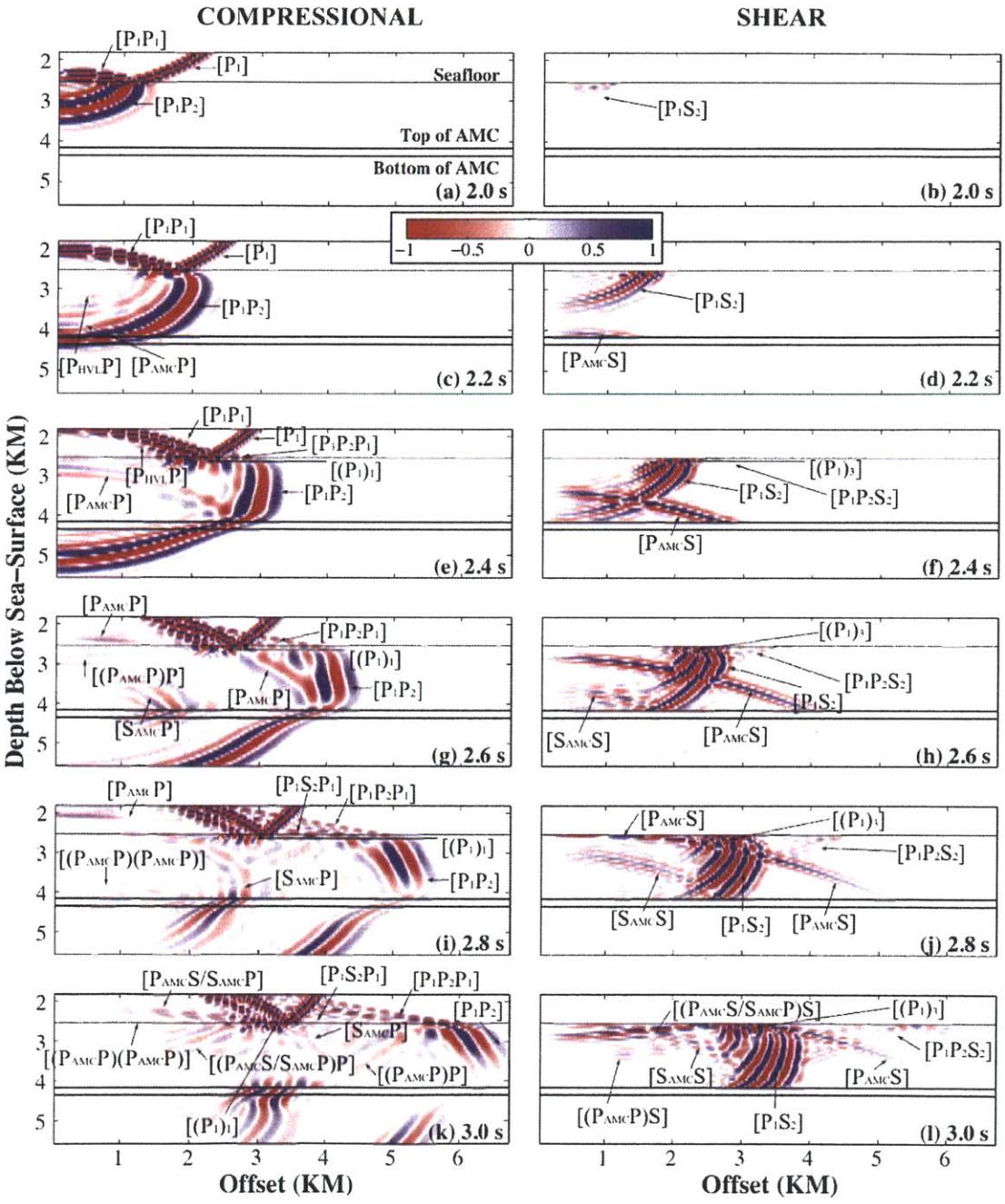
COMPRESSIONAL
SHEAR
Seafloor
Top of AMC
Bottom of AMC
(a) 2.0 s
(b) 2.0 s
(c) 2.2 s
(d) 2.2 s
(e) 2.4 s
(f) 2.4 s
(g) 2.6 s
(h) 2.6 s
(i) 2.8 s
(j) 2.8 s
(k) 3.0 s
(l) 3.0 s
Depth Below Sea–Surface (KM)
Offset (KM)
Offset (KM)

Figure 2-14. Wave front "snapshot" of compressional and shear wave energy for model ESP05. The snapshots are shown at increment of two periods (0.2 second for a pulse with a peak frequency of 10 Hz) with the first frame at 2 s and the last frame at 3 s. The direct wave [P_1], seafloor reflected wave [P_1P_1], direct roots [$(P_1)_1$] and [$(P_1)_3$] ("direct wave root" is an evanescent wave which is observed below the sea floor when the direct water wave is incident on the sea floor from above at supercritical angles), transmitted waves [P_1P_2] and [P_1S_2], interference head waves [$P_1P_2P_1$] and [$P_1P_2S_2$], reflected converted shear wave [$P_1P_2S_2$], and AMC reflections [$P_{AMC}P$], [$P_{AMC}S$], [$S_{AMC}S$] and their peg-leg multiples are indicated in the frames (seismic phases nomenclature in brackets are after *Brekhovskikh* [1960]). [$P_{HVL}P$] represents the *P*-wave reflection from the high velocity lid (*Vp* = 6.25 km/s, see Figure 2-3) in the model ESP05. The nomenclature of AMC reflections, e.g., [$P_{AMC}P$], [$P_{AMC}S$], and [$S_{AMC}S$], is modified to make them consistent with in Figure 2-2. Pure head waves, which are only defined at the interface between two homogeneous layers, are not generated in model ESP05. There is a velocity gradient immediately below the seafloor in model ESP05, thus the head waves shown in this figure are actually interference head waves [*Červený and Ravindra*, 1971].

In the 2.6-s snapshots (Figure 2-14g, h), the *S*-diving wave [P_1S_2] begins to propagate away from the direct wave roots [$(P_1)_1$] (compressional part) and [$(P_1)_3$] (shear part). The direct wave root is an exponentially decaying wave in the lower medium corresponding to supercritical reflections in the upper medium. The *S*-diving wave [P_1S_2] has reached the AMC and partitioned into reflected compressional wave [$S_{AMC}P$] and shear wave [$S_{AMC}S$]. In addition, the AMC reflected compressional wave [$P_{AMC}P$] has reached the seafloor from below and generates a peg-leg multiple phase [$(P_{AMC}P)P$] reflecting into the upper crust again. In the 2.8-s snapshots (Figure 2-14i, j), the peg-leg multiple phase [$(P_{AMC}P)(P_{AMC}P)$] has reached the AMC and reflected upward, and the AMC reflections [$P_{AMC}S$] and [$S_{AMC}P$] have reached the seafloor at the same time. The two AMC reflected phases partitioned into [$(P_{AMC}S/S_{AMC}P)P$] propagating upward to receivers, and [$(P_{AMC}S/S_{AMC}P)P$] and [$(P_{AMC}S/S_{AMC}P)S$] propagating downward to the upper crust generating peg-leg multiples (Figure 2-14k, l).

2.3.4. Laterally Heterogeneous Model Studies

The lateral heterogeneous models used for the TDFD calculation of the synthetic CMP gathers are shown in Figure 2-4. Two widths of the AMC, i.e., 0.5 and 2.0 km, are simulated for the models with flat and rough seafloor topography. The calculated synthetic CMP gathers are shown in Figure 2-15. The common midpoints are located in the middle of the models, i.e., the zero distance in Figure 2-4, to guarantee all of the seismic traces in the CMP gathers are sensing the finite-width AMC. The source-receiver geometry pattern for generating CMP gathers can be found in Appendix 2-B. The fold of

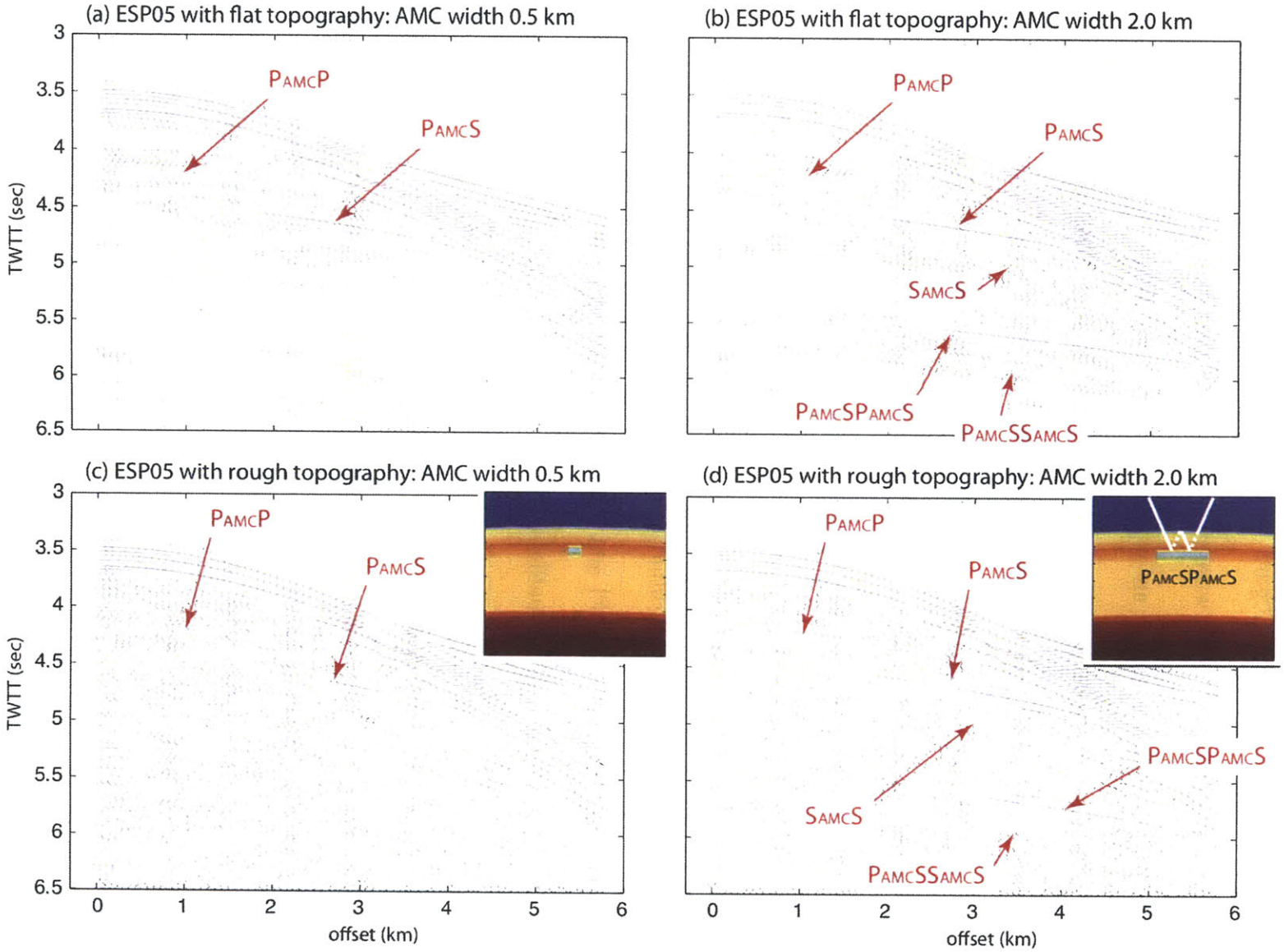
(a) ESP05 with flat topography: AMC width 0.5 km
(b) ESP05 with flat topography: AMC width 2.0 km
(c) ESP05 with rough topography: AMC width 0.5 km
(d) ESP05 with rough topography: AMC width 2.0 km
PAMCP
PAMCS
SAMCS
PAMCSPAMCS
PAMCSSAMCS
TWTT (sec)
offset (km)
3
3.5
4
4.5
5
5.5
6
6.5
0
1
2
3
4
5
6

Figure 2-15. Synthetic CMP gathers calculated for the cross-axis lateral heterogeneous models. (**a**) Model ESP05 with a 0.5-km-wide AMC with flat topography. (**b**) Model ESP05 with a 2.0-km-wide AMC with flat topography (see Figure 2-4a, c, e, g). (**c**) Model ESP05 with a 0.5-km-wide AMC with rough seafloor topography. (**d**) Model ESP05 with a 2.0-km-wide AMC with rough seafloor topography (see Figure 2-4b, d, f, h). Red arrows indicate all of the identifiable AMC reflections and peg-leg multiples. The common mid-points for calculating the CMP gathers are located in the middle of the models. The inserts in (**c**, **d**) show the *Vp* structures of model ESP05 with AMC width of 0.5 and 2.0 km with rough seafloor topography, respectively, and a schematic ray path for $P_{AMC}S$ peg-leg multiples.

the CMP gathers is 78 in this study, which means that it needs 78 individual TDFD runs to generate one CMP gather.

2.3.4.1. Effect of AMC Width

The two widths of the AMC, i.e., 0.5 and 2.0 km, are simulated and compared to investigate the effect of the AMC width on the synthetic CMP gathers. The finite width of the AMC causes diffractions at its edges. This effect is more pronounced for a narrower AMC (Figure 2-15a) than a wider one (Figure 2-15b) because for a narrow AMC, more energy partitions into the edge diffractions as waves propagate through the center of the AMC. We can see this phenomenon from the comparison of the synthetic CMP gathers of 0.5- (Figure 2-15a) and 2.0-km-wide (Figure 2-15b) AMC models. The 2.0-km-wide AMC cases show stronger AMC reflections, e.g., $P_{\mathrm{AMC}}P$ and $P_{\mathrm{AMC}}S$, than the 0.5-km-wide AMC cases, and the 2.0-km-wide AMC cases also show detectable $S_{\mathrm{AMC}}S$ reflection in the far offset, which is hard to detect if it exists in the 0.5-km-wide AMC cases. In addition, the 2.0-km-wide AMC cases generate very strong $P_{\mathrm{AMC}}SP_{\mathrm{AMC}}S$ and $P_{\mathrm{AMC}}SS_{\mathrm{AMC}}S$ peg-leg multiples, which are not observed in the 0.5-km-wide AMC cases, because the AMC is not wide enough for the propagation of the peg-leg multiple phases for the narrow AMC cases.

2.3.4.2. Effect of Seafloor Topography

The laterally heterogeneous models with flat (Figure 2-4a, c, e, g) and rough (Figure 2-4b, d, f, h) seafloor topography were calculated and compared to test the effect of

seafloor topography. The AVO behaviors of the principal AMC reflections described here for the synthetic cross-axis CMP gathers with rough seafloor topography (laterally heterogeneous, Figure 2-15c, d) are similar to the synthetic along-axis shot gathers (laterally homogeneous, Figure 2-12). This similarity suggests that the seafloor topography plays a small role on the AVO behaviors of all of the principal seismic phases.

However, the lateral heterogeneous structure has a strong effect on reducing the amplitude of the AMC reflections and peg-leg multiples. The vertical topographic variation (i.e., ~150 m, see Figure 2-4) is comparable to the vertical component of wavelength (i.e., 100s of meters), thus the seafloor topography reduces the amplitude of the AMC reflections and peg-leg multiples because interactions with the rough seafloor and AMC surface decrease amplitudes by scattering and destructive interference caused by the small phase shifts introduced by the topography. This will be most important for ray paths involving shear waves (e.g., $S_{AMC}S$) because they have much shorter wavelength with respect to the topographic roughness. This effect is more obvious for peg-leg multiples because: (1) peg-leg multiples have at least one more interaction at the seafloor, (2) peg-leg multiples have at least one more bounce from the AMC surface, which is also rough (in these models, the AMC surface follows the seafloor roughness).

High-amplitude seismic "noises" with arrival time below ~5.0 s are also observed in the near-offset traces of the synthetic CMP gathers (Figure 2-15c, d). Compared to the

far-offset seismic traces, the vertical component of wavelength is much longer for the near-offset seismic traces, thus these seismic "noises" are limited to the near-offset because of the stronger scattering and destructive interference.

2.4. DISCUSSION

2.4.1. Polarity Analyses of AMC Reflection Waveforms: Nature of the AMC

The reversed polarity of the $P_{AMC}P$ wave reflected from the top of the AMC with respect to the polarity of the seafloor reflection at near-vertical incidence is often used as a diagnostic tool for the nature of the AMC sill, and is commonly interpreted as indicating the presence of a low-velocity, partially molten sill [e.g., *Singh et al.*, 2006]. However, the nature of the AMC sill is complex and not well constrained: (1) The thickness of the AMC has not directly well constrained because of the lack of robust evidence for basal AMC reflections in field data, although the waveform modeling results suggest that they are generally about 100 m thick [*Canales et al.*, 2006] or less [*Collier and Singh*, 1997; *Hussenoeder et al.*, 1996; *Singh et al.*, 1998]; (2) Modeling of refraction data at EPR 9°N shows that there is a zone of large negative gradient velocity gradient immediately above the AMC [*Vera et al.*, 1990], and waveform inversion of reflection data at southern EPR suggests that the AMC is bounded by a solid roof and a solid floor [*Singh et al.*, 1999].

In this study, we investigated the effect of three features, based on a simple layered melt case model, in controlling AMC reflection waveform polarity at near offset: (1)

interference with free-surface reflections, (2) thickness of the AMC, and (3) a velocity gradient above the AMC. The TDFD synthetic modeling results show that free-surface interference does not have a detectable impact on the polarity of the waveforms reflected off the AMC (Figure 2-7), in other words, the reversed polarity of the top $P_{AMC}P$ reflection with respect to the seafloor reflection can be still used as a diagnostic tool for the nature of the AMC sill. However, under certain circumstances, the effects of AMC thickness and a gradient layer above the AMC can dramatically change the waveform polarity of the top $P_{AMC}P$ reflection, making it an unreliable indicator of the nature of the AMC sill. For example, for a thin AMC without a top gradient layer (e.g., AMC thickness of 100 m in Figure 2-8), $P_{AMC}P$ reflections from the top and bottom of the AMC interfere with each other, making them indistinguishable or difficult to identify their polarities. Also, for a thin AMC with a top gradient layer (e.g., AMC thickness of 50 m and gradient layer thickness of 200 m in Figure 2-9), the combined effect of the top gradient layer and interference of the bottom reflection can produce a top $P_{AMC}P$ reflection with polarity not reversed with respect to seafloor reflection. And for a thick AMC with a thick top gradient layer (e.g., AMC thickness ≥100 m and gradient layer thickness ≥150 m in Figure 2-9), the effect of the top gradient layer can make the top $P_{AMC}P$ reflection effectively inexistent and thus the bottom $P_{AMC}P$ reflection, which has the polarity as seafloor reflection, could be misinterpreted as the top $P_{AMC}P$ reflection. From what has been discussed above, we may safely draw the conclusion that the absence of observed reversed polarity in MCS data should not necessarily be interpreted

as absence of a molten sill, while observed reversed polarity can confidently be attributed to a low velocity sill.

2.4.2. AVO Analyses of AMC Reflection Waveforms: Implication for Qualitative Estimates of AMC Properties from the Analyses of Partial-offset *P*- and *S*-wave Stacks

The benchmark study of the AVO behaviors of the AMC reflected waves for the melt and mush cases shows agreement with the theoretically computed displacement reflection coefficients. The AVO behaviors of the AMC reflected waves, e.g., the top $P_{AMC}P$ and $P_{AMC}S$ reflections, are contrastingly different for the melt and mush cases: (1) a phase reversal occurs for the top $P_{AMC}P$ reflection at ~3.5 km offset in the melt case; (2) the melt case shows larger amplitude difference for the top $P_{AMC}P$ reflection at near and far offset than the mush case; and (3) $P_{AMC}S$ reflection has much higher amplitude for the melt case than for the melt case in the far offset. These differences between the melt and mush cases have been exploited for qualitatively imaging melt and mush distributions along ridge axis by *P*- and *S*-wave partial-offset stacking method [*Canales et al.*, 2006; *Singh et al.*, 1998].

The investigation of the effect of the AMC thickness on the AVO behavior of the AMC reflections shows that:

(1) For a thin AMC (e.g., 50-m-thick, Figure 2-10), the bottom $P_{AMC}P$ reflection disrupts the AVO behavior of the top $P_{AMC}P$ reflection. The consequence of this is that

the apparent amplitude of the top $P_{AMC}P$ reflection does not show clear differences between near- and far-offset for both melt and mush cases, and that the $P_{AMC}S$ reflection shows strong apparent amplitude for the mush case as for the melt case because of the interference from bottom AMC reflections, e.g., $P[P_{AMC}P(bottom)]S$ and $P[S_{AMC}S(bottom)]S$;

(2) For a thick AMC (e.g., 340-m-thick, Figure 2-11), the bottom $P_{AMC}P$ reflection disrupts the AVO behavior of the $P_{AMC}S$ reflection, making both melt and mush cases show apparently strong $P_{AMC}S$ reflection in the far offset.

Therefore, under any of these two scenarios, the comparing and interpreting partial-offset stacks of top $P_{AMC}P$ and $P_{AMC}S$ reflections at near and far offset in terms of melt/mush variations may not be as straightforward as predicted by simpler models (Figure 2-5).

The previous discussion is based on the TDFD synthetic calculations of an AMC with a solid floor. The large impedance contrast at the bottom of the AMC generates a strong bottom $P_{AMC}P$ reflection and other bottom AMC reflections, which will interfere with the top $P_{AMC}P$ (e.g., for the 50-m-thick AMC case) and $P_{AMC}S$ (e.g., for the 340-m-thick AMC case) reflections and thus disrupt their AVO behaviors. However, similar to the effect of the top gradient layer on the interference between the top and bottom $P_{AMC}P$ reflections (see section 2.3.2.1.3), if a positive velocity gradient exists below the AMC, the amplitude of the bottom $P_{AMC}P$ reflection will be greatly reduced or even disappear

when the thickness of the gradient layer is thick enough (e.g., 150 m). Figure 2-16 shows the synthetic seismograms of the model with a 50-m-thick AMC with a 150-m-thick lower gradient layer. We note that the lower gradient layer makes the bottom $P_{AMC}P$ and other bottom AMC reflections, e.g., $P[P_{AMC}P(bottom)]S$ and $P[S_{AMC}S(bottom)]S$, effectively inexistent and no interference on the top $P_{AMC}P$ and $P_{AMC}S$ reflections. Thus under these circumstances, partial-offset stacks of near- and far-offset top $P_{AMC}P$ and $P_{AMC}S$ reflections are likely to adequately represent the AVO behavior predicted by simple layered models (Figure 2-5) and thus easier to interpret in terms of melt and mush variations.

The idealized seismic source used for this study has been discussed in Appendix 2-A. For the pressure waveform with a peak frequency of 10 Hz, the minimum detectable thickness of the AMC sill is 150 m (i.e., half wavelength of the *Vp* within AMC) if we assume the *Vp* of the AMC sill is 3 km/s. In other words, the top and bottom $P_{AMC}P$ reflections will not interfere with each other when the AMC sill is thicker than 150 m, and it has been demonstrated in the TDFD synthetic modeling (see Figure 2-8). The Nyquist frequency for the data acquisition during the MCS cruise MGL0812 is 250 Hz, and strongest signal of a typical shot gather is found within the frequency range from about 5 to 80 Hz [*Mutter et al.*, 2008]. Thus, in theory, the data can detect the thickness of an AMC sill as small as ~20 m, or the top and bottom $P_{AMC}P$ reflections will interfere with each other only when the AMC sill is thinner than 20 m.

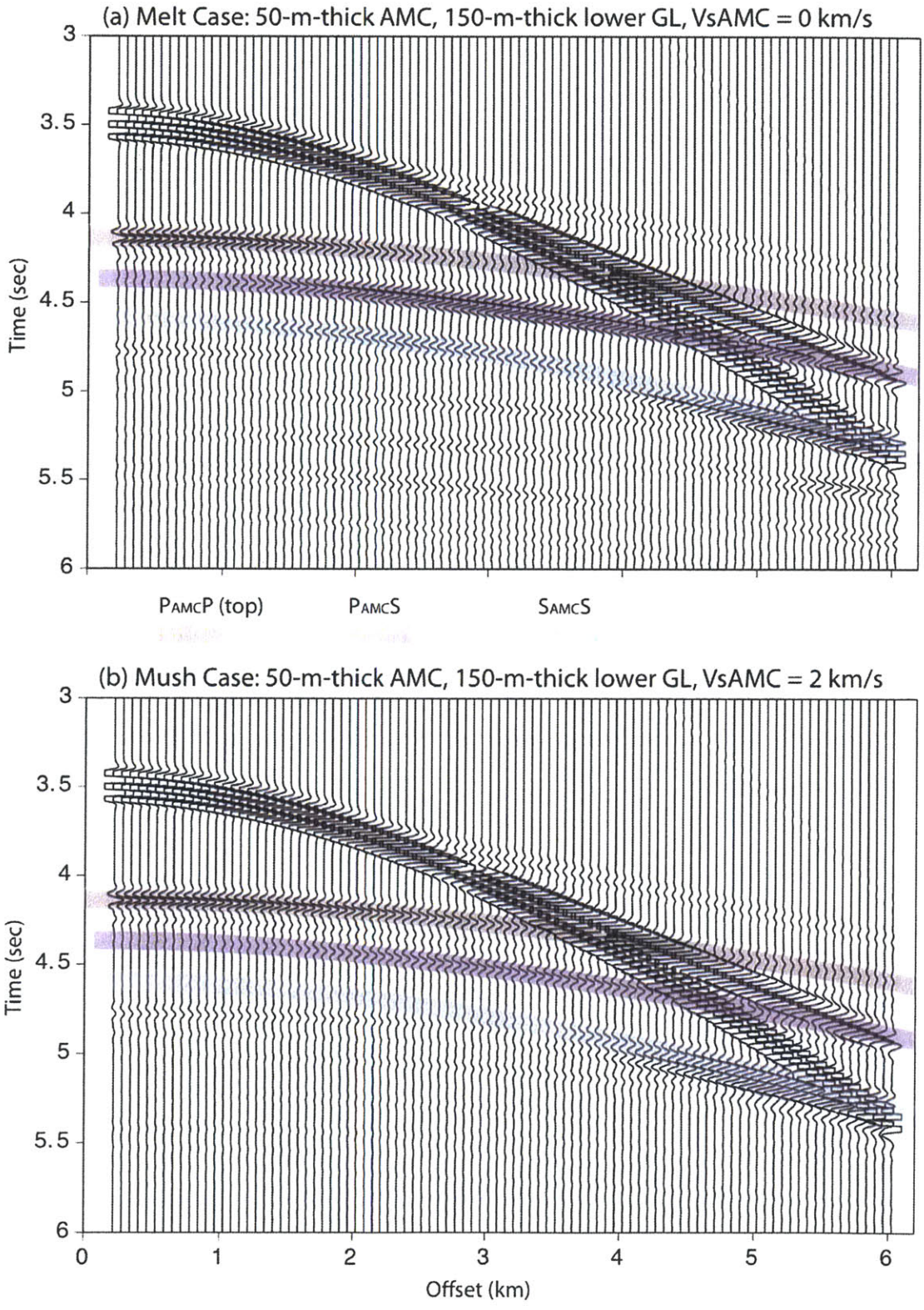
(a) Melt Case: 50-m-thick AMC, 150-m-thick lower GL, VsAMC = 0 km/s
Time (sec)
3
3.5
4
4.5
5
5.5
6
PAMCP (top)
PAMCS
SAMCS
(b) Mush Case: 50-m-thick AMC, 150-m-thick lower GL, VsAMC = 2 km/s
Time (sec)
3
3.5
4
4.5
5
5.5
6
0
1
2
3
4
5
6
Offset (km)

Figure 2-16. Synthetic seismograms plotted as a function of offset for (**a**) the melt case and (**b**) the mush case with a positive velocity gradient layer below the AMC. The AMC thickness is 50 m, and the thickness of the lower gradient layer is 150 m. Colored lines indicate the AMC reflections, including top $P_{AMC}P$, $P_{AMC}S$ and $S_{AMC}S$ reflections based on the calculated traveltime using ray theory (Note that the traveltime curves do not represent the time of the arrivals' first break; they have been delayed to match the maximum peak of the arrivals to facilitate the phase identification). Other features are the same as in Figure 2-10.

2.4.3. Origin of the Sub-AMC Reflectivity

The sub-AMC events observed in the preliminary inspection of the MGL0812 MCS dataset (Figure 2-1) could in theory be an imaging artifact due to out-of-plane reflections [e.g., *Kent et al.*, 1997]. However, if their presence is confirmed after 3D processing, their presence could arise from a variety of reasons. For example, (1) reflections from other deep sills, (2) multiples or reverberations within layer 2A or within the AMC sill, (3) *P* to *S* conversions at the seafloor, base of layer 2A, or top of the AMC, (4) reflections from the bottom of the AMC sill, or (5) scattering introduced by complex, heterogeneous shallow structure (i.e., rough seafloor).

The sub-AMC events are located ~0.25-0.5 s deeper than the top AMC reflections (Figure 2-1). Within this traveltime range, the TDFD synthetic calculations (Figures 2-12 and 2-15) generate three seismic phases: $P_{AMC}S$, $P_{AMC}P$ peg-leg multiple, and $S_{AMC}S$. However, The $S_{AMC}S$ wave is hard to detect in the field data because of the high shear wave attenuation. The $P_{AMC}P$ peg-leg multiple has very low amplitude shown in the synthetic shot gather (Figure 2-12), and cannot even detectable in the synthetic CMP gathers (Figure 2-15). The nature of the peg-leg multiple indicates that the $P_{AMC}PP_{AMC}P$ wave should be present everywhere where the $P_{AMC}P$ reflection is observed, and at a traveltime beneath the $P_{AMC}P$ that is exactly twice of the seafloor-to-AMC traveltime. These conditions are not met by the brute-stack image (Figure 2-1). The *P*-to-*S* converted $P_{AMC}S$ wave is weak/absent at near offset (Figures 2-12 and 2-15), and the brute-stack

shown in Figure 2-1 was done by stacking seismic traces only the near half of the streamer (i.e., 0-3 km). Thus, it is very unlikely that the deep events are $P_{AMC}S$ waves.

If the sub-AMC events were arisen from the bottom of the AMC sill, the 0.25-0.5 s below the top $P_{AMC}P$ reflection implies that the thick of the AMC sill is ~375-750 m and the bottom of the AMC sill should be a sharp interface. This thick AMC sill with a sharp bottom is very unusual since that investigations through waveform modeling suggest that they are generally about 100 m thick [*Canales et al.*, 2006] or less [*Collier and Singh*, 1997; *Hussenoeder et al.*, 1996; *Singh et al.*, 1998], and the AMC sill is bounded by a solid roof and a solid floor [*Singh et al.*, 1999]. The near-offset seismic "noises" generated by the rough seafloor (Figure 2-15c, d) are unlikely the source either, because they arrive ~0.5 below the seafloor reflection which is not within the traveltime range of the sub-AMC events.

To test the possibility of the sub-AMC events generated from a deeper melt lens, we created two double-melt-lens models based on the simple layered melt/mush case models (Figure 2-2). The double-melt-lens models are created by adding a deep melt lens exactly the same as the shallow lens at 1 km below it. The calculated synthetic shot gathers are shown in Figure 2-17. The most distinct difference between the synthetic seismograms of the single-melt-lens models and the double-melt-lens models is that the latter show clear $P_{AMC}P$ reflection from the top of the deeper melt lens. The newly generated $P_{AMC}P$ reflection is ~0.4 s deeper than the top $P_{AMC}P$ reflection from the shallow melt lens,

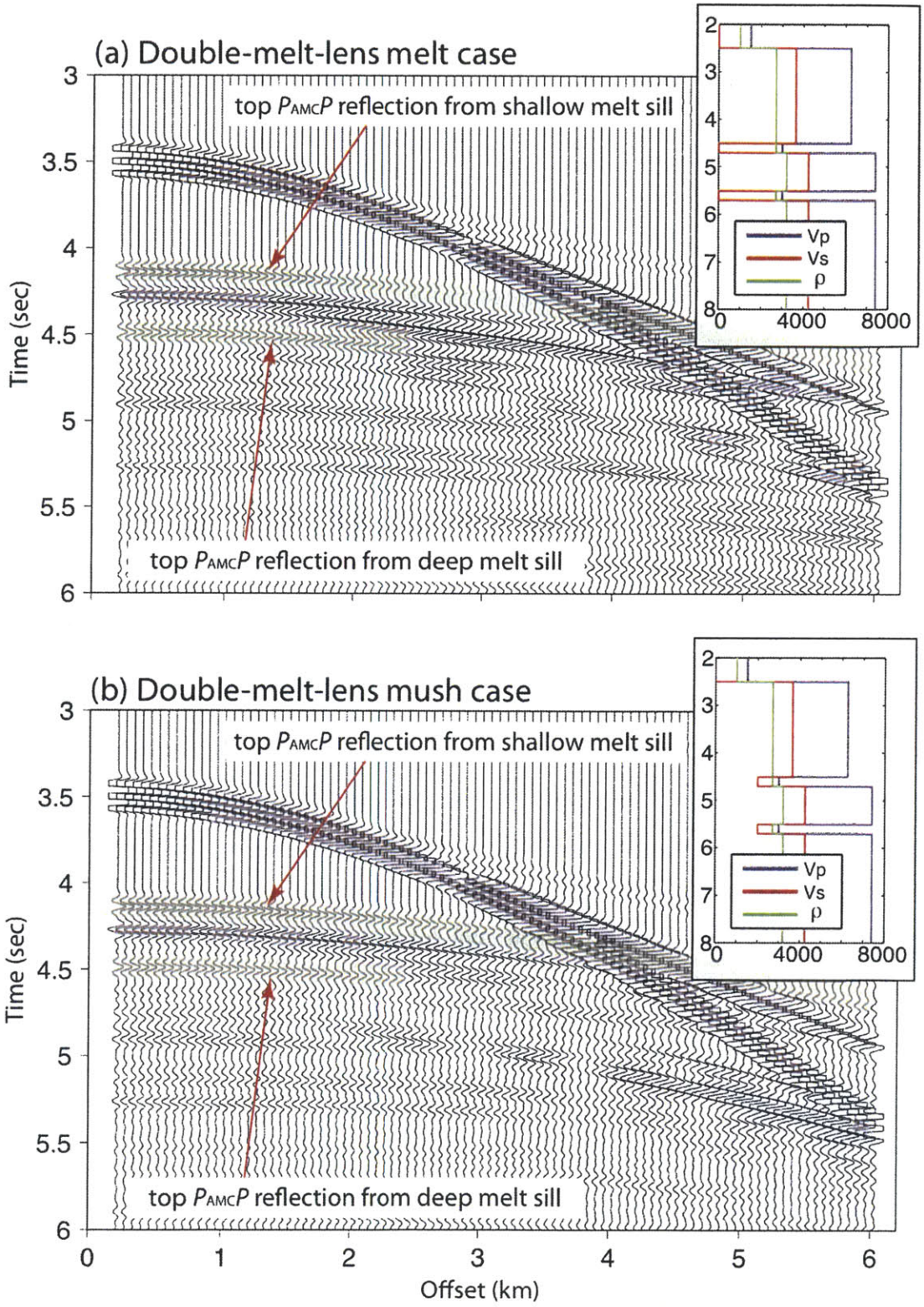
(a) Double-melt-lens melt case
top $P_{AMC}P$ reflection from shallow melt sill
top $P_{AMC}P$ reflection from deep melt sill
Vp
Vs
ρ
Time (sec)
(b) Double-melt-lens mush case
top $P_{AMC}P$ reflection from shallow melt sill
top $P_{AMC}P$ reflection from deep melt sill
Vp
Vs
ρ
Time (sec)
Offset (km)

Figure 2-17. Synthetic shot gathers calculated for double-melt-lens models. (**a**) Double-melt-lens model based on the simple layered melt case model. (**b**) Double-melt-lens model based on the simple layered mush case model. The double-melt-lens models are created by adding a deep melt lens exactly the same as the shallow lens at 1 km below it. Red arrows indicate $P_{AMC}P$ reflections from the top of both the shallow and deep melt lens. The inserts in (**a, b**) show the velocity/density structures of models used for the TDFD calculations. The vertical coordinate is the depth below the sea surface (measured in km). The compressional (*Vp*, blue lines) and shear (*Vs*, red lines) wave velocities are measured in m/s, and density (ρ, green lines) is measured in kg/m^3. The clear top $P_{AMC}P$ reflection from the deeper melt lens can be used to differentiate the single-melt-lens (Figure 2-2) and double-melt-lens models. More realistic shallow structures, however, can excite peg-leg multiples and shear wave conversions that would overlay, obscure and obfuscate any reflections from the deeper melt lens.

which is within the traveltime range of the sub-AMC events, and also shows high amplitude in the near offset. Thus we cannot rule out the possibility that the sub-AMC events may come from a deeper melt sill. On the basis of the discussion of all the possibilities considered for the source of the sub-AMC events, the multiple sill models are the one that seems more plausible.

In addition, the sub-AMC events are shown in a brute stack gather (Figure 2-1), comparison with one shot or one CMP gather may be too superficial to be used to constrain the origin and nature of the events. A lot of sub-seafloor features are imaged in the field data after a sequence of data processing. If the computed TDFD synthetic data can be processed following the same processing procedures applied to the real data, more confidence will be gained to assess the initial model by the comparisons. However, this 2D TDFD method has limited ability to deal with the actual processing with 3D MCS dataset, and to solve this problem, we need fully 3D synthetics.

2.5. CONCLUSIONS

We have used a TDFD solution to the full wave equation to test the feasibility of modeling seismic propagation in the 6.8 to 13.6 Hz frequency band through 2D representations of along-axis and cross-axis AMCs. Three classes of TDFD synthetic calculations were conducted in this study: (1) simple layered models were used to investigate the effect of different structural features on the polarities and AVO behaviors of the AMC reflections, which are commonly used to model the nature and physical

property of AMC sills; (2) a laterally homogeneous model ESP05 was used to identify the seismic phases generated during the synthetic modeling of wave propagation through a realistic crustal structure; and (3) laterally heterogeneous models were used to the test the effects of seafloor topography and the finite-width of the AMC. On the basis of the interpretation of these synthetic calculations, we make the following conclusions.

1. Polarity and AVO analyses of the AMC reflections indicate that:

1.1. Reversed polarity of the top $P_{AMC}P$ reflection with respect to the seafloor reflection can be used as a diagnostic tool to identify the nature of the AMC sill if the AMC sill is thicker than ~150 m (thickness depends on the frequency content of the signal). For a thinner AMC, the top and bottom $P_{AMC}P$ reflections interfere with each other, making them indistinguishable. In this scenario, the polarity of the top $P_{AMC}P$ reflection could be a poor indicator for the nature of the AMC sill.

1.2. The top $P_{AMC}P$ reflections decrease in amplitude, and eventually disappear, if the sharp interface forming the roof of the AMC is replaced with a velocity gradient layer. In this case, normal-polarity reflections from the bottom of the AMC could be misinterpreted as reflections from the top of the AMC, making the observed polarity of the AMC reflection a poor and unreliable indicator of the nature of the AMC sill.

1.3. The contrasting AVO behaviors of top $P_{AMC}P$ and $P_{AMC}S$ reflections between the melt and mush cases could be disrupted by the effect of the AMC thickness. For a thin AMC, the bottom AMC reflections disrupt the AVO behaviors of both top $P_{AMC}P$ and $P_{AMC}S$ reflections. This makes the apparent AVO behavior of the top $P_{AMC}P$

reflection less variable with respect to offset, and the apparent AVO behavior of $P_{AMC}S$ reflection more similar between the melt and mush cases. For a thick AMC, the bottom $P_{AMC}P$ reflection can disrupt the AVO behavior of $P_{AMC}S$ reflection, making it strong for both melt and mush cases. Any of these two scenarios would make comparing and interpreting partial-offset stacks of near- and far-offset *P*- and *S*-waves more complicated than anticipated by simpler models.

2. Synthetic along-axis shot gather and snapshots calculated from the laterally homogeneous model ESP05 show the complexity of the sub-seafloor seismic wave field, and all the generated principle seismic phases can be identified. The sub-AMC events preliminary observed in the 3D MCS dataset acquired over the RIDGE-2000 ISS at EPR (cruise MGL0812) are unlikely to arise from stacking of peg-leg multiples of AMC reflections, *S*-converted waves, or scattering due to rough topography. In constrast, those sub-AMC events could arise from reflections from deeper multiple magma sills.

3. Investigation of the synthetic cross-axis CMP gathers calculated from laterally heterogeneous models suggests that the finite-width AMC causes diffractions at its edges, reducing the amplitude of the AMC reflections, and the seafloor topography and the AMC surface which follows the seafloor roughness play a small role on the AVO behaviors of all of the principal seismic phases, but they reduce the amplitude of peg-leg multiples because of the scattering and destructive interference.

2.6. APPENDIX

Appendix 2-A: The Time-Domain Finite Difference Method

The wave equation for a perfectly elastic, isotropic, heterogeneous medium is

$$\rho \ddot{\boldsymbol{u}} = (\lambda+\mu)\nabla(\nabla\cdot\boldsymbol{u}) + \mu\nabla^2\boldsymbol{u} + \nabla\lambda(\nabla\cdot\boldsymbol{u}) + \nabla\mu\times(\nabla\times\boldsymbol{u}) + 2(\nabla\mu\cdot\nabla)\boldsymbol{u} \quad \text{(2-A1)}$$

where $\boldsymbol{u}$ is displacement, ρ is density, and λ and μ are the Lamé parameters. A major goal of computational seismology is the fast, accurate solution of this wave equation. Finite difference (FD) methods are becoming increasingly popular as the limitations of other techniques are fully appreciated. FD methods can be applied at realistic frequencies with finite bandwidth and in laterally varying media in which the elastic parameters change significantly over distances comparable to a seismic wavelength [e.g., *Kelly et al.*, 1976; *Stephen*, 1988]. Other schemes involve more restrictive approximations. For example, the reflectivity method [e.g., *Fuchs and Müller*, 1971] assumes lateral homogeneity, and ray methods [e.g., *Chapman*, 1978] assume that the seismic wavelength is short compared with the scale of heterogeneity (high frequency approximation). Amplitude analysis and energy partitioning in media that vary laterally on the scale of seismic wavelengths are not handled well with these methods. The seafloor and axial magma chamber (AMC) seismo-acoustic problems in this study, with high contrasts in Poisson's ratio at rough sharp interfaces, are particularly challenging, and many published formulations fail to solve them accurately [*Stephen*, 1988]. The FD method is one of the few methods capable of providing a full-wave solution to this problem. The resulting seismograms are a complete solution to the elastic wave equation including all *P-S* converted phases, diffractions, multiple scattering, and caustics.

2-A-1. Source Wavelet for Time-Domain Finite Difference Calculations

The source waveform is introduced into the grid in a manner similar to the method of *Alterman and Loewenthal* [1972]. The time dependence of the potential, far-field displacement, and pressure of the impulsive compressional point source is given by the first, second, and third derivative of a Gaussian curve, respectively [*Kelly et al.*, 1976; *Stephen*, 1984; *Stephen et al.*, 1985]

$$\phi(t) = -2\xi\left(t - t_s\right)e^{-\xi(t-t_s)^2} \tag{2-A2}$$

$$u(t) = -2\xi\left[1 - 2\xi\left(t - t_s\right)^2\right]e^{-\xi(t-t_s)^2} \tag{2-A3}$$

$$p(t) = 4\xi^2\left[3\left(t - t_s\right) - 2\xi\left(t - t_s\right)^3\right]e^{-\xi(t-t_s)^2} \tag{2-A4}$$

where $\xi = f_p^2 / 0.152$ governs the pulse width, f_p is the peak frequency of the source in pressure, and t_s is a time shift chosen such that $\phi(0) \cong 0$. The waveforms and spectra for displacement potential (Equation 2-A2), far-field displacement (Equation 2-A3) and pressure (Equation 2-A4) are shown in Figure 2-A.

Although the FD computations are essentially dimensionless, this study uses dimensions appropriate for a marine reflection experiment. Time will be in seconds and distance will be in kilometers. For the pressure waveform the peak frequency is 10 Hz, the upper and lower half-power frequencies are 13.6 Hz and 6.8 Hz, respectively. Since the FD calculations are conducted in terms of displacement (Equation 2-A1), the source frequencies for displacement may be more meaningful. The peak displacement frequency is 8.2 Hz, and the upper and lower half-power frequencies are 11.8 Hz and 5.0 Hz,

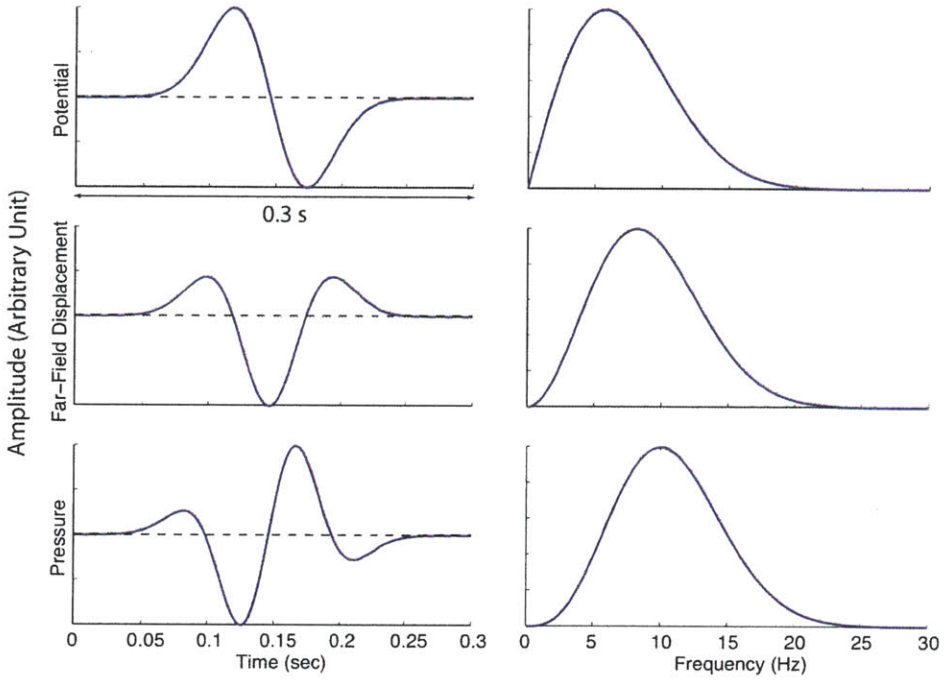

Figure 2-A. Source waveforms and amplitude spectra for time-domain finite difference (TDFD) calculations are shown in terms of compressional potential (Equation 2-A2), far-field displacement (Equation 2-A3) and pressure (Equation 2-A4). The pressure waveform has a peak frequency of 10 Hz and the corresponding half-power frequency band is 6.8-13.6 Hz.

respectively. If we double the peak frequency of the seismic source for the synthetic modeling from 10 to 20 Hz, the computational time for each TDFD run will increase to be 8 times as long as before (~1 week), which is an unrealistic computational load for us at this stage.

2-A-2. Grid Dispersion

In FD calculations there are two fundamental considerations: stability, which affects the possibility of a solution, and grid dispersion that affects the accuracy of a solution [*Stephen*, 1983]. Accuracy is constrained by the need to minimize grid dispersion while maximizing the computational speed. Grid dispersion is always present to some extent in FD modeling, but becomes problematic when the propagation distance if much greater than the wavelength. *Kelly et al.* [1976] suggest a rule of thumb for acceptable grid dispersion for second order approximations to the wave equation (Equation 2-A1) in homogeneous media: the grid spacing (Δx) should be at least ten grid points per wavelength (λ_{min}), i.e., $\Delta x \leq \lambda_{min}/10$. Since wavelength decreases with velocity for a given frequency, this rule of thumb places a constraint on the lowest velocity (v_{min}) that should be included in a geological model: $v_{min} = \lambda_{min} \cdot f_p = 10\Delta x \cdot f_p$, where f_p is the peak frequency of the source wave field. In our modeling f_p = 10 Hz and Δx = 2.5 m, so that v_{min} = 0.25 km/s.

Propagation over distances more than a wavelength in media with velocities lower than v_{min} will produce extended wavelets due to the grid dispersion. (This result is

generally true for compressional waves. For shear waves the dispersion relation is more complex and for some combinations of Poisson's ratio and propagation direction [*Bamberger et al.*, 1980]). However, in practice, when using laterally heterogeneous models, we found that significantly lower velocity regions can be included without causing unacceptable grid dispersion effects. This is due to the fact that the waves propagate only very short distances in these low velocity regions. In our modeling we were able to achieve acceptable results using the grid spacing (Δx) 2.5 m both horizontally and vertically, which is 1/60 of the source wavelength (150 m), much less than the required 1/10, at the peak frequency (10 Hz) of pressure in water.

2-A-3. Numerical Stability

The method we use employs a staggered grid scheme [*Virieux*, 1984, 1986] which has proven stable for a broad range of problems at fluid/solid boundaries. For the case of propagation in infinite homogeneous media, the second-order explicit FD formulation [*Virieux*, 1984, 1986] is stable only if it satisfies the Courant stability condition:

$$\Delta t \le \frac{\min(\Delta x, \Delta z)}{\sqrt{2}\alpha}, \quad \text{where } \alpha = \sqrt{\frac{\lambda + 2\mu}{\rho}} \tag{2-A5}$$

where Δt is the time increment for the differencing scheme, (Δx, Δz) are the horizontal and vertical space increments, ρ is density, and λ and μ are the Lamé parameters, and α is compressional wave velocity. *Kelly et al.* [1976] suggested that stability in heterogeneous media could be expected provided that the condition for homogeneous media, e.g., equation (2-A5), held everywhere on the grid. For our modeling, Δt was

chosen as 0.0002 s (i.e., 1/500 of a wave period at 10 Hz), which satisfies this stability criteria for v_{pmax}<=8.84 km/s, which is higher than the maximum velocity in our models. However, sufficient stability conditions for heterogeneous media have not been defined [*Stephen*, 1990]. Therefore, numerical stability in the modeling of heterogeneous media must be judged for each model computation. All of the simulations conducted with heterogeneous models in this study are found to be numerically stable.

2-A-4. Snapshots and Time Series

The numerical wave field obtained from the TDFD calculations can be "recorded" in two ways: snapshot and time series. Rather than displaying displacement vectors at each grid point, we display "amplitude density", which is proportional to the square root of the energy density and maintains the sign of the amplitude wave field [*Dougherty and Stephen*, 1988; *Stephen and Swift*, 1994]. Snapshots are outputted as compressional and shear energy density at all grid points at various times during the simulation. Compressional and shear energies were calculated by using spatial divergence and curl operators on the displacements. These snapshots of the time progression of the numerical wave field are particularly useful for gaining insight into the mechanisms of scattering, and they show the full variety of wave types that occur.

While snapshots are the best format for debugging and for understanding the physics, time series are useful for interpreting field and lab data. In this case, time series are recorded to simulate "receivers" as they would be used during real data acquisition. The

displacement or pressure, at chosen grid points, are recorded at every time step, producing a time series of the wave field amplitude observed at each point in space. Time series are output as normalized divergence and curl of the displacement field at the receiver. In our modeling, since both the source and receivers are located in the water, the shear modulus is zero, and the divergence, if properly normalized, is the same as pressure while the curl is always zero (pressure is the compressibility times the divergence of the displacement). The point source and receivers can be set to any positions to record different wave propagation phenomena. In our case, the recording geometry of the source-receiver pattern for the synthetic shot gathers corresponds to that of a 468-channel single-streamer seismic reflection experiment. The pressure time series are recorded at 7.5 m below sea surface, and the distance between source and receivers ranges from 200 to 6037.5 m at 12.5 m intervals. The synthetic seismograms are saved for every tenth time step (0.002 s sampling interval).

Appendix 2-B: Synthetic Seismogram Displaying: Shot Gather and CMP Gather

Synthetic seismograms (expressed as time series of pressure) from the TDFD calculations are collected in a gather according to some trace header parameters. It is defined as a side-by-side display of seismic traces of which have some acquisition parameters in common. A common-shotpoint (shot) gather is the collection of all the data from a single shot. A common-midpoint (CMP) gather displays data from source-receiver pairs sharing their midpoints. The recording geometries of the two different synthetic seismic gathers analyzed in this study are shown in Figure 2-B. For laterally

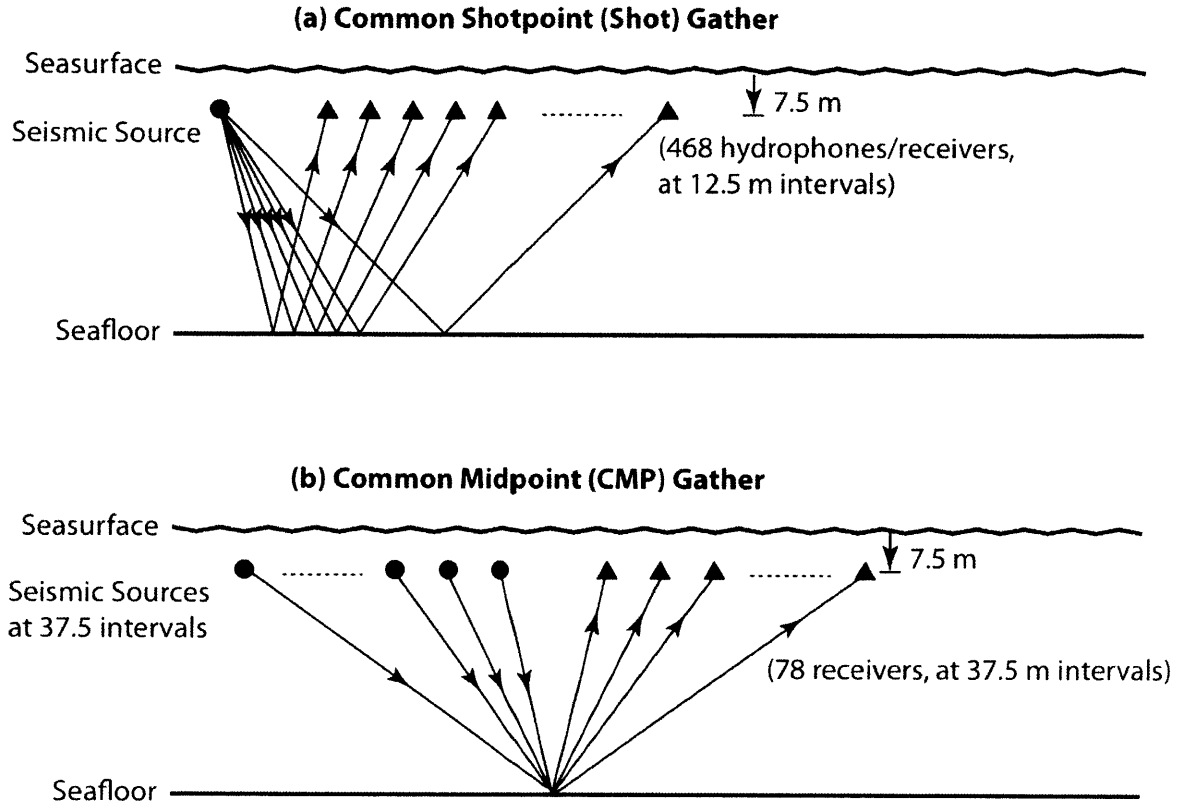

Figure 2-B. A cartoon showing the recording geometries of (**a**) common-shotpoint (shot) gathers and (**b**) common-midpoint (CMP) gathers. The sources (black dots) and receivers (triangles) are located 7.5 m below sea surface. For the shot gather, there are 468 receivers (hydrophones) on a single seismic streamer separated with a 12.5-m spacing, and the minimum offset is 200 m. For the CMP gather, the fold number is 78 for a 6-km-long seismic streamer, and no zero-offset trace recorded. One individual TDFD run can generate a synthetic shot gather, while a 78-fold synthetic CMP gather requires 78 individual TDFD runs for every source position with respect to the structure.

homogeneous models, shot and CMP gathers are equivalent, but for laterally heterogeneous models all traces of a CMP gather contain reflection energy arising from the same part of the reflecting interface.

References

Aki, K., and P. G. Richards (2002), *Quantitative seismology, Chapter 5: Plane waves in homogeneous media and their reflection and transmission at a plane boundary, University Science Books.*

Alterman, Z., D. Loewenthal, and M. Rotenberg (1972), *Computer generated seismograms*, 35-46 pp., Academic Press, New York.

Bamberger, A., G. Chavent, and P. Lailly (1980), *Etude de sch'emas num'eriques pour les 'equations de l''elastodynamique lin'eaire, Rapport de Recherche 41, Inria, B.P. 105, 78150 Le Chesnay, France.*

Brekhovskikh, L. M. (1960), Waves in Layered Media (Academic, New York), pp. 318-324.

Canales, J. P., S. C. Singh, R. S. Detrick, S. M. Carbotte, A. J. Harding, G. M. Kent, J. B. Diebold, J. Babcock, and M. R. Nedimovic (2006), Seismic evidence for variations in axial magma chamber properties along the southern Juan de Fuca Ridge, *Earth and Planet. Sci. Lett.*, *246*, 353-366.

Červený, V., and R. Ravindra (1971), *Theory of Seismic Head Waves. University of Toronto Press, Toronto*, 312 pp.

Chapman, C. H. (1978), A new method for computing synthetic seismograms, *Geophys. J. R. Astron. Soc.*, *54*(3), 481-518, doi: 10.1111/j.1365-246X.1978.tb05491.x.

Clayton, R., and B. Engquist (1977), Absorbing boundary conditions for acoustic and elastic wave equations, *Bull. Seismol. Soc. Am.*, *67*(6), 1529-1540.

Collier, J. S., and S. C. Singh (1997), Detailed structure of the top of the melt body beneath the East Pacific Rise at 9°40'N from waveform inversion of seismic reflection data, *J. Geophys. Res.*, *102*(B9), 20287-20304.

Detrick, R. S., P. Buhl, E. E. Vera, J. C. Mutter, J. A. Orcutt, J. A. Madsen, and T. M. Brocher (1987), Multi-channel seismic imaging of a crustal magma chamber along the East Pacific Rise, *Nature*, *326*, 35-41.

Dougherty, M. E., and R. A. Stephen (1988), Seismic energy partitioning and scattering in laterally heterogeneous ocean crust, *Pure and Applied Geophysics*, *128*, 195-229.

Dougherty, M. E., and R. A. Stephen (1991), Seismo/acoustic propagation through rough seafloors, *J. Acoust. Soc. Am.*, *90*, 2637-2651.

Ergin, K. (1952), Energy ratio of the seismic waves reflected and refracted at a rock-water boundary, *Bull. Seismol. Soc. Am.*, *42*(4), 349-372.

Fuchs, K., and G. Müller (1971), Computation of synthetic seismograms with the reflectivity method and comparison with observations, *Geophys. J. R. Astron. Soc.*, *23*(4), 417-433.

Herron, T. J., P. L. Stoffa, and P. Buhl (1980), Magma chamber and mantle reflections - East Pacific Rise, *Geophys. Res. Lett.*, *7*, 989-992.

Higdon, R. L. (1986), Absorbing Boundary Conditions for Difference Approximations to the Multi-Dimensional Wave Equation, *Mathematics of Computation*, *47*(176), 437-459.

Hussenoeder, S. A., J. A. Collins, G. M. Kent, R. S. Detrick, and the TERA Group (1996), Seismic analysis of the axial magma chamber reflector along the southern East Pacific Rise from conventional reflection profiling, *J. Geophys. Res.*, *101*, 22,087-22,105.

Karson, J. A., E. M. Klein, S. D. Hurst, C. D. Lee, P. A. Rivizzigno, D. Curewitz, A. R. Morris, and H. D. S. Party (2002), Structure of uppermost fast-spreading oceanic crust exposed at the Hess Deep Rift: Implications for subaxial processes at the East Pacific Rise, *Geochem. Geophys. Geosyst.*, *3*, 2001GC000155.

Kelly, K. R., R. W. Ward, S. Treitel, and R. M. Alford (1976), Synthetic seismograms; a finite-difference approach *Geophysics*, *41*(1), 2-27.

Kent, G. M., A. J. Harding, and J. A. Orcutt (1990), Evidence for a smaller magma chamber beneath the East Pacific Rise at 9°30'N, *Nature*, *344*, 650-653.

Kent, G. M., A. J. Harding, and J. A. Orcutt (1993a), Distribution of magma beneath the East Pacific Rise between the Clipperton transform and the 9°17'N deval from forward modeling of common depth point data, *J. Geophys. Res.*, *98*, 13,945-13,969.

Kent, G. M., A. J. Harding, and J. A. Orcutt (1993b), Distribution of magma beneath the East Pacific Rise near the 9°03'N overlapping spreading center from forward modeling of common depth point data, *J. Geophys. Res.*, *98*, 13,971-13,995.

Kent, G. M., R. S. Detrick, S. A. Swift, J. A. Collins, and I. I. Kim (1997), Evidence from Hole 504B for the origin of dipping events in oceanic crustal reflection profiles as out-of-plane scattering from basement topography, *Geology*, *25*(2), 131-134.

Korenaga, J., and P. B. Kelemen (1997), Origin of gabbro sills in the Moho transition zone of the Oman ophiolite: Implications for magma transport in the oceanic lower crust, *J. Geophys. Res.*, *102*, 27,729-27,749.

Mutter, J. C., S. M. Carbotte, J. P. Canales, and M. R. Nedimovic (2008), MGL0812 Cruise Report: A 3D MCS investigation of the magmatic-hydrothermal system at the East Pacific Rise 9°50'N.

Nafe, J. E. (1957), Reflection and transmission coefficients at a solid-solid interface of high velocity contrast, *Bulletin of Seismological Society of America*, *47*(3), 205-219.

Quick, J. E., and R. P. Delinger (1993), Ductile deformation and the origin of layered gabbro in ophiolites, *J. Geophys. Res.*, *98*(B8), 14015-14027.

Reynolds, A. C. (1978), Boundary conditions for the numerical solution of wave propagation problems, *Geophysics*, *43*(6), 1099-1110.

Singh, S. C., G. M. Kent, J. S. Collier, A. J. Harding, and J. A. Orcutt (1998), Melt to mush variations in crustal magma properties along the ridge crest at the southern East Pacific Rise, *Nature*, *394*, 874-878.

Singh, S. C., J. S. Collier, A. J. Harding, G. M. Kent, and J. A. Orcutt (1999), Seismic evidence for a hydrothermal layer above the solid roof of the axial magma chamber at the southern East Pacific Rise, *Geology*, *27*(3), 219-222.

Singh, S. C., et al. (2006), Discovery of a magma chamber and faults beneath a Mid-Atlantic Ridge hydrothermal field, *Nature*, *442*, 1029-1032.

Stephen, R. A. (1983), A comparison of finite difference and reflectivity seismograms for marine models, *Geophys. J. R. Astron. Soc.*, *72*(1), 39-57.

Stephen, R. A. (1984), Finite difference seismograms for laterally varying marine models, *The Journal of the Acoustical Society of America*, *76*(S1), S11.

Stephen, R. A., F. Cardo-Casas, and C. H. Cheng (1985), Finite-difference synthetic acoustic logs, *Geophysics*, *50*(10), 1588-1609.

Stephen, R. A. (1988), A review of finite difference methods for seismo - acoustics problems at the seafloor, *Reviews of Geophysics*, *26*(3), 445-458.

Stephen, R. A. (1990), Solutions to range-dependent benchmark problems by the finite-difference method, *The Journal of the Acoustical Society of America*, *87*(4), 1527-1534.

Stephen, R. A., and S. A. Swift (1994), Modeling seafloor geoacoustic interaction with a numerical scattering chamber, *Journal of the Acoustical Society of America*, *96*(2), 973-990.

Swift, S. A., M. E. Dougherty, and R. A. Stephen (1990), Finite difference seismic modeling of Axial Mamga Chambers, *Geophys. Res. Lett.*, *17*(No. 12), 2105-2108.

Vera, E. E., J. C. Mutter, P. Buhl, J. A. Orcutt, A. J. Harding, M. E. Kappus, R. S. Detrick, and T. M. Brocher (1990), The structure of 0- to 0.2-m.y.-old oceanic crust at 9°N on the East Pacific Rise from expanded spread profiles, *J. Geophys. Res.*, *95*, 15,529-15,556.

Virieux, J. (1984), SH-wave propagation in heterogeneous media: Velocity-stress finite-difference method, *Geophysics*, *49*(11), 1933-1942.

Virieux, J. (1986), P-SV wave propagation in heterogeneous media: Velocity-stress finite-difference method, *Geophysics*, *51*(4), 889-901.

Zelt, C. A., and R. B. Smith (1992), Seismic traveltime inversion for 2-D crustal velocity structure, *Geophys. J. Int.*, *108*(1), 16-34.

Chapter 3

Variations in axial magma chamber properties along the East Pacific Rise (9°30'-10°00'N) from 3D seismic imaging and 1D waveform inversion

Abstract

We use three-dimensional multi-streamer seismic reflection data to investigate the variations in axial magma chamber (AMC) properties along the East Pacific Rise between 9°30'N and 10°00'N (~60 km). This dataset contains clear *P* and *S*-converted waves reflecting off the top of the AMC, which allow us to qualitatively assess along-axis melt content variations within the AMC by *P*- and *S*-wave partial-offset stacks. Post-stack time-migrated reflection images show four prominent melt-rich sections, 2-4 km long and spaced 5-10 km from each other. Surprisingly, none of these melt-rich sections are located immediately beneath the region of most active hydrothermal activity at 9°50'N. One-dimensional waveform modeling in the time intercept-slowness domain was employed to investigate the physical properties of the AMC melt lens at two locations with contrasting melt content. The AMC melt lens is best modeled with a low *Vp* (2.98 km/s) and *Vs* (≤ 0.5 km/s) structure in the melt-rich section, whereas the melt-poor AMC melt lens requires higher *Vp* (4.67 km/s) and *Vs* (1.5-2.0 km/s). The thickness of the AMC melt lens is ~16-40 m. These results indicate that the melt fraction in the AMC melt lens can be as high as 95-100% in the melt-rich sections and as low as 41-46% in the melt-poor sections. Based on the melt-mush segmentation, two scenarios regarding the relationships between the 2005-06 eruption, the physical state of the AMC melt lens before and after this event, and hydrothermal activity are proposed: (1) The source of the 2005-06 eruption was a 10-km-long melt-rich lens, which has been driving hydrothermal circulation in this area. The eruption drained most of the melt in the 5-km-long central part, leaving behind a large fraction of connected crystals separating the distal ends of the lens from which melt was not fully drained; (2) Alternatively, prior to the 2005-06 eruption intense hydrothermal activity cooled the section of the AMC immediately beneath the dense hydrothermal vent field and prevented the formation of a melt-rich lens. The eruption was therefore fed from the accumulated melt in melt-rich sections immediately to the north and south of the hydrothermal field where the hydrothermal cooling was less effective. If the first scenario is correct, a total magma volume extracted from the AMC melt lens is estimated of ~46×10^6 m^3 during the 2005-06 eruption event, with ~24×10^6 m^3 left unerupted in the upper crust as dikes. The total width of the dike is 3.4 m if the dike fed the eruption extended over the 5-km-long central section, or 0.95 m

if the dike fed the eruption over the 18-km-long section where the seafloor eruption had been documented. No obvious correlations were found between the melt-mush segmentation, axial summit trough (AST) width, axial depth and MgO wt.%. This may be explained by the time scale difference of morphological (AST width and axial depth) and geochemical (MgO wt.%) features (~10^2-10^3 years) and the melt-mush segmentation stability (decades).

3.1. INTRODUCTION

The fast-spreading East Pacific Rise (EPR) has been intensively studied during the last three decades following the discovery of a bright seismic reflector beneath the ridge axis which was interpreted as the roof of an axial magma chamber (AMC) [*Herron et al.*, 1980]. The large number of multidisciplinary studies conducted at the EPR between ~9°-10°N led to the establishment of this region as a RIDGE2000 Integrated Study Site (R2K ISS) (http://www.ridge2000.org/). Here, scientists have been and are currently investigating the linkages between mantle flow, magma generation and migration, crustal accretion, volcanic, hydrothermal, and biological processes that result in chemical and physical exchanges of energy and matter between the Earth's mantle and oceans. Although the presence of an AMC along most of this section of the EPR was established in the 1990's [e.g., *Detrick*, 1991; *Detrick et al.*, 1987; *Dunn and Toomey*, 1997; *Kent et al.*, 1990, 1993a, 1993b; *Mutter et al.*, 1988; *Vera et al.*, 1990], the technology at that time precluded acquiring data at high enough resolution to accurately assess the distribution of crustal melt bodies and their fine-scale physical properties. This is a key piece of information that is currently missing from our knowledge of the EPR mantle-to-microbe system.

The size and shape of the AMC beneath the EPR have been the subject of several investigations [*Caress et al.*, 1992; *Collier and Singh*, 1997, 1998; *Detrick et al.*, 1987; *Detrick et al.*, 1993; *Harding et al.*, 1989; *Hussenoeder et al.*, 1996; *Kent et al.*, 1990, 1993a, 1993b; *Singh et al.*, 1999; *Singh et al.*, 1998; *Toomey et al.*, 1990; *Vera et al.*,

1990]. These studies have led to a model in which a thin (< 200 m) [e.g., *Hussenoeder et al.*, 1996], narrow (usually 1-2 km wide, with extreme values 0.25 km and 4.15 km [*Kent et al.*, 1993a]) lens or sill of magma 1-2 km below the seafloor [e.g., *Detrick et al.*, 1987] and overlies a zone of partial melt in the midcrust surrounded by a broader low-velocity volume (5-10 km wide) extending to the base of the crust and into the uppermost mantle [*Sinton and Detrick*, 1992]. The thickness of the sill forming the roof of the AMC has not been well constrained because of the lack of robust evidence for basal AMC sill reflections in field data. Investigations through waveform modeling suggest that the AMC is characterized by a decrease in seismic velocity at the impedance contrast between a ~50-m-thick solid roof (that separates the magma chamber from the upper crustal hydrothermal fluids) and a thin (~30-100 m) sill of melt and crystals [e.g., *Collier and Singh*, 1997, 1998; *Hussenoeder et al.*, 1996; *Singh et al.*, 1999; *Singh et al.*, 1998]. To avoid any confusion with the AMC and melt lens or sill, in this chapter the melt lens or sill refers to the AMC lid which is a very thin layer (< 200 m) and the AMC also includes the low velocity mush zone below the melt lens or sill.

Although the magma sill or lens is volumetrically small, it is thought to play a key role in the availability and composition of magma at the ridge axis [*Sinton and Detrick*, 1992]. Crustal accretion processes are also very sensitive to changes in the thermal balance between heat input from magma chambers and heat extraction by hydrothermal circulation [e.g., *Phipps Morgan and Chen*, 1993]. Therefore, understanding the nature

and physical state of the AMC sill at the EPR can provide key constrains for seafloor eruption processes, the chemistry of the erupted lavas, and the accretion of oceanic crust.

The internal properties (e.g., percentage of crystallinity and distribution of crystals) of the AMC sill and their spatial and temporal variations along the northern EPR are still poorly known. Shear properties of the AMC sill can only be inferred from their effect on amplitude versus offset (AVO) behavior of reflected seismic phases, including *P-S* converted phases. The AMC shear wave velocity (*Vs*) has been estimated at a few locations along the EPR with variable results. On the basis of plane wave reflection coefficient modeling of an expanding spread profile (ESP) on EPR 13°13'N, *Harding et al.* [1989] inferred the presence of a partially molten magma sill (i.e., $Vs \neq 0$ km/s) at the roof of the AMC. In contrast, an AVO analysis of the AMC event at EPR 9°30'N led *Vera et al.* [1990] to suggest the presence of a fully molten magma sill (i.e., $Vs = 0$ km/s). In some instances, results from the same location obtained by different investigators are inconsistent with each other. For example, estimates of AMC shear wave velocity at EPR 9°39'N range from 0 km/s [*Collier and Singh*, 1997] to 1.45 km/s [*Hussenoeder et al.*, 1996]. Other than the waveform modeling investigation at the southern EPR (~14°S) [*Singh et al.*, 1999; *Singh et al.*, 1998] none of these studies have used the information from shear waves reflected from the top of the AMC, which provides better constraints on *Vs* structure in the AMC sill.

A general conclusion extracted from these studies is that the AMC sill properties vary at different sections of the global mid-ocean ridge (MOR) system. The spatial scale of such variability was first established by *Singh et al.* [1998], who took advantage of the different AVO behaviors of *P*- and *S*-converted waves reflecting off a partially molten sill, and the AVO dependence with melt content, to produce qualitative estimates of along-axis variations in melt content within the AMC sill from what is known as *P*- and *S*-wave partial-offset stacks. This methodology has been employed at the southern EPR [*Singh et al.*, 1998], southern Juan de Fuca Ridge (JdFR) [*Canales et al.*, 2006], and the EPR 9°03'N overlapping spreading center (OSC) [*Singh et al.*, 2006].

However, at the EPR R2K ISS, neither the partial-offset stack method (except locally at the 9°03'N OSC [*Singh et al.*, 2006]) nor the waveform inversion using information from both AMC reflected *P*- and *S*-waves has been attempted, from which the results are important pieces of information currently missing for magmatic-hydrothermal system. In this chapter we employ *P*- and *S*-wave partial-offset stack [e.g., *Canales et al.*, 2006; *Singh et al.*, 1998] and 1D waveform inversion methods [e.g., *Collier and Singh*, 1997, 1998] to investigate the spatial variation of the melt content in the AMC and the physical properties of the AMC reflector along the northern EPR (~9°30'-10°N). Our results show four prominent 2-4-km-long melt-rich sections spaced 5-10 km from each other. The melt sill located in melt-rich sections is likely entirely molten (100% melt) whereas in melt-poor sections the melt content could be as low as ~41-46%.

3.2. GEOLOGICAL AND GEOPHYSICAL BACKGROUND

The EPR is the boundary between the Pacific and Cocos tectonic plates (Figure 3-1a). The EPR 8°-11°N R2K ISS includes a long first-order ridge-axis segment bounded by the Clipperton fracture zone to the north and the Siqueiros fracture zone to the south. This segment is one of the best studied portions of the world's MOR system [e.g., *Canales et al.*, 2003; *Carbotte and Macdonald*, 1992; *Christeson et al.*, 1996; *Christeson et al.*, 1994a; *Christeson et al.*, 1997; *Collier and Singh*, 1997; *Detrick et al.*, 1987; *Escartín et al.*, 2007; *Fornari et al.*, 1998a; *Fornari et al.*, 1998b; *Fornari et al.*, 2004; *Harding et al.*, 1993; *Haymon et al.*, 1991; *Haymon et al.*, 1993; *Kent et al.*, 1993a, 1993b; *Soule et al.*, 2009; *Soule et al.*, 2008; *Soule et al.*, 2005; *Soule et al.*, 2007; *Toomey et al.*, 1990; *Toomey et al.*, 1994; *Wright et al.*, 1995a; *Wright et al.*, 1995b]. The full spreading rate in this area has been approximately 110 mm yr^{-1} during the past 2 Myr [*Carbotte and Macdonald*, 1992]. The whole segment is believed to be magmatically active, as inferred from morphological observations [*Macdonald and Fox*, 1988; *Scheirer and Macdonald*, 1993], the along-axis continuity and brightness of seismic imaging of AMC [*Detrick et al.*, 1987; *Herron et al.*, 1980; *Kent et al.*, 1993a; *Mutter et al.*, 1988], the presence of crustal and upper mantle low seismic velocity and high attenuation zones [*Dunn and Toomey*, 1997; *Dunn et al.*, 2000; *Toomey et al.*, 1990; *Toomey et al.*, 1994; *Wilcock et al.*, 1992, 1995], and the abundance of hydrothermal vents [*Haymon et al.*, 1991].

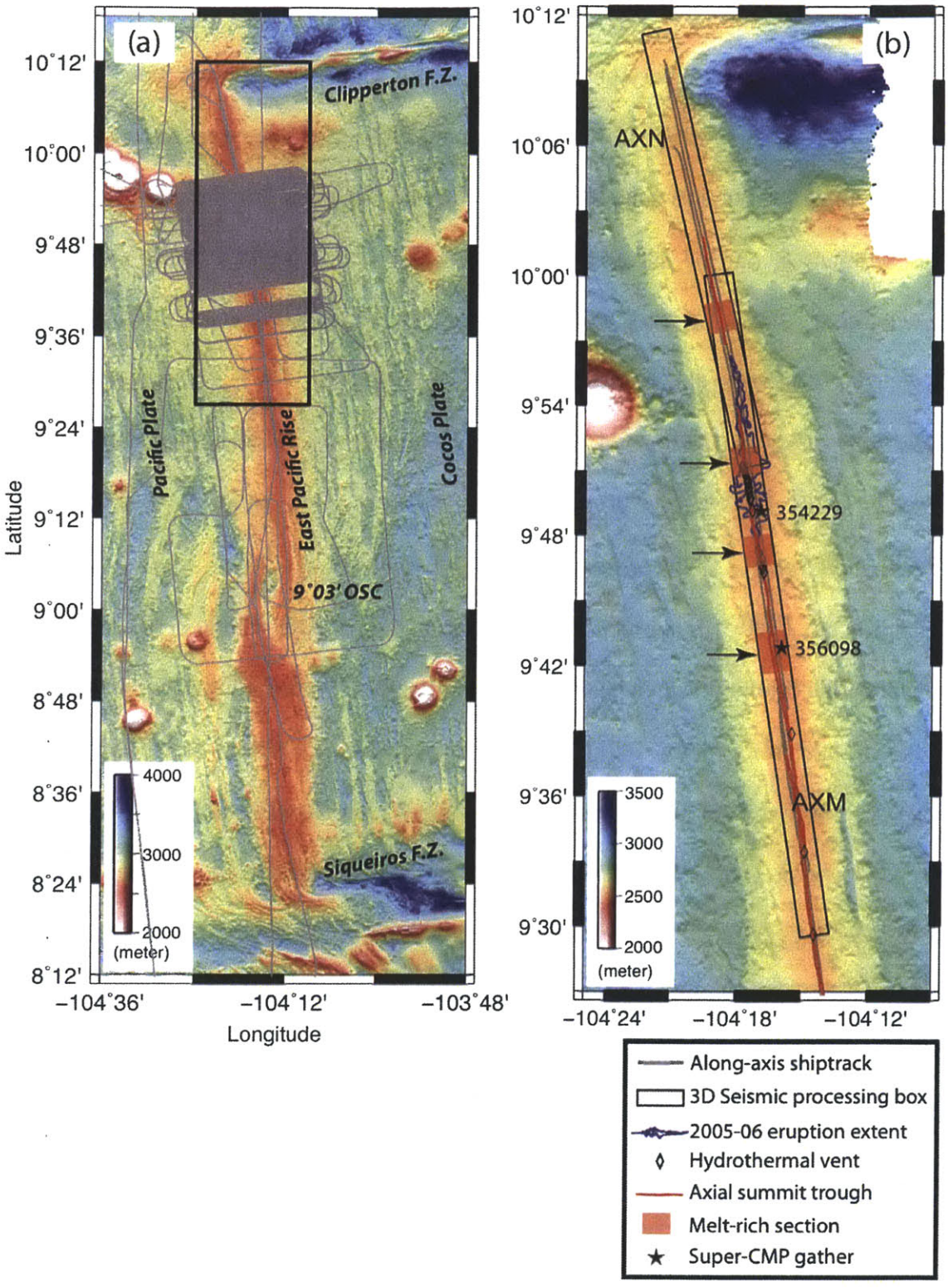
(a)
(b)
Clipperton F.Z.
Pacific Plate
East Pacific Rise
Cocos Plate
9°03' OSC
Siqueiros F.Z.
AXN
AXM
354229
356098
4000
3000
2000
(meter)
3500
3000
2500
2000
(meter)
10°12'
10°00'
9°48'
9°36'
9°24'
9°12'
9°00'
8°48'
8°36'
8°24'
8°12'
10°06'
9°54'
9°42'
9°30'
−104°36'
−104°12'
−103°48'
−104°24'
−104°18'
−104°12'
Latitude
Longitude
Along-axis shiptrack
3D Seismic processing box
2005-06 eruption extent
Hydrothermal vent
Axial summit trough
Melt-rich section
Super-CMP gather

Figure 3-1. (**a**) Shaded relief bathymetry of the East Pacific Rise between Siqueiros and Clipperton fracture zones (EPR, 8°12'-10°15'N). The gray lines show the shiptrack of the 3D multi-channel seismic (MCS) survey (cruise MGL0812). Data are from the Marine Geoscience Data System (http://www.marine-geo.org). The study area (expanded view in Figure 3-1b) is outlined by a black box. (**b**) Bathymetry map of our study area (EPR ~9°30'-10°N). Data are from cruise MGL0812 [*Mutter et al.*, 2009]. Two 3D along-axis seismic boxes (black rectangles) were investigated using *P*- and *S*-wave partial-offset stacking: AXM (~9°30'-10°N) and AXN (~9°51'-10°10'N). Results of the final interpretation of melt-rich sections are shown in red rectangles with black arrows: four prominent 2-4-km-long melt-rich sections spaced 5-10 km from each other at ~9°42'-9°43'N, 9°47'-9°48'N, 9°51'-9°52'N, and 9°57'-9°58'N. Gray lines show shiptracks of the four along-axis seismic lines used in this study. Blue line marks the extent of 2005-06 lava eruption derived from camera tow data [*Soule et al.*, 2007]. Red lines show axial summit trough (AST), and black diamonds indicate hydrothermal vents. Black stars with numbers show positions of the two super-common mid-point (CMP) gathers used for 1D waveform modeling.

Two second-order segments separated by the 9°03'N OSC (Figure 3-1a), and multiple finer-scale segments, including third-order volcanic segments, which are defined by discontinuities in the structure and morphology of the axial topographic high, and fourth-order segments bounded by smaller, more transient ridge-axis discontinuities, are identified through multibeam sonar system [e.g., *Haymon et al.*, 1991; *Macdonald and Sempéré*, 1984; *Scheirer and Macdonald*, 1993; *White et al.*, 2006; *White et al.*, 2002]. The morphotectonic/structural segmentation of the ridge crest at the fourth-order scale matches remarkably well with along-strike variability observed in axial hydrothermal activity, and the fourth-order segments appear to be in various stages of magmatic, tectonic, and hydrothermal development. *Haymon et al.* [1991] postulated the existence of a typical volcanic-hydrothermal-tectonic cycle on fast-spreading ridge crests that begins with diking and eruption, followed by magmatic drainback or drainage and gravitational collapse, possible development of an axial summit trough (AST), and the onset of hydrothermal activity.

The EPR 9°50'N area is the first MOR segment with multiple documented eruptions [e.g., *Haymon et al.*, 1993; *Soule et al.*, 2009]. The 2005-06 eruption (Figure 3-1b) occurred in approximately the same area as an eruption documented in 1991-92 [*Haymon et al.*, 1993; *Rubin et al.*, 1994; *Soule et al.*, 2009]. Using seafloor imagery collected on camera tows and *Alvin* dives, *Soule et al.* [2007] estimated that the 2005-06 eruption produced ~22 $\times$ 10^6 m^3 of lava, 4-5 times larger than estimated volumes of 1991-92

erupted lava flows. This estimated lava volume may only represent <15% of the magma available in the AMC.

Forty-four hydrothermal vents have been identified along the EPR 9°-10°N (Figure 3-1b). Nine of these are active, thirteen are inactive, and the activities of others are still unknown (http://www.marine-geo.org/tools/search/targets.php?id=EPR). Before the 2005-06 eruption, high-temperature (≥ 350°C) hydrothermal vents were present in several areas within the EPR AST where the 1991-92 eruption had been focused and where drainback of lava into the primary eruptive fissure occurred. These areas were also coincident with ~10-30 m-wide channels that serve to transport lava across the ridge crest. In addition, regions of diffuse hydrothermal flow at low temperatures (< 35°C) and vent animal communities are concentrated along the primary eruptive fissure that fed the 1991-92 eruption [*Fornari et al.*, 2004].

Potential eruptions from melt pockets within an AMC depend on a number of parameters including the internal properties of the AMC sill [*Singh et al.*, 1998], which have only been investigated in two locations at this EPR section. Beneath 9°48'N, *Collier and Singh* [1997, 1998] showed that the ridge is underlain by a thin (30 m) layer with low *Vp* (2.4 km/s) and *Vs* ≅ 0 km/s. This layer was interpreted as a magma sill with less than 20 ± 10% crystals underlain by a mostly solid floor. The melt layer was inferred to have been newly emplaced, suggesting that this segment was at the onset of a renewed volcanic stage. Beneath 9°39'N, the base of the mostly molten layer was underlain by a velocity gradient (*Vp* increases from 2.6 to 3.5 km/s in ~50 m), suggesting that this

segment was at an intermediate stage in its volcanic cycle. However, at this same location and using the same data, *Hussenoeder et al.* [1996] inferred that the AMC sill at 9°39'N is ~82 m thick with Vp = 3.40 km/s and Vs = 1.45 km/s.

3.3. SEISMIC DATA ACQUISTION AND PROCESSING

In Summer 2008 we conducted a 3D multi-streamer, multi-channel sesimic (MCS) reflection experiment on board the R/V *Marcus G. Langseth* across and along the northern EPR between the Siqueiros and Clipperton fracture zones (cruise MGL0812 [*Mutter et al.*, 2009], Figure 3-1a). The primary goals of cruise MGL0812 were to create an accurate 3D seismic reflection image of the magmatic-hydrothermal system within the EPR 9°50'N site by imaging the structure of the AMC lid and shallow oceanic crust at a resolution, geometric accuracy, and scale comparable to seafloor observations of hydrothermal, biological, and volcanic activity [*Mutter et al.*, 2009]. In this chapter we present results from a subset of along-axis MCS data collected along axis-parallel profiles between ~9°30'-10°00'N (Figure 3-1b).

Seismic data acquisition parameters for cruise MGL0812 are listed in Table 3-1. Accurate locations of shot positions and hydrophone groups were obtained from the ship's Global Positioning System (GPS), GPS receivers in the tail bouys at the end of the streamers, and acoustic transponders and compasses placed along the streamers. For each pass of a sail line, the experimental configuration [*Mutter et al.*, 2009] resulted in eight

Table 3-1. Summary of Main Acquisition Parameters During Cruise MGL0812

Sources (air gun arrays)	Number of source arrays: 2 (each with 2 strings) Number of guns: 10 per array (1 spare) Source separation: 75 m Volume: 54 L (3,300 in^3) per source Shot interval: alternate every 37.5 m Source depth: 7.5 m
Receivers (hydrophone streamers)	Number: 4 Spacing: 150 m Length: 6,000 m Number of channels: 468 per streamer Channel spacing: 12.5 m Receiver depth: 7.5 m (AXIS3, AXIS2R1) 10 m (AXIS4, AXIS3P2)[a]
Source to nearest channel distance	200 m
Data recording	Sampling interval: 2 ms Record length: 8.190 s (AXIS3, AXIS2R1) 10.240 s (AXIS4, AXIS3P2) Format: SEG-D

For profiles AXIS4 and AXIS3P2:

[a] due to the weather conditions, the depth of the steamers were lowered from 7.5 to 10 m to help alleviate persistent cable swell noise.

common-mid-point (CMP) seismic reflection profiles (i.e., sub-lines, oriented parallel to the ridge axis) separated 37.5 m from each other, and a 37.5 m by 6.25 m static bin cell size that allows 3D seismic processing (Figure 3-2). Two 3D along-axis boxes were created for this study: the southern box AXM includes seismic data from sail lines AXIS2R1, AXIS3, AXIS4, and AXIS3P2, and the northern box AXN includes seismic data from sail lines AXIS2R1, AXIS4, and AXIS3P2 (Figure 3-1b). More details of the data acquisition can be found in MGL0812 cruise report [*Mutter et al.*, 2008].

The detailed seismic processing sequence and the parameters used are listed in Table 3-2. Seismic processing was designed to enhance stacking of the AMC reflected $P_{AMC}P$ and $P_{AMC}S$ waves. It consisted of conventional steps [e.g., *Yilmaz*, 1987] such as trace editing, sorting to CMP gathers, band-pass filtering, flexible binning (Figure 3-3), creating super-CMP gathers, trace interpolation, normal moveout (NMO) corrections, frequency-wavenumber (*f-k*) filtering, stacking, and migration (Table 3-2). In our data, the far-offset $P_{AMC}P$ and converted $P_{AMC}S$ waves reflected from the top of AMC are not easily recognized in the super-CMP gathers because they are contaminated by seafloor reflections, shallow crustal reflections and refractions, or the presence of noise from side-echoes due to the rough cross-axis seafloor topography [*Canales et al.*, 2006] (Figures 3-4a, b). The *f-k* filter was designed to eliminate arrivals with apparent dips exceeding 6.25 ms per trace, thus enhancing AMC reflected *P*- and *S*-waves for partial-offset stacking (Figures 3-4c, d).

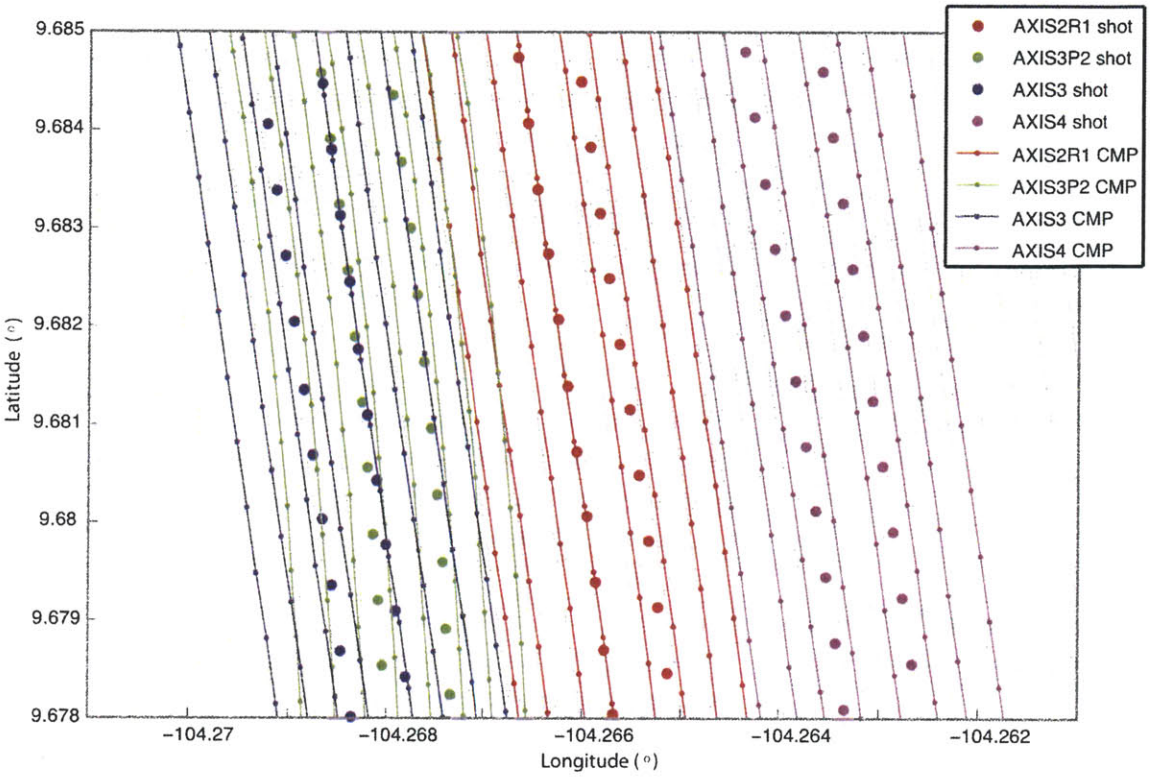

Figure 3-2. A zoom-in view of the experimental configuration of cruise MGL0812 [*Mutter et al.*, 2009] for 3D box AXM. The colored lines represent the seismic lines with shot locations indicated by big dots, and the small dots show the CMP locations (one out of every 12 CMPs is shown along each CMP profile). Both shot and CMP locations are plotted with the same color as corresponding seismic lines. For each pass of a sail line, eight seismic reflection profiles, or CMP profiles (oriented parallel to the ridge axis) are created and separated by 37.5 m from each other. The background gray grids show the 3D geometry setup with the 37.5 m by 6.25 m static bins that forms the basis for the 3D seismic processing in this study.

Table 3-2. Data Processing Sequence and Parameters

Sequence	Steps and parameters
Trace editing	
3-D geometry definition	CMP gather, 40-fold bin (bin size: 6.25 m × 37.5 m in along-axis and cross-axis direction respectively) angles of 3D boxes: AXM NW 8.3323° AXN: NW 12.5056°
Band-pass filtering	5-7-200-225 Hz
Gain (spherical divergence correction)	input velocity source: esp05 [*Vera et al.*, 1990]
Surface-consistent amplitude correction for shot and channel	
Flexible binning	offset distribution regularization (cross-line direction): 0.5 × bin size for offsets ≤ 1,662 m; 1.5 × bin size for offsets ≥ 4,587 m (linear interpolation offsets in between those values) (Figure 3-3)
Resample	4 ms and 7-s long
Creating super-CMP gathers (along sub-line direction)	band-pass filter 2-7-30-50 Hz combining 24 consecutive CMP gathers and median-stacking constant-offset traces
Trace Interpolation	super-CMP gather: regularized 468-fold trace gathers, offset range: 190-6027.5 m (with an interval of 12.5 m)
Frequency-wavenumber (*f-k*) filtering	band-pass filter 2-7-30-50 Hz NMO (2.0 km/s) *f-k* dip filter (apparent dips exceeding 6.25 ms/trace) remove NMO (2.0 km/s)
P- and *S*-wave partial-offset stacking	mute (stretch amount 65%) near-offset *P*-wave stack: NMO (2.6 km/s), 0-2 km far-offset *P*-wave stack: NMO (2.6 km/s), 2-4 km far-offset *S*-wave stack: NMO (2.4 km/s), 0-2 km
Post-stack time migration	band-pass filter 2-7-30-50 Hz top mute at the seafloor finite difference algorithm [*Lowenthal et al.*, 1976] (maximum dip 15 ms/trace, layer thickness 40 ms)
Display	band-pass filter 2-7-30-50 Hz energy attribute of trace segment: time window for *P*-wave stack: 3.9 - 4.15 s time window for *S*-wave stack: 4.15 - 4.4 s

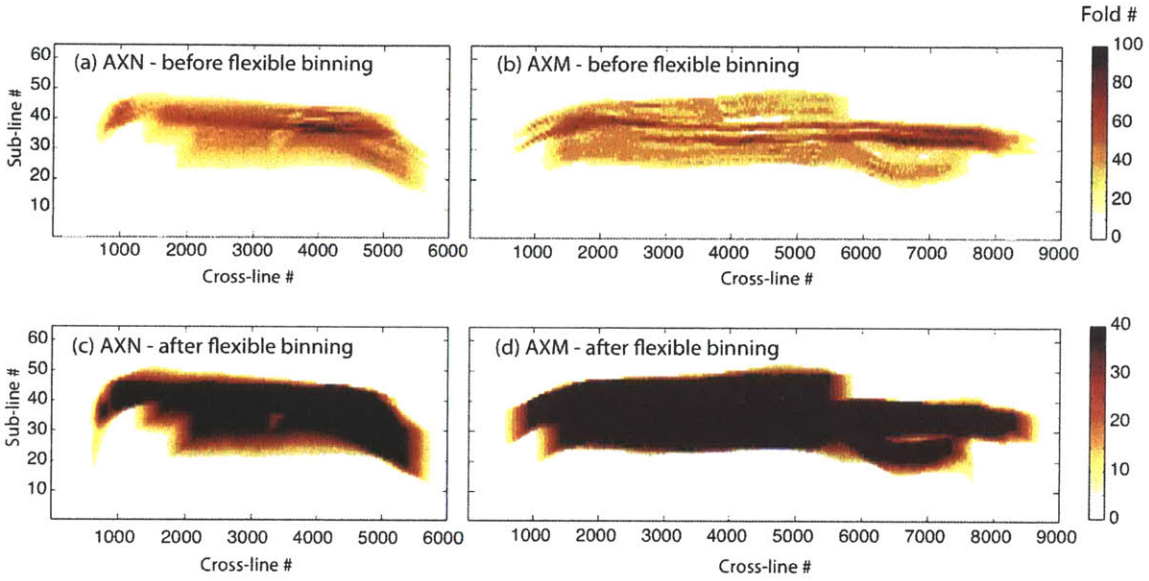

Figure 3-3. Bin fold map for 3D seismic boxes AXN (**a**) before and (**c**) after flexible binning, and AXM (**b**) before and (**d**) after flexible binning. The flexible binning is based on offset distribution regularization (cross-line direction) using 0.5 × bin size for offsets ≤ 1,662 m, 1.5 × bin size for offsets ≥ 4,587 m (linear interpolation offsets in between those values). The nominal bin fold after flexible binning is 40.

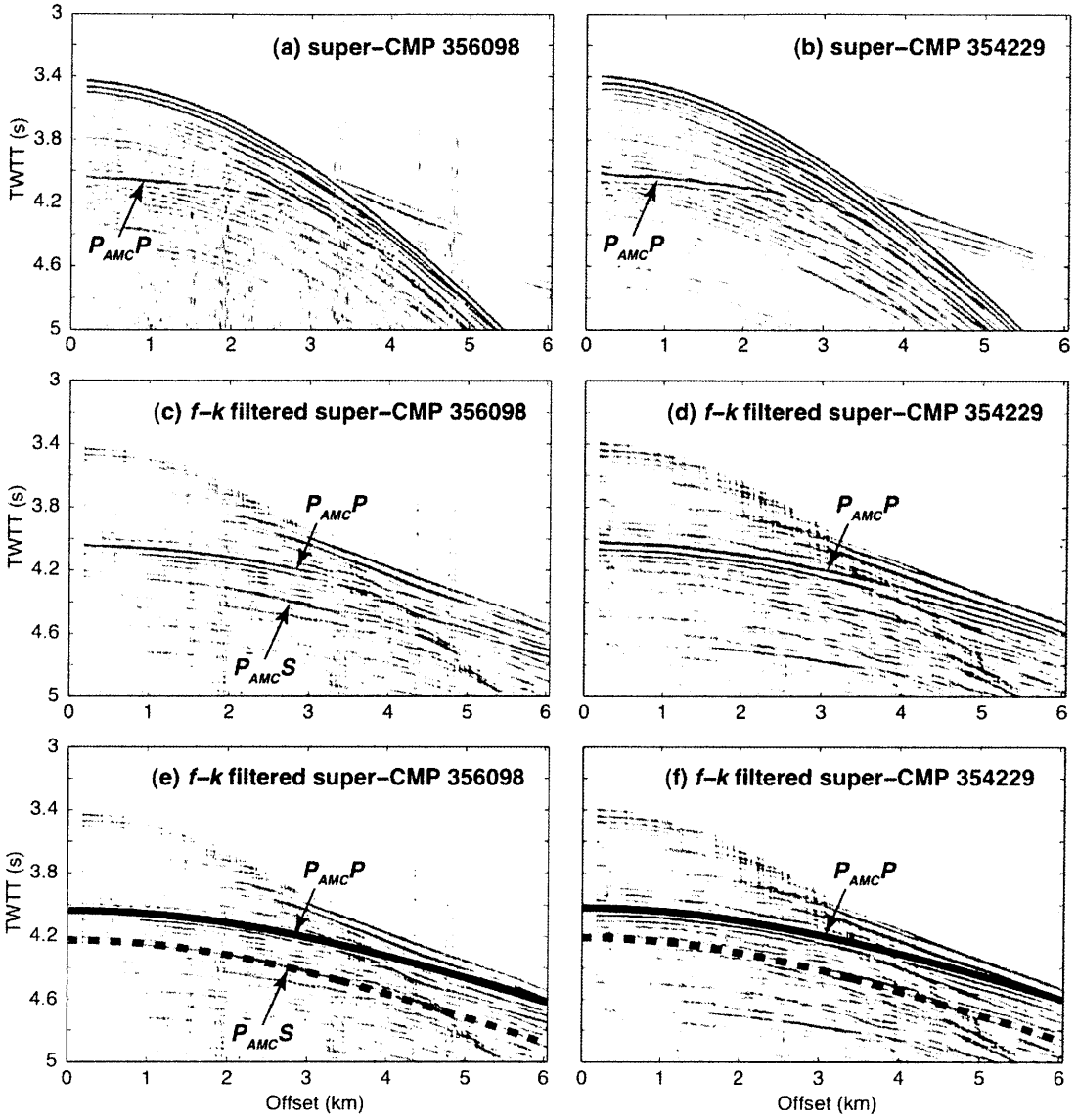

Figure 3-4. Bin-extended super-CMP gathers from 3D seismic box AXM. (**a**) Super-CMP gather 356098. (**b**) Super-CMP gather 354229. Their corresponding frequency-wavenumber (*f-k*) filtered gathers are shown in (**c**) and (**d**), respectively. The axial magma chamber (AMC) reflections, $P_{AMC}P$ and $P_{AMC}S$, are indicated by black arrows. (**e**, **f**) Same as (**c**, **d**) with predicted $P_{AMC}P$ and $P_{AMC}S$ traveltime curves calculated from velocity model ESP05 [*Vera et al.*, 1990], which are shown in solid and dashed black lines respectively. TWTT = two-way traveltime.

3.4. *P*- AND *S*-WAVE PARTIAL-OFFSET STACKING

Melt has a particularly strong effect on the crustal shear velocity [*Anderson and Spetzler*, 1970; *Mavko*, 1980], and therefore affects the AVO behaviors of *P*- ($P_{AMC}P$) and *S*-converted ($P_{AMC}S$) waves reflected off a crustal melt lens (Figure 3-5). The detection of $P_{AMC}S$ waves allowed *Singh et al.* [1998] and *Canales et al.* [2006] to build seismic reflection images of melt-rich and melt-poor sections of the AMC along the southern EPR and JdFR using 2D MCS data. However, there is inherent ambiguity in imaging melt-rich and melt-poor sections of an AMC with 2D MCS data using *P*- and *S*-wave partial-offset stacks. This is because the AMC can be as narrow as just a few hundred meters, and apparent AVO variations could be due to the misalignment of sources and receivers from the top of the AMC [*Kent et al.*, 1993a, 1993b], and not to true changes in AMC physical properties. This problem can be avoided with 3D seismic data. Using 3D MCS reflection data from the survey ARAD (Anatomy of a Ridge Axis Discontinuity) and the partial-offset stacking method, *Singh et al.* [2006] reported a region of higher melt fraction overlying the Moho at zero-aged crust. In this section we applied the *P*- and *S*-wave partial-offset stacking method [e.g., *Canales et al.*, 2006; *Singh et al.*, 1998] to the AMC reflected $P_{AMC}P$ and $P_{AMC}S$ waves in the recorded 3D MCS data (cruise MGL0812) to qualitatively image melt-rich and melt-poor sections of the AMC at the EPR R2K ISS (~9°30'-10°00'N, Figure 3-1b).

A preliminary inspection of *f-k* filtered super-CMP gathers from the 3D along-axis seismic data shows clear $P_{AMC}P$ waves at ~4.0 s within shot-receiver offsets of ~0-4 km

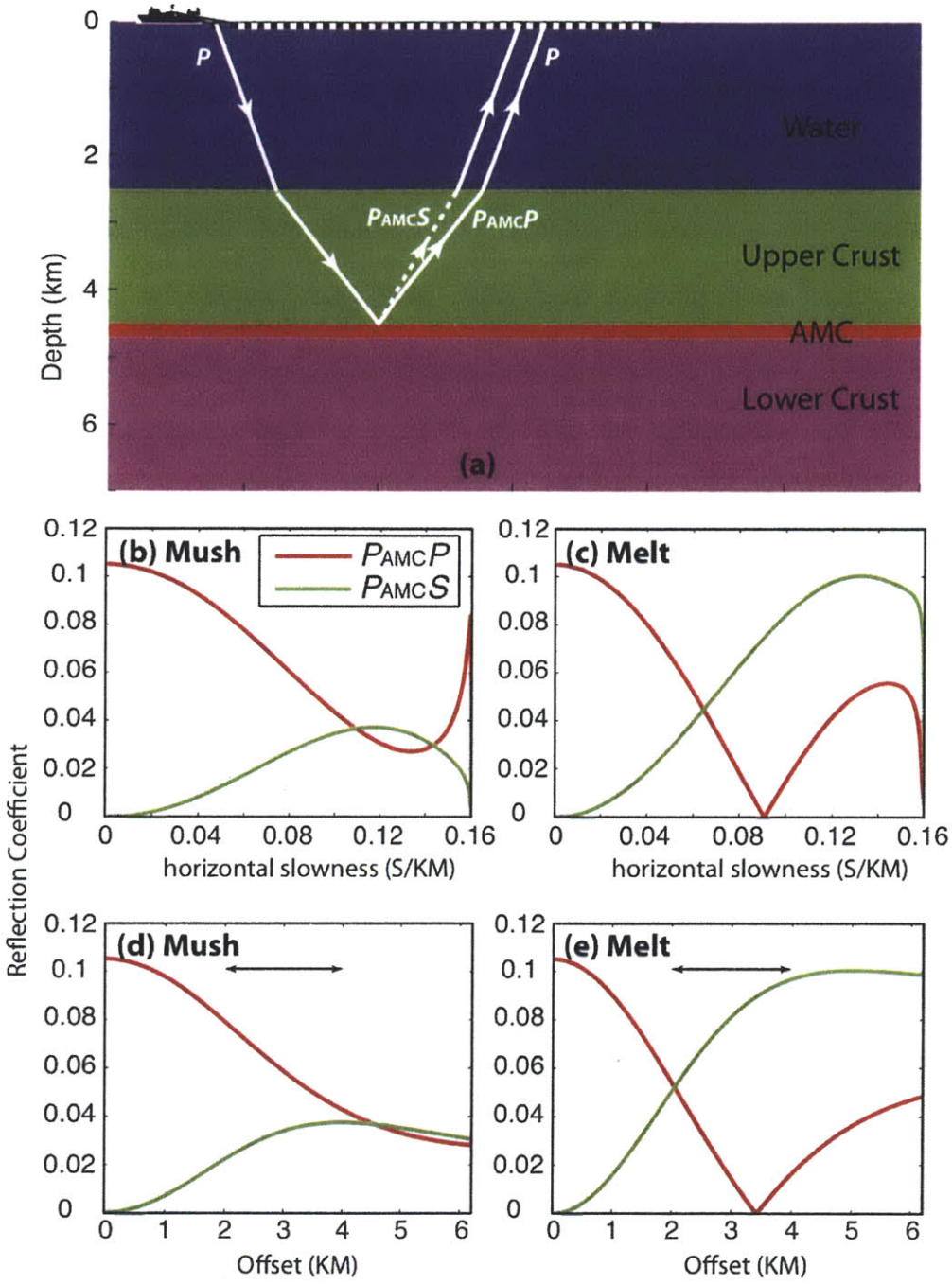

Water:	Vp = 1.5 km/s	Vs = 0.0 km/s	ρ = 1000 kg/m^3
Upper Crust:	Vp = 6.25 km/s	Vs = 3.65 km/s	ρ = 2700 kg/m^3
Mush:	Vp = 3.0 km/s	Vs = 2.0 km/s	ρ = 2700 kg/m^3
Melt:	Vp = 3.0 km/s	Vs = 0.0 km/s	ρ = 2700 kg/m^3

Figure 3-5. (**a**) Simplified oceanic crust and schematic ray paths for $P_{AMC}P$ and $P_{AMC}S$ reflections. Model parameters are listed below. Two AMC cases are shown, the mush case is for Vs = 2.0 km/s within the AMC, while the melt case is for Vs = 0 km/s within the AMC. (**b**, **c**) Theoretically computed reflection coefficients (displacement) versus horizontal slowness for a *P*-wave incident at seafloor. (**d**, **e**) Reflection coefficients plotted versus source-receiver offsets. We expect to see (1) that a phase reversal occurs for the $P_{AMC}P$ reflection in the melt case, and (2) that $P_{AMC}S$ has a much higher reflection coefficient in the far-offset for the case of melt than for mush. The high-amplitude $P_{AMC}S$ and low-amplitude $P_{AMC}P$ reflections at offset ~2-4 km can be used for partial-offset stacking to identify the presence of melt.

(Figures 3-4c, d). The *f-k* filtered super-CMP gather 356098 also shows a coherent event between 2 and 4 km offset observed at ~0.2 s below the $P_{AMC}P$ waves (Figure 3-4c) that was difficult to identify in the unfiltered gather (Figure 3-4a). Based on its traveltime and the extensive modeling presented in Chapter 2, we confidently interpret this phase as a conversion from an incident *P*- to an *S*-wave reflected at the top of the AMC and then converted back to a *P*-wave at the seafloor ($P_{AMC}S$ waves, Figure 3-4e). Other possible origins for the $P_{AMC}S$ waves, such as a peg-leg multiple from layer 2A or an *S*-wave conversion at the base of layer 2A, do not predict the observed AVO and traveltime behavior with offset. The comparison between super-CMP gathers 356098 and 354229 shows that the character of the AMC reflections varies beneath different sections of the ridge (Figure 3-4). At super-CMP gather 354229, the $P_{AMC}P$ reflection is a strong event out to at least 4 km range and there is no detectable $P_{AMC}S$ reflection (Figures 3-4d, f), whereas the amplitude of the $P_{AMC}P$ reflection at super-CMP gather 356098 decreases beyond ~2 km range and there is a strong $P_{AMC}S$ reflection with an amplitude comparable to the $P_{AMC}P$ reflection present at ~2-4 km offset range (Figures 3-4c, e). The amplitude of the theoretical reflection coefficient patterns (Figure 3-5) suggests the presence of melt at super-CMP gather 356098 and mush at super-CMP gather 354229.

From the theoretical calculations of the AVO behavior of the AMC reflections for melt and mush cases described above (Figure 3-5), it is clear that the crucial offset window for discriminating between the two super-CMP gathers is ~2-4 km. For a melt-rich sill, the amplitude of the $P_{AMC}P$ waves decreases, and the amplitude of the *S*-

converted $P_{AMC}S$ waves increases at this offset. We constructed three partial-offset stacks using a constant NMO velocity (V_{NMO}) in each of them: (1) using 0-2 km offsets and V_{NMO} = 2.6 km/s that we call "$P_{AMC}P$ near-offset stack"; (2) using 2-4 km offsets and V_{NMO} = 2.6 km/s that we call "$P_{AMC}P$ far-offset stack"; and (3) using 2-4 km offsets and V_{NMO} = 2.4 km/s that we call "$P_{AMC}S$ far-offset stack".

The post-stack migrated along-axis sub-line 29 in the northern box AXN and sub-line 40 in the southern box AXM calculated from the three stacks are shown in Figures 3-6a, b. The energy attributes of the two 3D seismic boxes calculated within a 0.25-s window along the sub-line direction are shown in Figures 3-6c, d. The near-offset $P_{AMC}P$ reflection is observed at ~4.0-4.1 s two-way travel time (TWTT) along most of the study area. In contrast, the far-offset $P_{AMC}S$ (~4.2-4.3 s TWTT) is clearly observed and strongest at only four separate sections (Figure 3-6). As expected, the stacked $P_{AMC}S$ reflection is strong near super-CMP gather 356098, and the amplitude of the far-offset $P_{AMC}P$ reflection is greatly decreased compared to the near-offset. The AVO behaviors of the AMC reflections shown in super-CMP gather 356098 are used as our criterion to define melt-rich sections in this study. Based on this criterion, we find four prominent 2-4-km-long melt-rich zones spaced 5-10 km from each other at ~9°42'N-9°43'N, 9°47'N-9°48'N, 9°51'N-9°52'N, and ~9°57'N-9°58'N (Figures 3-1b and 3-6). While other reflections with similar characteristics are present at similar depth at other parts of the segment, they are more ambiguous and lack the lateral continuity of the $P_{AMC}S$ reflection mentioned above, so we will not attempt to interpret them.

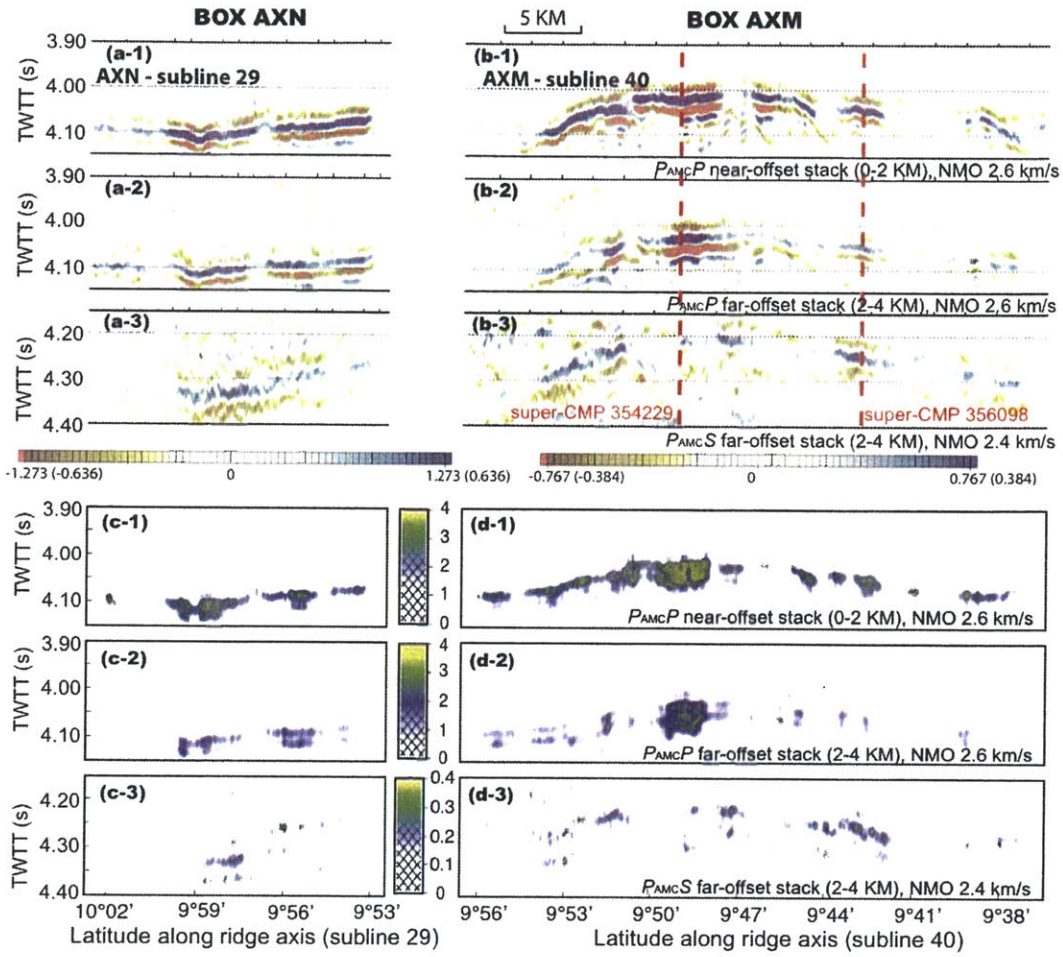

Figure 3-6. (**a**, **b**) Seismic section of time-migrated partial offset stacks. (**a**) Subline 29 for 3D box AXN: near- (**a-1**) and far-offset (**a-2**) *P*AMC*P* and far-offset (**a-3**) *P*AMC*S* stacks. (**b**) Subline 40 for 3D box AXM: near- (**b-1**) and far-offset (**b-2**) *P*AMC*P* and far-offset (**b-3**) *P*AMC*S* stacks. (**c**, **d**) Energy attribute of post-stack time-migrated volume for *P*- and *S*-wave partial-offset stacks. **(c)** 3D box AXM: near- (**c-1**) and far-offset (**c-2**) *P*AMC*P* and far-offset (**c-3**) *P*AMC*S* stacks. **(d)** 3D box AXN: near- (**d-1**) and far-offset (**d-2**) *P*AMC*P* and far-offset (**d-3**) *P*AMC*S* stacks. The gray shadings highlight the presence of strong *P*AMC*S* reflections with changes in *P*AMC*P* waves amplitude between near- and far-offset stacks. These sections were interpreted as melt-rich sections in this study. Red dashed lines indicate the locations of the two super-CMP gathers shown in Figure 3-4 and used for 1D waveform modeling.

3.5. WAVEFORM INVERSION

The *P*- and *S*-wave partial-offset stacks (Figure 3-6) described above provide an efficient way to qualitatively constrain the length scales of variations in AMC properties along a large portion of the ridge. However it does not provide constraints on the fine-scale physical properties of the AMC that produce the observed variations. To this end, we conducted 1D waveform inversion of MGL0812 MCS data selected from two locations with contrasting melt content where the AMC is best imaged: super-CMP gather 356098 located within a melt-rich section, and super-CMP gather 354229 located within a melt-poor section at the site of the 2005-06 eruption event and a cluster of hydrothermal vents (Figure 3-1b).

To improve the trace distribution with offset and avoid duplicating traces, we constructed super-CMP gathers by combining 12 consecutive CMP gathers (instead of 24 used for the partial-offset stacking) along a sub-line (e.g., sub-line 40 in the southern 3D box AXM). Each CMP has a maximum of 40 nominal fold after flexible bin extension (see section 3.3 and Figure 3-3), thus the theoretically maximum number of traces for each super-CMP gather is 480.

3.5.1. The τ–p Transform

The delay time-slowness (τ-p) mapping of seismic data is particularly useful for 1D seismic analysis since it decomposes the medium response into a series of non-interacting cylindrical waves [*Harding*, 1985]. The τ-p transform of time-offset (t-x) domain data

appropriate for a point source or 3D geometry may be considered as three successive transformations [*Harding*, 1985]:

(1) Fourier transform

$$\hat{u}(\omega,x)=\int_{-\infty}^{\infty}u(t,x)\exp(i\omega t)dt \tag{3-1}$$

where u is the displacement, and ω is the frequency.

(2) Hankel transform

$$\hat{u}(\omega,p)=\int_{0}^{\infty}xJ_0(\omega px)\hat{u}(\omega,x)dx \tag{3-2}$$

where J_0 is the zero-order Bessel function.

(3) Inverse Fourier transform

$$u(\tau,p)=\frac{1}{2\pi}\int_{-\infty}^{\infty}\hat{u}(\omega,p)\exp(-i\omega\tau)d\omega \tag{3-3}$$

Incompleteness of field data (finite time, offset, and bandwidth) results in transform artifacts, which must be removed for successful waveform inversion. We used the time-domain finite difference (TDFD) synthetic shot gather (same as CMP gather) based on the laterally homogeneous model esp05 [*Vera et al.*, 1990] (see Chapter 2 and Figure 2-15) to test the feasibility of the τ-p transform method and to guide us in choosing the appropriate parameters applied for the τ-p transform of the field data (Figure 3-7). By comparing the synthetic τ-p gather based on model esp05 (Figure 3-7a) with τ-p transformed gathers from the TDFD synthetic CMP gather (Figures 3-7b, c), the parameters were chosen to minimize transform artifacts (Figure 3-7d) while keeping the principle phases, e.g., seafloor reflection, AMC reflections $P_{AMC}P$ and $P_{AMC}S$. For the

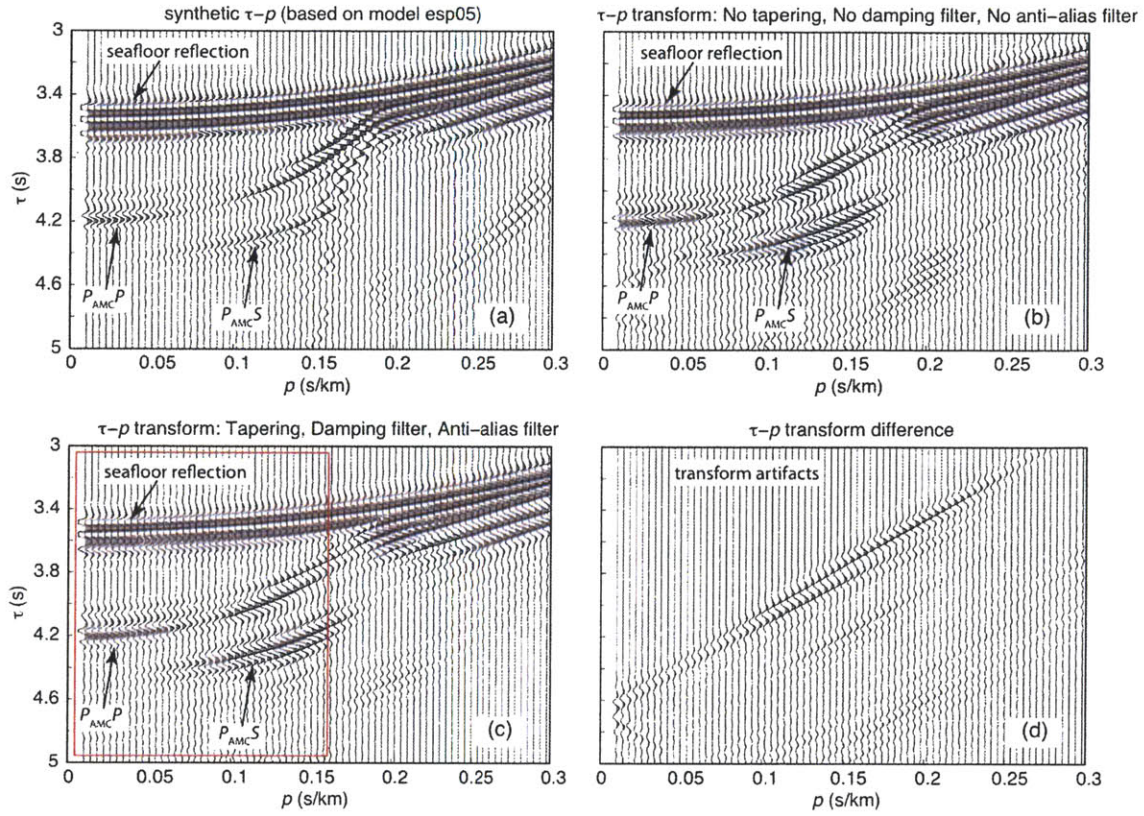

Figure 3-7. Tests of the feasibility of the delay time-slowness (τ-p) transform method. (**a**) Synthetic τ-p gather using velocity model esp05 [*Vera et al.*, 1990]. (**b**) τ-p transformed gather from the time-domain finite-difference synthetic CMP gather calculated for velocity model esp05. Tapering, damping and anti-alias filters have not been applied. (**c**) Same as (**b**) but with applying tapering, damping and anti-alias filters. The red box outlines the slowness range (0.01-0.158 s/km) of the τ-p transformed gather which used for 1D waveform inversion in this study. (**d**) The difference between τ-p transformed gathers (**b**) and (**c**), which represents the transform artifacts when using inappropriate parameters. The seafloor, $P_{AMC}P$ and $P_{AMC}S$ reflections are indicated by the black arrows.

traces with slowness higher than 0.16 s/km, which constrains the shallow velocity structure, the τ-p transformed gather with best-chosen parameters not only removes the transform artifacts but also significantly reduces the amplitude of the principle phases (Figures 3-7b, c). Thus we chose traces within a slowness window from 0.01 to 0.158 s/km (mainly constraining the AMC structure) for the 1D waveform inversion.

Similar to the τ-p transform tests with model esp05 (Figure 3-7), three major types of artifacts are identified in the τ-p transform gathers of the field data: (1) truncation effect due to limited data extent in the t-x domain, (2) aliasing due to sparse sampling (mainly with respect to offset), and (3) pseudo-truncation effect due to inconsistent air-gun signatures [*Harding*, 1985; *Korenaga et al.*, 1997]. The truncation effect can be alleviated by tapering in time and offset prior to the Fourier transform (Equation 3-1), thus we applied a cosine taper for traces from 4.0 to 5.8 km. The $+p$ aliasing effect was reduced by using a damping filter proposed by *Singh et al.* [1989], and the $-p$ aliasing effect was avoided by using the Hankel function instead of the Bessel function for large slownesses [*Harding*, 1985]. We used the Hankel function for all the slownesses.

Because the minimum offset for MCS recording in this study is ~200 m, the absence of information near zero offset significantly reduced the contributions to amplitude of the inner slowness traces, causing a diminution and slight signal distortion [*Harding*, 1985]. To avoid this effect, the super-CMP gathers were then interpolated to be evenly-distributed over 468 traces, with offset ranging from 0 to 5837.5 m with an interval of

12.5 m (Figures 3-8a, b). Figures 3-8c, d show the results of the τ-p transform of the two super-CMP gathers with the above treatments. Thirty-eight traces with slowness of 0.01-0.158 s/km and a frequency range of 5-30 Hz are shown (Figures 3-8c, d) and used for the following waveform inversions. Because of the relatively small slownesses used in this study, we did not correct for source and receiver directivity effects (which discriminates against waves with large slowness) [e.g., *Collier and Singh*, 1997].

3.5.2. Full Waveform Inversion

The full waveform inversion method is described in detail by *Kormendi and Dietrich* [1991], and more details on the inversion procedure can be found in *Collier and Singh* [1997], *Korenaga et al.* [1997], and *Minshull et al.* [1994]. We give only a brief outline here. The waveform inversion scheme was designed to find the 1D velocity structure that minimizes the misfit between the observed and predicted seismograms in frequency-slowness (ω–p) domain. The misfit function can be defined as

$$S(m) = \frac{1}{2}\left(\left\| d_{cal}(p,\omega) - d_{obs}(p,\omega) \right\|_D^2 + \left\| m - m_0 \right\|_M^2 \right) \tag{3-4}$$

where d_{cal} is the calculated wave field corresponding to the model m, d_{obs} is the observed wave field, and m_0 is the initial model. The norms $\| \|_D^2$ and $\| \|_M^2$ are weighted L_2 norms defined as

$$\|d\|_D^2 = d^{*T} C_D^{-1} d \tag{3-5}$$

and

$$||m||_M^2 = m^T C_M^{-1} m \tag{3-6}$$

where C_D is the data covariance matrix, C_M is the a priori model covariance matrix, the superscript T denotes the transpose of the matrix, and * denotes the complex conjugate. We tested several different combinations of C_D and C_M, ranging from $C_M = 2.0I$ to $C_M = 0.001I$ with fixing $C_D = I$, where I is the identity matrix, in order to find a C_M that yields stable model evolution. C_D and C_M were set as I and $0.025I$ respectively in the following inversions, and changing these values by a small factor would produce almost the same results. Synthetic seismograms were calculated using the generalized reflection transmission matrix method of *Kennett and Kerry* [1979], and the partial derivatives for the conjugate gradient algorithm were calculated from an analytical expression of *Kormendi and Dietrich* [1991].

3.5.3. Source Wavelet

The inversion results are highly sensitive to the input source wavelet. Since we do not have information on the far-field response of the air-gun signal for our experiment, the source wavelet used for the inversion was obtained following an indirect method (method 4 of *Collier and Singh* [1997]). We estimated the source wavelet by averaging 10 ω–p traces at the lowest slowness (i.e., from 0.01-0.046 s/km), and then transformed the resulting averaged spectrum back to the τ–p domain. The source wavelets used for the waveform inversions of super-CMP gathers 356098 and 354229 are shown in Figures 3-8e, f, respectively.

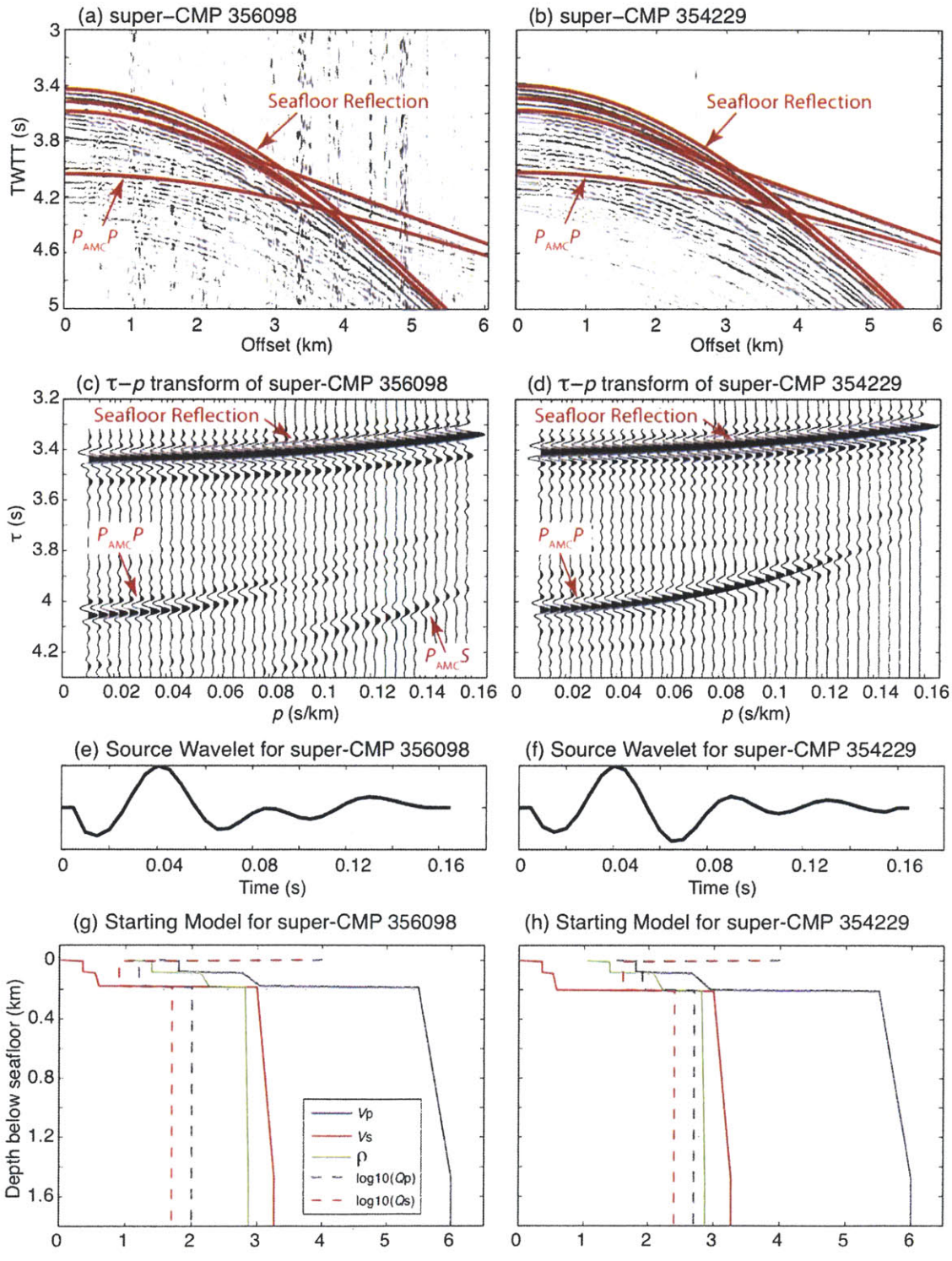
(a) super–CMP 356098
(b) super–CMP 354229
Seafloor Reflection
$P_{AMC}P$
TWTT (s)
Offset (km)
(c) τ–p transform of super-CMP 356098
(d) τ–p transform of super-CMP 354229
τ (s)
p (s/km)
$P_{AMC}S$
(e) Source Wavelet for super-CMP 356098
(f) Source Wavelet for super-CMP 354229
Time (s)
(g) Starting Model for super-CMP 356098
(h) Starting Model for super-CMP 354229
Depth below seafloor (km)
Vp
Vs
ρ
log10(Qp)
log10(Qs)

Figure 3-8. Trace-interpolated super-CMP gathers from (**a**) the melt-rich section (356098) and (**b**) the melt-poor section (354229). All gains were removed before the τ-p transform. The traveltime curves calculated from starting models (**g**, **h**) used for 1D waveform inversion are shown in red lines. (**c**, **d**) Corresponding τ-p transformed gathers, with seafloor, $P_{AMC}P$ and $P_{AMC}S$ reflections indicated by red arrows. Note that super-CMP gather 356098 shows a strong $P_{AMC}S$ reflection in the slowness range of 0.058-0.158 s/km, while super-CMP gather 354229 does not show a detectable $P_{AMC}S$ reflection. (**e**, **f**) The estimated source wavelets for super-CMP gathers 356098 and 354229, respectively. (**g**, **h**) Estimated starting models for the 1D waveform inversion. The starting Vp models were derived from fitting the main seismic phases shown in (**a**, **b**) (see text for details).

3.5.4. Starting Model

The starting model consists of a stack of 8-m-thick layers, for which the *P*- and *S*-waves velocities, density (ρ) and attenuation (Q) are defined. The thickness of 8 m was so chosen to be less than one-quarter of a wavelength for the dominant frequencies of 5-30 Hz, which is required for the precise computation of the synthetics [*Chapman and Orcutt*, 1985].

We used initial *Vp* models (Figures 3-8g, h) obtained from forward modeling of traveltimes of the seafloor reflection, the crustal reflection and refraction, and the AMC reflections for both super-CMP gathers (Figures 3-8a, b). ρ was defined from the initial *Vp* structures using a *Vp*-ρ relationship [*Carlson and Raskin*, 1984] (except at the seafloor and within the AMC where densities were fixed at 2240 kg/m^3 [*Gilbert and Johnson*, 1999] and 2600 kg/m^3, respectively). *Vs* structures were derived from the initial *Vp* structures assuming a Poisson's ratio structure as described below.

For the super-CMP gather 356098, Poisson's ratio was set to be 0.48 for the upper 180 m and 0.29 everywhere else [*Christeson et al.*, 1996; *Christeson et al.*, 1997; *Hyndman*, 1976] (Figure 3-8g). The Poisson's ratio of 0.29 was chosen to best fit the traveltime of the $P_{AMC}S$ reflection. The *P*-wave attenuation quality factor (Q_p) was set to 16 in the upper 180 m, and 100 below this depth [*Christeson et al.*, 1994b] (Figure 3-8g). The high level of attenuation in the uppermost crust results from the combined effect of

frictional, fluid flow, and scattering mechanisms [*Christeson et al.*, 1994b; *Toksöz et al.*, 1987; *Wilcock et al.*, 1995].

For the super-CMP gather 354229, Poisson's ratio was set to be 0.48 for the upper 200 m and 0.29 everywhere else [*Christeson et al.*, 1996; *Christeson et al.*, 1997; *Hyndman*, 1976] (Figure 3-8h). To obtain a reasonable result in fitting the relative amplitude of seafloor and AMC reflections, Q_p was set to 80 in the upper 200 m, and 500 below this depth [*Christeson et al.*, 1994a] (Figure 3-8h) which is five times greater than the values for super-CMP gather 356098. The relatively low attenuation might be caused by the cooling effect from the dense hydrothermal venting system located here since the attenuation quality factor is strongly dependent on temperature [*Kampfmann and Berckhemer*, 1985]. The *S*-wave attenuation quality factor (Q_s) was set to half that of the *P*-wave.

3.5.5. Inversion Scheme

The 38 τ–p traces were inverted simultaneously. The inverted result contains a model which is consistent with the data from all slownesses, and is therefore less likely to be influenced by incoherent noise due to 2D and 3D effects [*Singh et al.*, 1998]. In this study, the model parameter m in Equation 3-4 in the full waveform inversion is *Vp*; *Vs* and ρ were not inverted for during the inversion procedure. To obtain the best *Vs* structure, we conducted a series of inversions with different *Vs* values. The preferred *Vp*

solution and estimates of *Vs* within the AMC sill and of the sill thickness were obtained through a procedure involving three modeling parts (Figure 3-9) summarized here:

Part I: First we used a series of inversions to obtain *Vp*. After the iterative inversion converged, we updated *Vs* and ρ (as described in the previous section) and conducted another inversion for *Vp*. This procedure was repeated until updating *Vs* and ρ did not produce any additional convergence in a subsequent inversion. The final results from this step are what we call "best *Vp* models".

Part II: To constrain *Vs* within the AMC we conducted another set of inversions as described in Part I using as starting model the best *Vp* model of Part I and modifying the starting *Vs* within the AMC. The final results from this step are what we call "best combined *Vp* and *Vs* models".

Part III: In this last part we constrained the thickness of the low velocity AMC sill. We conducted a set of forward models starting with the best combined *Vp* and *Vs* models of Part II and modifying the AMC sill thickness.

To evaluate the goodness of the models obtained from the inversion scheme, we compared the slopes of linear fits to the root mean square (RMS) amplitude versus slowness (AVP) between the obtained models and the real seismic data. The comparison was done for both the $P_{AMC}P$ and $P_{AMC}S$ reflections The RMS amplitudes are calculated within a 50 ms window centered with $P_{AMC}P$ and $P_{AMC}S$ reflections.

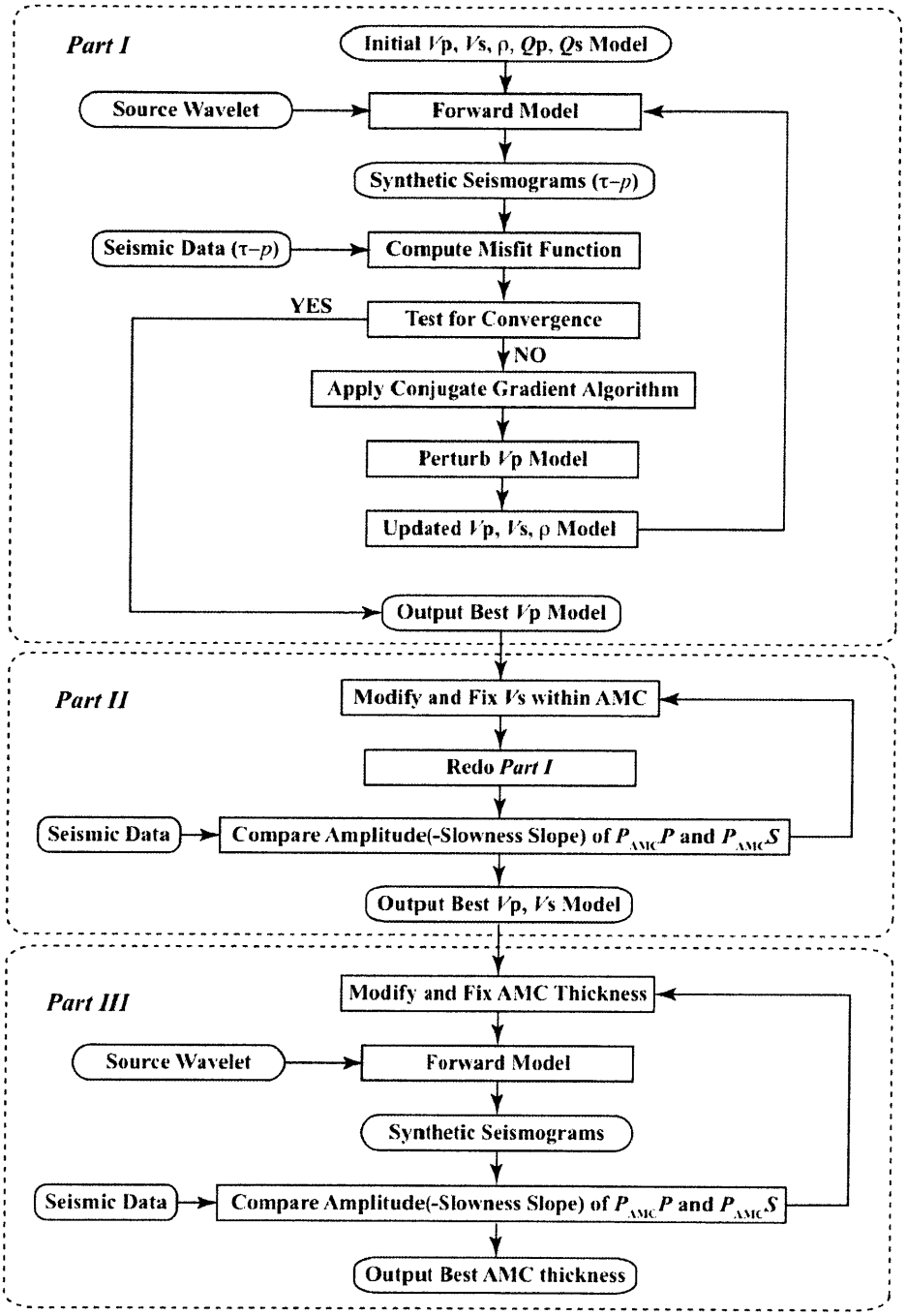

Figure 3-9. Schematic flow chart of the 1D waveform modeling procedure applied in this study. Three parts are included: part I is designed for obtaining best AMC *Vp* model, part II is for estimating best AMC *Vs*, and part III is for estimating best AMC thickness.

3.5.6. Waveform Inversion Results

3.5.6.1. Part I: Best *Vp* Models

The best *Vp* models obtained from Part I of the inversion scheme (Figure 3-9) for super-CMP gathers 356098 and 354229 are shown in Figures 3-10b and 3-11b, respectively. Observed and predicted seismograms are shown in Figures 3-10a and 3-11a. Our results show that at the melt-rich site of super-CMP gather 356098, the AMC is characterized by a tens of meters thick low velocity zone in which *Vp* decreases sharply from ~ 6.41 km/s to 3.35 km/s at 1.44 km depth.

At the melt-poor site of super-CMP gather 354229, the AMC is also tens of meters thick, but shows a smaller decrease in *Vp* (from ~6.44 to 4.67 km/s), and is located at a similar depth (1.41 km). The best *Vp* models have an uncertainty of 0.10-0.15 km/s (Figures 3-10b and 3-11b), which is valid only if the starting model is close to the global minimum of the misfit function.

Figures 3-10c, d show the comparisons of the RMS AVP slopes of $P_{AMC}P$ and $P_{AMC}S$ reflections between the best *Vp* models and real seismic data for super-CMP gathers 356098. The best *Vp* models fit the $P_{AMC}P$ reflection very well (Figure 3-10c), but are still not accurate enough for fitting the $P_{AMC}S$ reflection (Figure 3-10d). Figure 3-11c shows the comparison of the RMS AVP slopes of $P_{AMC}P$ reflections between the best *Vp* models and real seismic data for super-CMP gathers 354229. The best *Vp* models fit the $P_{AMC}P$ reflection very well (Figure 3-11c). Since no clear $P_{AMC}S$ reflection was

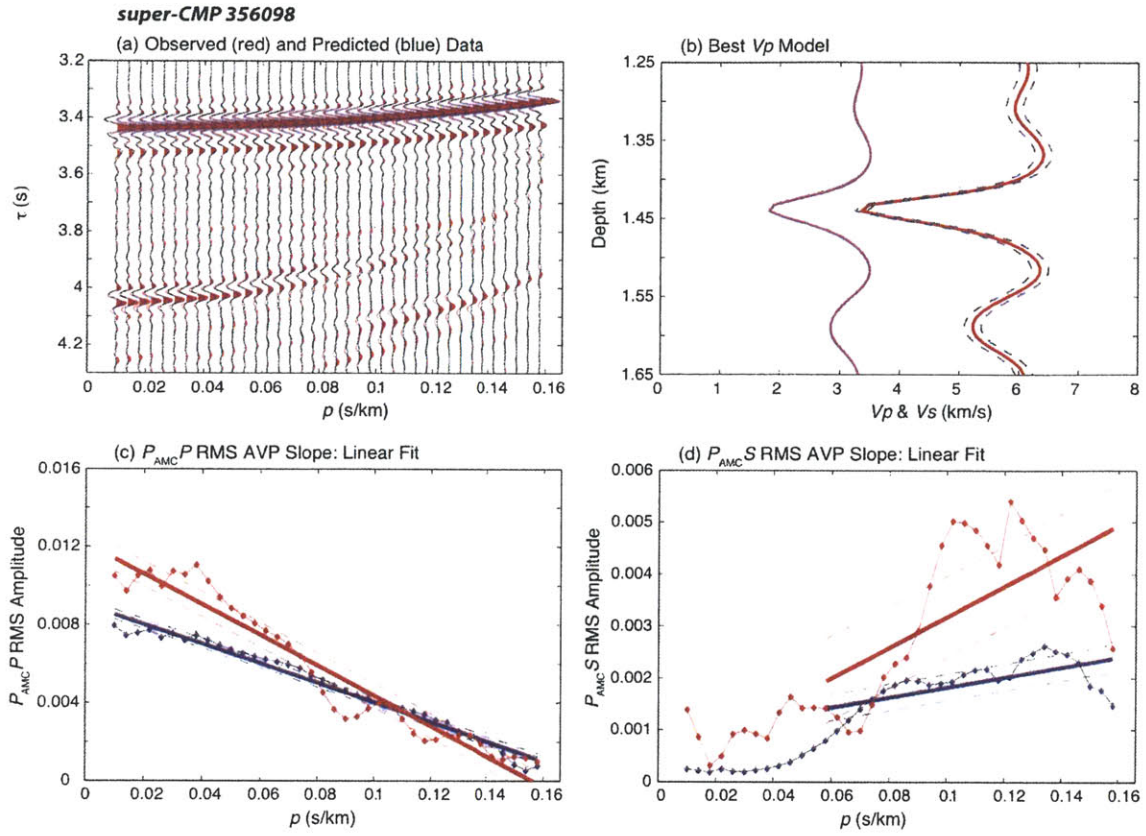

Figure 3-10. (**a**) Observed (red) and predicted (blue, from best *Vp* model) τ-p gathers for super-CMP gather 356098. (**b**) The best *Vp* model (red) obtained from inversion scheme part I, and the *Vs* model (purple) calculated from the *Vp* model with a constant Poisson's ratio 0.29. The blue dashed lines show the best *Vp* model ± one standard deviation error that was estimated from the Hessian matrix. (**c**) Comparison of linear regreesions of *P*AMC*P* root-mean-square (RMS) amplitude versus slowness (AVP) between observed (red) and predicted (blue) τ-p gathers. (**d**) Comparison of linear regreesions of *P*AMC*S* RMS AVP between observed (red) and predicted (blue) τ-p gathers. The slowness ranges for fitting slopes of *P*AMC*P* and *P*AMC*S* RMS AVP are 0.01-0.158 s/km and 0.058-0.158 s/km, respectively.

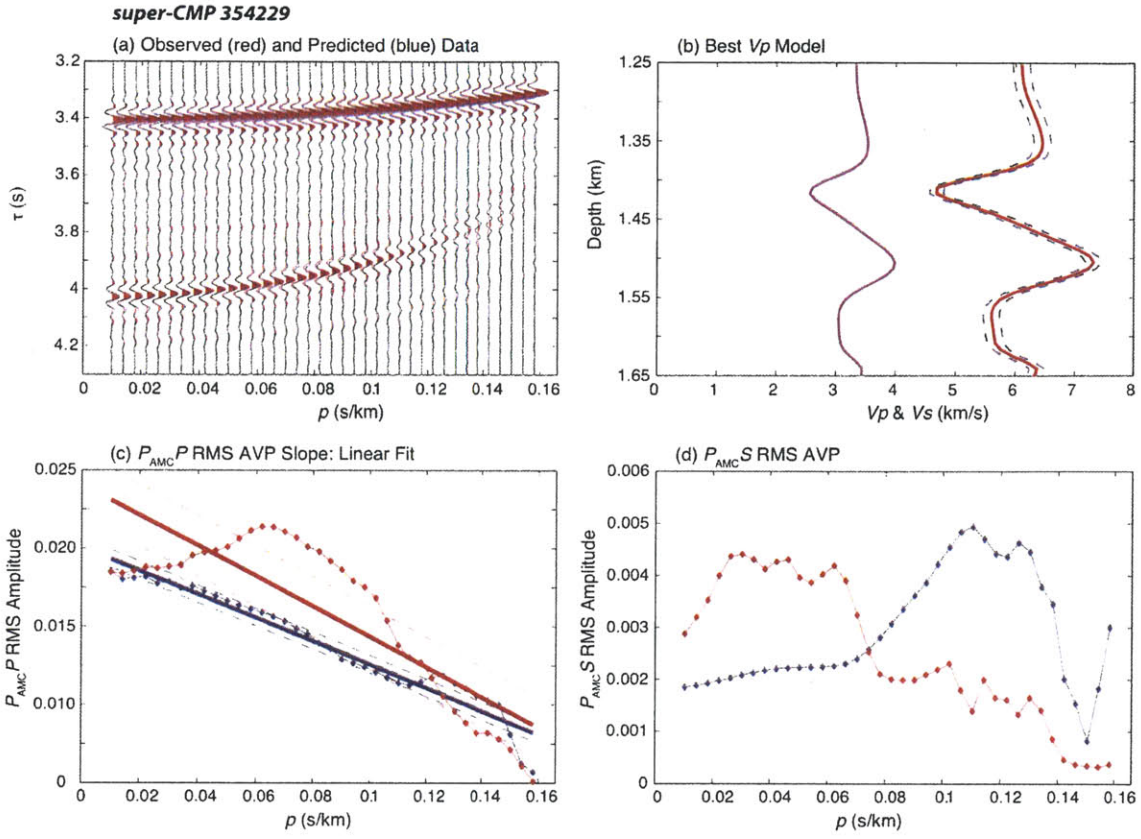

Figure 3-11. (**a**) Observed (red) and predicted (blue, from best *Vp* model) τ-p gathers for super-CMP gather 354229. (**b**) The best *Vp* model (red) obtained from inversion scheme part I, and the *Vs* model (purple) calculated from the *Vp* model with a constant Poisson's ratio 0.29. The blue dashed lines show the best *Vp* model ± one standard deviation error estimated from the Hessian matrix. (**c**) Comparison of linear regressions of *P*AMC*P* RMS AVP between observed (red) and predicted (blue) τ-p gathers. (**d**) Comparison of *P*AMC*S* RMS AVP between observed (red) and predicted (blue) τ-p gathers. The slowness range for fitting slopes of *P*AMC*P* RMS AVP is 0.01-0.158 s/km.

observed in super-CMP gathers 354229, we compared the total RMS amplitude within slowness range 0.058-0.158 s/km instead of AVP slopes of $P_{AMC}S$ reflections between the best *Vp* models and real seismic data (Figure 3-11d).

3.5.6.2. Part II: Best Combined *Vp* and *Vs* Models

Inversion scheme Part II (Figure 3-9) was executed in order to better constrain the *Vs* structure within the AMC sill. Inversions were carried out with various, fixed values of *Vs* within the AMC sill. For each case, RMS AVP slopes of the predicted $P_{AMC}P$ and $P_{AMC}S$ reflections were calculated and compared to those of the observed seismic data. To estimate the best *Vs* structure within the AMC, for super-CMP gather 356098, ten different *Vs* values, from 0 to 0.5 km/s with an interval of 0.1 km/s and from 0.75 to 1.5 km/s with an interval of 0.25 km/s, were tested, and for super-CMP gather 354229, eleven different *Vs* values, from 0 to 2.5 km/s with an interval of 0.5 km/s and from 2.6 to 3.0 km/s with an interval of 0.1 km/s, were tested.

Comparisons of the observed and modeled RMS AVP slopes are shown in Figures 3-12a, b and 3-12c for super-CMP gathers 356098 and 354229, respectively. Comparison of the observed and modeled $P_{AMC}S$ RMS amplitude is shown in Figure 3-12d for super-CMP gather 354229, respectively. For super-CMP gather 356098, in order to fit both $P_{AMC}P$ and $P_{AMC}S$ slopes at the same time, the final model needs to have a *Vs* within the AMC less than 0.5 km/s (Figures 3-12a, b), and the best combined *Vp* is 2.98 ± 0.08 km/s (one standard deviation error estimated from the Hessian matrix) and *Vs* is 0 km/s.

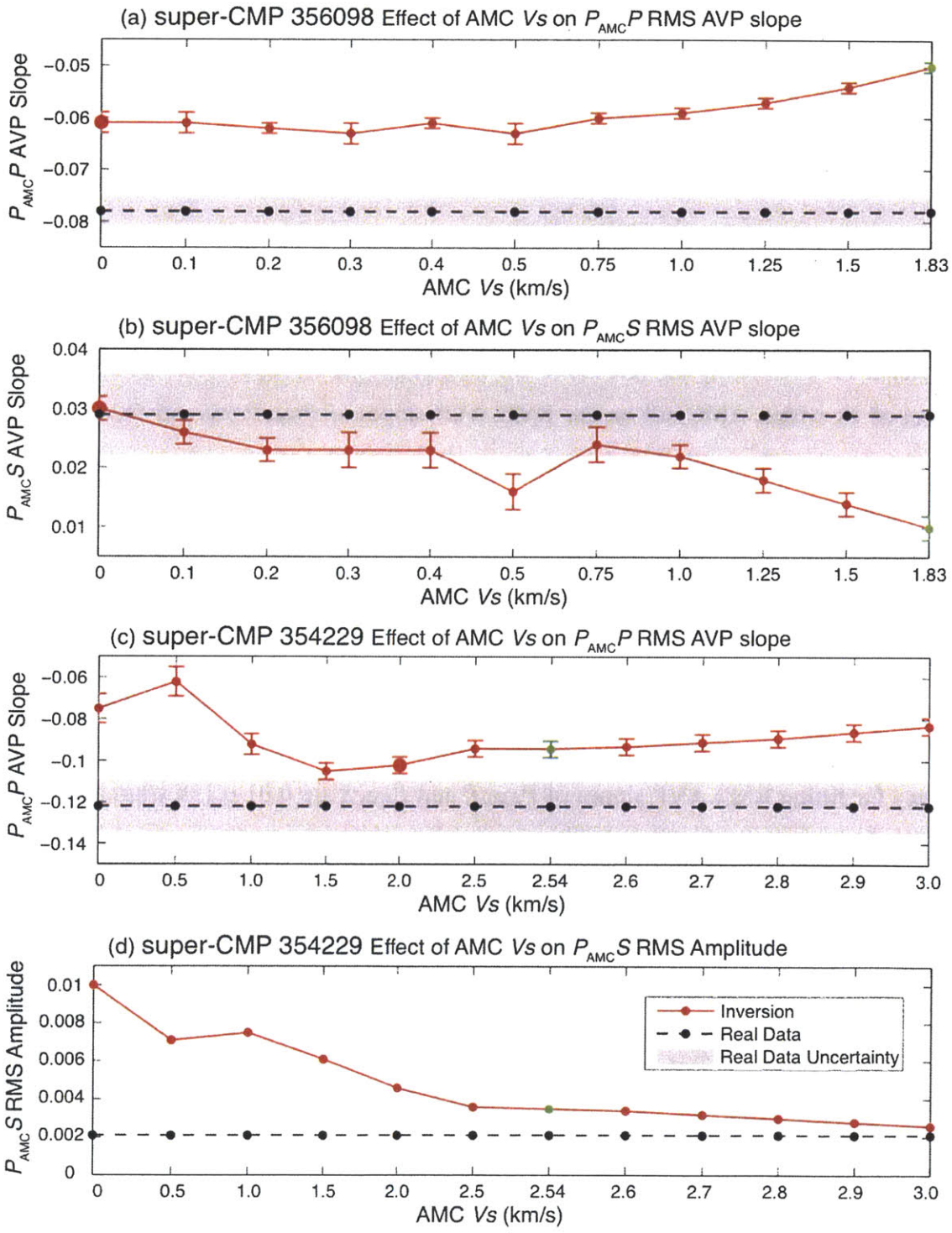
(a) super-CMP 356098 Effect of AMC Vs on $P_{AMC}P$ RMS AVP slope
$P_{AMC}P$ AVP Slope
−0.05
−0.06
−0.07
−0.08
0
0.1
0.2
0.3
0.4
0.5
0.75
1.0
1.25
1.5
1.83
AMC Vs (km/s)
(b) super-CMP 356098 Effect of AMC Vs on $P_{AMC}S$ RMS AVP slope
$P_{AMC}S$ AVP Slope
0.04
0.03
0.02
0.01
0
0.1
0.2
0.3
0.4
0.5
0.75
1.0
1.25
1.5
1.83
AMC Vs (km/s)
(c) super-CMP 354229 Effect of AMC Vs on $P_{AMC}P$ RMS AVP slope
$P_{AMC}P$ AVP Slope
−0.06
−0.08
−0.1
−0.12
−0.14
0
0.5
1.0
1.5
2.0
2.5
2.54
2.6
2.7
2.8
2.9
3.0
AMC Vs (km/s)
(d) super-CMP 354229 Effect of AMC Vs on $P_{AMC}S$ RMS Amplitude
$P_{AMC}S$ RMS Amplitude
0.01
0.008
0.006
0.004
0.002
0
Inversion
Real Data
Real Data Uncertainty
0
0.5
1.0
1.5
2.0
2.5
2.54
2.6
2.7
2.8
2.9
3.0
AMC Vs (km/s)

Figure 3-12. Estimating the best AMC sill *Vs* models. (**a**, **b**) Super-CMP gather 356098: effect of *Vs* within AMC sill on the RMS AVP slopes of $P_{AMC}P$ (**a**) and $P_{AMC}S$ (**b**) for predicted τ-p gathers (Red dots and line). The vertical red bars show one standard deviation error for linear fitting. The linear-fitted slope (black dots) and one standard deviation error (gray shaded) calculated for observed τ-p gathers are also shown for comparisons. (**c**) Same as (**a**) but for super-CMP gather 354229. (**d**) Effect of *Vs* within AMC sill on the RMS amplitude of $P_{AMC}S$ for predicted τ-p gathers (Red dots and line) for super-CMP gather 354229. The green dots are the *Vs* models calculated from the best *Vp* models (Figures 3-10 and 3-11) with a constant Poisson's ratio 0.29. The slowness ranges for fitting RMS AVP slopes of $P_{AMC}P$ and $P_{AMC}S$ are 0.01-0.158 s/km and 0.058-0.158 s/km, respectively. The slowness range for calculating RMS amplitude of $P_{AMC}S$ for super-CMP gather 354229 is 0.058-0.158 s/km.

However, for super-CMP gather 354229, the final model needs to have a *Vs* within the AMC 1.5-2.0 km/s (Figures 3-12c, d), and the best combined *Vp* is 4.47 ± 0.08 km/s and *Vs* is 2.0 km/s.

Figure 3-13 shows the inversion result by setting *Vs* = 0 km/s within the AMC based on the best *Vp* model (Figure 3-10b) for super-CMP gather 356098. The minimum *Vp* within the AMC in the final model (2.98 km/s, Figure 3-13b) is smaller than in the best *Vp* model (3.35 km/s, Figure 3-10b). This model greatly improves the RMS AVP slope fitting of $P_{AMC}S$ reflection (Figure 3-13d), and also a little bit for $P_{AMC}P$ reflection (Figure 3-13c). Compared to the best *Vp* model obtained from inversion scheme Part I (Figure 3-10b), this best combined *Vp* and *Vs* model (Figure 3-13b) explains better the AVP of both the $P_{AMC}P$ and $P_{AMC}S$ phases. We chose *Vp* = 2.98 km/s, and *Vs* = 0 km/s as our preferred model for super-CMP gather 356098, and *Vp* = 4.47 km/s, and *Vs* = 2.0 km/s as our preferred model for super-CMP gather 354229 because the model with *Vs* = 1.5 km/s is still generating clear $P_{AMC}S$ reflection.

3.5.6.3. Part III: Estimate of AMC Thickness

In order to estimate the AMC sill thickness, inversion scheme Part III (Figure 3-9) was executed based on the preferred best combined *Vp* and *Vs* models. We refer to AMC sill thickness as the thickness of the minimum velocity layer in this chapter. The final results of inversion scheme Part III are shown in Figures 3-14a, b and 3-14c, d for super-CMP gathers 356098 and 354229, respectively. For super-CMP gather 356098, based on

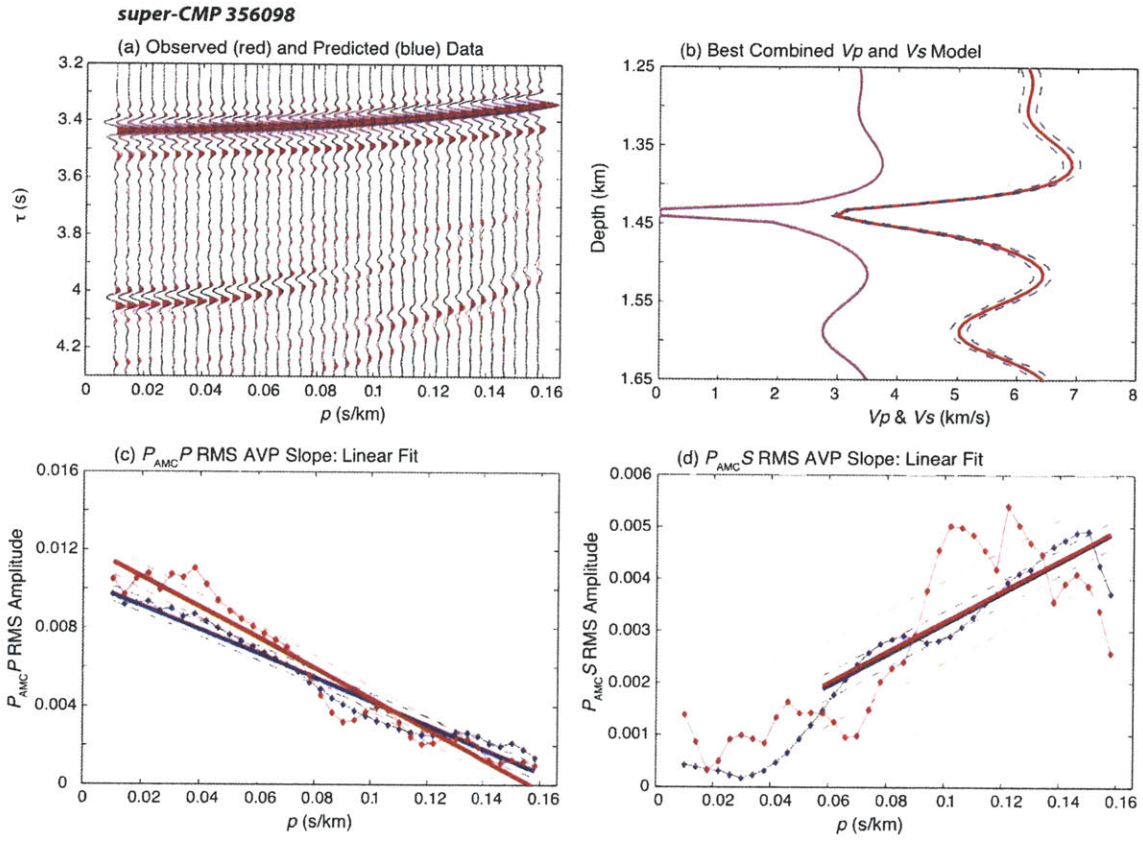

Figure 3-13. (**a**) Observed (red) and predicted (blue, from best combined *Vp* and *Vs* model) τ-p gathers for super-CMP gather 356098. (**b**) The best combined *Vp* (red) and *Vs* (purple) model obtained from inversion scheme part II. The blue dashed lines show the *Vp* model ± one standard deviation error estimated from the Hessian matrix. (**c**) Comparison of linear regreesions of *P*AMC*P* RMS AVP between observed (red) and predicted (blue) τ-p gathers. (**d**) Comparison of linear regreesions of *P*AMC*S* RMS AVP between observed (red) and predicted (blue) τ-p gathers. The slowness ranges for fitting RMS AVP slopes of *P*AMC*P* and *P*AMC*S* are 0.01-0.158 s/km and 0.058-0.158 s/km, respectively.

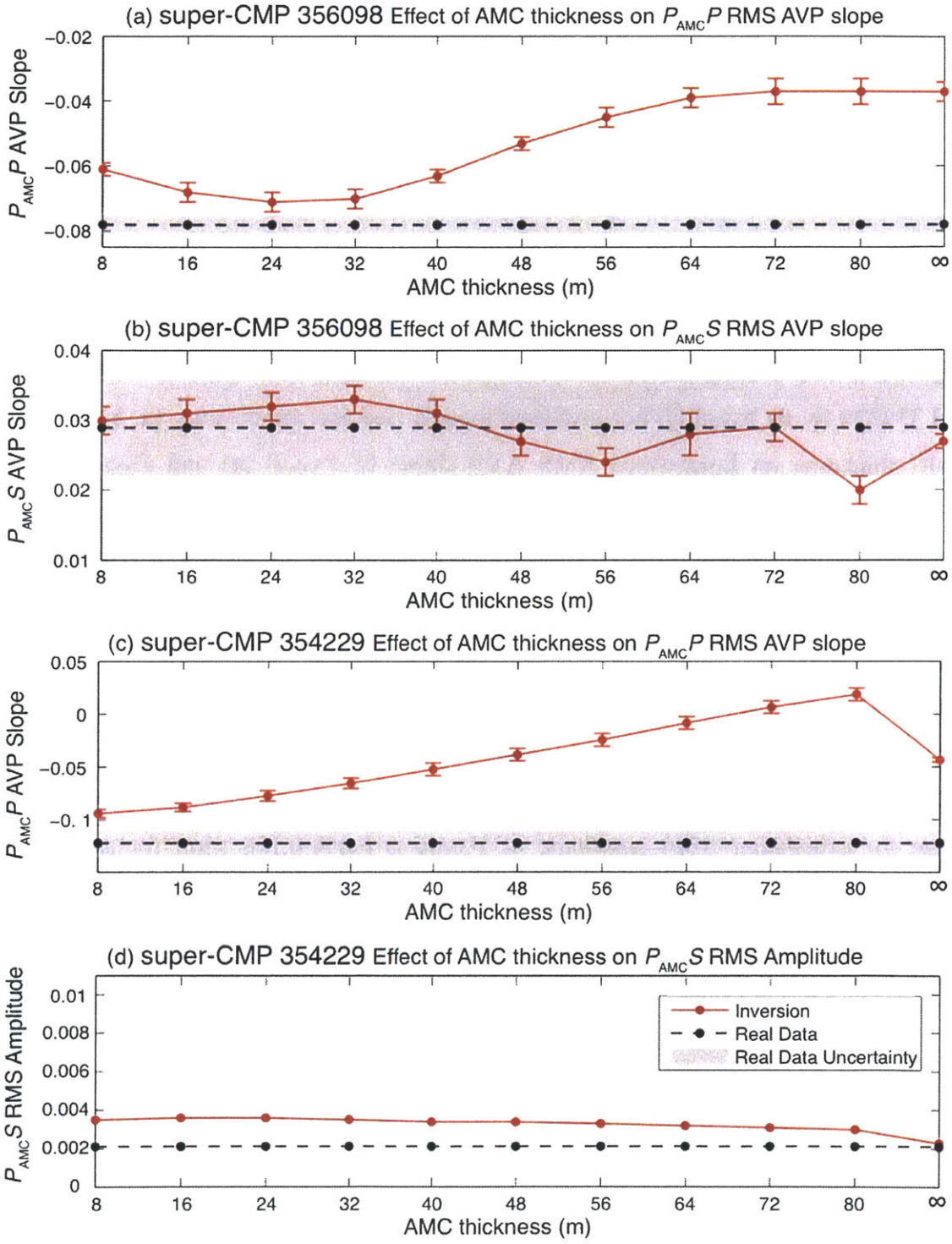
(a) super-CMP 356098 Effect of AMC thickness on $P_{AMC}P$ RMS AVP slope
$P_{AMC}P$ AVP Slope
−0.02
−0.04
−0.06
−0.08
8
16
24
32
40
48
56
64
72
80
∞
AMC thickness (m)
(b) super-CMP 356098 Effect of AMC thickness on $P_{AMC}S$ RMS AVP slope
$P_{AMC}S$ AVP Slope
0.04
0.03
0.02
0.01
AMC thickness (m)
(c) super-CMP 354229 Effect of AMC thickness on $P_{AMC}P$ RMS AVP slope
$P_{AMC}P$ AVP Slope
0.05
0
−0.05
−0. 1
AMC thickness (m)
(d) super-CMP 354229 Effect of AMC thickness on $P_{AMC}S$ RMS Amplitude
$P_{AMC}S$ RMS Amplitude
0.01
0.008
0.006
0.004
0.002
0
Inversion
Real Data
Real Data Uncertainty
AMC thickness (m)

Figure 3-14. Estimating the best AMC thickness for super-CMP gathers 356098 (**a**, **b**) and 354229 (**c**, **d**) based on our preferred models (see text for details). (**a**, **b**) Effect of AMC thickness on linear-fitted RMS AVP slopes of $P_{AMC}P$ (**a**) and $P_{AMC}S$ (**b**) for predicted τ-p gathers (red dots and line). The vertical red bars show one standard deviation error for linear fitting. The linear-fitted RMS AVP slopes (black dots) and one standard deviation error (gray shaded) calculated for observed τ-p gathers are also shown for comparisons. (**c**) Same as (**a**) but for super-CMP gather 354229. (**d**) Effect of AMC thickness on the RMS amplitude of $P_{AMC}S$ for predicted τ-p gathers (Red dots and line) for super-CMP gather 354229. The slowness ranges for fitting RMS AVP slopes of $P_{AMC}P$ and $P_{AMC}S$ are 0.01-0.158 s/km and 0.058-0.158 s/km, respectively. The slowness range for calculating RMS amplitude of $P_{AMC}S$ is 0.058-0.158 s/km for super-CMP gather 354229.

the RMS AVP slope fitting of $P_{AMC}P$ and $P_{AMC}S$ reflections (Figures 3-14a, b), the preferred AMC thickness is ~16-40 m. For super-CMP gather 354229, the RMS AVP slope fitting for the $P_{AMC}P$ reflections gets worse with increasing AMC thickness (Figure 3-14c), and the AMC thickness does not effect the fitting of the RMS amplitdue for the $P_{AMC}P$ reflections (Figure 3-14d). The AMC thickness <40 m is preferred.

3.5.6.4. Robustness of the Best *Vp* Solutions

For a quantitative comparison of the results, it is important to inspect the reliability of each result. Furthermore, some of the features of the preferred models may be dependent on the initial assumptions and not fully required by the data [e.g., *Canales et al.*, 2006]. One important aspect is the thickness of the melt lens and the structure immediately beneath it. In particular, our preferred models for the two sites show very different velocity structures immediately beneath the melt lens (Figure 3-15a), so we investigated how the complex structures correspond to the observed data. Similar investigations at the southern EPR have shown that the melt lens is bounded by a solid roof and a solid floor [*Singh et al.*, 1999], and they are also indicated by the relatively high *Vp* immediately above and below the melt lens in our preferred *Vp* models (Figure 3-15a).

We performed two series of inversions with different constraints to investigate the necessity of having a solid floor. We inverted the data from super-CMP gather 356098 (melt-rich case) using initial velocity models modified from the best *Vp* model (Figure 3-

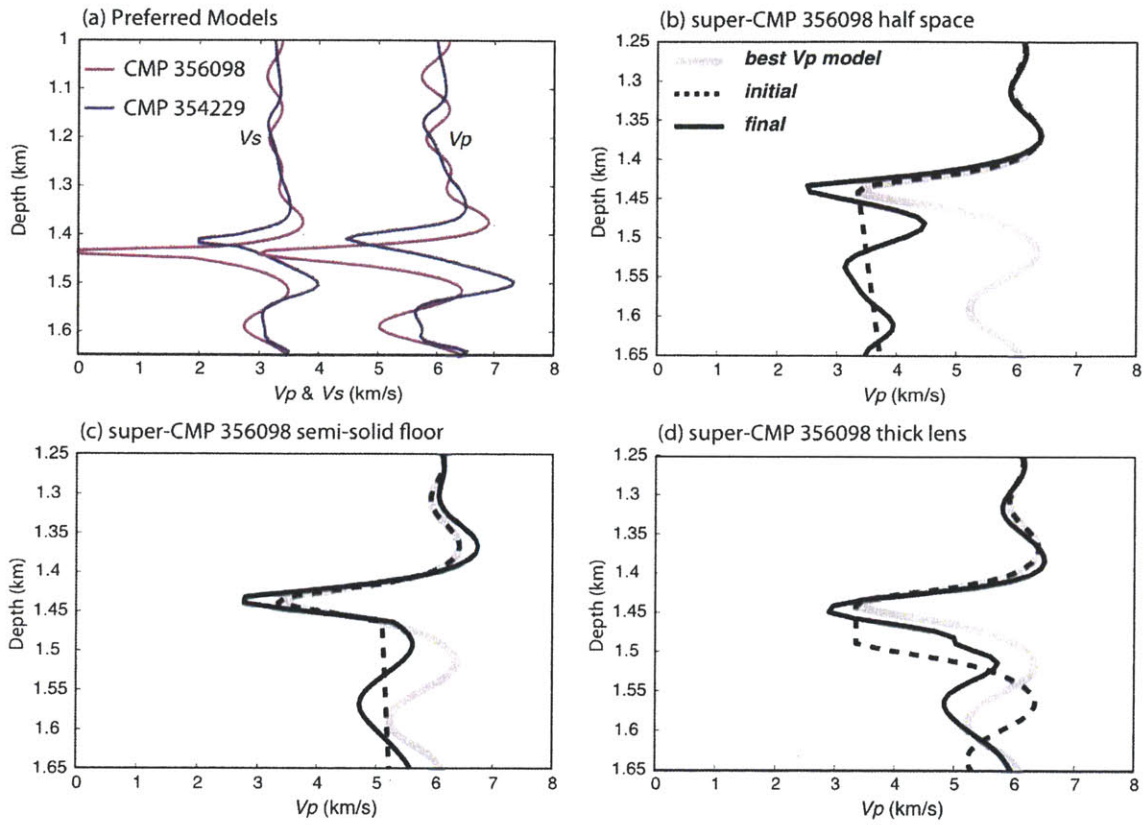

Figure 3-15. (**a**) Preferred 1D *Vp* and *Vs* models for super-CMP gathers 356098 and 354229. (**b-d**) Tests for the robustness of the best *Vp* solution for the structure of the melt lens for super-CMP gather 356098: (**b**) a purely molten half space model modified from the best *Vp* model (Figure 3-10b, thick gray line) is used as an initial model (dashed line), black line show the final inversion result; (**c**) same as (**b**) with an initial model assuming a partially molten floor; (**d**) same as (**b**) assuming a thick (~100 m) melt lens as starting model.

10b): one where *Vp* is low everywhere beneath the top of the AMC (Figure 3-15b), and a second one in which the velocity of the melt lens floor increases moderately, simulating a semi-solid floor (Figure 3-15c). In both cases, the new inversions result in models that fit the data with the same degree of accuracy as the best *Vp* solution. These two tests show that our data cannot discriminate between a solid and a semi-solid floor, but that the data require an increase in *Vp* with respect to the initial velocity model immediately beneath the melt lens. Thus, our tests indicate that the top of the AMC is a partially molten thin lens overlaying a more crystalline medium.

We performed another test where we imposed a thicker (~100 m) AMC, and then inverted the data (Figure 3-15d). The solution from this test shows that the data require a thin lens no more than 50 m thick, which is consistent with our estimations of the AMC thickness (16-40 m, see section 3.5.6.3).

3.6. DISCUSSION

3.6.1. Nature of the AMC along EPR 9°30'-10°00'N Segment

3.6.1.1. Melt Content of the AMC Sill

The best combined *Vp* and *Vs* structures of the AMC obtained from the 1D waveform inversion (Figure 3-15a) provide constraints on the crystallinity of the melt lens. To estimate the melt content in the AMC, we used a statistical approach derived from effective medium theory, Hashin-Shtrikman bounds [*Hashin and Shtrikman*, 1963], to compute the upper and lower velocity bounds for a constant melt fraction (Figure 3-

16). The maximum bounds correspond to an end-member model of unconnected melt inclusions in a solid host, and the minimum bounds represent the opposite end-member model: unconnected crystals in a molten host. There are six model parameters used for calculating the Hashin-Shtrikman bounds: *Vp*, *Vs*, and ρ for both crystals and pure melt. We tested different combinations of these parameters, the melt fraction for the melt-rich site is almost the same and there are some uncertainties (<10%) of the melt fraction for the melt-poor site. In this study, we chose *Vp* = 6.2 km/s, *Vs* = 3.0 km/s, and ρ = 2800 kg/m^3 for the crysals, and *Vp* = 2.9 km/s, *Vs* = 0 km/s, and ρ = 2700 kg/m^3 for the pure melt. Calculations using various methods show a wide range of predicted melt fractions for a given seismic velocity [*Mainprice*, 1997].

At the melt-rich site (super-CMP gather 356098), the low *Vp* (2.98 km/s) and *Vs* (≤0.5 km/s) indicate that the AMC has a very high percentage of melt (95-100%). The very high percentage of melt (95-100%) in the melt-rich site suggests that the crystals, if there are any, in the AMC sill are disconnected and surrounded by a fully molten host.

In contrast, at the melt-poor site (super-CMP gather 354229), the larger *Vp* (4.47 km/s) suggest ~15-46% of melt content, while *Vs* (1.5-2.0 km/s) is consistent with a magma body with moderate melt content (41-62%). Therefore, in the melt-poor site, the best value of melt fraction converted from both *Vp* and *Vs* is ~41-46%, and corresponds to the maximum bound, which suggests that here the melt inclusions are disconnected in a solid host. This finding that here the AMC is mostly a solid body agrees with the lack

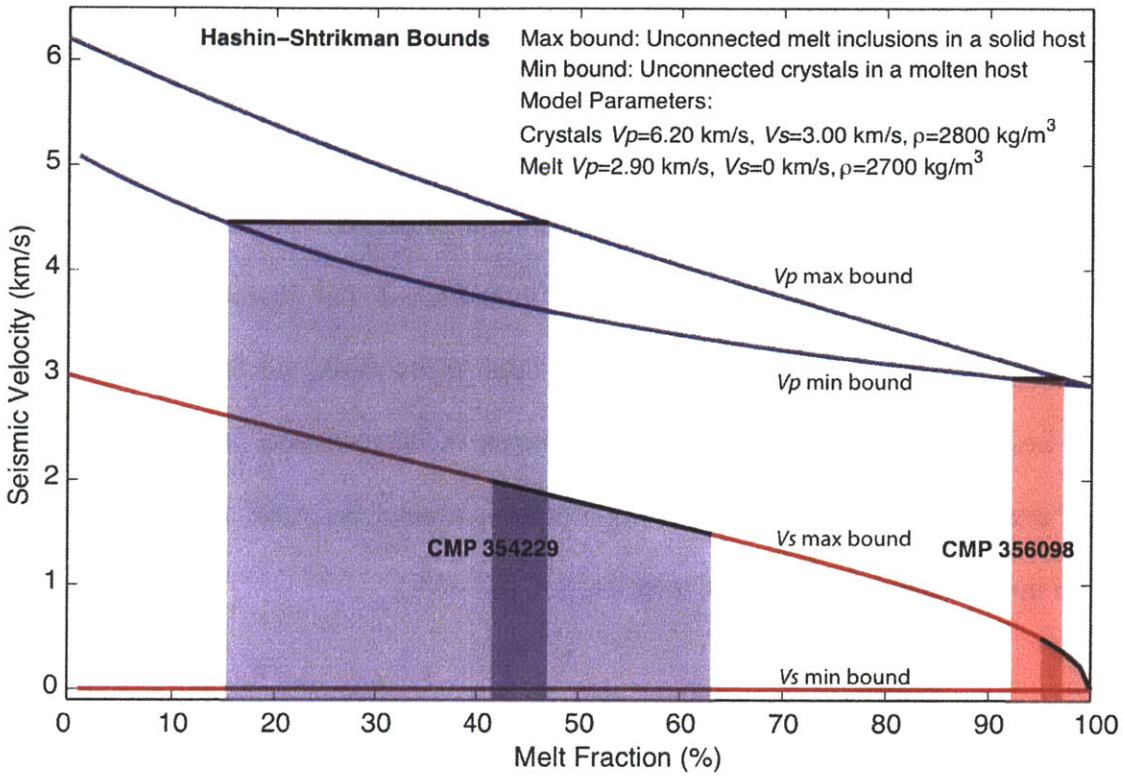

Figure 3-16. Hashin-Shtrikman bounds on seismic velocities for a two-phase material (melt and crystals in this study). The *Vp* and *Vs* bounds are shown in blue and red lines, respectively. The transparent red and blue blocks indicate the inferred melt fraction ranges based on our preferred *Vp* and *Vs* models for super-CMP gathers 356098 and 354229. The overlapping area between the *Vp*- and *Vs*-inferred melt fractions gives us the final melt fraction value. Model parameters used from calculating the Hashin-Shtrikman bounds are listed in the figure.

of converted *S*-waves in the MCS data at this location, indicating efficient propagation of shear energy through the AMC sill.

These two estimates of melt content within the AMC sill (Figure 3-16), together with the results from *P*- and *S*-wave partial-offset stacks (Figure 3-6), provide a more complete picture about the along-axis spatial variation of the internal properties of the AMC sill. At the melt-rich sections, where both $P_{AMC}P$ and $P_{AMC}S$ events are well imaged and laterally continuous, the melt fraction in the AMC sill is likely as high as 100%, i.e., pure melt in the AMC sill. In contrast, at the melt-poor sections, where the $P_{AMC}P$ event is well imaged but the $P_{AMC}S$ event is absent, the AMC sill is mostly solid with an intermediate percentage of melt fraction (41-46%).

3.6.1.2. Melt Layer Thickness

Without a *priori* assumptions we have shown that the AMC sill at the northern EPR is ~16-40 m thick both in melt-rich and melt-poor sections (Figure 3-14). Here we compare our seismically determined melt layer thickness with estimates from other seismic studies and field observations.

The melt layer thickness has been seismically investigated through waveform modeling and analysis of AVO or AVP behaviors of AMC reflections [e.g., *Canales et al.*, 2006; *Collier and Singh*, 1997; *Hussenoeder et al.*, 1996; *Kent et al.*, 1990; *Singh et al.*, 1999; *Singh et al.*, 1998]. Along the northern EPR, *Kent et al.* [1990] derived a lower

bound on the thickness of the magma body by reflectivity modeling of the interference effects between a wavelet reflecting off the top and bottom of a thin layer of melt as its thickness decreases. A layer thickness of ~10-50 m is required to explain the lack of a distinct basal reflection in the observed data. However, the absence of this basal reflection can also be explained by a gradual increase in velocities across a transitional lower boundary of a thicker magma body due to a transition from melt to crystal mush (see sections 2.3.2.1.2 and 2.3.2.1.3 in Chapter 2). Through waveform modeling of AMC reflections, *Hussenoeder et al.* [1996] and *Collier and Singh* [1997, 1998] also showed the thickness of the sill to be of the order of 30-80 m beneath the EPR near 10°N. Similar results were obtained at the southern EPR [*Hussenoeder et al.*, 1996; *Singh et al.*, 1999; *Singh et al.*, 1998], southern JdFR [*Canales et al.*, 2006], Valu Fa ridge in the Lau Basin [*Collier and Sinha*, 1990], and the East Scotia Ridge in the South Atlantic [*Livermore et al.*, 1997]. Our determined AMC sill thickness (16-40 m) is consistent with the thicknesses mentioned above (<100 m).

The study of ophiolites has played an important role in the development of models for MOR magma chambers [e.g., *Casey and Karson*, 1981; *Greenbaum*, 1972; *MacLeod and Yaouancq*, 2000; *Nicolas et al.*, 1993; *Nicolas et al.*, 1988; *Pallister and Hopson*, 1981]. Arguably the best analogue for fast spreading crust is the Oman ophiolite. *Browning* [1984] and *Browning et al.* [1989] showed that the observed cryptic (mineral, chemical) variation of the cumulate layers within the cyclic layered gabbro sequences of the Troodos and Oman ophiolites is best modeled by formation from melts with

thicknesses that are no more than about 100-200 m thick. From structural and petrological mapping of the upper gabbro and dyke contact in the Oman ophiolite, *MacLeod and Yaouancq* [2000] proposed the presence of a 150-m-thick fossil melt lens. These estimates are in approximately agreement with our seismic determination of AMC sill thickness.

3.6.1.3. Roof and Floor of the AMC

Previous studies based on modeling of refraction data suggested the presence of low velocities immediately above and below the melt sill [*Toomey et al.*, 1990; *Vera et al.*, 1990]. The low velocity just above the AMC has been interpreted to be due to a thermal anomaly, and the low velocity below the AMC is thought to represent a mush zone underlying the melt sill [*Toomey et al.*, 1990; *Vera et al.*, 1990]. *Vera et al.* [1990] also showed an 80-m-thick layer with a high *Vp* (6.2 km/s) at 250 m above the AMC. Through waveform inversion of long-offset reflection data, *Singh et al.* [1999] determined that at the southern EPR the AMC is overlain by a 50-60-m-thick, high-velocity (6.0-6.2 km/s) roof layer and is underlain by at least a 150-200-m-thick high-velocity floor. They also found that the roof is overlain by a 150-200-m-thick low-velocity zone that may correspond to a fracture zone that hosts the hydrothermal circulation and the roof itself may be the transition zone separating the magma chamber from circulating fluids. The presence of the solid floor indicates that at least the upper gabbros of the oceanic lower crust are formed by cooling and crystallization of melt in magma chamber [*Singh et al.*, 1999].

Our modeling results also show that the thin AMC sill (16-40 m, Figure 3-14) is embedded within a high-*Vp* roof and floor (Figure 3-15a). Based on the Hashin-Shtrikman bounds [*Hashin and Shtrikman*, 1963] shown in Figure 3-16, the high *Vp* immediately above and below the AMC sill suggest a mostly solid roof and floor. However the robustness tests (see section 3.5.6.4) show that our data cannot discriminate between a solid and a semi-solid floor. The AMC structures (Figure 3-15a) obtained at the melt-rich (super-CMP gather 356098) and melt-poor sections (super-CMP gather 354229) are different from each other. This difference, best described by their unique vertical velocity structures, may be related to distinct volcanic and hydrothermal stages. For super-CMP gather 356098 (at 9°42.8'N), we have determined a simple, three-layer sill structure where the AMC roof and floor have similar velocities (Figure 3-15a). For super-CMP gather 354229 (at 9°49.1'N), we have determined a ~100-m-thick positive velocity gradient layer where the velocity of AMC floor is ~1 km/s higher than the roof, and a ~150-m-thick low velocity layer above the AMC (Figure 3-15a) which may correspond to a fracture zone that hosts the hydrothermal circulation [*Singh et al.*, 1999].

3.6.2. Relations between the Physical State of AMC Sill Pre- and Post- 2005-06 Eruption and Hydrothermal Activity

Based on the along-axis variations in melt content inferred from the partial-offset stacks within the 2005-06 eruption site, we propose and discuss two possible scenarios regarding the relationship between the physical state of the AMC melt lens before and

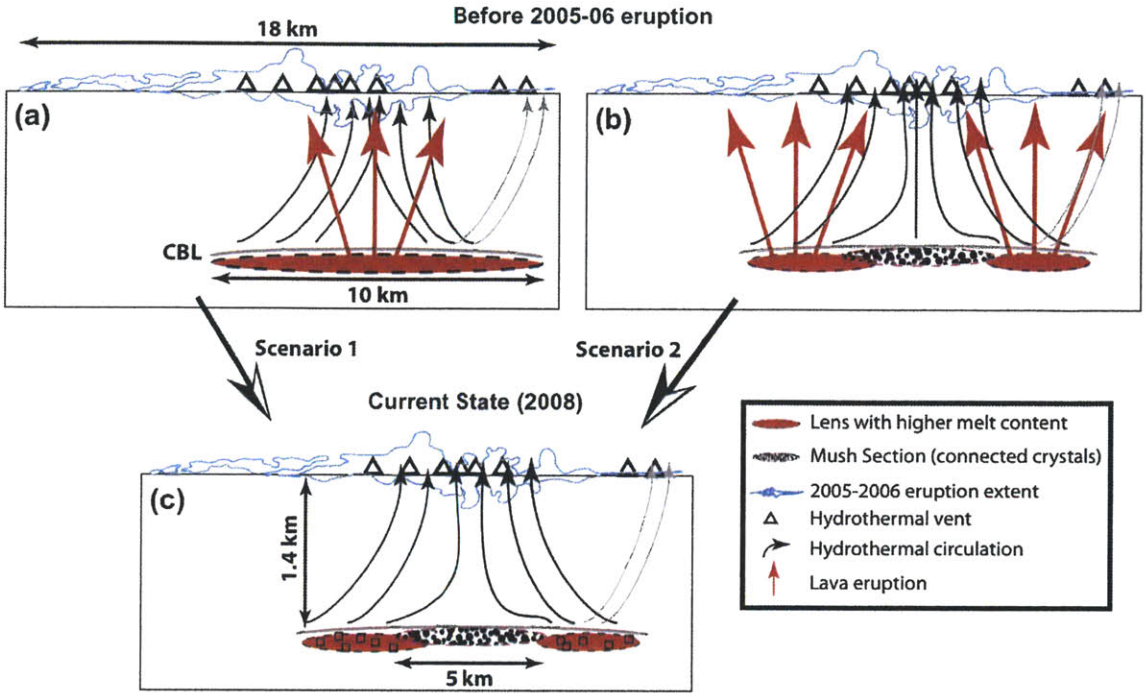

Figure 3-17. A cartoon showing two possible scenarios regarding the relationships between the physical state of AMC sill before and after 2005-06 eruption and hydrothermal activity. (**a→c**) Scenario 1: the 2005-06 eruption drained most of the melt in a 5-km-long central part from an initial 10-km-long melt-rich section which had been driving hydrothermal circulation in this area, leaving behind a large fraction of connected crystals separating the distal ends of the lens from which melt was not fully drained. (**b→c**) Scenario 2: prior to the 2005-06 eruption, intense hydrothermal activity cools the section of the AMC immediately beneath the dense hydrothermal vents filed and prevents the formation of a melt-rich lens, and thus the eruption was fed from the melt accumulated south and/or north of the hydrothermal vent fields where the hydrothermal cooling was less effective. The gray line above the AMC sill represents a conductive boundary layer (CBL) which separates the hydrothermal circulation and the AMC sill.

after the 2005-06 eruption, and hydrothermal activity (Figure 3-17): (1) In the first scenario, we assume that the source of the 2005-06 eruption was a 10-km-long melt-rich lens extending between 9°46.5'-9°52'N. This lens has been driving vigorous hydrothermal circulation in this area over the past decade. The eruption drained most of the melt in the 5-km-long central part of this lens, leaving behind a large fraction of connected crystals separating the distal ends of the lens from which melt was not fully drained (Figures 3-17a, c). (2) In the second scenario, we hypothesize that the physical state of the AMC was not much different from what the post-eruption partial-offset stacks indicate (Figure 3-6). Thus, the 5-km-long melt-poor section at the center of the eruption site could be interpreted, pre- and post-eruption, as the result of intense hydrothermal activity that cooled the section of the AMC immediately beneath the dense hydrothermal vents, preventing the formation of a melt-rich lens. The eruption was therefore fed by melt accumulated south (melt-rich section 2, Figure 3-18) and north (melt-rich section 3, Figure 3-18) of the hydrothermal field where hydrothermal cooling was less effective. The second scenario is less preferred than the first scenario, because the 2005-06 seafloor eruption center is unlikely located above a melt-poor section of the AMC before the eruption ocurred.

The first scenario assumes that the lava that erupted on the seafloor during the 2005-06 eruption comes from a 5-km-long melt-rich (now melt-poor) section centered at ~9°49.5'N. We can put constrains on the volume of magma involved in the eruption. The width of the AMC near 9°50'N is 500-700 m [*Harding et al.*, 1993] and the thickness is

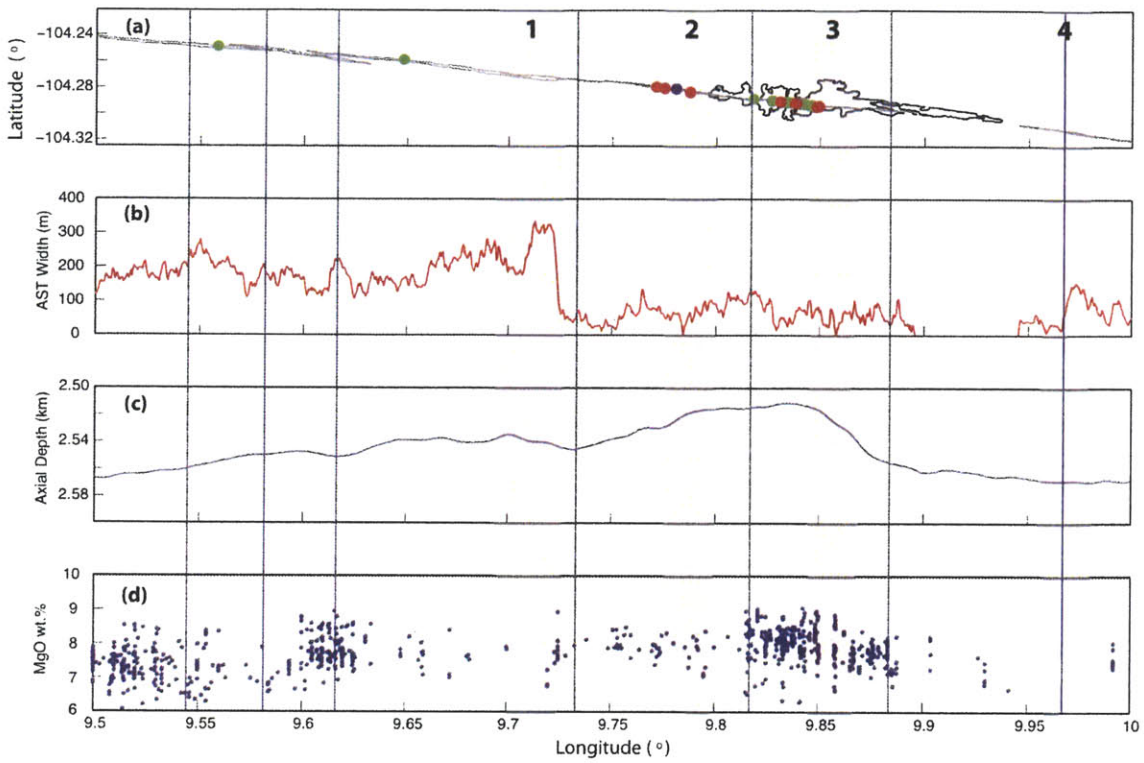

Figure 3-18. Small-scale melt-mush segmentation at northern EPR 9°30'-10°00'N. The red shadings with sequence numbers highlight the four identified melt-rich sections. The blue vertical lines indicate the fourth-order segment locations [*White et al.*, 2006]. (**a**) The black line marks the extent of the 2005-06 eruption derived from camera tow data [*Soule et al.*, 2007], the gray lines outline the axial summit trough (AST), and hydrothermal vents are indicated by dots, with red dots for active vents, blue dots for inactive vents and green dots for vents with unknown activities. (**b**) AST width. (**c**) Axial depth along ridge axis. (**d**) MgO wt.%, data are from petrological database of the ocean floor (http://www.petdb.org/). No obvious correlations between the melt-mush segmentation and hydrothermal vent locations, AST width, the axial depth and MgO wt.%. can be found.

~16-40 m (this study). Based on the mean values of AMC dimensions here (600 m × 28 m) for a 5-km-long segment of the ridge, and assuming the melt fractions calculated for melt-rich (~100%) and melt-poor (~45%) sections in the magma lens represent the melt content prior to and after the eruption respectively, we calculated a volume of melt erupted of ~46 × 10^6 m^3. Based on the analysis of digital seafloor imagery collected on camera tows and *Alvin* dives, *Soule et al.* [2007] estimated the 2005-06 eruption produced ~22 × 10^6 m^3 of lava on the seafloor. Therefore there was still a volume of melt ~24 × 10^6 m^3 left in the upper crust as dikes. If we presume the melt was contained within a 1.4-km-high and 5-km-long dike section, the width of the dike is 3.4 m, which is much wider than the mean dike width (0.5-1.5 m) obtained from data analysis of ophiolites and tectonic windows into recently active spreading ridges [*Gudmundsson*, 1995; *Harper*, 1984; *Kidd*, 1977; *Oliver and McAlpine*, 1998; *Rosencrantz*, 1983; *Tryggvason*, 1994; *Umino et al.*, 2003]. However, *Soule et al.* [2007] suggested that the dike fed the eruption over the whole 18-km-long section covered by the erupted lava flows on the seafloor, and using this length the calculated width of the dike is more reasonable 0.95 m. The 0.95-m-wide dike indicates that every eruption results in 0.95-m of spreading along this segment, thus the full spreading rate 110 mm yr^{-1} results in an interval of ~8.6 years between consecutive eruptions in this area. This estimate is roughly half the time interval between the 1991-92 and 2005-06 eruptions and slightly less than previous estimates of the eruption recurrence interval at fast spreading ridges [e.g., *Perfit and Chadwick*, 1998].

The second scenario suggests the 2005-06 eruption was fed from the accumulated southern and northern melt-rich sections. If this was correct, then the melt contents of the two melt-rich sections (total length ~5 km) would be decreased by ~55%. However, the melt contents of the two sections are currently ~100%, thus the newly supplied melt from mantle should had been delivered in less than 2 years. Further investigation is needed to ascertain whether this scenario is plausible.

3.6.3. Spatial Variations of Melt Content within AMC Sill

Combining the results of qualitatively imaging melt-rich and melt-poor sections from *P*- and *S*-wave partial-offset stacks and the melt content estimates from the seismic velocities obtained from 1D waveform inversion, we find that over the 60-km-long EPR segment (~9°30'-10°00'N), there are four prominent 2-4-km-long melt-rich to fully-molten sections contained within an otherwise melt-poor AMC (Figures 3-1b and 3-18). The melt-rich sections are spaced every ~5-10 km along the ridge axis, which is about half of the spacing found for the southern EPR (~15-20 km, [*Singh et al.*, 1998]).

3.6.3.1 Implications for Crustal Accretion

The melt-rich sections may correspond to zones of fresh magma, supplied from the mantle, that are more capable of erupting. The mushy sections may have undergone more efficient or longer periods of cooling and crystallization [*Singh et al.*, 1998]. These lateral variations in AMC physical properties may inhibit large-scale mixing or flow of magma along the ridge axis. The small-scale melt-mush segmentation provides insight into the

melt delivery, eruption history, hydrothermal activity, and crustal accretion along the spreading axis.

Based on the melt content conversions from the seismic velocities (Hashin-Shtrikman bounds, Figure 3-16), we suggest that 95-100% melt could be present in the melt-rich sections and 41-46% melt in the melt-poor sections. Studies of lava lakes suggest that a basalt melt with a cystallinity higher than 25% develops a yield strength and is unlikely to be erupted [*Marsh*, 1989]. Over this 60-km-long section (9°30'-10°00'N), the presence of melt-poor sections occupies >75% of the length. This means that at a given time, only ~25% of the ridge axis is capable of producing diking and seafloor eruptions, with the remaining ~75% of the AMC temporarily playing a passive role in the crustal accretion and primarily contributing to the accretion of the lower crust.

The melt-rich sections associated with replenishment of the AMC by magma from a deeper reservoir (e.g., mantle) seem to shift along this segment on decadal time scales. A seismic waveform inversion study of the AMC beneath the northern EPR by *Collier and Singh* [1998] showed melt contents as high as ~90% within the AMC sill at 9°39'N and 9°48'N that were identified as melt-poor sections (~41-46% melt) in this study. These spatial variations, and probably the temporal variations of melt-rich and melt-poor sections, may explain the temporal variations observed from petrological studies [*Langmuir et al.*, 1986]. More important, this along-axis change of locations of the melt-

rich sections which are responsible for upper crustal accretion can explain the continuity of seismic layer 2a along the axis.

3.6.3.2 Implications for Volcanic-hydrothermal-tectonic Cycle

The melt-rich sections are located within fourth-order segments except the northern one (melt-rich section 4 in Figure 3-18) where overlapping axial pillow ridges are observed [*White et al.*, 2002]. *Haymon et al.* [1991] proposed that the individual morphotectonically defined fourth-order segments at EPR between 9°09'N and 9°54'N are in different stages of a repetitive volcanic-hydrothermal-tectonic cycle. A typical cycle on fast-spreading ridge crests begins with an episode of dike injection and volcanic eruption from discontinuous eruptive fissures along the length of a segment. This volcanic activity is accompanied, or immediately followed by hydrothermal activity, along with magma drainage and consequent gravitational collapse leading to formation of an AST. The cycle continues with waxing of hydrothermal activity and onset of amagmatic tectonic cracking, and concludes with waning of hydrothermal activity, continued crustal cracking, and widening of the AST by mass wasting along its margins. At a fast-spreading center the full cycle may occur in 10^2-10^3 years [*Haymon et al.*, 1991]. However, at EPR near 9°50'N area, the ~10-year interval between two consecutive eruptions (e.g., 13-year interval between the 1991-92 and 2005-06 eruptions) is much shorter than the cycle period, and this area lacks a late tectonic phase.

None of the melt-rich sections are located immediately beneath the most abundant hydrothermal vents field. Thirty-nine out of forty-one vents, including all the active vents, observed between 9°30'N and 10°00'N, are located near the melt-rich sections 2 and 3 and the melt-poor section inbetween (Figure 3-18a). As discussed above, before the 2005-06 eruption, the melt-rich sections 2 and 3 may have been connected and formed a large melt-rich section that provided heat to the hydrothermal system.

The different structures of the AMC may be also related to the distinct stages of the volcanic-hydrothermal cycle. Beneath the melt-poor section that is in between the melt-rich sections 2 and 3 (Figure 3-18), the detection of a 150-200-m-thick low-velocity zone above the AMC roof suggests that it may correspond to a fracture zone that hosts the hydrothermal circulation and the high-*Vp* roof itself may be the transition zone separating the magma chamber from circulating fluids. The ~100-m-thick positive velocity gradient layer below the AMC sill could be formed by cooling and crystallization of melt within the AMC, as suggested by *Worster et al.* [1990], who showed that the crystallization occurs predominantly in the interior or at the floor of the AMC owing to convection, even if the heat is predominantly lost from the roof. This feature could be modified by a new batch of melt from the mantle, reverting into a simple three-layer sill structure as shown in the melt-rich sections. Obvious correlations between the melt-mush segmentation and the AST width, the axial depth and MgO wt.%. cannot be found (Figures 3-18b, c, d), which suggests that the time scale of morphological (e.g., axial depth and AST width)

and geochemical (e.g., MgO wt.%.) features is much longer than that of melt-mush segmentation stability.

3.7. CONCLUSIONS

We have used the *P*- and *S*-wave partial-offset stacking method to qualitatively image melt-rich and melt-poor sections along the northern EPR 9°30'-10°00'N, and we have used 1D waveform modeling to quantitatively determine the detailed physical properties of the AMC at two locations with contrasting melt content. On the basis of the interpretations of the nature of the AMC, correlations between melt-mush segmentation, hydrothermal activity and 2005-06 lava eruption, and spatial variations of melt content within AMC sill, we make the following conclusions.

1. Between 9°30'-10°00'N, the melt content of the AMC sill varies along the EPR axis. We found four prominent melt-rich sections ~2-4 km long and spaced every ~5-10 km along the ridge axis.

2. The AMC sill is located ~1.4 km beneath the seafloor. The AMC reflections observed in the melt-rich sections are best modeled with a low *Vp* (2.98 km/s) and *Vs* (≤ 0.5 km/s) structure in the AMC sill, while in the melt-poor sections, they are best modeled with a higher *Vp* (4.67 km/s) and *Vs* (1.5-2.0 km/s) in the AMC sill. The thickness of the AMC sill is ~16-40 m in both settings.

3. The melt-mush segmentation, together with the melt content estimates obtained based on the Hashin-Shtrikman bounds, indicate that the crystallinity of the AMC varies along the ridge-axis. Within the melt-rich sections, the melt fraction in the AMC sill can

be as high as 95-100%, i.e., pure melt. In contrast, within the melt-poor sections the AMC sill has an intermediate percentage of melt fraction (41-46%).

4. Over this 60-km-long section (9°30'-10°00'N), the presence of melt-poor sections occupies >75% of the length. This means that at a given time, only ~25% of the ridge axis is capable of producing diking and seafloor eruptions, with the remaining ~75% of the AMC temporarily playing a passive role in the crustal accretion and primarily contributing to the accretion of the lower crust.

5. None of the melt-rich sections are located immediately beneath the most abundant hydrothermal vent field, but most of the hydrothermal vents (39 out of 41) are located near and between two melt-rich sections.

6. Two scenarios regarding the relationships between the 2005-06 eruption, the physical state of the AMC melt lens before and after this event, and hydrothermal activity are proposed: (1) The source of the 2005-06 eruption was a 10-km-long melt-rich lens. The eruption drained most of the melt in the 5-km-long central part, leaving behind a large fraction of connected crystals separating the distal ends of the lens from which melt was not fully drained. (2) Alternatively, prior to the 2005-06 eruption intense hydrothermal activity cooled the section of the AMC immediately beneath the dense hydrothermal vent field and prevented the formation of a melt-rich lens. The eruption was therefore fed from the accumulated melt in the melt-rich sections immediately to the north and south of the hydrothermal field where the hydrothermal cooling was less effective. The first scenario is more preferred.

7. If the first scenario is correct, the volume of the 2005-06 eruption from the 5-km-long section has been estimated using the mean values of AMC dimensions (600 m × 28 m) and the 55% melt fraction decrease within the AMC. Our calculation suggests a volume of magma extracted from the AMC of ~46 × 10^6 m^3, with ~24 × 10^6 m^3 left unerupted in the upper crust as dikes. The width of the dike is 3.4 m if the dike feeding the eruption extended over the 5-km-long central section, or 0.95 m if the dike fed the eruption over the 18-km-long section where the seafloor eruption has been documented.

8. No obvious correlations were found between the melt-mush segmentation, AST width, axial depth and MgO wt.%. This suggests that the time scale of morphological (AST width and axial depth) and geochemical (MgO wt.%) features (~10^2-10^3 years) is much longer than that of melt-mush segmentation stability (decades).

Acknowledgements

We are grateful to the captain, crew, technical staff, and scientific party of the R/V *Marcus Langseth* Cruise MGL0812 for their valuable assistance in collecting the MCS data used in this study. The R2K program was essential in coordinating this cruise. We thank S.A. Soule for providing digital information about the AST and 2005-06 eruption. We also thank R. Stephen, D. Lizarralde and S.A. Soule for insightful discussions. This research was supported by NSF grants OCE-0327885.

References

Anderson, D. L., and H. Spetzler (1970), Partial melting and the low-velocity zone, *Phys. Earth. Planet. Int.*, *4*(1), 62-64, doi:10.1016/0031-9201(70)90030-0.

Browning, P. (1984), Cryptic variation within the cumulate sequence of the Oman ophiolite: Magma chamber depth and petrological implications in Ophiolites and Oceanic Lithosphere, I.G. Gass, S.J. Lippard and A.W. Shelton, eds., *Geol. Soc. London Spec. Publ.*, *13*, 71-82.

Browning, P., S. Roberts, and T. Alabaster (1989), Fine-scale modal layering and cyclic units in ultramafic cumumlates from the CY-4 borehole, Troodos ophiolite: evidence for an open system magma chamber, I.L. Gibson, J. Malpas, P.T. Robinson, C. Xenophontos, Editors , Drillhole CY-4, the Troodos Ophiolite, Cyprus (Cyprus Crustal Study Project: Initial Report, Hole CY-4), *Geol. Surv. Can*, 193–220.

Canales, J. P., R. S. Detrick, D. R. Toomey, and S. D. Wilcock (2003), Segment-scale variations in crustal structure of 150- to 300-k.y.-old fast spreading oceanic crust (East Pacific Rise, 8°15'N-10°15'N from wide-angle seismic refraction profiles, *Geophys. J. Int.*, *152*, 766-794.

Canales, J. P., S. C. Singh, R. S. Detrick, S. M. Carbotte, A. J. Harding, G. M. Kent, J. B. Diebold, J. Babcock, and M. R. Nedimovic (2006), Seismic evidence for variations in axial magma chamber properties along the southern Juan de Fuca Ridge, *Earth and Planet. Sci. Lett.*, *246*, 353-366.

Carbotte, S. M., and K. C. Macdonald (1992), East Pacific Rise 8°-10°30'N: Evolution of ridge segment and discontinuities from SeaMARC II and three-dimensional magnetic studies, *J. Geophys. Res.*, *97*, 6959-6982.

Caress, D. W., M. S. Burnett, and J. A. Orcutt (1992), Tomographic image of the axial-low velocity zone at 12°50'N on the East Pacific Rise, *J. Geophys. Res.*, *97*, 9243-9264.

Carlson, R. L., and G. S. Raskin (1984), Density of the ocean crust, *Nature*, *311*, 555-558.

Casey, J. F., and J. A. Karson (1981), Magma chamber profiles from the Bay of Islands ophiolite complex, *Nature*, *292*, 295-301.

Chapman, C. H., and J. A. Orcutt (1985), The computation of body wave synthetic seismograms in laterally homogeneous media, Rev. Geophys., 23(2), 105–163, doi:10.1029/RG023i002p00105.

Christeson, G. L., G. M. Purdy, and G. J. Fryer (1994a), Seismic constraints on shallow crustal emplacement processes at the fast spreading East Pacific Rise, *J. Geophys. Res.*, *99*, 17,957-17,973.

Christeson, G. L., W. S. D. Wilcock, and G. M. Purdy (1994b), The shallow attenuation structure of the fast-spreading East Pacific Rise near 9°30'N, *Geophys. Res. Lett.*, *21*(5), 321-324.

Christeson, G. L., G. M. Kent, G. M. Purdy, and R. S. Detrick (1996), Extrusive thickness variability at the East Pacific Rise, 9°-10°N: Constraints from seismic techniques, *J. Geophys. Res.*, *101*, 2859-2873.

Christeson, G. L., P. R. Shaw, and J. D. Garmany (1997), Shear and compressional wave structure of the East Pacific Rise, 9°-10°N, *J. Geophys. Res.*, *102*, 7821-7835.

Collier, J. S., and M. C. Sinha (1990), Seismic images of a magma chamber beneath the Lau Basin back-arc spreading center, *Nature*, *346*, 646-648.

Collier, J. S., and S. C. Singh (1997), Detailed structure of the top of the melt body beneath the East Pacific Rise at 9°40'N from waveform inversion of seismic reflection data, *J. Geophys. Res.*, *102*(B9), 20287-20304.

Collier, J. S., and S. C. Singh (1998), A seismic inversion study of the axial magma chamber reflector beneath the East Pacific Rise near 10°N, in *Modern Ocean Floor Processes and the Geological Record*, edited by R. A. Mills and K. Harrison, pp. 17-28, Geological Society, London.

Detrick, R. S., P. Buhl, E. E. Vera, J. C. Mutter, J. A. Orcutt, J. A. Madsen, and T. M. Brocher (1987), Multi-channel seismic imaging of a crustal magma chamber along the East Pacific Rise, *Nature*, *326*, 35-41.

Detrick, R. S. (1991), Ridge crest magma chambers: a review of results from marine seismic experiments at the East Pacific Rise, in *Ophiolite genesis and evolution of*

the oceanic lithosphere, edited by T. J. Peters, A. Nicolas and R. G. Coleman, pp. 7-20, Kluwer Academic Publishers, Dordrecht.

Detrick, R. S., A. J. Harding, G. M. Kent, J. A. Orcutt, J. C. Mutter, and P. Buhl (1993), Seismic structure of the Southern East Pacific Rise, *Science*, *259*, 499-503.

Dunn, R. A., and D. R. Toomey (1997), Seismological evidence for the three-dimensional melt migration beneath the East Pacific Rise, *Nature*, *388*, 259-262.

Dunn, R. A., D. R. Toomey, and S. C. Solomon (2000), Three-dimensional seismic structure and physical properties of the crust and shallow mantle beneath the East Pacific Rise at 9° 30'N, *J. Geophys. Res.*, *105*, 23,537-23,555.

Escartín, J., S. A. Soule, D. J. Fornari, M. A. Tivey, H. Schouten, and M. R. Perfit (2007), Interplay between faults and lava flows in construction of the upper oceanic crust: The East Pacific Rise crest 9°25'-9°58'N, *Geochem. Geophys. Geosyst.*, *8*(6), Q06005, doi:10.1029/2006GC001399.

Fornari, D. J., R. M. Haymon, M. R. Perfit, T. K. P. Gregg, and M. H. Edwards (1998a), Axial summit trough of the East Pacific Rice 9°–10°N: Geological characteristics and evolution of the axial zone on fast spreading mid-ocean ridge, *J. Geophys. Res.*, *103*(B5), 9827-9855.

Fornari, D. J., et al. (1998b), Time-series temperature measurements at high-temperature hydrothermal vents, East Pacific Rise 9°49'-51'N: evidence for monitoring a crustal cracking event, *Earth and Planet. Sci. Lett.*, *160*, 419-431.

Fornari, D. J., et al. (2004), Submarine lava flow emplacement at the East Pacific Rise 9°50'N: Implications for uppermost ocean crust stratigraphy and hydrothermal fluid circulation, in *The Thermal Structure of the Ocean Crust and the Dynamics of Hydrothermal Circulation*, edited, pp. 187-217, AGU, Washington, D. C.

Gilbert, L. A., and H. P. Johnson (1999), Direct measurement of oceanic crustal density at the northern Juan de Fuca Ridge, *Geophys. Res. Lett.*, *26*(24), 3633-3636.

Greenbaum, D. (1972), Magmatic Processes at Ocean Ridges: Evidence from the Troodos Massif, Cyprus, *Nature Physical Science*, *238*, 18-21.

Gudmundsson, A. (1995), The geometry and growth of dykes, in *Physics and Chemistry of Dykes*, edited by A. H. G. Baer, pp. 23-34, A A BALKEMA, ROTTERDAM.

Harding, A. J. (1985), Slowness-time mapping of near offset seismic reflection data, *Geophys. J. R. Astron. Soc.*, *80*, 463-492.

Harding, A. J., J. A. Orcutt, M. E. Kappus, E. E. Vera, J. C. Mutter, P. Buhl, R. S. Detrick, and T. M. Brocher (1989), The structure of young oceanic crust at 13°N on the East Pacific Rise from expanding spread profiles, *J. Geophys. Res.*, *94*, 12,163-12,196.

Harding, A. J., G. M. Kent, and J. A. Orcutt (1993), A multichannel seismic investigation of upper crustal structure at 9°N on the East Pacific Rise: Implications for crustal accretion, *J. Geophys. Res.*, *98*, 13,925-13,944.

Harper, G. D. (1984), The Josephine ophiolite, northwestern California, *Geol. Soc. Am. Bull.*, *95*, 1009-1026.

Hashin, Z., and S. Shtrikman (1963), A variational approach to the theory of the elastic behaviour of multiphase materials, *Journal of the Mechanics and Physics of Solids*, *11*(2), 127-140, doi:10.1016/0022-5096(63)90060-7.

Haymon, R. M., D. J. Fornari, M. H. Edwards, S. M. Carbotte, D. J. Wright, and K. C. Macdonald (1991), Hydrothermal vent distribution along the East Pacific Rise crest (9°09'-54'N) and its relationship to magmatic and tectonic processes on fast-spreading mid-ocean ridges, *Earth and Planet. Sci. Lett.*, *104*, 513-534.

Haymon, R. M., et al. (1993), Volcanic eruption of the mid-ocean ridge along the East Pacific Rise crest at 9°45-52'N: Direct submersible observations of seafloor phenomena associated with an eruption event in April, 1991, *Earth and Planet. Sci. Lett.*, *119*, 85-101.

Herron, T. J., P. L. Stoffa, and P. Buhl (1980), Magma chamber and mantle reflections - East Pacific Rise, *Geophys. Res. Lett.*, *7*, 989-992.

Hussenoeder, S. A., J. A. Collins, G. M. Kent, R. S. Detrick, and the TERA Group (1996), Seismic analysis of the axial magma chamber reflector along the southern

East Pacific Rise from conventional reflection profiling, *J. Geophys. Res.*, *101*, 22,087-22,105.

Hyndman, R. D. a. M. J. D. (1976), The physical properties of oceanic basement rocks from deep drilling on the Mid-Atlantic Ridge, J. Geophys. Res., 81, 4042-4052.

Kampfmann, W., and H. Berckhemer (1985), High temperature experiments on the elastic and anelastic behaviour of magmatic rocks, *Phys. Earth. Planet. Int.*, *40*(3), 223-247, doi:10.1016/0031-9201(85)90132-3.

Kennett, B. L. N., and N. J. Kerry (1979), Seismic waves in a stratified half-space, *Geophys. J. R. Astron. Soc.*, *57*, 557-583, doi: 10.1111/j.1365-246X.1979.tb06779.x.

Kent, G. M., A. J. Harding, and J. A. Orcutt (1990), Evidence for a smaller magma chamber beneath the East Pacific Rise at 9°30'N, *Nature*, *344*, 650-653.

Kent, G. M., A. J. Harding, and J. A. Orcutt (1993a), Distribution of magma beneath the East Pacific Rise between the Clipperton transform and the 9°17'N deval from forward modeling of common depth point data, *J. Geophys. Res.*, *98*, 13,945-13,969.

Kent, G. M., A. J. Harding, and J. A. Orcutt (1993b), Distribution of magma beneath the East Pacific Rise near the 9°03'N overlapping spreading center from forward modeling of common depth point data, *J. Geophys. Res.*, *98*, 13,971-13,995.

Kidd, R. G. W. (1977), A model for the process of formation of the upper oceanic crust, *Geophys. J. R. Astr. Soc*, *50*, 149-183.

Korenaga, J., W. S. Holbrook, S. C. Singh, and T. A. Minshull (1997), Natural gas hydrates on the southeast U.S. margin: Constraints from full waveform and travel time inversions of wide-angle seismic data, *J. Geophys. Res.*, *102*(B7), 15,345-15,365.

Kormendi, F., and M. Dietrich (1991), Nonlinear waveform inversion of plane-wave seismograms in stratified elastic media, *Geophysics*, *56*(5), 664-674.

Langmuir, C. H., J. F. Bender, and R. Batiza (1986), Petrological and tectonic segmentation of the East Pacific Rise, 5°30'-14°30'N, *Nature*, *322*, 422-429.

Livermore, R., A. Cunningham, L. Vanneste, and R. Larter (1997), Subduction influence on magma supply at the East Scotia Ridge, *Earth and Planet. Sci. Lett.*, *150*, 261-275.

Macdonald, K. C., and J.-C. Sempéré (1984), East Pacific Rise from Siqueiros to Orozco fracture zones: Along-strike continuity of axial neovolcanic zone and structure and evolution of overlapping spreading centers, *J. Geophys. Res.*, *89*, 6049-6069.

Macdonald, K. C., and P. J. Fox (1988), The axial summit graben and cross-sectional shape of the East Pacific Rise as indicators of axial magma chambers and recent volcanic eruptions, *Earth and Planet. Sci. Lett.*, *88*, 119-131.

MacLeod, C. J., and G. Yaouancq (2000), A fossil melt lens in the Oman ophiolite: implications for magma chamber processes at fast spreading ridges, *Earth and Planet. Sci. Lett.*, *176*, 357-373.

Mainprice, D. (1997), Modelling the anisotropic seismic properties of partially molten rocks found at mid-ocean ridges, Tectonophysics, 279, 161-179.

Marsh, B. D. (1989), Magma Chambers, *Ann. Rev. Earth Planet. Sci.*, *17*, 439-474.

Mavko, G. M. (1980), Velocity and attenuation in partially molten rocks, *J. Geophys. Res.*, *85*(B10), 5173-5189.

Minshull, T. A., S. C. Singh, and G. K. Westbrook (1994), Seismic velocity structure at a gas hydrate reflector, offshore western Colombia, from full waveform inversion, *J. Geophys. Res.*, *99*(B3), 4715-4734.

Mutter, J. C., G. A. Barth, P. Buhl, R. S. Detrick, J. A. Orcutt, and A. J. Harding (1988), Magma distribution across ridge-axis discontinuities on the East Pacific Rise from multichannel seismic images, *Nature*, *336*, 156-158.

Mutter, J. C., S. M. Carbotte, J. P. Canales, and M. R. Nedimovic (2008), MGL0812 Cruise Report: A 3D MCS investigation of the magmatic-hydrothermal system at the East Pacific Rise 9°50'N.

Mutter, J. C., S. Carbotte, M. Nedimovic, J. P. Canales, and H. Carton (2009), Seismic Imaging in Three Dimensions on the East Pacific Rise, *Eos Trans. AGU*, *90*(42), 374, doi:10.1029/2009EO420002.

Nicolas, A., I. Reuber, and K. Benn (1988), A new magma chamber model based on structural studies in the Oman ophiolite, *Tectonophysics*, *151*, 87-105.

Nicolas, A., C. Freydier, M. Godard, and A. Vauchez (1993), Magma chambers at oceanic ridges: How large?, *Geology*, *21*(1), 53-56.

Oliver, G. J. H., and R. R. McAlpine (1998), Occurrence of a sheeted dolerite dyke complex in the Ballantrae Ophiolite, *Scotland. Geol. Mag.*, *135*, 509-517.

Pallister, J. S., and C. A. Hopson (1981), Samail ophiolite plutonic suite: field relations, phase variation, cryptic variation and layering, and a model of a spreading ridge magma chamber, *J. Geophys. Res.*, *86*, 2593-2644.

Perfit, M. R., and W. W. Chadwick (Eds.) (1998), *Magmatism at mid-ocean ridges: constraints from volcanological and geochemical investigations*, 59-115 pp., AGU, Washington, DC.

Phipps Morgan, J., and Y. J. Chen (1993), Dependence of ridge-axis morphology on magma supply and spreading rate, *Nature*, *364*, 706-708.

Rosencrantz, E. (1983), The structure of sheeted dikes and associated rocks in North Arm Massif, Bay of Islands ophiolite complex, and the intrusive process at oceanic spreading centers, *Can. J. Earth Sci.*, *20*, 787-801.

Rubin, K. H., J. D. Macdougall, and M. R. Perfit (1994), 210Po-210Pb dating of recent volcanic eruptions on the sea floor, *Nature*, *368*, 841-844.

Scheirer, D. S., and K. C. Macdonald (1993), Variation in cross-sectional area of the axial ridge along the East Pacific Rise: Evidence for the magmatic budget of a fast spreading center, *J. Geophys. Res.*, *98*(B5), 7871-7885.

Singh, S. C., G. F. West, and C. H. Chapman (1989), On plane-wave decomposition: alias removal, *Geophysics*, *54*(10), 1339-1343.

Singh, S. C., G. M. Kent, J. S. Collier, A. J. Harding, and J. A. Orcutt (1998), Melt to mush variations in crustal magma properties along the ridge crest at the southern East Pacific Rise, *Nature*, *394*, 874-878.

Singh, S. C., J. S. Collier, A. J. Harding, G. M. Kent, and J. A. Orcutt (1999), Seismic evidence for a hydrothermal layer above the solid roof of the axial magma chamber at the southern East Pacific Rise, *Geology*, *27*(3), 219-222.

Singh, S. C., et al. (2006), Seismic reflection images of the Moho underlying melt sills at the East Pacific Rise, *Nature*, *442*, doi:10.1038/nature04939.

Sinton, J. M., and R. S. Detrick (1992), Mid-ocean ridge magma chambers, *J. Geophys. Res.*, *97*(B1), 197-216.

Soule, S. A., D. J. Fornari, M. P. Perfit, M. A. Tivey, W. I. Ridley, and H. Schouten (2005), Channelized lava flows at the East Pacific Rise crest 9-10°N: the importance of off-axis lava transport in developing the architecture of young oceanic crust, *Geochem. Geophys. Geosys.*, *6*, Q08005, doi:10.1029/2005GC000912.

Soule, S. A., D. J. Fornari, M. R. Perfit, and K. H. Rubin (2007), New insights into mid-ocean ridge volcanic processes from the 2005-2006 eruption of the East Pacific Rise, 9°46'N-9°56'N, *Geology*, *35*(12), 1079-1082.

Soule, S. A., V. L. Ferrini, J. C. Kinsey, D. J. Fornari, C. Sellers, S. M. White, K. Von Damm, and S. M. Carbotte (2008), Navigational infrastructure at the East Pacific Rise 9°50'N area following the 2005-2006 eruption: Seafloor benchmarks and near-bottom multibeam surveys, *Geochem. Geophys. Geosyst.*, *9*(11, Q11T04), doi: 10.1029/2008GC002070

Soule, S. A., J. Escartín, and D. J. Fornari (2009), A record of eruption and intrusion at a fast spreading ridge axis: Axial summit trough of the East Pacific Rise at 9–10°N, *Geochem. Geophys. Geosyst.*, *10*, Q10T07, doi:10.1029/2008GC002354.

Toksöz, M. N., R. S. Wu, and D. P. Schmitt (1987), Physical mechanisms contributing to seismic attenuation in the crust, in, Strong Ground Motion Seismology, M. Erdik and M.N. Toksöz (eds.), NATO ASI Series C, D. Reidel, Dordrecht, 225-247.

Toomey, D. R., G. M. Purdy, S. C. Solomon, and W. S. D. Wilcock (1990), The three-dimensional seismic velocity structure of the East Pacific Rise near latitude 9°30'N, *Nature*, *347*, 639-645.

Toomey, D. R., S. C. Solomon, and G. M. Purdy (1994), Tomographic imaging of the shallow crustal structure of the East Pacific Rise at 9°30'N, *J. Geophys. Res.*, *99*, 24,135-24,157.

Tryggvason, E. (1994), Surface deformation at the Krafla Volcano, North Iceland, 1982-1992, *Bull. Volcanol.*, *56*(2), 98-107, DOI: 10.1007/BF00304105.

Umino, S., S. Miyashita, F. Hotta, and Y. Adachi (2003), Along-strike variation of the sheeted dike complex in the Oman Ophiolite: Insights into subaxial ridge segment structures and the magma plumbing system, *Geochem. Geophys. Geosyst.*, *4*(9), 8618, doi:10.1029/2001GC000233.

Vera, E. E., J. C. Mutter, P. Buhl, J. A. Orcutt, A. J. Harding, M. E. Kappus, R. S. Detrick, and T. M. Brocher (1990), The structure of 0- to 0.2-m.y.-old oceanic crust at 9°N on the East Pacific Rise from expanded spread profiles, *J. Geophys. Res.*, *95*, 15,529-15,556.

White, S. M., R. M. Haymon, D. J. Fornari, M. R. Perfit, and K. C. Macdonald (2002), Correlation between volcanic and tectonic segmentation of fast-spreading ridges: Evidence from volcanic structures and lava flow morphology on the East Pacific Rise at 9°-10°N, *J. Geophys. Res.*, *107*(B8), 10.1029/2001JB000571.

White, S. M., R. M. Haymon, and S. Carbotte (2006), A new view of ridge segmentation and near-axis volcanism at the East Pacific Rise, 8°-12°N, from EM300 multibeam bathymetry, *Geochem. Geophys. Geosyst.*, *7*(12), Q12O05, doi:10.1029/2006GC001407.

Wilcock, W. S. D., S. C. Solomon, G. M. Purdy, and D. R. Toomey (1992), The seismic attenuation structure of a fast-spreading mid-ocean ridge, *Science*, *258*, 1470-1474.

Wilcock, W. S. D., S. C. Solomon, G. M. Purdy, and D. R. Toomey (1995), Seismic attenuation structure of the East Pacific Rise near 9°30'N, *J. Geophys. Res.*, *100*, 24,147-24,165.

Worster, M. G., H. E. Huppert, and R. S. J. Sparks (1990), Convection and crystallization in magma cooled from above, *Earth and Planet. Sci. Lett.*, *101*, 78-89.

Wright, D. J., R. M. Haymon, and D. J. Fornari (1995a), Crustal fissuring and its relationship to magmatic and hydrothermal processes on the East Pacific Rise crest (9°12' to 9°54'N), *J. Geophys. Res.*, *100*(B4), 6097-6120.

Wright, D. J., R. M. Haymon, and K. C. MacDonald (1995b), Breaking new ground: estimates of crack depth along the axial zone of the East Pacific Rise (9°12'-9°54'N), *Earth and Planet. Sci. Lett.*, *134*, 441-457.

Yilmaz, Ö. (1987), *Seismic Data Processing*, 526 pp., Society of Exploration Geophysicists, Tulsa, OK.

Chapter 4

Heterogeneous seismic velocity structure of the upper lithosphere at Kane oceanic core complex, Mid-Atlantic Ridge[1]

Abstract

The Kane oceanic core complex (OCC) is a large, corrugated megamullion that was formed by a long-lived detachment fault at the axis of the Mid-Atlantic Ridge adjacent to Kane Fracture Zone between 2.1 and 3.3 Ma. We use refracted arrivals recorded along a 6-km-long hydrophone streamer during a multichannel seismic survey to constrain the shallow seismic velocity structure of the OCC. Results are presented in high-resolution traveltime seismic tomographic models along six lines that cover all of the main morphological features of the megamullion. The models show large lateral variability in *P* wave velocity within the upper ~0.5–2.0 km of the lithosphere, and these variations correlate to first order with observed variations in lithology, documented by in situ basement samples and seafloor morphology. Lithological interpretation of the velocity models indicates that there is marked lateral variability in distribution of gabbroic intrusions, serpentinized peridotites, and basalts at scales of a few kilometers to ~10 km. Serpentinized peridotites appear to dominate the central and older parts of the OCC. High-velocity gabbros are consistently (but not exclusively) present closer to the termination of the Kane detachment fault and toward the ends of the OCC. The structure of the lithosphere exhumed by the Kane detachment fault is far from the standard ophiolite-based Penrose model, and it does not show segment-centered magmatism that is commonly interpreted at slow spreading ridges. If the gabbros exhumed toward the termination of the OCC were emplaced deep (~10 km) beneath the spreading axis, they may have constituted a weak zone that focused initiation of the Kane detachment fault. Alternately, as the OCC footwall was being exhumed the gabbros may have been emplaced because of dynamic changes in melt supply, changes in mantle fertility, or decompression melting. Late stage volcanism is clearly associated with a major high-angle normal fault that cuts the detachment surface; this volcanism may have been stimulated or enhanced by bending stresses in the bending footwall. The shape of the

[1] **Published as:** Xu, M., J. P. Canales, B. E. Tucholke, and D. L. DuBois (2009), Heterogeneous seismic velocity structure of the upper lithosphere at Kane oceanic core complex, Mid-Atlantic Ridge, Geochem. Geophys. Geosyst., 10, Q10001, doi:10.1029/2009GC002586. **Reprinted with permission of AGU**

large-scale corrugated morphology of the OCC is nearly invariant in the dip direction across major changes in basement lithology, indicating that once established, the form of the Kane detachment fault was highly resistant to modification.

Geochemistry Geophysics Geosystems G3
AN ELECTRONIC JOURNAL OF THE EARTH SCIENCES
Published by AGU and the Geochemical Society

Article
Volume 10, Number 10
10 October 2009
Q10001, doi:10.1029/2009GC002586
ISSN: 1525-2027

Heterogeneous seismic velocity structure of the upper lithosphere at Kane oceanic core complex, Mid-Atlantic Ridge

Min Xu
Massachusetts Institute of Technology–Woods Hole Oceanographic Institution Joint Program, Woods Hole, Massachusetts 02543, USA (minxu@mit.edu)

J. Pablo Canales, Brian E. Tucholke, and David L. DuBois
Department of Geology and Geophysics, Woods Hole Oceanographic Institution, Woods Hole, Massachusetts 02543, USA

[1] The Kane oceanic core complex (OCC) is a large, corrugated megamullion that was formed by a long-lived detachment fault at the axis of the Mid-Atlantic Ridge adjacent to Kane Fracture Zone between 2.1 and 3.3 Ma. We use refracted arrivals recorded along a 6-km-long hydrophone streamer during a multichannel seismic survey to constrain the shallow seismic velocity structure of the OCC. Results are presented in high-resolution traveltime seismic tomographic models along six lines that cover all of the main morphological features of the megamullion. The models show large lateral variability in *P* wave velocity within the upper ~0.5–2.0 km of the lithosphere, and these variations correlate to first order with observed variations in lithology, documented by in situ basement samples and seafloor morphology. Lithological interpretation of the velocity models indicates that there is marked lateral variability in distribution of gabbroic intrusions, serpentinized peridotites, and basalts at scales of a few kilometers to ~10 km. Serpentinized peridotites appear to dominate the central and older parts of the OCC. High-velocity gabbros are consistently (but not exclusively) present closer to the termination of the Kane detachment fault and toward the ends of the OCC. The structure of the lithosphere exhumed by the Kane detachment fault is far from the standard ophiolite-based Penrose model, and it does not show segment-centered magmatism that is commonly interpreted at slow spreading ridges. If the gabbros exhumed toward the termination of the OCC were emplaced deep (~10 km) beneath the spreading axis, they may have constituted a weak zone that focused initiation of the Kane detachment fault. Alternately, as the OCC footwall was being exhumed the gabbros may have been emplaced because of dynamic changes in melt supply, changes in mantle fertility, or decompression melting. Late stage volcanism is clearly associated with a major high-angle normal fault that cuts the detachment surface; this volcanism may have been stimulated or enhanced by bending stresses in the bending footwall. The shape of the large-scale corrugated morphology of the OCC is nearly invariant in the dip direction across major changes in basement lithology, indicating that once established, the form of the Kane detachment fault was highly resistant to modification.

Components: 15,812 words, 21 figures.

Keywords: Kane oceanic core complex; ocean crustal structure; detachment faulting; Mid-Atlantic Ridge; seismic tomography; lithology.

Index Terms: 3045 Marine Geology and Geophysics: Seafloor morphology, geology, and geophysics; 7270 Seismology: Tomography (6982, 8180); 7218 Seismology: Lithosphere (1236).

Received 27 April 2009; **Revised** 1 July 2009; **Accepted** 10 July 2009; **Published** 10 October 2009.

Xu, M., J. P. Canales, B. E. Tucholke, and D. L. DuBois (2009), Heterogeneous seismic velocity structure of the upper lithosphere at Kane oceanic core complex, Mid-Atlantic Ridge, *Geochem. Geophys. Geosyst.*, *10*, Q10001, doi:10.1029/2009GC002586.

1. Introduction

[2] Footwalls of long-lived, or "detachment" faults at mid-ocean ridges (MORs) uplift and expose deep sections of the oceanic lithosphere on the seafloor [*Tucholke et al.*, 1996; *Cann et al.*, 1997; *Tucholke et al.*, 1998; *MacLeod et al.*, 2002] and form oceanic core complexes (OCCs). When the amount of the offset is sufficiently large, the footwalls roll over and form megamullions that are characterized by smooth dome-shaped surfaces and prominent spreading-parallel corrugations (mullion structures) that have amplitudes up to several hundred meters [*Tucholke et al.*, 1996, 1998]. Numerous OCCs in the form of megamullions have been identified along slow and intermediate spreading ridges [*Cann et al.*, 1997; *Tucholke et al.*, 1998; *Ohara et al.*, 2001; *Tucholke et al.*, 2001; *Reston et al.*, 2002; *Searle et al.*, 2003; *Okino et al.*, 2004; *Cannat et al.*, 2006; *Smith et al.*, 2006, 2008; *Tucholke et al.*, 2008], suggesting that exhumation of OCCs is a fundamental process in seafloor formation at MORs where melt supply is limited [*Smith et al.*, 2006; *Escartín et al.*, 2008; *Tucholke et al.*, 2008]. Most of these features are located at the ends of spreading segments where magmatism is inferred to be low [e.g., *Cannat et al.*, 1995a]. This observation led to the hypothesis that they form during periods of relatively amagmatic extension [e.g., *Tucholke et al.*, 1998]. However, drilling has shown that thick gabbro sections can be present in OCCs [*Dick et al.*, 2000; *Kelemen et al.*, 2004; *Blackman et al.*, 2006], and it recently has been proposed that OCCs form when moderate amounts of total plate separation are accommodated by magmatism [*Buck et al.*, 2005; *Tucholke et al.*, 2008].

[3] Both gabbros and peridotites are abundant at OCCs [e.g., *Tucholke et al.*, 1998], which suggests that OCCs may be excellent locations to study melt generation and migration in the mantle, as well as crustal accretion processes [e.g., *Dick et al.*, 2008]. However, there generally are poor constraints on how lithologies are distributed across and especially beneath OCCs. Seafloor sampling of OCCs is usually restricted to the exposed detachment surface where abundant allochthonous rocks of unknown provenance are present; only in areas where the detachment is cut by high-angle normal faults or slide scar headwalls is the underlying bedrock exposed. Deep drilling has been accomplished at three OCCs [*Dick et al.*, 2000; *Kelemen et al.*, 2004; *Blackman et al.*, 2006] and has recovered dominantly gabbroic sequences up to 1.4 km thick that may or may not be representative of the OCCs as a whole.

[4] To better understand lithological relations within OCCs, it is useful to employ remote geophysical methods to obtain broad coverage, to map lateral and vertical variations in rock properties, and to correlate these variations to changes in lithology as documented by in situ samples. In this paper we present results from a detailed seismic study of the OCC at Kane megamullion, which is one of the best developed and most sampled OCCs on the Mid-Atlantic Ridge (MAR) (Figure 1). Our work builds upon and expands that of *Canales et al.* [2008], who presented a comparative seismic study of three MAR OCCs (including the Kane OCC). Seismic tomography models along six strike and dip profiles over the Kane OCC show large lateral variations in velocity structure within the upper 1–2 km of lithosphere. There is an excellent correlation between seismic structure and lithology of in situ basement samples, which allows us to infer the large-scale distribution of the dominant lithologies across the Kane OCC. We use the seismically inferred spatial distribution of gabbroic intrusions, serpentinized peridotites, and volcanic rocks to provide new insights into the origin and evolution of the Kane OCC, as well as into the general process of magmatic accretion within segments of slow spreading ridges.

2. Background

2.1. Previous Seismic Tomographic Studies of MAR OCCs

[5] *Canales et al.* [2008] presented seismic tomography models derived from large-offset (6 km) multichannel seismic (MCS) data for three of the best developed OCCs known along the MAR: Atlantis Massif, Dante's Domes, and Kane OCC. Using only two profiles (orthogonal to each other

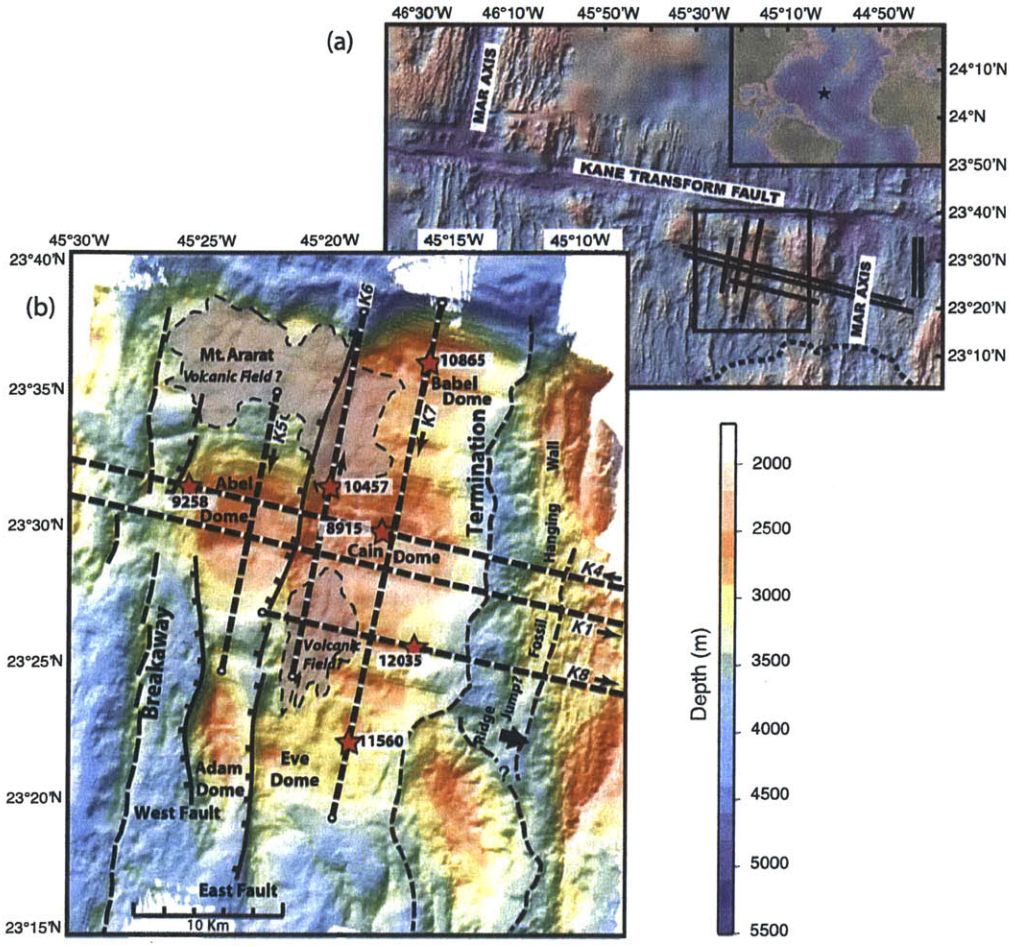

Figure 1. (a) Shaded relief bathymetry of the Mid-Atlantic Ridge (MAR) around Kane Transform Fault. Data are from the Marine Geoscience Data System (http://www.marine-geo.org/). The star in the inset shows the study location on the MAR. The Kane OCC study area (expanded view in Figure 1b) is outlined by a box, and black lines show eight multichannel seismic lines that were acquired during cruise EW0102. A nontransform discontinuity marking the southern boundary of the spreading segment that contains the Kane OCC is shown by a dotted line. (b) Bathymetric map and simplified tectonic interpretation of the Kane OCC based on SeaBeam bathymetry from R/V *Knorr* Cruise 180-2 (adapted from *Dick et al.* [2008]). Straight dashed lines locate seismic profiles with shooting direction indicated by arrows. Red stars with shot numbers show positions of six shot gathers displayed in Figure 2. Other dashed lines show locations of the breakaway and termination of the Kane detachment fault. The whole detachment surface is cut by a west facing normal fault (East Fault), and other normal faults are indicated by ticked lines. Shaded regions outlined by dashes indicate areas of possible volcanic fields, interpreted on the basis of seafloor samples, morphology, and, where available, subseafloor velocity structure.

along the dip and strike directions) at each of the three OCCs, they reported the large-scale structural characteristics that are common to all of the studied OCCs, and therefore could be interpreted in terms of the general processes controlling the formation and evolution of OCCs. Their interpretations were based on the observation that the shallow (~0.5–1.7 km) *P* wave velocity structure of the OCCs could be broadly grouped into three classes, and that each class correlates with different footwall lithologies documented by in situ geological samples and seafloor morphology: class V1, corresponding to areas with low uppermost velocities (<3.4 km s^{-1}) and low vertical velocity gradients (<~1 s^{-1}),

correlates with volcanics and hummocky morphology; class V2, for areas with intermediate velocities (~3.4–4.2 km s^{-1}) and intermediate velocity gradients (1–3 s^{-1}), correlates with massive outcrops of dominantly serpentinized peridotite; and class V3, for areas with high velocities (>4.2 km s^{-1}) and large velocity gradients (>3 s^{-1}), corresponding to gabbros.

[6] This classification allowed *Canales et al.* [2008] to show that at MAR OCC gabbros are heterogeneously distributed as large (tens to >100 km^2) bodies within serpentinized peridotites, and that they are consistently present near the terminations of the detachment faults. They hypothesized that this fact could indicate enhanced magmatism during the late stages of OCC formation due either to natural variability in the magmatic cycle or decompression melting stimulated during rapid exhumation of the footwall.

2.2. Geological Setting of the Kane OCC

[7] The near-axis section of the MAR between the Kane Fracture Zone at 23°40′N and ~22°30′N (i.e., the MARK area) has been studied by numerous geophysical and geological investigations. These include SeaBeam bathymetric mapping of the Kane transform [*Pockalny et al.*, 1988] and the adjacent ridge axis extending south to ~22°30′N [*Kong et al.*, 1988], a Sea MARC I side-scan sonar survey of the inner rift valley [*Kong et al.*, 1988], submersible investigations and sampling of the northern rift valley and eastern Kane ridge-transform intersection [e.g., *Karson and Dick*, 1983; *Karson et al.*, 1987; *Brown and Karson*, 1988; *Mével et al.*, 1991; *Auzende et al.*, 1994], drilling (ODP Legs 109 [*Detrick et al.*, 1988] and 153 [*Cannat et al.*, 1995b]), and seismic refraction experiments in the Kane fracture zone [*Detrick and Purdy*, 1980; *Cormier et al.*, 1984] and in the rift valley to the south [*Purdy and Detrick*, 1986; *Canales et al.*, 2000a]. Magnetic anomaly profiles across the rift valley indicate asymmetric spreading during the last 3–4 Myr [*Schulz et al.*, 1988], with faster rates to the west (~14.1 mm/a) than to the east (~11.3 mm/a). This asymmetry has been caused by a series of small eastward ridge jumps [*Schulz et al.*, 1988]. Off-axis geophysical studies within and immediately to the south of the MARK area [*Gente et al.*, 1995; *Pockalny et al.*, 1995; *Maia and Gente*, 1998] have shown complex tectonic patterns generated by along-axis growth and contraction of spreading segments during the last 10 Myr.

[8] Bathymetric [*Kong et al.*, 1988], magnetic [*Schulz et al.*, 1988] and submersible data [*Karson et al.*, 1987; *Brown and Karson*, 1988] indicate that the MARK area consists of at least two distinct second-order segments that are separated by a nontransform discontinuity near ~23°10′N at the MAR axis [*Karson et al.*, 1987; *Kong et al.*, 1988; *Cannat et al.*, 1995a]. The northern segment is ~40 km long and highly asymmetrical at its northern end, with a prominent elevated inside-corner massif at the intersection of the rift valley with the Kane transform [*Karson and Dick*, 1983] (Figure 1). The western rift valley wall has large fault scarps that expose gabbros and serpentinized peridotites along most of the segment [e.g., *Mével et al.*, 1991]. This has been interpreted to represent the initial stages of formation of an OCC. The eastern flank is characterized by smaller faults and a continuous basaltic carapace that indicates volcanic constructional morphology [*Karson and Dick*, 1983; *Karson et al.*, 1987; *Kong et al.*, 1988]. Seismic reflection profiles over the rift valley of the northern segment have not provided conclusive evidence for melt accumulations within the axial crust [*Detrick et al.*, 1990; *Calvert*, 1995], but a seismic refraction profile suggests that the segment is presently magmatically active [*Canales et al.*, 2000a]. Mantle Bouguer anomalies in the MARK area [*Morris and Detrick*, 1991; *Ballu et al.*, 1998; *Maia and Gente*, 1998] are irregular and more complex than the simple "bull's eye" pattern that characterizes other parts of the MAR [*Lin et al.*, 1990; *Detrick et al.*, 1995].

[9] The Kane OCC is a large megamullion (~23 km by ~40 km in dip and strike directions, respectively) formed by a long-lived detachment fault between ~3.3 and 2.1 Ma [*Williams et al.*, 2006] (Figure 1). It is located immediately south of the Kane Transform Fault (TF), ~30–55 km off-axis on the western side of the northern MARK segment, occupying about two thirds of the length of the paleospreading segment (Figure 1). It shows the key features that characterize megamullions [*Tucholke et al.*, 1998]. The breakaway zone, where the detachment fault initially nucleated, correlates with a linear, isochron-parallel ridge that is continuous for more than 40 km (with the exception of a small offset near latitude 23° 30′N) (Figure 1). The exposed detachment fault constitutes the megamullion surface, which is dome-shaped and exhibits slip-parallel corrugations (mullion structures) up to a few hundred meters in amplitude. The termination is defined by a valley located between the smooth

detachment fault surface and the rough, younger terrain of the fossil hanging wall. The Kane OCC contains several domes (Babel, Abel, Cain, Adam, and Eve, following the nomenclature of *Dick et al.* [2008] (Figure 1)) that are elevated up to a kilometer or more above adjacent seafloor. The largest domes forming the central part of the OCC (Abel and Cain Domes) are separated by a major west dipping, high-angle normal fault that cuts the detachment surface (East Fault, Figure 1). Most of the geological sampling on the Kane OCC has been done by dredge and ROV on R/V *Knorr* cruise 180-2 [*Dick et al.*, 2008]; this is complemented by sampling done along the southern wall of the Kane TF (northern wall of the OCC) during submersible dives of the KANAUT Expedition [*Auzende et al.*, 1994]. Details of the lithological structure of the Kane OCC are given by *Dick et al.* [2008]. The extensive geological sampling of the Kane OCC provides an excellent opportunity to calibrate our seismic results according to lithology, and thus to interpret the broader scope of geological structure within the Kane OCC.

3. Data and Methods

3.1. Seismic Data Acquisition and Processing

[10] The MCS data used in this study were acquired in 2001 aboard R/V *Maurice Ewing* (cruise EW0102). Details of the data acquisition are in Appendix A. A total of eight MCS lines were acquired over the Kane OCC, across the MAR axis, and over conjugate crust east of the axis (Figure 1). We applied traveltime tomography methods to the streamer refracted arrivals in the recorded data to derive the subseafloor structure along the profiles [e.g., *Zelt et al.*, 2004]. We here present results from the six ~20- to 50-km-long profiles located over the Kane OCC. Data from profiles that cross the spreading axis and conjugate crust could not be used for our traveltime tomography analysis because the seafloor is too deep to observe subseafloor refractions in advance of seafloor reflections. Results from profiles K1 and K7 were recently published in a comparative study of several OCCs [*Canales et al.*, 2008]; here we expand the analysis to the remaining profiles. The MCS lines employed in this study include 3 dip lines (K4, K1, K8) and 3 strike lines (K5, K6, K7) (Figure 1). These six lines cover most of the main domes of the Kane OCC. The dip lines extend to the east across the hanging wall remnant, and two of them (K1 and K4) extend westward across the breakaway zone.

[11] The long shot-receiver offsets provided by the hydrophone steamer, combined with the relatively shallow seafloor depths across the Kane OCC, allowed us to record clear subseafloor refractions (Figure 2) that we use in traveltime tomography modeling. During data processing, we first edited out bad traces. In order to increase the signal-to-noise ratio (SNR), every five consecutive shots were gathered, and the common offset traces were stacked and averaged to form 480-fold "supershot gathers." The supershot gathers were filtered in the frequency–wave number domain to remove low-frequency cable noise, and they were band-pass filtered (minimum phase) with frequency bands of 3-5-15-30 Hz or 3-5-30-50 Hz, depending on the data quality. Figure 2 shows six representative supershot gathers located over areas with different seafloor geology. In general, shot gathers exhibit clear subseafloor refractions that arrive before the seafloor reflections at ranges larger than ~2–3 km. Note that as the water depth beneath the shot and streamer increases, the crossover distance between the seafloor reflection and subseafloor refracted first arrivals increases (e.g., profile K4 shot 9258 and shot 8915, Figure 2). Data quality is generally very good, although some areas exhibit poor SNR (e.g., profile K8 shot 12035, Figure 2). In such cases rough seafloor topography and complex subsurface structure may be affecting the propagation of seismic energy and thus reducing the SNR.

3.2. Traveltime Picks

[12] The data used in the tomographic modeling are *P* wave first-arrival traveltime picks. In some regions, it is possible to discern a number of secondary refracted branches from different layers (e.g., profile K6 shot 10457 and profile K7 shot 11560, Figure 2). However, in this study we focus our analysis on modeling the travel times of the first-arriving refractions that precede the direct water wave. Because we employ a 2-D analysis procedure, we use only data from shot-receiver pairs that are located approximately along the linear parts of the profiles, excluding shot-receiver pairs collected during ship turns and where feathering was excessive. All traveltime picks were made using a semiautomatic first-break picking method using the software Focus (Paradigm®). First, traveltimes were picked within a supershot gather and then extrapolated to the next 10 gathers, automatically adjusting to the nearest waveform

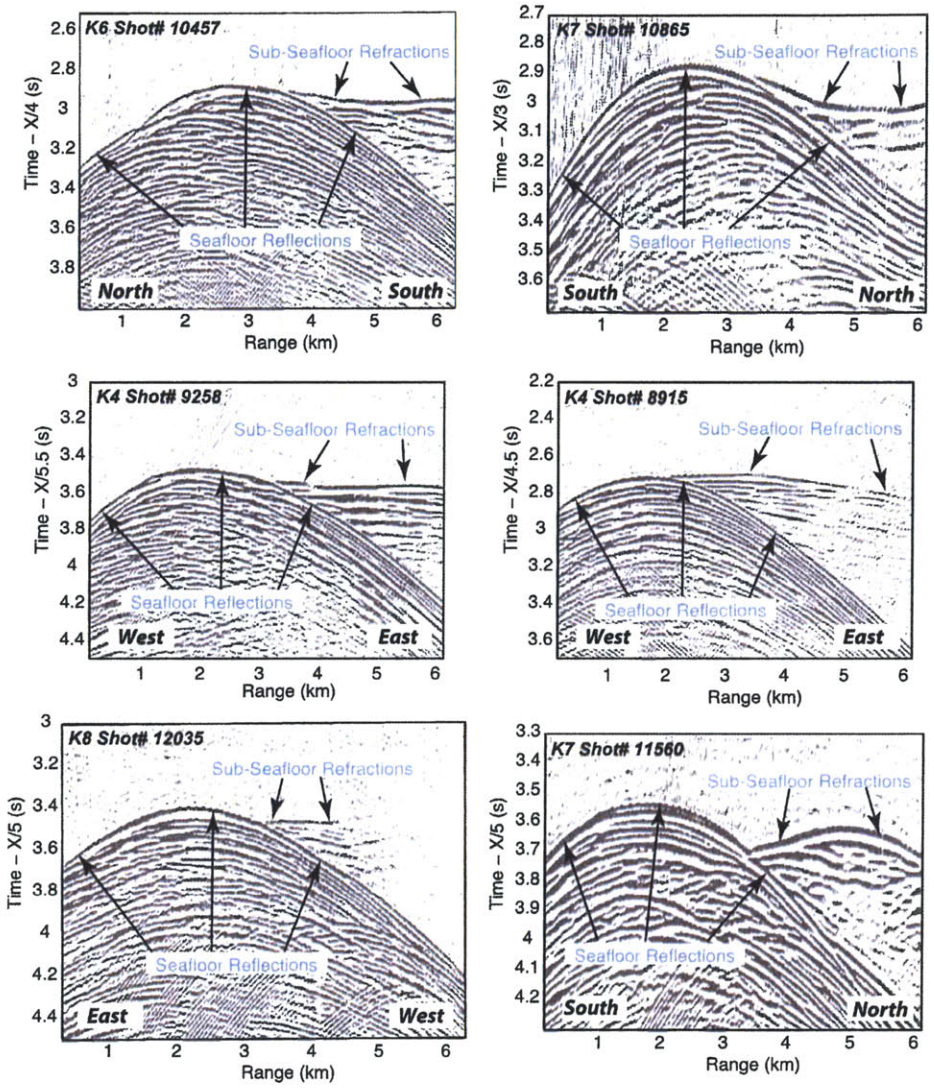

Figure 2. Six representative shot gathers from seismic profiles over the Kane OCC. Horizontal axes are distances from source to receivers along the streamer, and vertical axes are reduced two-way traveltime with different reduction velocities as indicated. Shot gather positions are shown in Figure 1 by red stars. In general, shot gathers of our data exhibit clear seafloor reflections and subseafloor refractions.

peak. Picks were then visually inspected and, if necessary, adjusted by hand. The accuracy of traveltime picking in noisy traces was improved by comparing the seismic signature with that of traces at similar offsets in nearby shots with higher SNR. This process guarantees consistency across all shots.

[13] Pick uncertainties were calculated on the basis of the SNR in a 100-ms window around the pick [*Zelt and Forsyth*, 1994]. As in the method of *Zelt and Forsyth* [1994], SNR was calculated as the square root of the ratio between the maximum trace amplitude in a 100-ms window before and after the pick. The relation between the SNR and the assigned traveltime uncertainty was established using the empirical equation $\sigma = 45 \cdot \mathrm{SNR}^{-0.9535}$, where σ represents traveltime uncertainty in milli-

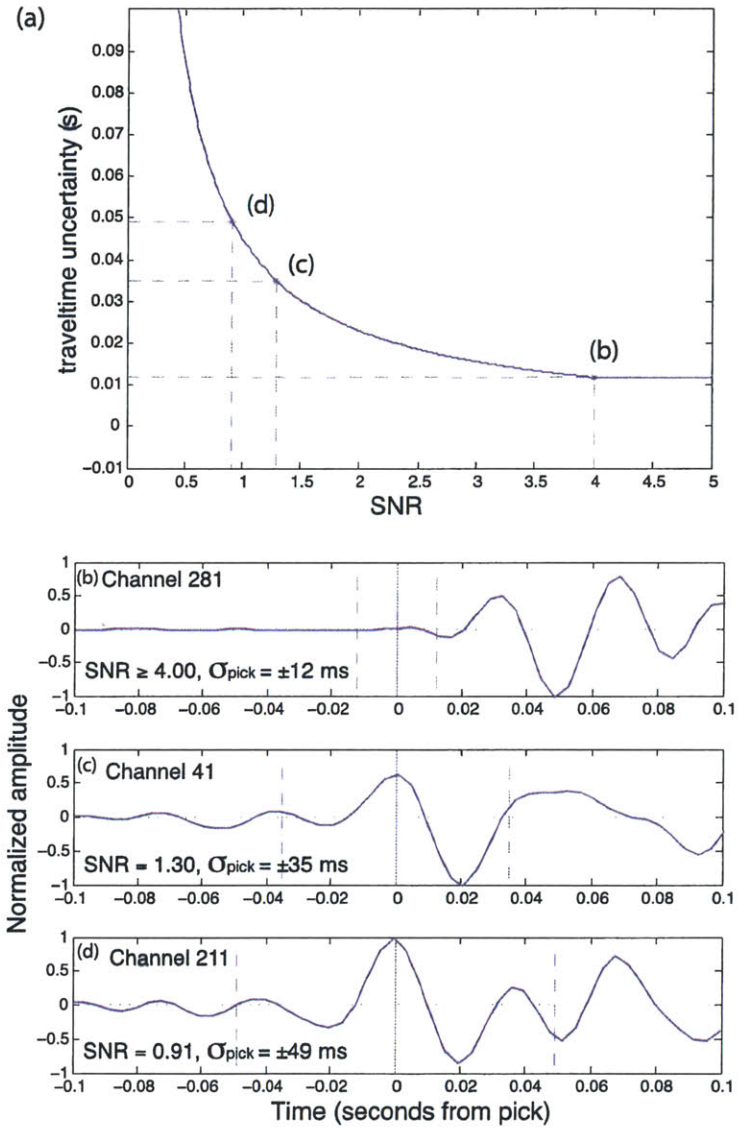

Figure 3. (a) Empirical relationship between signal-to-noise ratio (SNR) and traveltime uncertainty (σ). The three points on the curve represent three examples shown in Figures 3b–3d. For any traces with SNR $\geq$ 4.00, traveltime uncertainties were assigned as 12 ms. (b–d) Selected seismic traces from shot 11200 of profile K7, representing three different SNR values. Horizontal axis is time, with 0 s corresponding to the pick identification (vertical solid line). Vertical dashed lines indicate total traveltime uncertainties. Vertical axis is trace amplitude, normalized to the maximum value observed in the window displayed. Note that in Figure 3b seismic amplitudes are dominated by secondary high-amplitude seafloor reflections, making the pick amplitude appear small; however, amplitude of the traveltime pick is still significantly larger than that of the noise preceding the pick.

seconds (Figure 3a). Errors both in the shot-receiver offset and in seafloor depth at the ray entry point affect traveltime uncertainties, and we therefore adopted 12 ms (3 data samples) as the minimum traveltime uncertainty (uncertainties smaller than the minimum value were reassigned to 12 ms). In Figures 3b–3d we show three selected traces from shot 11200 of profile K7, together with their trav-

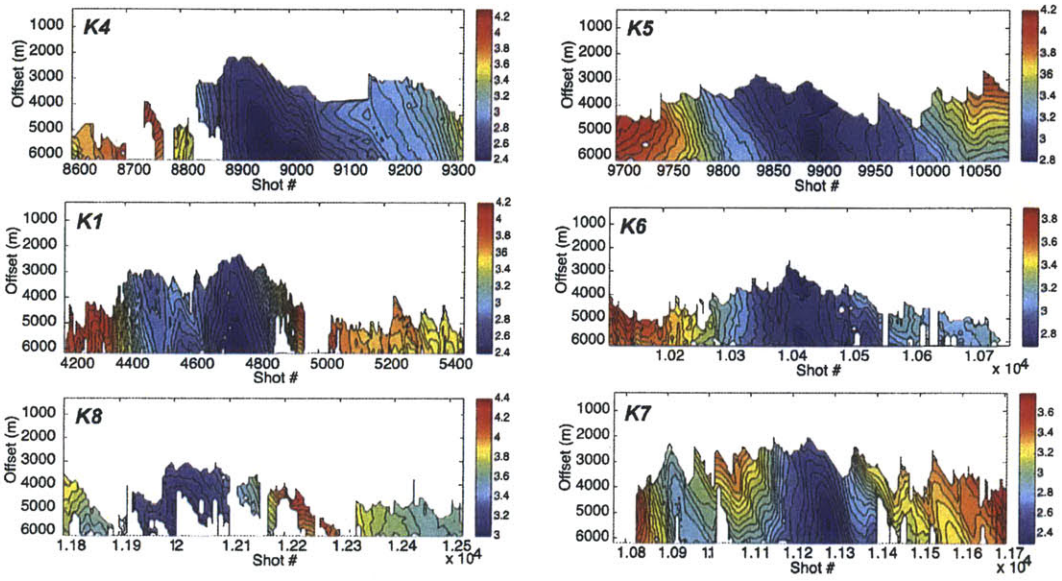

Figure 4. Picked first-arrival traveltimes (two-way traveltimes reduced at 3.7 km s^{-1}). A vertical column indicates the time along the streamer for a single shot. Near offsets (high channel numbers) are at the tops of the plots. In white regions, no traveltimes were picked for a particular shot-receiver pair because of noisy data or because subseafloor refractions arrive later than the seafloor reflection at short offsets. Contour interval is 0.1 s.

eltime picks and uncertainties representative of three different SNR values.

[14] Traveltime picks were decimated in the shot and receiver domains before the inversion to alleviate the computational load and because the original shot and receiver spacing is below the resolving power of ray theory (the radius of the first Fresnel zone at the seafloor is ~275 m, assuming an average seafloor depth of 3 km, a dominant frequency of 30 Hz and a velocity of 1.5 km/s). Therefore we used traveltime picks from one out of every 5 shot gathers, and from one out of every 10 receivers within each shot gather. The decimated sets of traveltime picks are shown in Figure 4 as color plots of traveltime versus shot number and source-receiver offset. Blue areas correspond to small traveltimes, which can be caused by either shallow water depth or high subseafloor velocity. The corresponding calculated traveltime uncertainties are shown in Figure 5. The plots of the pick uncertainties show that low uncertainty generally corresponds to smaller offsets.

3.3. Streamer Traveltime Tomography

[15] We performed 2-D tomographic inversions using first-arrival traveltimes recorded along the streamer [e.g., *Calvert et al.*, 2003; *Zelt et al.*, 2004]. Our objective was to derive the smoothest 2-D velocity model for each line, i.e., a model with the least amount of structure that fits the observed traveltimes within their uncertainty in the least number of iterations. We used the software FAST [*Zelt and Barton*, 1998] to obtain P wave velocity models by minimizing the data residuals and the roughness of perturbations from a background model. As a measure of the goodness of traveltime fit we use the weighted misfit function χ^2 defined as:

$$\chi^2 = \frac{1}{N}\sum_{i=1}^{N}\left(\frac{T_i^{obs} - T_i^{pre}}{T_i^{unc}}\right)^2,$$

where N is the total number of data, T_i^{obs} is the ith observed traveltime, T_i^{pre} is the ith predicted traveltime, and T_i^{unc} is traveltime uncertainty for the ith data point. Ideally $\chi^2 = 1$ indicates fitting of the observations within their uncertainties. The forward problem, ray tracing and traveltime calculation, was solved in a regular grid with 25 m node spacing both vertically and horizontally. Because of the water depth in the study area, the observed subseafloor refractions are not true first arrivals (first arrivals are actually direct waves

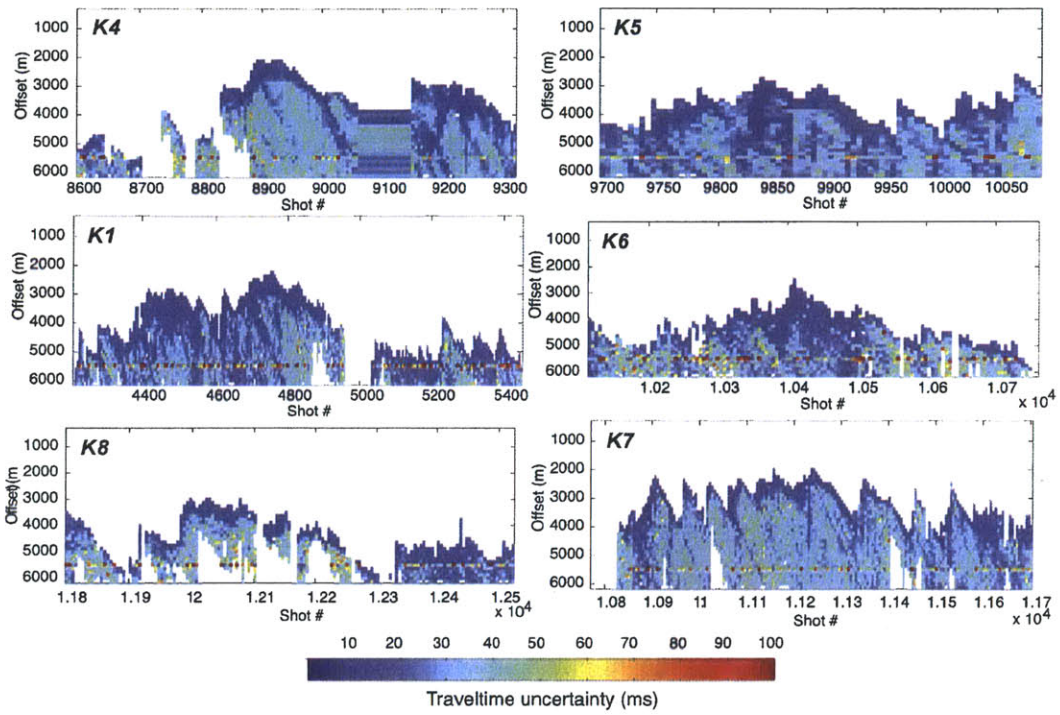

Figure 5. Pick uncertainties for traveltimes shown in Figure 4. The plot reveals regions of relatively low uncertainty as well as more diffuse regions of higher uncertainty. The higher uncertainty at 5500 m offset is due to a noisy channel on the streamer.

propagating from sources to receivers). Thus we use a modified ray-tracing algorithm in order to calculate raypaths and traveltimes only from subseafloor arrivals [*Canales et al.*, 2008].

[16] All the nonlinear inversions were performed on a uniform 200-m grid, using a regularized, damped least squares solution [*Zelt and Barton*, 1998]. The regularization is obtained by minimizing an objective function $\Phi(m)$:

$$\Phi(m) = \delta t^T C_d^{-1} \delta t + \lambda \left[m^T C_h^{-1} m + s_z m^T C_v^{-1} m \right]$$

where $\delta t^T C_d^{-1} \delta t$ are traveltime residuals (weighted by their uncertainty C_d); C_h and C_v are the horizontal and vertical second spatial partial derivatives, respectively, of the model parameters m. The tradeoff between minimizing traveltime residuals and obtaining a smooth solution is controlled by the damping parameter λ, and s_z controls the importance (weighting) of vertical versus horizontal smoothness [*Zelt and Barton*, 1998], with $s_z = 0$ indicating no smoothing in the vertical direction, $s_z = 1$ meaning equally vertical and horizontal smoothing, and $s_z > 1$ resulting in models with stronger vertical smoothing constraints.

[17] As a starting model, we use a simple model defined by a seafloor velocity and a constant vertical velocity gradient that represents the average 1-D structure of all our profiles (see Appendix B and Figure B1). The traveltime residuals predicted by the 1-D starting model are shown in Figure 6. The large positive (blue) and negative (red) residuals indicate that the 1-D model is a poor representation of the subseafloor structure; thus our data require large lateral velocity variations. On the basis of the traveltime residuals, we can anticipate that the dip profiles K1, K4, and K8 will be characterized by alternating regions with structures both faster and slower than the starting model, while the strike profiles will be characterized, on average, by a somewhat more homogeneous structure that is either faster (profile K7) or slower (profiles K5 and K6) than the starting model.

[18] Our preferred 2-D models (Figure 7) were chosen with different values of the damping parameter λ and iteration number for each profile

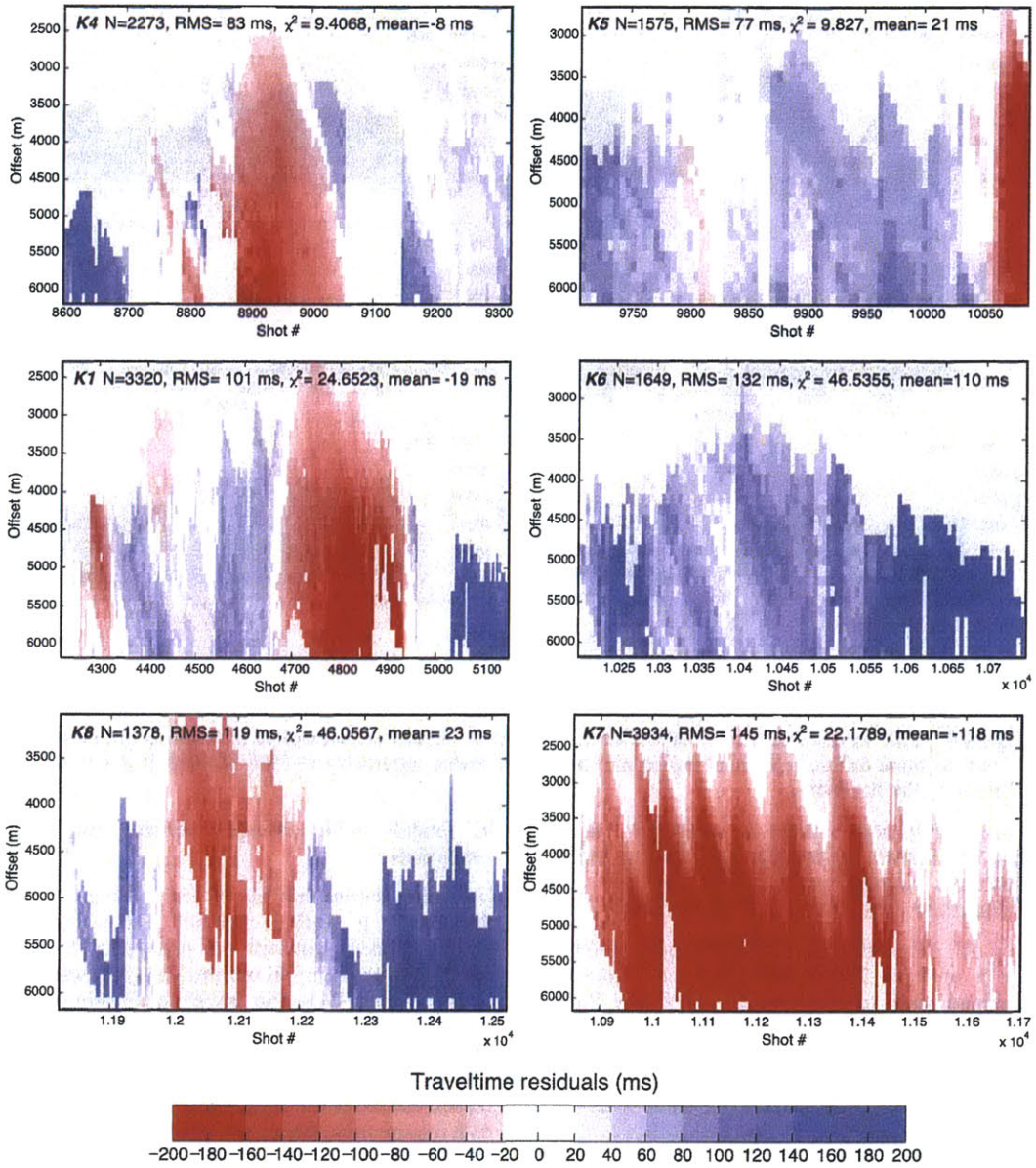

Figure 6. Color maps of traveltime residuals predicted from the initial 1-D starting model displayed as a function of shot number and source-receiver offset for each seismic profile. Color breaks are every 20 ms. Light gray indicates sections with no traveltime pick. N is number of observations, RMS is root-mean-squared traveltime residuals, χ^2 is weighted misfit function, and mean is the mean of the distributions.

(see Appendix B). This allows us to image seismic heterogeneities at different scales along each profile as the data may require different amounts of structure in each profile. We note that our preferred solution for profile K7 is somewhat different than that published by *Canales et al.* [2008], who used a smaller value of λ. However, the differences between these two acceptable models are minimal and do not affect the interpretation of this study or the study of *Canales et al.* [2008].

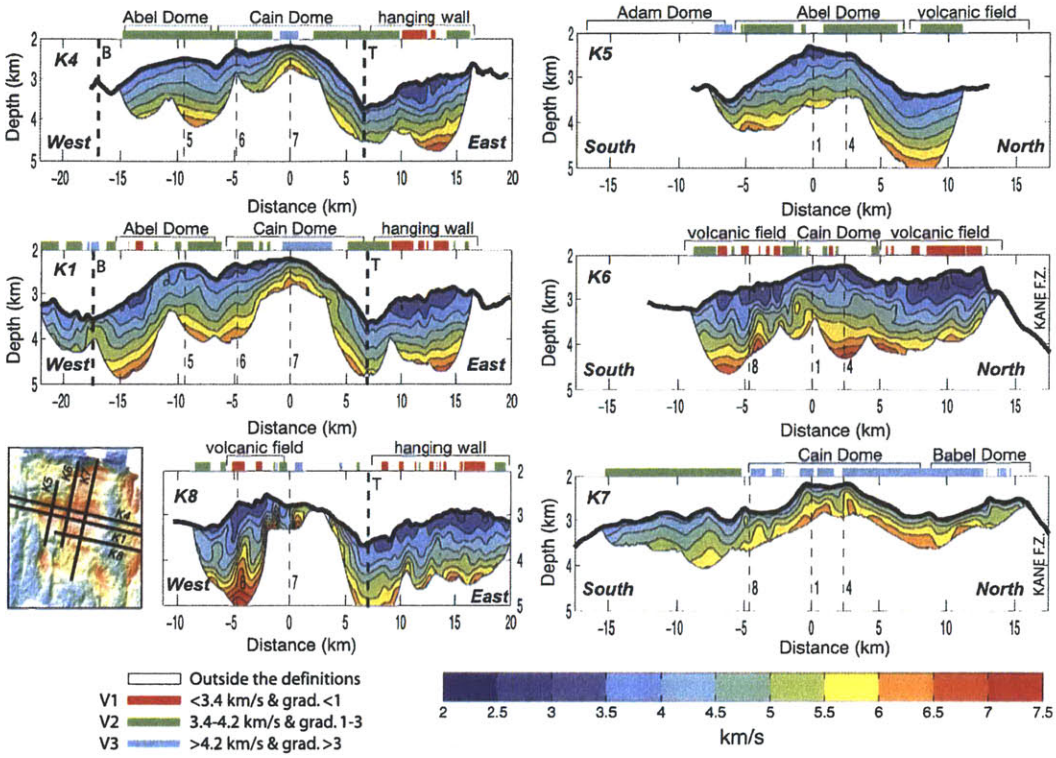

Figure 7. Two-dimensional tomographic models of *P* wave velocity beneath Kane OCC (profile locations are in the bottom left inset). Contour interval is 0.5 km s^{-1}. (left) Dip profiles and (right) strike profiles. Thicker dashed lines on dip profiles indicate locations of breakaway (B) and termination (T). Thinner dashed lines show crossings between dip and strike profiles. Dip profiles are aligned on the crossings of strike profile K7, and strike profiles are aligned on the crossings of dip profile K1. Morphological features are labeled at the top of the profiles. The along-profile extents of V1, V2, and V3 velocity characteristics in the upper ~500 m of the tomographic models are indicated by color bars at the top of each profile (key at bottom left; see section 4 for explanation). These three classes of velocity characteristics encompass most of the observed velocity structure.

[19] The preferred velocity models (Figure 7) are discussed in detail in section 4. Figure 8 shows the traveltime residuals calculated by subtracting traveltimes predicted from the preferred velocity models from the observed traveltimes. Note that, compared to Figure 6, the large positive and negative traveltime residuals predicted by the initial model have been largely reduced by the preferred models. The traveltime residuals are nearly evenly distributed, indicating that all the data are equally well fitted across all source-receiver offsets and shots, except at some locations with rougher topography and/or deeper seafloor (e.g., near shot 4900 along profile K1, Figure 8).

[20] The strong lateral variations in seismic velocity shown in the preferred models are required to fit the observed data and are not just simply consistent with the data. For example, Figure 9 shows an example of two representative shots for profile K4 that sample different velocity structures. Figure 9 (top) shows the observed supershot gathers with the observed traveltime picks and the predicted traveltime curves calculated from the initial and final models. The initial velocity model fits reasonably well the observed traveltimes for shot 9258, but it is too slow for shot 8915, indicating the presence of higher velocities beneath shot 8915. The final velocity model recovers such high velocity well and provides a good fit to the observed traveltimes. Figure 9 also shows the complete ray coverage for profile K4. Ray coverage is dense and relatively homogenous, except in

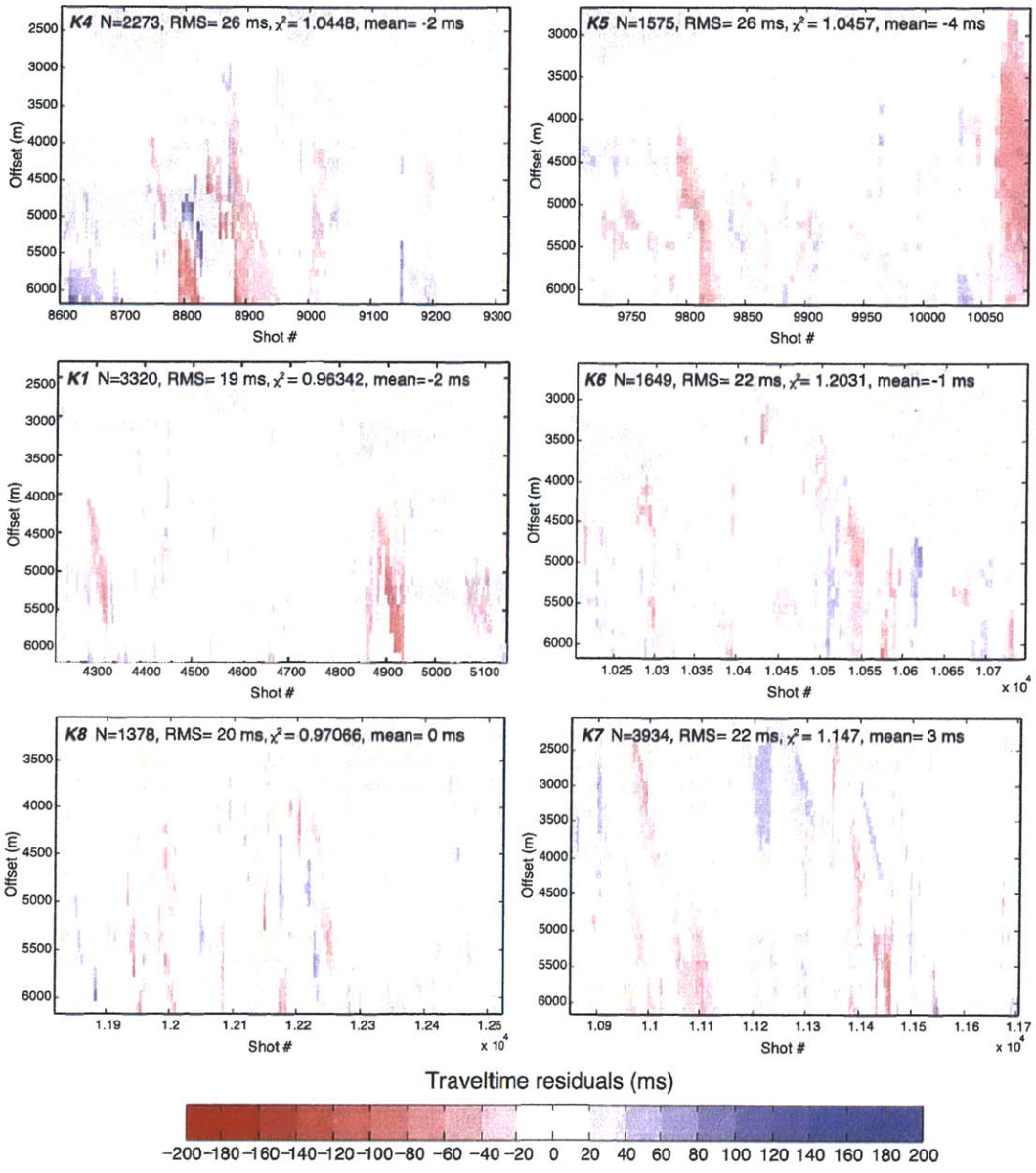

Figure 8. Color maps of traveltime residuals predicted from the final tomographic models (Figure 7) displayed as a function of shot number and source-receiver offset for each seismic profile. Color breaks are every 20 ms. All the other items are as explained in Figure 6.

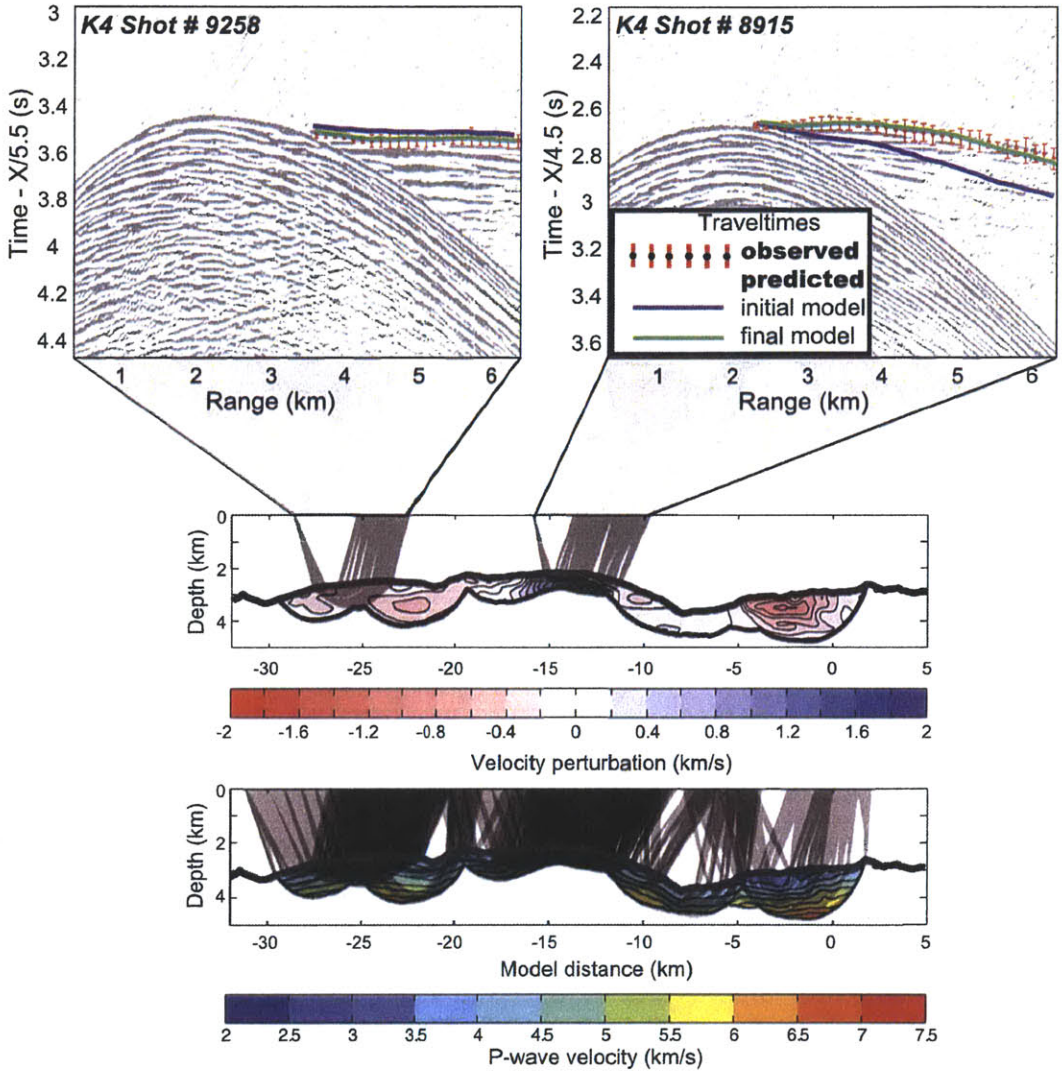

Figure 9. (top) Two representative shot gathers from profile K4 (Figure 2) with observed traveltimes and their assigned uncertainty (circles with red error bars). Traveltime curves are shown in blue as predicted by the initial model (Figure B1b) and in green as predicted by the final model (Figure 7). (middle) Final velocity model for profile K4, shown as perturbations with respect to the initial model, and contoured every 0.2 km s^{-1}. Raypaths (gray lines) for the two source-receiver pairs in Figure 9 (top) are shown. (bottom) Final velocity model for profile K4 with complete ray coverage and contours every 0.5 km s^{-1}.

areas of deeper seafloor that usually are sampled by fewer rays.

4. Seismic Tomography Results

[21] Our tomographic results show large lateral variations in P wave velocity structure in both strike and dip directions down to scales of 1 km or less within the upper ~0.5–2.0 km of the lithosphere across the Kane OCC (Figure 7). Velocities are greater than 3 km s^{-1} everywhere but rarely exceed 7 km s^{-1}. The lateral variations can be seen most easily by displaying the preferred velocity models relative to the initial 1-D model

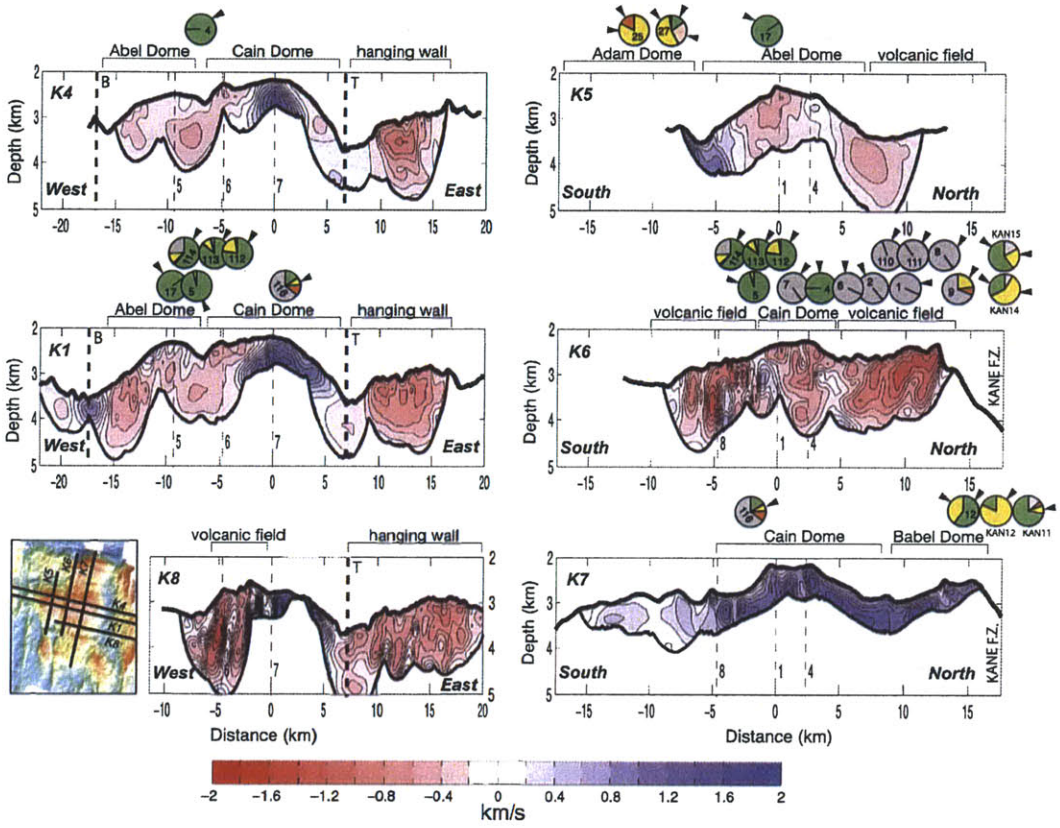

Figure 10. Final velocity models from Figure 7, here shown as perturbations with respect to the initial 1-D velocity model (Figure B1b) and contoured every 0.2 km s^{-1}. Rock types sampled from slide scar headwalls and high-angle fault scarps within ~2 km of the seismic profiles (larger pie diagrams in Figure 15) are shown above the profiles; small arrows on the pie diagrams indicate which rock types (color coded as in Figure 15) are known or reasonably interpreted to represent bedrock composition. The bottom left inset shows locations of the six seismic profiles on the Kane OCC.

(Figure 10). Lateral resolution tests (see section C1 and Figure C1) indicate that anomalies that are ~2.0 km wide and less than 0.5 km subseafloor can be trusted and interpreted, except at the ends of profiles where resolution is poorer.

[22] We use the *P* wave velocity models to calculate vertical velocity gradients over 200 m depth intervals along the profiles (Figure 11). We find that in the upper ~500 m velocity and vertical velocity gradient are positively correlated (Figure 12). This correlation allowed *Canales et al.* [2008] to define three broad classes of velocity structure in the shallow part of the basement beneath MAR OCCs (see section 2.1). Our results also fall into these three classes of velocity structure, which encompass almost all combinations of velocity and velocity gradient (Figures 7, 11, and 12): Class V1 occurs primarily in the hanging wall at the eastern ends of the dip lines and in the northern and southern parts of profile K6; class V2 is the most commonly observed velocity configuration, and it is prevalent over the terminations and in the western parts of the dip lines, over most of profile K5, in the central part of profile K6, and in the southern one third of profile K7; class V3 is observed in the central sections of the dip lines, the southern end of profile K5, and the northern two thirds of profile K7. The along-profile extents of V1, V2, and V3 velocity characteristics in the upper ~500 m of the tomographic models are

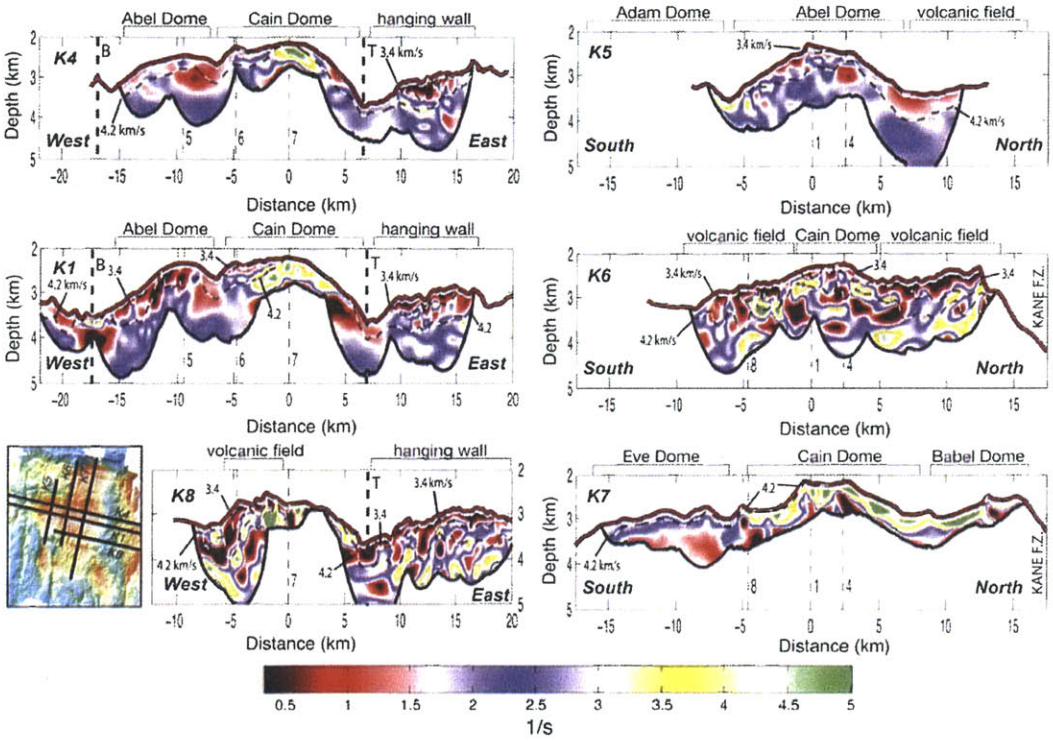

Figure 11. Vertical velocity gradient along the Kane profiles, calculated from the tomographic models of *P* wave velocity (Figure 7). Profile locations are indicated in the bottom left inset. Gradients were calculated in vertical windows at a grid spacing of 200 m (i.e., the grid spacing for tomographic inversions). The 3.4 km s^{-1} and 4.2 km s^{-1} isovelocity contours from Figure 7 are shown as dashed lines and are labeled. Morphological features are labeled at the top of the profiles.

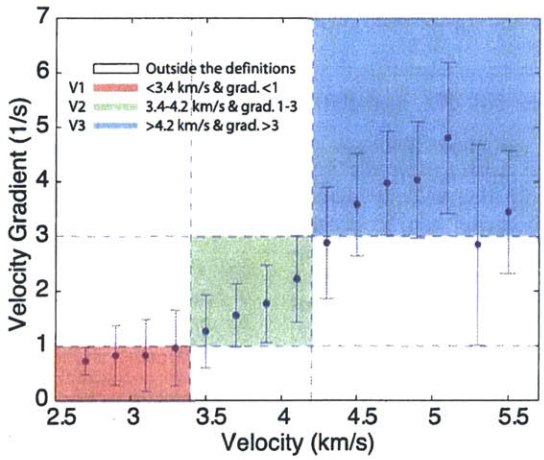

Figure 12. Correlation between the shallow (~500 m subseafloor) velocity and vertical velocity gradient structures. The data are binned in 0.2 km s^{-1} increments of the velocity. Vertical bars are one standard deviation of the average shallow vertical velocity gradient within each bin. Definitions of the three classes of velocity structures are indicated (same as in Figure 7; see section 4 for explanation).

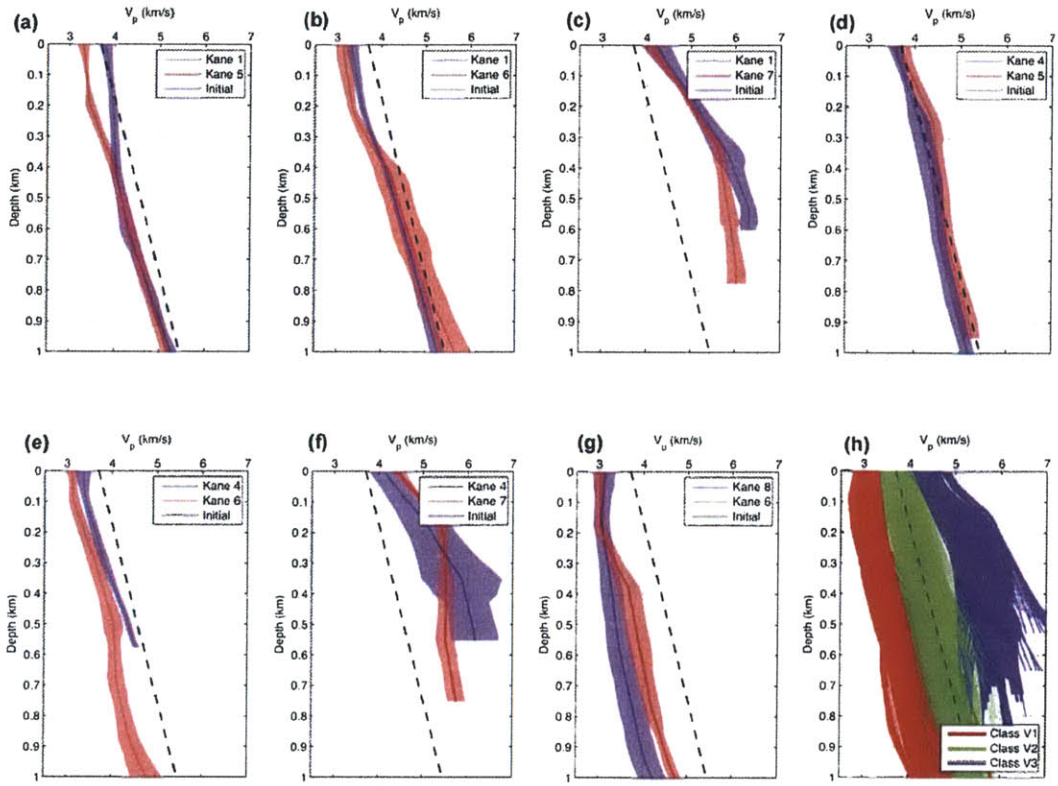

Figure 13. (a–g) Comparison of velocity-depth profiles at crossing points of dip and strike profiles (shown in blue and red, respectively). The shaded areas indicate $\pm 1\sigma$ velocity uncertainty (Figure 14). The initial average 1-D velocity model (Figure B1b) is shown by dashed lines. (h) Velocity-depth bands extracted from the six profiles within regions defined as class V1, V2, and V3.

indicated by color bars at the top of each profile in Figure 7.

4.1. Dip Lines (Profiles K4, K1, and K8)

[23] Patterns of velocity variations between the breakaway zone and the termination are very similar among the three dip line velocity models (Figures 7 and 10). Each model can be divided laterally into three zones: an eastern zone consisting of hanging wall terrain that has V1 structure; a central zone over the central and eastern sections of Cain Dome that is characterized by V3 structure; and a western zone over Abel Dome and the western side of Cain Dome that has V2 structure. The western end of profile K8 falls between Cain and Eve Domes (Figure 1) and crosses a possible volcanic field with V1 structure [*Dick et al.*, 2008]. At the western end of profile K1, there is a small high-velocity body present near the detachment breakaway (V3 structure).

4.2. Strike Lines (Profiles K5, K6, and K7)

[24] The velocity structure along the strike lines shows greater variability between lines (Figures 7 and 10). The central part of profile K5 crosses Abel Dome and stops at a possible volcanic field at its northern end. Most of the profile has V2 structure, but the southern end impinges on the northern part of Adam Dome and shows V3 structure.

[25] Profile K6 runs along the crest of the footwall at East Fault. V1 structure characterizes the northern one third of the profile where a volcanic ridge caps the crest of East Fault, and intermediate V2 structure is present in the central section. Mixed intermediate to low velocities and V1/V2 structure appear in the southern one third of the profile where volcanics appear to be present.

[26] The northern and central parts of profile K7 correspond to Babel Dome and the shallowest part of Cain Dome, respectively, and both exhibit V3

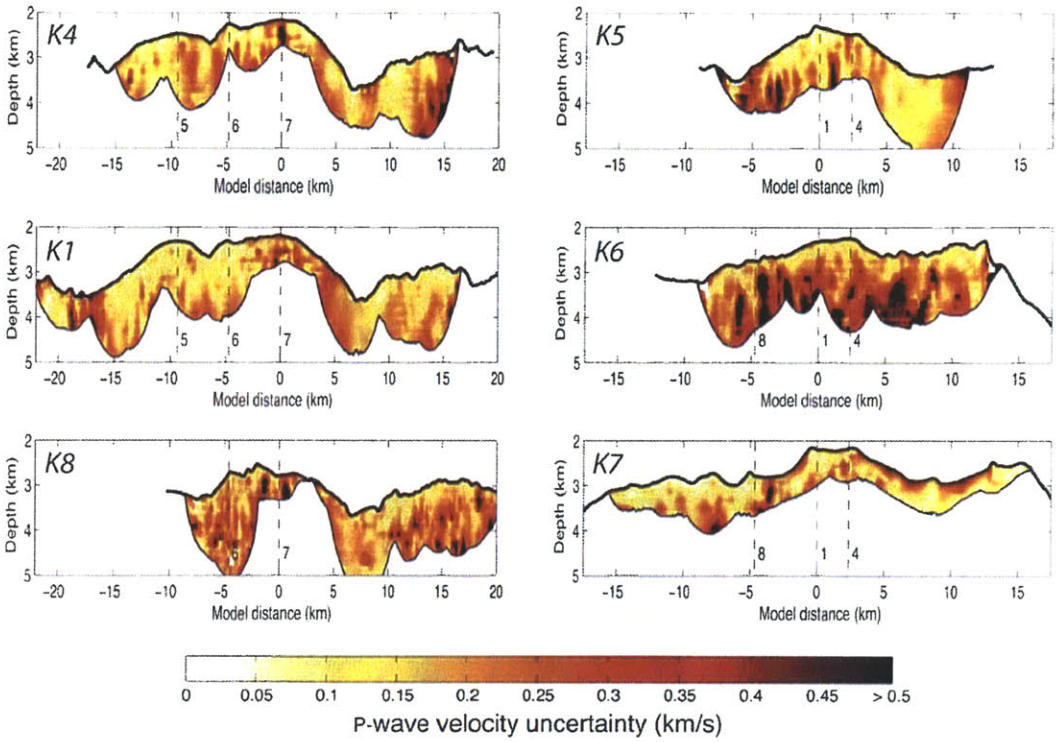

Figure 14. Results of *P* wave velocity uncertainty estimation. The bottom of all profiles is the maximum raypath depth of the corresponding final tomographic models (Figure 7). The estimated velocity uncertainty is approximated by the standard deviation of 100 Monte Carlo realizations. Note that the dominant velocity uncertainty is $\leq$0.3 km s^{-1}, although there are regions where the uncertainty can be as large as 0.4–0.5 km s^{-1} or even higher. Profile crossings are indicated by vertical dashed lines as in Figure 7.

structure. The southern part of profile K7 crosses a pair of domes east of Eve Dome, where intermediate V2 structure is present.

[27] Figure 13 compares velocity-depth profiles at intersection points of the strike lines and dip lines within the range of velocity uncertainties (Figure 14). Details of the velocity uncertainty estimation are given in section C2. With the exception of the structure at the intersection between profiles K1 and K5 in the upper 400 m, all of the other profiles agree with each other, considering the estimates of the velocity uncertainty (the locally large velocity uncertainty of profile K4 at its intersection with profile K7 is due to the inability of the modeling approach to accurately determine the magnitude of the high-velocity anomaly that characterizes this area (Figure 10)). Therefore we do not find in our results any convincing signal of seismic anisotropy that could be associated with aligned cracks [e.g., *Stephen*, 1981, 1985; *Dunn and Toomey*, 2001], mineral alignment, or lithology [e.g., *Miller and Christensen*, 1997; *Christensen*, 2004]. In places where intersecting profiles do not match, the discrepancy may be due, at least in part, to three-dimensional complexity and small-scale heterogeneity that cannot be captured and modeled with our 2-D approximations and assumptions.

5. Interpretation: Lithology-Velocity Correlation

[28] In this section, we use constraints provided by geological samples to interpret the seismic velocity structure of the Kane OCC in terms of dominant lithologies. We also use geological and seismic observations from other MAR OCCs [*Canales et al.*, 2008] to assist in this interpretation.

[29] The extensive suite of geological samples from the Kane OCC reported by *Dick et al.* [2008] and *Auzende et al.* [1994] (Figure 15) can

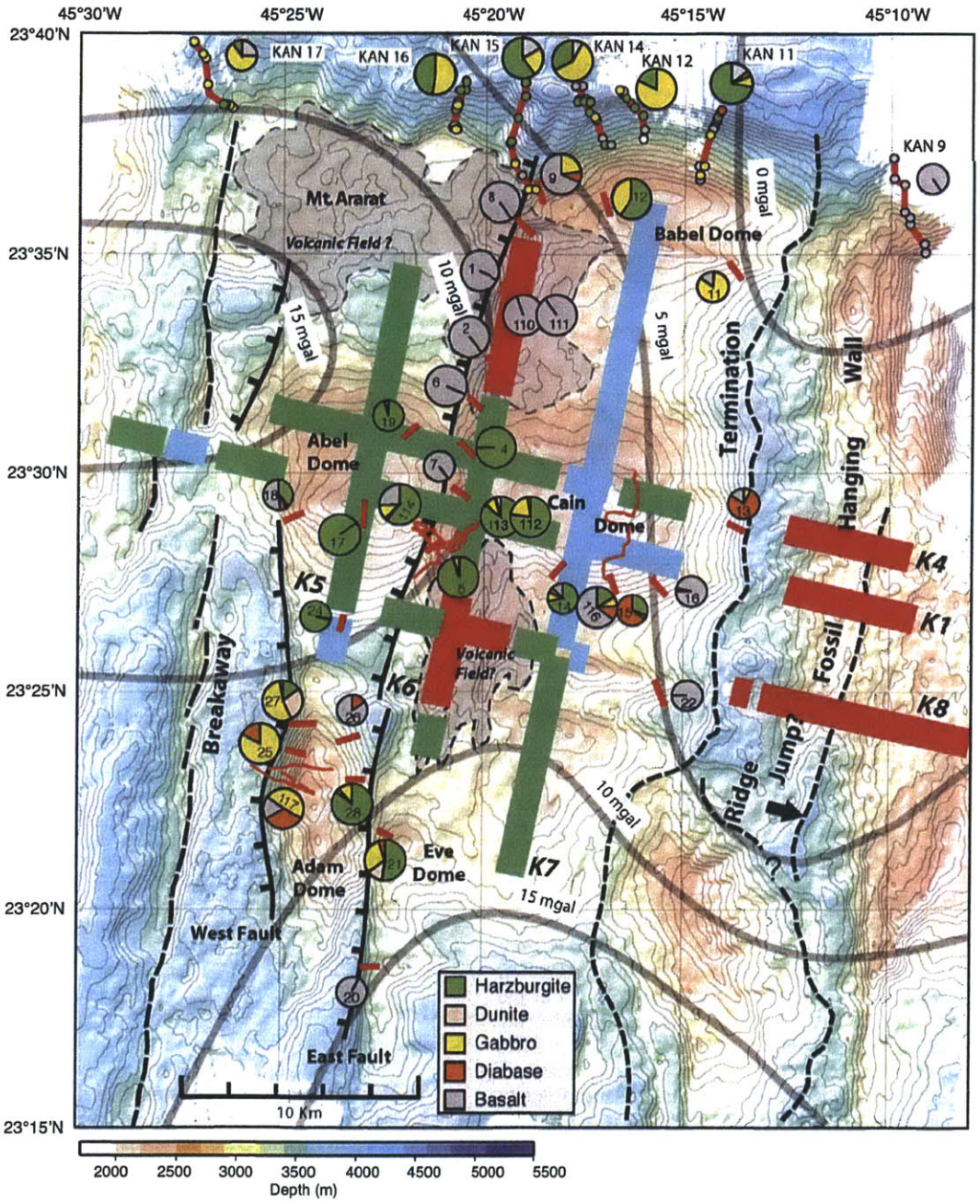
45°30'W
45°25'W
45°20'W
45°15'W
45°10'W
23°40'N
23°35'N
23°30'N
23°25'N
23°20'N
23°15'N
KAN 17
KAN 16
KAN 15
KAN 14
KAN 12
KAN 11
KAN 9
Mt Ararat
Volcanic Field ?
Babel Dome
0 mgal
10 mgal
15 mgal
5 mgal
Termination
Wall
Hanging
Abel Dome
Cain Dome
K5
K6
K7
K4
K1
K8
Fossil
Ridge Jump?
Volcanic Field?
Breakaway
Adam Dome
Eve Dome
West Fault
East Fault
10 Km
Harzburgite
Dunite
Gabbro
Diabase
Basalt
2000
2500
3000
3500
4000
4500
5000
5500
Depth (m)

Figure 15

be divided into (1) samples obtained from beneath the detachment surface on slide scar headwalls or high-angle fault scarps; (2) rock assemblages commonly associated with detachment shear zones, such as mylonites and serpentine schists, that may displaced along the fault and thus are not necessarily representative of the underlying bedrock; and (3) allochthonous debris clipped from the hanging wall or otherwise dispersed across the detachment surface. We rely here on the first type of samples, which consists of massive, partially serpentinized peridotites (Jason dives 112, 113, 114, dredges 4, 5, 12, 17, 21, 27, 28, and KANAUT dives 11, 14, 15 and 16), gabbros (Jason dives 116, 117, dredges 9, 12, 21, 25, 27, 28, and KANAUT dives 12, 14, 15 and 16), autochthonous pillow basalts (Jason dives 110, 111), and abundant pillow basalts obtained in dredges 1, 2, 6, 7, and 8 (Figure 15). In Figure 10, locations of bedrock samples are projected onto the seismic velocity profiles where the samples are within ~2 km of the profiles. This allows us to identify clear velocity-lithology correlations.

[30] The low velocities and velocity gradients (V1 structure) found along the northern part of profile K6 correlate systematically with pillow basalts that form a volcanic ridge along the crest of the footwall of East Fault in its northern part (Figures 7, 10, and 11). Comparable velocity structure occurs in the hanging wall on the three dip profiles. Although the hanging wall has not been sampled, it has irregular, hummocky morphology that is characteristic of volcanic terrain (Figures 1 and 15), and it therefore is likely to be dominantly volcanic rocks, possibly with sheeted dikes in the deeper part of the section. V1 structure is also found at the southern end of profile K6 and the western end of intersecting profile K8 where irregular, hummocky morphology suggests that a volcanic field is present [*Dick et al.*, 2008] (Figures 1 and 15). From all these correlations, it appears that portions of the profiles that are characterized by V1 structure represent dominantly volcanic rocks, plus or minus an uncertain component of underlying sheeted dikes.

[31] The mostly intermediate velocities and velocity gradients (V2 structure) across Abel Dome and the western part of Cain Dome correlate with massive outcrops of serpentinized peridotites (profiles K1, K5, and K6, Figures 7, 10, and 11). Thus we interpret these velocity characteristics to be associated dominantly with basement consisting of serpentinized peridotite.

[32] There are very few bedrock samples at the Kane OCC where class V3 dominates. However, the available samples support the interpretation of *Canales et al.* [2008] (based on drilling of 1415 m of gabbros at IODP Hole 1309D in Atlantis Massif OCC) that class V3 is associated primarily with gabbros (Figures 7, 10, and 11). V3 structure is prominent where profile K5 approaches Adam Dome, and both Jason dive samples and dredges show that this dome is dominantly gabbroic, with secondary sheeted dikes. Along profile K1, Jason Dive 116 sampled in-place, altered gabbros from basement exposed in a small scarp in the area of V3 structure over the crest of Cain Dome. At the northern ends of profiles K6 and K7, submersible samples from outcrops and dredge samples from scarps suggest a dominance of gabbros with lesser peridotites. Thus, we argue that the V3 structure observed beneath the crests of Babel and Cain Domes indicates a dominantly gabbroic composition, much as appears to be the case to the southwest at Adam Dome. One small body with V3 structure is located at the breakaway on profile K1; however, we do not know the along-isochron extent of this anomaly, and its size is at the limit of what we feel comfortable interpreting on the basis of our lateral resolution tests (see section C1 and Figure C1). Although the V3-gabbro correlation

Figure 15. Interpretation of upper basement composition along the Kane MCS profiles based on velocity characteristics (smoothed from Figure 7) and their lithologic correlations deduced in this paper. Along the profiles, red presents pillow basalts (±sheeted dikes), blue is dominantly gabbros, and green indicates serpentinized peridotites. Areas of significant size where velocity characteristics are uncertain (on the basis of the model assessment, Appendix C) are not included. Pie diagrams show lithologic proportions by weight of samples obtained from ROV/submersible dives and dredges on two cruises: KANAUT Expedition [*Auzende et al.*, 1994] and R/V *Knorr* cruise 180-2 [*Dick et al.*, 2008]; inset at bottom shows the key to lithology. The diagrams represent all samples including allochthonous debris. The larger pie diagrams show locations where at least part of the sample suite is known or is reasonably interpreted to represent true basement; see Figure 10 for identification of these samples, which are used to interpret velocity-lithology correlations. Tracks of Jason dives 110–117 and Nautile dives KAN 9–17 are shown in red; small colored circles along Nautile tracks show lithology at sample locations. Red bars locate dredge tracks. Gray contours are residual mantle Bouguer anomaly (RMBA) from *Maia and Gente* [1998]. Contour interval in the underlying bathymetry map is 100 m. Other features are as described in Figure 1.

appears to be good to a first order, we note that V3 zones may include other lithologies, notably peridotite, as indicated by rocks from dredge 12 and Nautile dives in the area of Babel Dome. Following this reasoning, it may be that some areas that have moderately elevated velocity but lack high-velocity gradient (e.g., the southern one third of profile K7, Figures 7, 10, and 11) could include a mixture of gabbros and serpentinized peridotites. Along the southern part of profile K6 (Figures 7 and 10), the more prominent differentiation of moderately high to moderately low velocities could similarly indicate interspersed peridotites, intrusives, and volcanics on scales of a few kilometers or less.

6. Discussion

6.1. Variations in Velocity Structure

[33] We have attributed observed lateral variations in velocity structure primarily to lithological composition, but other contributing factors are possible. For example, the observed variations in *P* wave velocity might be due to lateral changes in porosity within a single type of lithology [e.g., *Wilkens et al.*, 1991; *Berge et al.*, 1992]. In basalt saturated with pore fluid (brine), a velocity change of ~2 km s^{-1} (i.e., the average variation observed along our dip profiles, Figures 7 and 10) could be explained by ~3–15% change in porosity; this assumes a bulk modulus of 95.0 and 2.44 MPa, shear modulus of 42.0 and 0.0 MPa, densities of 3.0 and 1.023 g cm^{-3}, for matrix (basalt) and inclusions (brine), respectively, and an aspect ratio of the inclusions of 0.01–0.1 [*Kuster and Töksoz*, 1974]. Such variations in porosity are not unusual [e.g., *Wilkens et al.*, 1991], and they have been proposed to explain the documented increase in seismic velocity of the upper oceanic crust with age [*Houtz and Ewing*, 1976] as pore spaces are filled with mineral precipitates and alteration products [*Carlson and Herrick*, 1990; *Grevemeyer and Weigel*, 1997]. One might expect that changes in velocity due to fractures and alteration would show some correlation with tectonic context, with lower velocities expected near the presumably more tectonized northern end of the paleospreading segment bounding the Kane FZ than near the center of the segment [e.g., *Minshull et al.*, 1991; *Detrick et al.*, 1993; *Canales et al.*, 2000b]. However, we do not find clear evidence for this, as structure along strike profiles is more homogeneous than along dip profiles (Figure 10). Thus, we know of no reasonable explanation for how such lateral, multikilometer-scale porosity variations would develop in the Kane OCC basement if it were of uniform composition.

[34] If porosity changes do influence the observed seismic velocity structure, they most likely are closely linked to the lithological changes already described. For example, the velocity gradient found in the shallow part of areas characterized by V3 structure can be interpreted as resulting from a highly fractured thin uppermost layer of gabbros that has porosity rapidly decreasing with depth. This effect could also be present in serpentine-dominated areas characterized by V2 structure, although a significant degree of serpentinization would also reduce velocities so that the velocity gradient of class V2 is lower than in V3 regions.

[35] Are the velocity-lithology relationships that we have described reasonable? Although the elastic *P* wave velocities of intact, relatively unaltered, saturated samples of oceanic basalts range from approximately 5 to 6 km s^{-1} [*Johnson and Semyan*, 1994], *P* wave velocities of the uppermost oceanic crust measured in situ by seismic refraction are as low as 2.2 km s^{-1} at near-zero age [*Purdy and Detrick*, 1986; *Harding et al.*, 1989; *Vera et al.*, 1990]. Our V1 velocity class, assigned to basalts (±dikes), falls well within the range noted above. To a first order, observed velocities in the lower part of this range can be taken as a reasonable indicator of the presence of basalts rather than serpentinized peridotites and gabbros.

[36] For intact samples of gabbro and serpentinized peridotite cored from the MARK area, laboratory-measured *P* wave velocities at appropriate confining pressures range from 6.7 to 7.4 km s^{-1} for gabbros, and from 4.7 to 6.8 km s^{-1} for fully serpentinized and ~30%-serpentinized peridotite [*Miller and Christensen*, 1997]. These velocities are at the high end of the range of velocities that we observe at the Kane OCC. However, our refraction data sample large volumes of rock that are permeated by fractures and other porosity with varying geometry, so it is to be expected that the refraction velocities will be lower (perhaps significantly lower) than velocities measured on intact laboratory samples. This effect is clearly illustrated by velocity measurements of gabbros in the upper part of IODP Hole 1309D in the Atlantic Massif OCC, where meter-scale sonic log velocities and kilometer-scale refraction velocities are ~5–6 km s^{-1} [*Canales et al.*, 2008], much lower than the 6.7–7.4 km s^{-1} velocities measured on laboratory samples. It should be noted that the lack of solid-rock integrity at seismic scales probably can also

reduce velocities of serpentinized peridotites well into the range of basalt velocities; *Canales et al.* [2008] found that the upper part of the well sampled serpentinite edifice at the south edge of Atlantic Massif OCC produced refraction velocities of only ~3.5–4 km s^{-1}.

[37] The above considerations demonstrate that the velocity-lithology relationships we have proposed are entirely reasonable. However, it is also clear that refraction velocities do not uniquely define rock type in OCC settings, so it is important that the scales and limits of the correlations be tested by future sampling in as much detail as possible. Future constraints can also be imposed by independent parameters such as V_P/V_S ratio.

[38] Up to this point we have discussed lateral variations defined by apparently robust velocity, velocity gradient, and lithologic correlations within the upper ~0.5 km of the OCC. Vertical variations in the deeper record are more difficult to evaluate. To a first approximation, it seems reasonable to assume that areas with shallow V2 signature together with a low velocity gradient at deeper levels are likely to be peridotites with progressively decreasing serpentinization to the full depth of our observations. If this is correct, it implies that substantial serpentinization can occur to depths of at least 1.5 to 2 km. For example, observed 6 km s^{-1} velocities at 1.5 km depth below Abel Dome (Figure 7) would imply ~60–65% serpentinization, on the basis of the measurements of *Christensen* [2004]. Elsewhere, it also seems reasonable to interpret high-velocity, high-(vertical) gradient zones within this presumed "serpentinite matrix" as the upper margins of gabbro plutons, just as V3 characteristics correlate to gabbros in the shallow section. In this context, prominent, irregular deep structure, as for example in profile K6 at and south of Cain Dome, and beneath the hanging wall in profile K8, may indicate gabbro bodies with sizes on the order of ~2km or less (Figure 7).

6.2. Seafloor Morphology, Rock Samples, and Subseafloor Geology

[39] We observe a consistent and apparently robust correlation between subseafloor velocity characteristics and lithology of samples that are either documented, or highly likely, to be from intact basement outcrops along high-angle fault scarps and slide scars. These samples commonly represent only a small fraction of recovered rocks (Figure 15), which emphasizes the well known difficulty of interpreting basement composition from surficial rock assemblages, particularly those obtained in dredges. Seismic observations such as those reported here, constrained by bedrock lithology determined at high-angle fault scarps or slide scars, are potentially a very useful tool for assisting geological mapping outside the often very limited areas where bedrock sampling is possible.

[40] An important result of our analysis is that the morphology of individual domes on the Kane OCC cannot be uniquely associated with any particular lithology. For example, Abel and Cain Domes, although separated by East Fault, exhibit morphologic continuity in terms of shape, size, and style of corrugations, even though Abel Dome and western Cain Dome are predominantly serpentinized peridotite, whereas the central part of Cain Dome is dominantly gabbro. This morphologic continuity implies that, once established, the form of a detachment fault surface may be very persistent despite changes in pattern of magmatism.

6.3. Relation of Gravity Anomalies and Velocity Structure

[41] Gravity studies show elevated residual mantle Bouguer anomalies (RMBA) over most of the Kane OCC [*Morris and Detrick*, 1991; *Ballu et al.*, 1998; *Maia and Gente*, 1998], indicating relatively high lithospheric densities that are commonly interpreted as thinned crust [e.g., *Tucholke et al.*, 1998]. There is a reasonable correlation between seafloor sample lithology and RMBA pattern [*Cannat et al.*, 1995a; *Dick et al.*, 2008], and we find that the RMBA is also generally consistent with the subseafloor velocity structure (Figures 15 and 16). However, such correlations should be viewed with the caveat that RMBA represents lithospheric structure at much lower resolution and deeper levels than seafloor samples and shallow velocity structure do. Elevated RMBA occurs over Abel Dome to western Cain Dome where V2 velocity structure indicative of serpentinized peridotite predominates. Elevated RMBA also occurs over the southern part of the OCC both at and southeast of Eve Dome where moderate velocities (profile K7, Figure 7) might indicate a mixture of gabbros and peridotites. Reduced RMBA occurs over Babel Dome, the central to eastern parts of Cain Dome, and Adam Dome where there is geological evidence of gabbroic plutons, where V3 velocity structure occurs (Figure 15), and where the highest velocities generally are observed (Figure 16). The lowest RMBA occurs east of the detachment termination

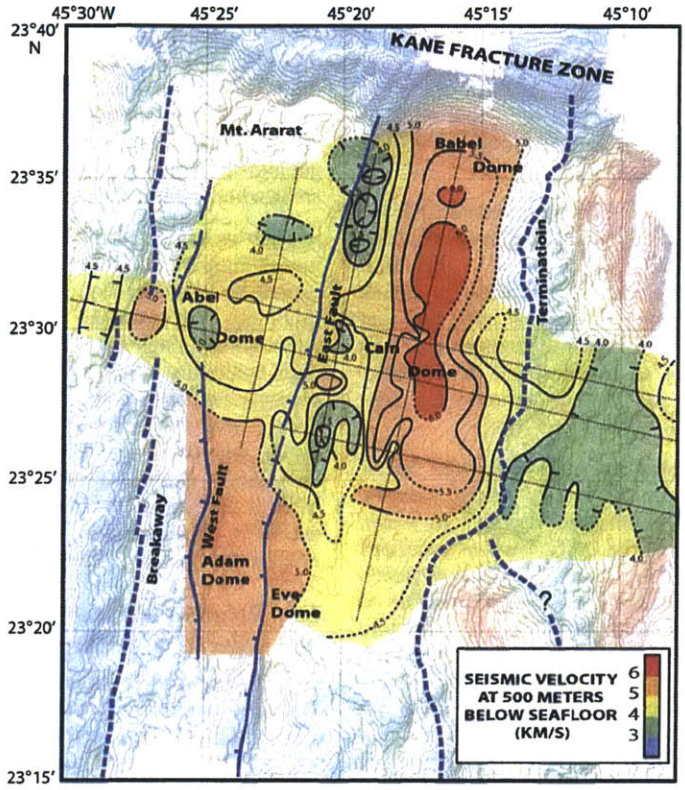

Figure 16. *P* wave isovelocity contours (interval 0.5 km s^{-1}) at 500 m below seafloor superimposed on bathymetry and simplified tectonic interpretation. Contours are dashed in unconstrained regions. Velocity in the area of Adam Dome is speculative and is inferred from gabbroic composition of basement demonstrated by geological sampling (Figure 15). Seismic profiles are shown as thin dotted lines.

over the volcanic hanging wall where V1 structure is present.

[42] Although the above correlation appears to be meaningful, it is the reverse of what would be expected in the V2 and V3 provinces (i.e., higher RMBA, and therefore higher density, such as is observed over exhumed mantle in the V2 region, would be expected to correlate with the highest velocities). This discrepancy may be explained by serpentinization of peridotites at shallow levels. Our seismic data only sample the uppermost lithosphere and therefore appear to be dominated by the velocity-reducing effects of this alteration, whereas unaltered, high-velocity mantle peridotite certainly lies at somewhat greater depths in the V2 region. The gravity effect of this deeper, high-density rock probably explains the elevated long-wavelength RMBA anomaly, despite the reduced density and velocity of serpentinized peridotite that is sampled at shallow levels. It will be necessary to achieve larger source-receiver offsets using either longer streamers or ocean bottom seismometers to resolve the depth of the transition to unaltered mantle.

6.4. Magmatism During the Evolution of Kane OCC

[43] Our lithological interpretation of the seismic profiles (Figure 15) indicates that there is marked variability in the shallow spatial distribution of gabbroic intrusions, serpentinized peridotites, and basalts over the Kane OCC at lateral scales of a few kilometers to >10 km. Here we discuss interpretation of magmatic conditions at the spreading axis as the Kane OCC formed and evolved. We note that our tomography models are only valid for the uppermost (<2 km) section of the lithosphere exhumed along the Kane detachment fault; there-

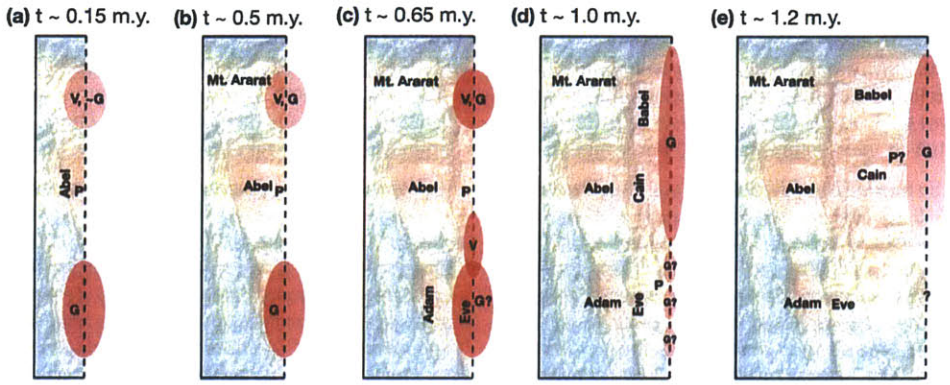

Figure 17. Schematic illustration of the temporal pattern of magmatism and/or exhumation of gabbro bodies during the evolution of the Kane OCC, inferred from lithological interpretation of the seismic profiles and basement samples (Figure 15) and from seafloor morphology. Note that the times of gabbro exposures are only minimum ages for emplacement because the gabbros could have been intruded many kilometers below the spreading axis. Plots show times following initiation of the Kane detachment fault. V and G refer to volcanics and gabbro, respectively, and P indicates peridotite. Pink and red ellipses indicate weaker and stronger magmatism that affected the footwall. See section 6.4 for discussion.

fore the following interpretation assumes that relative lateral changes in intrusive activity (or lack thereof) deeper in the lithosphere are similar to those inferred from the structure of the shallow lithosphere, an assumption that may not be valid if a significant proportion of melt is retained in mantle [e.g., *Lizarralde et al.*, 2004]. Also, we assume that lateral (i.e., temporal and spatial) changes in magmatism represent variations in melt supply to the ridge axis, but they could also represent changes in the efficiency of melt extraction from the mantle.

[44] We include interpretations made by *Dick et al.* [2008] based on geological sampling, particularly where we lack seismic constraints. Most importantly, our results allow us to expand the model of *Dick et al.* [2008] to areas where we have good seismic coverage but where there is limited geological sampling of bedrock in the footwall; this is particularly helpful for the younger (i.e., eastern) parts of the Kane OCC where sampling is limited to fault-rock assemblages and allochthonous debris scattered across the detachment surface (Figure 15).

[45] It is important to note that the time of exhumation of the plutonic igneous rocks at the seafloor gives only a minimum age for their intrusion because they could have been emplaced at a significant depth beneath the spreading axis [e.g., *Schwartz et al.*, 2005; *Grimes et al.*, 2008]. Conversely, the age of the lithosphere on which volcanics appear provides a maximum age for those rocks, which could have been extruded at any time after that lithosphere was exhumed.

6.4.1. Early Stages of OCC Formation

[46] The detachment fault that exhumed the Kane OCC initiated at ~3.3 Ma. Along the northern 2/3 of the enclosing spreading segment, this fault formed the western wall of the MAR rift valley and probably constituted the sole plate boundary while the OCC was being emplaced. Results from dip profiles K1 and K4 indicate that exhumation of peridotite commenced within ~2 km of the breakaway in the central part of the OCC as Abel Dome was being formed (Figure 15), although a narrow high-velocity zone at the breakaway in profile K1 might represent a small gabbroic body there (Figure 7). Thus this part of the Kane detachment fault initially cut through thin crust and to an uncertain depth into mantle in an area that had been experiencing relatively low magma supply (Figure 17a).

[47] To the north of Abel Dome we have no seismic control along strike near the breakaway zone, but samples from the southern wall of the Kane TF suggest that gabbros at least several hundred meters thick are present below the likely volcanic carapace of Mt. Ararat [*Auzende et al.*, 1994; *Dick et al.*, 2008] (Figures 15 and 17a). To the south of Abel Dome, geological samples [*Dick et al.*, 2008] and the southern end of profile K5

also indicate that robust magmatism emplaced gabbros beneath Adam Dome within ~4 km of the breakaway. Thus both north and south of Abel Dome the detachment fault appears to have reached gabbros at relatively shallow depths, which resulted in early exhumation of these rocks.

[48] Exhumation of peridotites continued for ~0.5–0.65 Myr in the central part of Kane OCC as Abel Dome and the western side of Cain Dome were emplaced (Figures 17b and 17c). Exhumed magmatic sections during this period remained focused at centers to the south in the area of Adam and Eve Domes and probably to the north in the area of Mt. Ararat. Corresponding bathymetric highs in volcanic, conjugate crust substantiate the interpretation that these were magmatically active zones [*Dick et al.*, 2008]. In the northern area, magmatism appears to have increased about ~0.65 Myr after breakaway, producing thick gabbro sequences that begin near East Fault and are exposed along the northern side of Babel Dome [*Dick et al.*, 2008] (Figure 17c).

[49] Although it is possible that there was robust magmatism in the intervening area of Abel and Cain Domes where peridotites have been sampled, but that the igneous section was removed in the hanging wall, this seems unlikely for two reasons. First, conjugate crust on the east flank of the MAR has deeper bathymetry in this zone, which suggests more limited magmatism. Second, this scenario would require that the detachment rooted below the gabbro-peridotite transition in the area of Cain and Abel Domes; thus, gabbro remnants from the hanging wall should be scattered across the exposed detachment fault surface, but this is not observed [*Dick et al.*, 2008]. To resolve this question more fully, it will be necessary to obtain seismic constraints on conjugate crust on the African plate.

6.4.2. Late Stages of OCC Formation

[50] The lithosphere that was exhumed about 1.0 Myr after breakaway shows a significant change in the distribution of magmatic crust, relative to the distribution of gabbro bodies observed in areas exhumed prior to that time (Figure 17d). Lithosphere of Babel Dome was affected by robust magmatism, as indicated by V3 seismic structure that we interpret as representing gabbro plutons along the northern part of profile K7 (Figures 7 and 15). However, the same structure occurs along strike to the south, which indicates that similar magmatism affected lithosphere exhumed in the central part of Cain Dome (Figure 16). It is uncertain whether the large along-strike extent of this zone (20+ km) resulted from southward propagation of magma from Babel Dome, or whether a separate magmatic center at Cain Dome became linked to that of Babel Dome (Figure 17d).

[51] Significantly lower (albeit still relatively high) velocities are associated with V2 velocity structure farther south along profile K7 to the east of Eve Dome (Figure 7). We suggest that these may be a mixture of gabbros and serpentinized peridotites, which implies that magmatism affecting the lithosphere exhumed in this area was reduced compared to that both to the north and at the older Adam Dome.

[52] Velocity characteristics in the youngest part of the footwall, ~2.2–2.1 Ma, may revert to V2 structure in the dip lines over Cain Dome and the saddle to the south of the dome (Figure 7), although this is uncertain because lateral resolution is decreased (Figure C1) and velocity uncertainty (Figure 14) is increased in this zone. If V2 structure is indeed present there, it suggests that the last lithosphere exhumed in the central part of the Kane OCC was not affected by significant magmatism and that serpentinized peridotite was once again being unroofed there (Figure 17e). We have no velocity control to the north of the youngest part of Cain Dome, but samples from KAN dive 11 along the northeast margin of Babel Dome imply that that part of the footwall continued to be intruded by gabbros [*Dick et al.*, 2008]. There are no velocity or sample constraints for the last part of the footwall exhumed to the south of Cain Dome.

[53] The detachment fault that exhumed the Kane OCC was abandoned at about 2.1 Ma when an eastward "ridge jump" occurred, i.e., when a new normal fault formed farther into the rift valley and captured a segment of the hanging wall from the African plate. The distance over which this jump occurred is unclear from available magnetic data, but it probably captured at least 4–5 km of the hanging wall in the dip direction (Figure 1). The distribution of depth along this captured hanging wall provides further insight into the along-strike state of magmatism in the last stage of OCC exhumation, and it appears to be consistent with observations noted above. The hanging wall is elevated adjacent to Babel Dome which, as noted above, appears to have been affected by late stage magmatism. In contrast, the hanging wall is deeper adjacent to Cain Dome where peridotite may have been last exhumed. The southern 1/3 of the fossil

hanging wall is still deeper; this could indicate that the nearby footwall was devoid of magmatic products, although there is an intervening large edifice at 23°20′N, 45°15′W that presently is unexplained, and this makes such an interpretation uncertain.

[54] It is commonly presumed that at slow spreading segments melt delivery from the mantle is focused at segment centers [*Whitehead et al.*, 1984]. While this may be the norm in many cases [*Lin et al.*, 1990], the compositional heterogeneity that we document across the Kane OCC demonstrates that there was strong spatial and temporal variability in magmatism along at least 2/3 of the northern MARK segment, and at least within the shallow lithosphere (~0.5–2.0 km). The variability occurs at spatial scales of less than a few kilometers to >10 km and at temporal scales of several hundred thousand years. Notwithstanding the spatial (lateral and vertical) limitations of our study, our results therefore suggest that magmatism was not focused at the segment center, and at times it was most robust at the northern segment end near the cold transform wall where magma supply commonly is thought to be limited [e.g., *Cannat et al.*, 1995a].

6.4.3. Surficial Volcanism

[55] Hummocky seafloor morphology typical of volcanic terrain is observed in the area of Mt. Ararat and eastward to the northern part of East Fault, as well as around East Fault to the south of Cain Dome (Figure 1). Jason dives along the northern part of East fault show that this morphology correlates with in situ pillow basalts [*Dick et al.*, 2008]. The time at which these volcanics were emplaced is unclear, but their spatial association with East Fault suggests that the magma was extruded along the fault during exhumation of the detachment footwall [*Dick et al.*, 2008]. Rotation of the footwall can result in bending-related normal faulting, with compression in lower part of the plate and extension in upper part, and this stress differential could force melts from the lower part into the upper part of the footwall [*Tucholke et al.*, 2001]. The low velocities observed along the northern part of East Fault in profile K6 indicate that the basalts emplaced there may have a thickness of a kilometer or more (Figure 7). The region of low velocities thickens toward the northern end of the profile, suggesting that the most extensive magmatism was near the transform wall; this is consistent with the development or enhancement of a northern magmatic center beginning ~0.65 Myr after breakaway (Figures 17c and 17d).

6.5. Implications for the Origin and Evolution of OCCs

[56] The recovery of predominantly gabbros in three deep holes thus far drilled in OCCs [*Dick et al.*, 2000; *Kelemen et al.*, 2004; *Blackman et al.*, 2006] and the consistent presence of gabbros near the termination of the Kane, Atlantis Massif, and Dante's Domes OCCs inferred from velocity models [*Canales et al.*, 2008] indicates that understanding the origin of the gabbro plutons is a key step toward understanding how OCCs form and evolve [*Ildefonse et al.*, 2007]. *Canales et al.* [2008] discussed three possible scenarios:

[57] 1. Detachment faulting was initiated by intrusions. A detachment fault may nucleate at depth where strain localizes around the margins of gabbro plutons intruded into peridotite [*Ildefonse et al.*, 2007; *Tucholke et al.*, 2008].

[58] 2. Intrusions were stimulated by detachment faulting. Following initiation of the detachment, intrusion of the plutons was stimulated, or enhanced, by decompression melting in the rapidly exhuming footwall.

[59] 3. Detachment faulting and intrusions are independent. The gabbros were intruded into the footwall as it was exhumed because of natural variability in the magmatic cycle (or variations in mantle fertility).

[60] Our detailed study of the Kane OCC provides some constraints on the first two hypotheses.

[61] In the first scenario, sufficient slip on the detachment may eventually exhume the gabbro pluton around which the fault nucleated. In the instance of the Kane OCC, the distance from breakaway to the gabbros ranges between about 12 and 18 km, depending on where the gabbro margins are defined in the velocity models along our dip lines (Figure 7). Therefore if the detachment initially dipped at ~45° (a reasonable dip according to Andersonian fault theory), it would have had to cut to ~10–13 km depth to reach the gabbros. If the fault dipped more steeply it would have to cut to greater depth.

[62] Microearthquake studies along the MAR axis [*Toomey et al.*, 1988; *Kong et al.*, 1992; *deMartin et al.*, 2007] indicate that detected seismicity extends only to ~7–8 km subseafloor depth, shallower than the above projected depth for the Kane detachment. However, the microearthquake studies are only short-term samples of longer-term brittle deformation of the lithosphere, and it may be

that long-term brittle deformation extends to greater depths. It is also possible that deep deformation associated with a detachment is largely ductile and thus is aseismic. Thus the idea that the Kane detachment nucleated on deep gabbro plutons in the mantle is not unreasonable.

[63] In the second scenario, the resultant unloading of the footwall as it was rapidly exhumed at the full spreading rate of ~23 mm/a, together with increased advection of heat [*Tucholke et al.*, 2008], may have stimulated decompression melting within the footwall [*Canales et al.*, 2008]. The possibility that serpentinized peridotite (V2 velocity structure) is present in the youngest part of the Kane OCC (dip lines K1, K4 and K8, Figures 7 and 15) would seem to argue against this mechanism, because we might expect that such melting would persist until the Kane detachment was finally abandoned. However, it is possible that refractory mantle was exhumed during the last stage of OCC formation and thus that melt generation was attenuated.

[64] At present, it is difficult to determine which of the above scenarios (or combination thereof) best explains the distribution of gabbros in the Kane OCC. Three kinds of future studies will provide important constraints. First, more complete coverage of seismic data, particularly near the breakaway, will help to resolve the distribution of likely gabbro bodies and thus determine the potential that the Kane detachment initially nucleated on deep intrusions. Second, age data on zircons in gabbros sampled from the footwall will help constrain the time at which the intrusions were emplaced, relative to the time of exhumation [e.g., *Baines et al.*, 2008; *Grimes et al.*, 2008]. Finally, drilling to obtain samples of peridotite from below the detachment shear zone will help to resolve questions about the fertility of the mantle that was exhumed in the footwall.

[65] Uninterrupted dip of Kane OCC surface corrugations at the contact with the hummocky fossil hanging wall shows that termination of slip on the detachment was accomplished by an eastward jump of the plate boundary (Figure 1). Reduced RMBA gravity east of the termination indicates that crust is thicker there, so there presumably was increased magmatism and heat in the axial lithosphere that stimulated the jump and the abandonment of the Kane detachment fault [*Canales et al.*, 2008]. By considering maximum and minimum ages for emplacement of the gabbro body under Cain Dome, we can place bounds on the time interval between that emplacement and the renewed magmatism and ridge jump at ~2.1 Ma. The earliest emplacement of the Cain gabbros would have been at 3.3 Ma (scenario 1, above), and the latest possible emplacement would have been when the western edge of the gabbros began to be exhumed from beneath the hanging wall, ~2.5 Ma. Thus the interval between the two magmatic pulses was at least 0.4 Myr but less than 1.2 Myr, although it most likely was in the higher part of the range (i.e., the Cain Dome gabbros were intruded when the footwall was well beneath the hanging wall).

7. Conclusions

[66] On the basis of interpretation of our seismic velocity models in conjunction with geological samples from the Kane OCC basement, we make the following conclusions.

[67] 1. We have successfully acquired and modeled long-offset MCS data over the relatively smooth and shallow surface of Kane OCC and have demonstrated that velocity structure can be reasonably correlated to basement lithology where appropriate in situ samples are available. This indicates that multichannel seismic reflection/refraction with a long streamer can be a powerful tool to constrain the shallow distribution of dominant lithologies within oceanic core complexes.

[68] 2. Two-dimensional traveltime tomography models reveal significant lateral variations in *P* wave velocity within the upper ~0.5–2.0 km of the lithosphere beneath the Kane OCC. The variations correlate to first order with lithologic variations in basement documented by in situ basement samples. With very limited exceptions, observed velocity characteristics fall into three categories: V1, low near-seafloor velocities (<3.4 km s^{-1}) and vertical velocity gradients (<~1 s^{-1}) at shallow levels; V2, intermediate shallow velocities (~3.4–4.2 km s^{-1}) and velocity gradients (1–3 s^{-1}); and V3, high shallow velocities (>4.2 km s^{-1}) and velocity gradients (>3 s^{-1}). Correlation with basement samples suggests that these velocity characteristics correlate predominantly with volcanics (±sheeted dikes), serpentinized peridotite, and gabbro, respectively. The observed distribution of V2 characteristics implies that serpentinization can extend deeply (>1.5 km) into the mantle.

[69] 3. The large-scale corrugated morphology that defines domes on the Kane OCC is not a good indicator of dominant basement lithology. A prime example is Abel and Cain domes, which are nearly

identical morphologically and lie in tandem along the same detachment slip line, but which have very different seismic structures that are representative of serpentinized peridotites and gabbros.

[70] 4. The detachment fault that formed the Kane OCC initiated at ~3.3 Ma and terminated at ~2.1 Ma. Within the exhumed footwall the velocity/lithology data document heterogeneous distribution of gabbroic intrusions, serpentinized peridotites, and volcanics at lateral scales of several kilometers to >10 km. Magmatism was not focused at the center of the enclosing spreading segment, as has been interpreted for some slow spreading ridge segments [*Dick et al.*, 2008].

[71] 5. Magmatism initially affected the northern and southern parts of the Kane OCC, while peridotites were exhumed in the central section. Within about 1 Myr after detachment faulting initiated, extensive gabbros were exhumed in the central to northern part of the OCC, with the southern part apparently affected by an intermediate level of magmatism. Within the last ~0.2 Myr of OCC formation, gabbros probably continued to be exhumed in the northern section up to the Kane transform wall, but peridotites probably were again exhumed in the central section; composition of basement in the southern part of the OCC at this time is uncertain.

[72] 6. A major, west facing high-angle normal fault (East fault) cuts the detachment surface along-isochron in the center of the Kane OCC and is associated with low seismic velocities and velocity gradients representative of volcanic rocks. We suggest that extrusion of the volcanics was facilitated by the stress differential between the upper and lower parts of the bending footwall as it was exhumed.

Appendix A: Details of Data Acquisition

[73] The seismic data employed in this study were recorded on a 6-km-long, 480-channel Syntron digital hydrophone streamer towed at a nominal depth of 10 m. Hydrophone group (i.e., receiver) spacing along the streamer was 12.5 m. The seismic source was a 10-element tuned air gun array with a total volume of 51L (3100 in^3) triggered by distance every 37.5 m and towed at a nominal depth of 8 m. Data were recorded in 10-s long records at a sampling rate of 4 ms. Positions of sources and receivers were derived from shipboard and tail buoy GPS receivers and compass-enhanced DigiCourse birds placed along the streamer.

Appendix B: Selecting a Starting Model and Inversion Parameters

[74] Figure B1a shows an example of how we selected the starting model for profile K4. First we calculated traveltimes for different starting models, with seafloor velocities ranging from 2 to 6 km s^{-1} at 0.2 km s^{-1} intervals, and vertical velocity gradients ranging from 0.5 to 3 s^{-1} at 0.25 s^{-1} intervals, and we identified the pair of parameters resulting in the lowest χ^2. Then we refined our starting model search in the vicinity of these parameters using a narrower range of seafloor velocities and vertical velocity gradients and chose the best 1-D model as the one that resulted in the smallest χ^2 (Figure B1a). The best 1-D models for all lines are shown in Figure B1b. All of the best 1-D models are similar to one another except for profile K7, which shows much higher seafloor velocity than the other five profiles. To make our results easier to compare between lines, we chose the average of the six best 1-D models as our preferred starting model for all six lines (Figure B1b). This averaged starting model has a velocity of 3.7 km s^{-1} at the seafloor and a vertical gradient of 1.75 s^{-1}; this is referred to simply as the starting model.

[75] To find the optimal inversion parameters for each profile, we ran inversions with different values of the damping parameter λ and calculated after each iteration the χ^2 for individual profiles (Figure B2). We selected the damping parameter λ as the one resulting in χ^2 as close as possible to 1.1 with the least number of iterations. After two iterations, profiles K1 (λ = 10), K4 (λ = 18), K5 (λ = 18) and K7 (λ = 30) achieve an acceptable statistical fit to the data, while data from profiles K6 and K8 (λ = 6) can be statistically fit after four iterations. For vertical smoothing we used s_z = 0.075 in all of the inversions; results were not significantly sensitive to values of $s_z < 0.075$, while larger s_z values resulted in large χ^2 misfits.

Appendix C: Model Assessment

C1. Lateral Resolution Tests

[76] The ability of the data to resolve lateral velocity variations can be assessed by performing corrugation tests [e.g., *Calvert et al.*, 2003; *Zelt et*

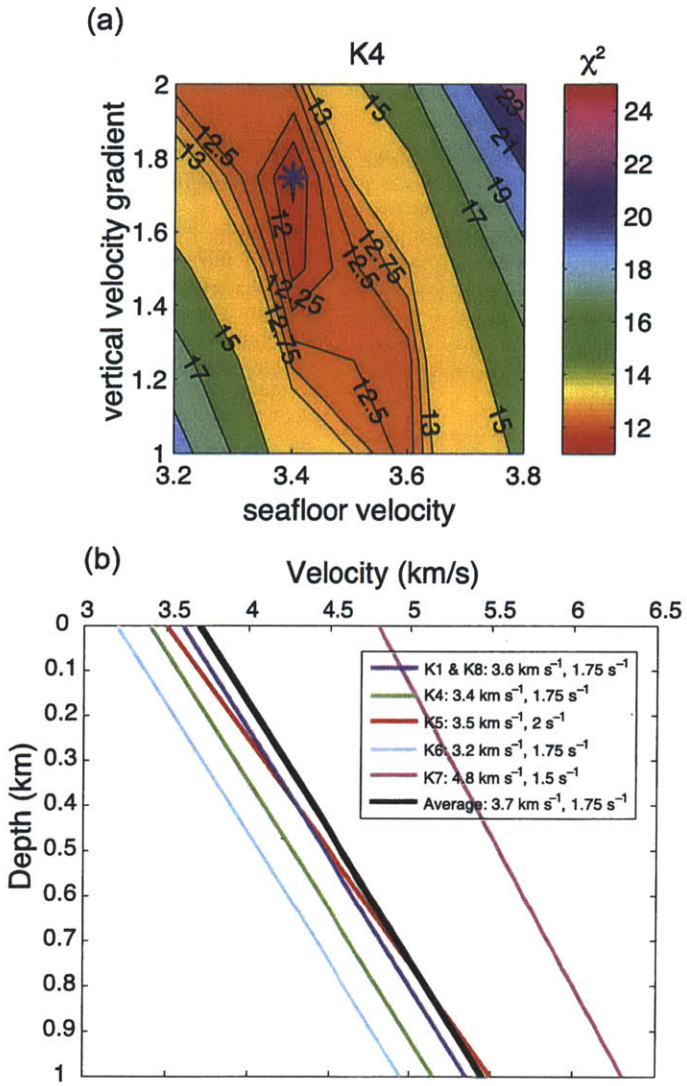

Figure B1. (a) Contour of traveltime residuals χ^2 (after one iteration) calculated for profile K4 using different seafloor velocities and vertical velocity gradients. The asterisk shows the best starting model that minimizes the traveltime residuals. (b) Best starting models for all six profiles are shown by colored lines, with the average model used for tomographic inversions shown in black. Note that all the best starting models are similar except for profile k7, which shows much higher seafloor velocity than the other profiles.

al., 2004], which are the 1-D equivalent of 2-D checkerboard tests commonly used in tomographic problems [*Zelt and Barton*, 1998]. In the corrugation test, a velocity anomaly pattern consisting of fixed width, vertical columns of alternating positive and negative anomalies were added to the initial model (Figure B1b) to create a perturbed velocity model. We varied the amplitude of the anomalies laterally by ±0.5 km s^{-1}, following a sinusoidal function. Synthetic first-arrival traveltime data were generated using the perturbed velocity model and the same source-receiver geometry as for the real data. We added random Gaussian noise to the synthetic traveltime gradients, $N(0, \sigma =$ 30 ms km^{-1}), following the method of *Zhang and Toksöz* [1998]. The synthetic data were then

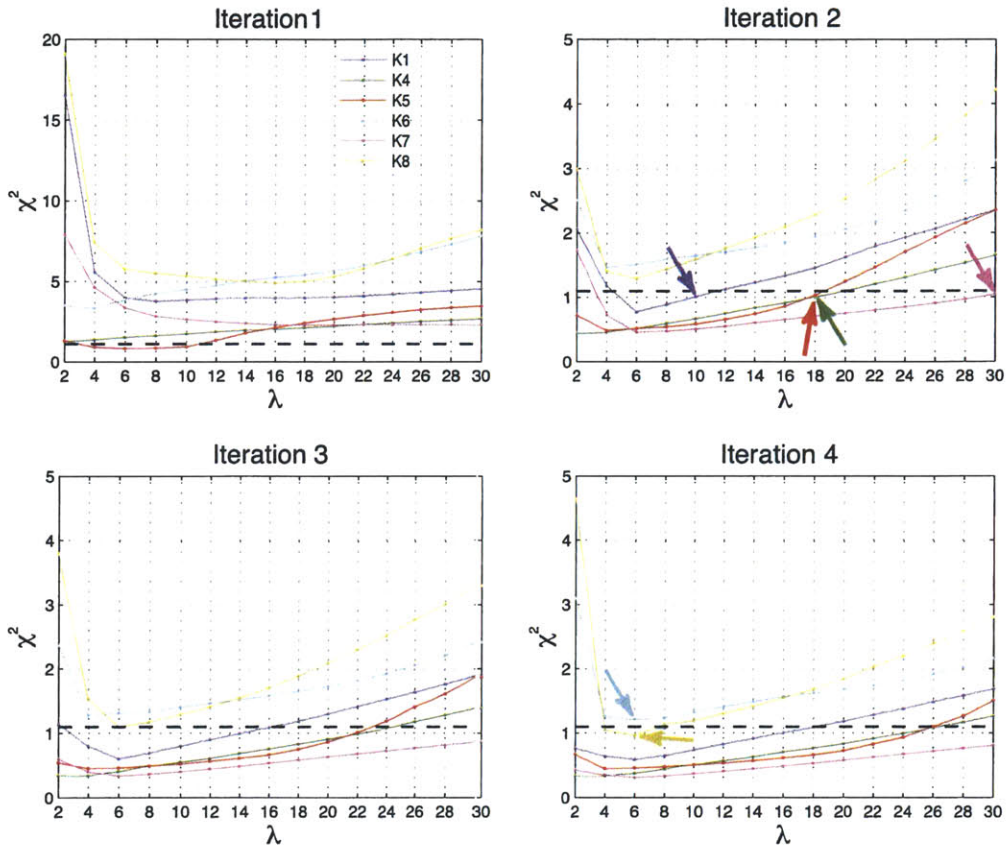

Figure B2. Variation in misfit function χ^2 between observed and predicted traveltimes as a function of damping parameter λ, for four inversion iterations. Colored arrows indicate the preferred solutions used for the tomographic inversion for each profile. Horizontal dashed black line corresponds to $\chi^2 = 1.1$, the adopted threshold value for the misfit function.

inverted following the same tomographic procedure used for the real data, using the same parameters as in our preferred solutions. If the resolution were perfect, the recovered model would reproduce the velocity anomaly pattern of the starting model. Regions that do resemble the anomaly pattern indicate that data are resolving lateral velocity variations of a length scale equal to the anomaly width.

[77] We show the results of two sets of corrugation tests in Figure C1. The first test was conducted for profile K1 using four different anomaly widths (i.e., half wavelength of the sinusoidal perturbation): 1.5, 2.0, 2.5 and 5.0 km (Figures C1a–C1d). The 1.5-km-wide anomaly pattern is recovered reasonably well up to a depth of 0.5 km below the seafloor. However, the amplitude of the recovered anomalies is smaller, particularly in areas of rough and/or deep seafloor. This is not surprising given the lower ray density at these locations (Figure 9, bottom). The maximum depth at which anomalies are well recovered increases with the size of the anomalies. For anomaly widths 1.5–2.5 km, the data resolve the anomalies down to the depth of approximately 0.5 km below the seafloor, while for an anomaly width of 5.0 km the data resolve the anomalies down to a depth of approximately 1.0 km below the seafloor. Thus, features as small as 1.5 km wide in the final velocity model (Figure 7) are meaningful and well resolved at subseafloor depths less than ~0.5 km within the shallow parts of the profile away from the profile ends, while features at scales of 5 km or larger

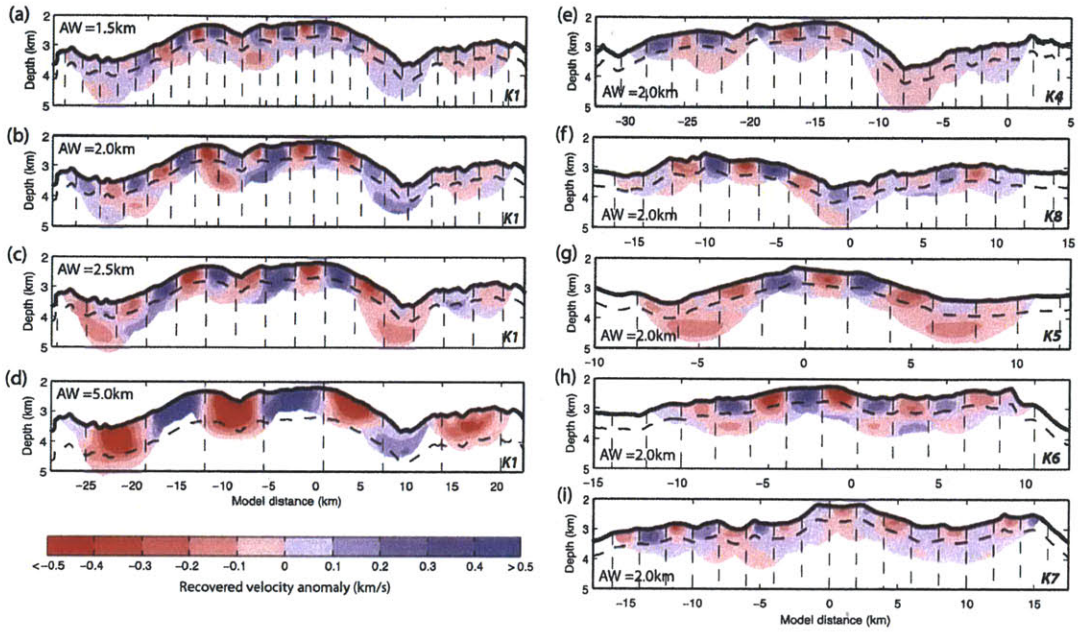

Figure C1. Results of lateral resolution tests. True anomaly pattern is created by a sine function with maximum amplitude of ±0.5 km s^{-1}, and vertical dashed lines show the positions of true anomaly equal to zero. Thick dashed lines denote estimates of maximum depth of good resolution. (a–d) Results of corrugation tests for profile K1, with varying anomaly widths (AW) indicated. Bold dashed lines are at a depth of 0.5 km in Figures C1a–C1c and at 1 km in Figure C1d. (e–i) Results of corrugation tests for the other five profiles with AW = 2.0 km. Bold dashed lines are at a depth of 0.5 km.

along the profile are meaningful at subseafloor depths to about 1.0 km.

[78] A second set of corrugation tests was conducted for the other five profiles using a constant anomaly width of 2.0 km (Figures C1e–C1i). In those tests, the depth to which the anomalies are well resolved is approximately 0.5 km. The main conclusion from these tests is that anomalies that are ~2.0 km wide and less than 0.5 km subseafloor can be trusted and interpreted, except at the ends of profiles where resolution is poorer.

C2. Velocity Uncertainty Estimate

[79] To estimate the uncertainty in our velocity models we followed a Monte Carlo approach [e.g., *Korenaga et al.*, 2000]. We constructed 100 different initial velocity models and used the observed traveltime with noise added to obtain 100 Monte Carlo solutions. Random Gaussian noise was added to the observed traveltime gradients, $N(0, \sigma = 30$ ms $km^{-1})$, following the method of *Zhang and Toksöz* [1998]. The 100 different initial velocity models were selected using the following procedure. First, we ran several 2-D inversions using a wide variety of initial models to constrain the range of 1-D models that converged to a stable and reliable solution. This was done to avoid using extreme initial 1-D models (e.g., with very high or low seafloor velocity, or unrealistic vertical velocity gradients) that cannot converge to an acceptable data fit. For the case of profile K7, Figure C2a shows the range of models explored (seafloor velocity 3 to 6 km s^{-1}, every 1 km s^{-1}, and vertical velocity gradient 0.25 to 3.25 s^{-1}, every 0.75 s^{-1}) and their resulting data fit expressed in terms of χ^2. We then selected 100 1-D models within the range of models that converge to a $\chi^2 \leq 2.5$ (Figure C2). Finally we ran 100 tomographic inversions using all the initial velocity models, following the same tomographic procedure used for the real data and using the same model parameterizations as in our preferred solutions. Assuming that all the Monte Carlo realizations have the same probability, the estimated velocity uncertainty can be approximated by the standard deviation of the

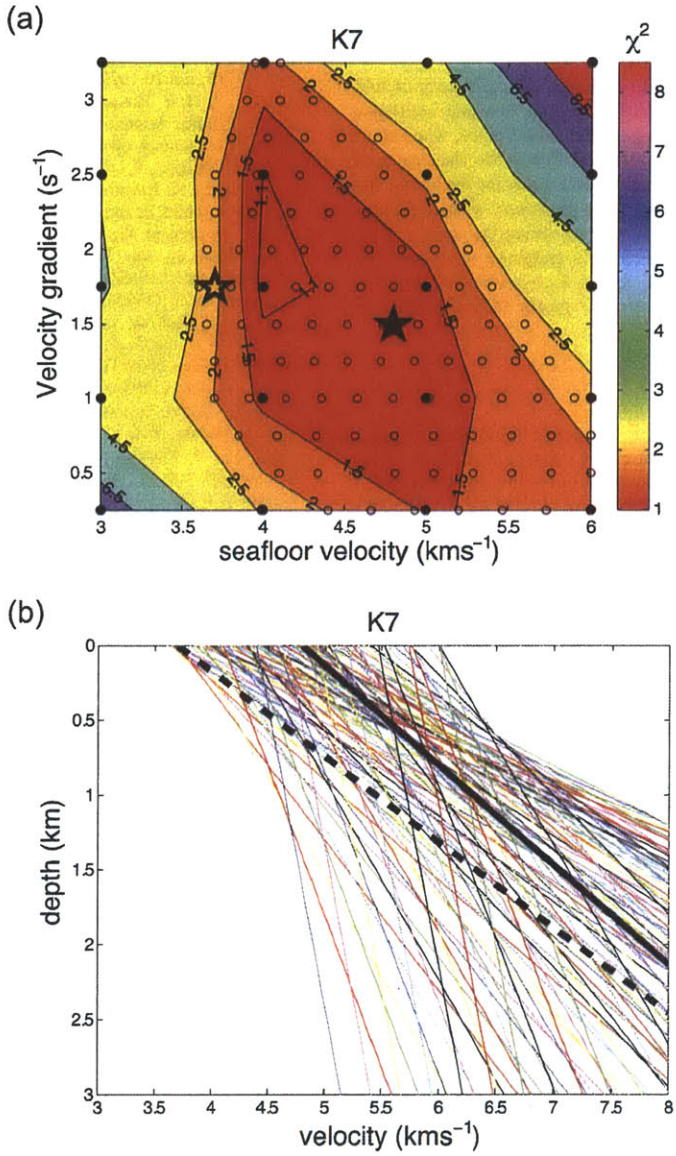

Figure C2. (a) Contour of traveltime residuals χ^2 (after five iterations) calculated for profile K7 using different seafloor velocities and vertical velocity gradients (black dots). The 100 black circles show equally spaced initial velocity structures used for estimating velocity uncertainties. The solid black star represents the best 1-D initial velocity model for profile K7, and the open black star shows the best average 1-D model for all lines. (b) The 100 1-D starting models for estimating the traveltime uncertainties for profile K7. The thick black line shows the starting model for profile K7 (Figure B1b), corresponding to the solid black star in Figure C2a, and the thick dashed line shows the average starting model (Figure B1b), corresponding to the open black star in Figure C2a.

100 Monte Carlo realizations [e.g., *Korenaga et al.*, 2000].

Acknowledgments

[80] We thank the captain, crew, and scientific party of R/V *Maurice Ewing* Cruise 0102 for their valuable assistance during the MCS field program and John Collins, who served as cruise Co-Chief Scientist with B.E.T. We also thank H. Dick and the WHOI geodynamics group for insightful discussions. H. Dick and M. Tivey generously shared geologic sample data on Kane OCC with us during the course of this study. This study benefited from insightful reviews by D. Shillington, D. Blackman, and an anonymous reviewer. This research was supported by NSF grants OCE-9987004 and OCE-0621660.

References

Auzende, J.-M., M. Cannat, P. Gente, J.-P. Henriet, T. Juteau, J. A. Karson, Y. Lagabrielle, C. Mével, and M. A. Tivey (1994), Observation of sections of oceanic crust and mantle cropping out on the southern wall of Kane FZ (N. Atlantic), *Terra Nova*, *6*, 143–148, doi:10.1111/j.1365-3121.1994.tb00647.x.

Baines, A. G., M. J. Cheadle, B. E. John, and J. J. Schwartz (2008), The rate of oceanic detachment faulting at Atlantis Bank, SW Indian Ridge, *Earth Planet. Sci. Lett.*, *273*(1–2), 105–114, doi:10.1016/j.epsl.2008.06.013.

Ballu, V., J. Dubois, C. Deplus, M. Diament, and S. Bonvalot (1998), Crustal structure of the Mid-Atlantic Ridge south of the Kane fracture zone from seafloor and sea surface gravity data, *J. Geophys. Res.*, *103*, 2615–2631, doi:10.1029/97JB02542.

Berge, P. A., G. J. Fryer, and R. H. Wilkens (1992), Velocity-porosity relationships in the upper oceanic crust: theoretical considerations, *J. Geophys. Res.*, *97*(B11), 15,239–15,254, doi:10.1029/92JB01464.

Blackman, D. K., B. Ildefonse, B. E. John, Y. Ohara, D. J. Miller, C. J. MacLeod, and Expedition 304/305 Scientists (2006), *Oceanic Core Complex Formation, Atlantis Massif, Proc. Integrated Ocean Drill. Program*, vol. 304/305, doi:10.2204/iodp.proc.304305.2006, Ocean Drill. Program, College Station, Tex.

Brown, J. R., and J. A. Karson (1988), Variations in axial processes on the Mid-Atlantic Ridge: The median valley of the MARK area, *Mar. Geophys. Res.*, *10*, 109–138, doi:10.1007/BF02424663.

Buck, W. R., L. L. Lavier, and A. N. B. Poliakov (2005), Modes of faulting at mid-ocean ridges, *Nature*, *434*, 719–723, doi:10.1038/nature03358.

Calvert, A. J. (1995), Seismic evidence for a magma chamber beneath the slow-spreading Mid-Atlantic Ridge, *Nature*, *377*, 410–414, doi:10.1038/377410a0.

Calvert, A. J., M. A. Fisher, S. Y. Johnson, and the SHIPS Working Group (2003), Along-strike variations in the shallow seismic velocity structure of the Seattle fault zone: Evidence for fault segmentation beneath Puget Sound, *J. Geophys. Res.*, *108*(B1), 2005, doi:10.1029/2001JB001703.

Canales, J. P., J. A. Collins, J. Escartín, and R. S. Detrick (2000a), Seismic structure across the rift valley of the Mid-Atlantic Ridge at 23°20′N (MARK area): Implications for crustal accretion processes at slow spreading ridges, *J. Geophys. Res.*, *105*, 28,411–28,425.

Canales, J. P., R. S. Detrick, J. Lin, J. A. Collins, and D. R. Toomey (2000b), Crustal and upper mantle seismic structure beneath the rift mountains and across a non-transform offset at the Mid-Atlantic Ridge (35°N), *J. Geophys. Res.*, *105*, 2699–2719, doi:10.1029/1999JB900379.

Canales, J. P., B. E. Tucholke, M. Xu, J. A. Collins, and D. L. Dubois (2008), Seismic evidence for large-scale compositional heterogeneity of oceanic core complexes, *Geochem. Geophys. Geosyst.*, *9*, Q08002, doi:10.1029/2008GC002009.

Cann, J. R., D. K. Blackman, D. K. Smith, E. McAllister, B. Janssen, S. Mello, E. Avgerinos, A. R. Pascoe, and J. Escartín (1997), Corrugated slip surfaces formed at ridge-transform intersections on the Mid-Atlantic Ridge, *Nature*, *385*, 329–332, doi:10.1038/385329a0.

Cannat, M., et al. (1995a), Thin crust, ultramafic exposures, and rugged faulting patterns at the Mid-Atlantic Ridge (22°–24°N), *Geology*, *23*, 49–52, doi:10.1130/0091-7613(1995)023<0049:TCUEAR>2.3.CO;2.

Cannat, M., et al. (1995b), *Proceedings of the Ocean Drilling Program, Initial Reports*, vol. 153, Ocean Drill Program, College Station, Tex.

Cannat, M., V. Mendel, E. Ruellan, K. Okino, J. Escartín, V. Combier, and M. Baala (2006), Modes of seafloor generation at a melt-poor ultraslow-spreading ridge, *Geology*, *34*(7), 605–608, doi:10.1130/G22486.1.

Carlson, R. L., and C. N. Herrick (1990), Densities and porosities in the oceanic crust and their variations with depth and age, *J. Geophys. Res.*, *95*(B6), 9153–9170, doi:10.1029/JB095iB06p09153.

Christensen, N. I. (2004), Serpentinites, peridotites, and seismology, *Int. Geol. Rev.*, *46*(9), 795–816, doi:10.2747/0020-6814.2746.2749.2795.

Cormier, M.-H., R. S. Detrick, and G. M. Purdy (1984), Anomalously thin crust in oceanic fracture zones: New seismic constraints from the Kane fracture zone, *J. Geophys. Res.*, *89*, 10,249–10,266.

deMartin, B. J., R. Reves-Sohn, J. P. Canales, and S. E. Humphris (2007), Kinematics and geometry of active detachment faulting beneath the Trans-Atlantic Geotraverse (TAG) hydrothermal field on the Mid-Atlantic Ridge, *Geology*, *35*(8), 711–714, doi:10.1130/G23718A.1.

Detrick, R. S., and G. M. Purdy (1980), The crustal structure of the Kane fracture zone from seismic refraction studies, *J. Geophys. Res.*, *85*, 3759–3778, doi:10.1029/JB085iB07p03759.

Detrick, R. S., et al. (1988), *Proceedings of the Ocean Drilling Program, Initial Reports*, vol. 106/109/111, Ocean Drill. Program, College Station, Tex.

Detrick, R. S., J. C. Mutter, P. Buhl, and I. I. Kim (1990), No evidence from multichannel reflection data for a crustal magma chamber in the MARK area on the Mid-Atlantic Ridge, *Nature*, *347*, 61–64, doi:10.1038/347061a0.

Detrick, R. S., R. S. White, and G. M. Purdy (1993), Crustal structure of North Atlantic fracture zones, *Rev. Geophys.*, *31*, 439–458, doi:10.1029/93RG01952.

Detrick, R. S., H. D. Needham, and V. Renard (1995), Gravity anomalies and crustal thickness variations along the Mid-Atlantic Ridge between 33°N and 40°N, *J. Geophys. Res.*, *100*, 3767–3787, doi:10.1029/94JB02649.

Dick, H. J. B., et al. (2000), A long in situ section of the lower ocean crust: Results of ODP Leg 176 drilling at the Southwest Indian ridge, *Earth Planet. Sci. Lett.*, *179*, 31–51, doi:10.1016/S0012-821X(00)00102-3.

Dick, H. J. B., M. A. Tivey, and B. E. Tucholke (2008), Plutonic foundation of a slow-spread ridge segment: The oceanic core complex at Kane Megamullion, 23°30′N, 45°20′W, *Geochem. Geophys. Geosyst.*, *9*, Q05014, doi:10.1029/2007GC001645.

Dunn, R. A., and D. R. Toomey (2001), Crack-induced seismic anisotropy in the oceanic crust across the East Pacific Rise (9° 30′N), *Earth Planet. Sci. Lett.*, *189*, 9–17, doi:10.1016/S0012-821X(01)00353-3.

Escartín, J., D. K. Smith, J. Cann, H. Schouten, C. H. Langmuir, and S. Escrig (2008), Central role of detachment faults in accretion of slow-spreading oceanic lithosphere, *Nature*, *455*, 790–794, doi:10.1038/nature07333.

Gente, P., R. A. Pockalny, C. Durand, C. Deplus, M. Maia, G. Ceuleneer, C. Mével, M. Cannat, and C. Laverne (1995), Characteristics and evolution of the segmentation of the Mid-Atlantic Ridge between 20°N and 24°N during the last 10 million years, *Earth Planet. Sci. Lett.*, *129*, 55–71, doi:10.1016/0012-821X(94)00233-O.

Grevemeyer, I., and W. Weigel (1997), Increase of seismic velocities in upper oceanic crust: The "superfast" spreading East Pacific Rise at 14°14′S, *Geophys. Res. Lett.*, *24*(3), 217–220, doi:10.1029/96GL04005.

Grimes, C. B., B. E. John, M. J. Cheadle, and J. L. Wooden (2008), Protracted construction of gabbroic crust at a slow-spreading ridge: Constraints from 206Pb/238U zircon ages from Atlantis Massif and IODP Hole U1309D (30°N MAR), *Geochem. Geophys. Geosyst.*, *9*, Q08012, doi:10.1029/2008GC002063.

Harding, A. J., J. A. Orcutt, M. E. Kappus, E. E. Vera, J. C. Mutter, P. Buhl, R. S. Detrick, and T. M. Brocher (1989), The structure of young oceanic crust at 13°N on the East Pacific Rise from expanding spread profiles, *J. Geophys. Res.*, *94*, 12,163–12,196.

Houtz, R. E., and J. Ewing (1976), Upper crustal structure as a function of plate age, *J. Geophys. Res.*, *81*, 2490–2498, doi:10.1029/JB081i014p02490.

Ildefonse, B., D. K. Blackman, B. E. John, Y. Ohara, D. J. Miller, C. J. MacLeod, and Integrated Ocean Drilling Program Expeditions 304/305 Science Party (2007), Oceanic core complexes and crustal accretion at slow-spreading ridges, *Geology*, *35*(7), 623–626, doi:10.1130/G23531A.1.

Johnson, H. P., and S. W. Semyan (1994), Age variation in the physical properties of oceanic basalts: Implications for crustal formation and evolution, *J. Geophys. Res.*, *99*(B2), 3123–3134, doi:10.1029/93JB00717.

Karson, J. A., and H. J. B. Dick (1983), Tectonics of ridge-transform intersection at the Kane Fracture Zone, *Mar. Geophys. Res.*, *6*, 51–98, doi:10.1007/BF00300398.

Karson, J. A., et al. (1987), Along-axis variations in seafloor spreading in the MARK area, *Nature*, *328*, 681–685, doi:10.1038/328681a0.

Kelemen, P. B., E. Kikawa, and D. J. Miller (2004), *Proceedings of the Ocean Drilling Program, Initial Reports*, vol. 209, Ocean Drill. Program, College Station, Tex.

Kong, L. S. L., R. S. Detrick, P. J. Fox, L. A. Mayer, and W. B. F. Ryan (1988), The morphology and tectonics of the MARK area from SeaBeam and Sea MARC I observations (Mid-Atlantic Ridge 23°N), *Mar. Geophys. Res.*, *10*, 59–90, doi:10.1007/BF02424661.

Kong, L. S. L., S. C. Solomon, and G. M. Purdy (1992), Microearthquake characteristics of a mid-ocean ridge along-axis high, *J. Geophys. Res.*, *97*, 1659–1685, doi:10.1029/91JB02566.

Korenaga, J., W. S. Holbrook, G. M. Kent, P. B. Kelemen, R. S. Detrick, H.-C. Larsen, J. R. Hopper, and T. Dahl-Jensen (2000), Crustal structure of the southeast Greenland margin from joint refraction and reflection seismic tomography, *J. Geophys. Res.*, *105*, 21,591–21,614.

Kuster, G. T., and M. N. Töksoz (1974), Velocity and attenuation of seismic waves in two-phase media: Part I. Theoretical formulations, *Geophysics*, *39*(5), 587–606, doi:10.1190/1.1440450.

Lin, J., G. M. Purdy, H. Schouten, J.-C. Sempéré, and C. Zervas (1990), Evidence from gravity data for focused magmatic accretion along the Mid-Atlantic Ridge, *Nature*, *344*, 627–632, doi:10.1038/344627a0.

Lizarralde, D., J. B. Gaherty, J. A. Collins, G. Hirth, and S. D. Kim (2004), Spreading-rate dependence of melt extraction at mid-ocean ridges from mantle seismic refraction data, *Nature*, *432*, 744–747, doi:10.1038/nature03140.

MacLeod, C. J., et al. (2002), Direct geological evidence for oceanic detachment faulting: The Mid-Atlantic Ridge, 15°45′N, *Geology*, *30*(10), 879–882, doi:10.1130/0091-7613(2002)030<0879:DGEFOD>2.0.CO;2.

Maia, M., and P. Gente (1998), Three-dimensional gravity and bathymetry analysis of the Mid-Atlantic Ridge between 20°N and 24°N: Flow geometry and temporal evolution of the segmentation, *J. Geophys. Res.*, *103*, 951–974, doi:10.1029/97JB01635.

Mével, C., M. Cannat, P. Gente, E. Marion, J.-M. Auzende, and J. A. Karson (1991), Emplacement of deep crustal and mantle rocks on the west median valley wall of the MARK area (MAR, 23°N), *Tectonophysics*, *190*, 31–53, doi:10.1016/0040-1951(91)90353-T.

Miller, D. J., and N. I. Christensen (1997), Seismic velocities of lower crustal and upper mantle rocks from the slow spreading Mid-Atlantic Ridge, south of the Kane transform zone (MARK), *Proc. Ocean Drill. Program Sci. Results*, *153*, 437–454.

Minshull, T. A., R. S. White, J. C. Mutter, P. Buhl, R. S. Detrick, C. A. Williams, and E. Morris (1991), Crustal structure at the Blake Spur fracture zone from expanding spread profiles, *J. Geophys. Res.*, *96*, 9955–9984, doi:10.1029/91JB00431.

Morris, E., and R. S. Detrick (1991), Three-dimensional analysis of gravity anomalies in the MARK area, Mid-Atlantic Ridge 23°N, *J. Geophys. Res.*, *96*, 4355–4366, doi:10.1029/90JB02173.

Ohara, Y., T. Yoshida, and S. Kasuga (2001), Giant megamullion in the Parece Vela Backarc basin, *Mar. Geophys. Res.*, *22*, 47–61, doi:10.1023/A:1004818225642.

Okino, K., K. Matsuda, D. M. Christie, Y. Nogie, and K. Koizumi (2004), Development of oceanic detachment and asymmetric spreading at the Australian-Antarctic Discordance, *Geochem. Geophys. Geosyst.*, *5*, Q12012, doi:10.1029/2004GC000793.

Pockalny, R. A., R. S. Detrick, and P. J. Fox (1988), Morphology and tectonics of the Kane transform from SeaBeam bathymetry data, *J. Geophys. Res.*, *93*, 3179–3193, doi:10.1029/JB093iB04p03179.

Pockalny, R. A., A. Smith, P. Gente (1995), Spatial and temporal variability of crustal magnetization of a slow spreading ridge: Mid-Atlantic Ridge (20°–24°N), *Mar. Geophys. Res.*, *17*, 301–320, doi:10.1007/BF01203467.

Purdy, G. M., and R. S. Detrick (1986), Crustal structure of the Mid-Atlantic ridge at 23°N from seismic refraction studies, *J. Geophys. Res.*, *91*, 3739–3762, doi:10.1029/JB091iB03p03739.

Reston, T. J., W. Weinrebe, I. Grevemeyer, E. R. Flueh, N. C. Mitchell, L. Kirstein, C. Kopp, H. Kopp, and participants of *Meteor* 47/2 (2002), A rifted inside corner massif on the

Mid-Atlantic Ridge at 5°S, *Earth Planet. Sci. Lett.*, *200*, 255–269, doi:10.1016/S0012-821X(02)00636-2.

Schulz, R. J., R. S. Detrick, and S. P. Miller (1988), Two-and three-dimensional inversions of magnetic anomalies in the MARK area (Mid-Atlantic Ridge 23°N), *Mar. Geophys. Res.*, *10*, 41–57, doi:10.1007/BF02424660.

Schwartz, J. J., B. E. John, M. J. Cheadle, E. A. Miranda, C. B. Grimes, J. L. Wooden, and H. J. B. Dick (2005), Dating the growth of oceanic crust at a slow-spreading ridge, *Science*, *310*, 654–657, doi:10.1126/science.1116349.

Searle, R. C., M. Cannat, K. Fujioka, C. Mével, H. Fujimoto, A. Bralee, and L. M. Parson (2003), FUJI Dome: A large detachment fault near 64°E on the very slow-spreading southwest Indian Ridge, *Geochem. Geophys. Geosyst.*, *4*(8), 9105, doi:10.1029/2003GC000519.

Smith, D. K., J. R. Cann, and J. Escartín (2006), Widespread active detachment faulting and core complex formation near 13°N on the Mid-Atlantic Ridge, *Nature*, *442*, 440–443, doi:10.1038/nature04950.

Smith, D. K., J. Escartín, H. Schouten, and J. R. Cann (2008), Fault rotation and core complex formation: Significant processes in seafloor formation at slow-spreading mid-ocean ridges (Mid-Atlantic Ridge, 13°–15°N), *Geochem. Geophys. Geosyst.*, *9*, Q03003, doi:10.1029/2007GC001699.

Stephen, R. A. (1981), Seismic anisotropy observed in upper oceanic crust, *Geophys. Res. Lett.*, *8*(8), 865–868, doi:10.1029/GL008i008p00865.

Stephen, R. A. (1985), Seismic anisotropy in the upper oceanic crust, *J. Geophys. Res.*, *90*(B13), 11,383–11,396.

Toomey, D. R., G. M. Purdy, and S. C. Solomon (1988), Microearthquakes beneath the median valley of the Mid-Atlantic Ridge near 23°N: Tomography and tectonics, *J. Geophys. Res.*, *93*, 9093–9112, doi:10.1029/JB093iB08p09093.

Tucholke, B. E., J. Lin, and M. C. Kleinrock (1996), Mullions, megamullions, and metamorphic core complexes on the Mid-Atlantic Ridge, *Eos Trans. AGU*, *77*, Fall Meet. Suppl., F724.

Tucholke, B. E., J. Lin, and M. C. Kleinrock (1998), Megamullions and mullion structure defining oceanic metamorphic core complexes on the Mid-Atlantic Ridge, *J. Geophys. Res.*, *103*, 9857–9866, doi:10.1029/98JB00167.

Tucholke, B. E., K. Fujioka, T. Ishihara, G. Hirth, and M. Kinoshita (2001), Submersible study of an oceanic megamullion in the central North Atlantic, *J. Geophys. Res.*, *106*(B8), 16,145–16,161.

Tucholke, B. E., M. D. Behn, R. Buck, and J. Lin (2008), The role of melt supply in detachment faulting and the formation of oceanic core complexes, *Geology*, *36*(6), 455–458, doi:10.1130/G24639A.

Vera, E. E., J. C. Mutter, P. Buhl, J. A. Orcutt, A. J. Harding, M. E. Kappus, R. S. Detrick, and T. M. Brocher (1990), The structure of 0- to 0.2-m.y.-old oceanic crust at 9°N on the East Pacific Rise from expanded spread profiles, *J. Geophys. Res.*, *95*, 15,529–15,556.

Whitehead, J. A., H. J. B. Dick, and H. Schouten (1984), A mechanism for magmatic accretion under spreading centers, *Nature*, *312*, 146–148, doi:10.1038/312146a0.

Wilkens, R. H., G. J. Fryer, and J. Karsten (1991), Evolution of porosity and seismic structure of upper oceanic crust: Importance of aspect ratios, *J. Geophys. Res.*, *96*, 17,981–17,995.

Williams, C. M., M. A. Tivey, and M. D. Behn (2006), The magnetic structure of Kane megamullion: Results from marine magnetic anomalies, paleomagnetic data and thermal modeling, *Eos Trans. AGU*, *87*(52), Fall Meet. Suppl., Abstract T42A-03.

Zelt, B. C., B. Taylor, J. R. Weiss, A. M. Goodliffe, M. Sachpazi, and A. Hirn (2004), Streamer tomography velocity models for the Gulf of Corinth and Gulf of Itea, Greece, *Geophys. J. Int.*, *159*, 333–346, doi:10.1111/j.1365-246X.2004.02388.x.

Zelt, C. A., and P. J. Barton (1998), Three-dimensional seismic refraction tomography: A comparison of two methods applied to data from the Faeroe Basin, *J. Geophys. Res.*, *103*(B4), 7187–7210, doi:10.1029/97JB03536.

Zelt, C. A., and D. A. Forsyth (1994), Modeling wide-angle seismic data for crustal structure: Southeastern Grenville Province, *J. Geophys. Res.*, *99*(B6), 11,687–11,704.

Zhang, J., and M. N. Toksöz (1998), Nonlinear refraction traveltime tomography, *Geophysics*, *63*, 1726–1737, doi:10.1190/1.1444468.

Chapter 5

Investigation of a marine magnetic polarity reversal boundary in cross-section at the northern boundary of the Kane Megamullion, Mid-Atlantic Ridge 23°40'N

Abstract

Near-bottom magnetic field measurements made by the submersible *Nautile* during the 1992 *Kanaut Expedition* define the cross-section geometry of a magnetic polarity reversal boundary and the vertical variation of crustal magnetization in upper oceanic crust exposed along the Kane Transform Fault (TF) at the northern boundary of the Kane Megamullion (KMM). The KMM exposes lower crust and upper mantle rocks on a low-angle normal fault that was active between 3.3 Ma and 2.1 Ma. The geometry of the polarity boundary is estimated from an inversion of the submarine magnetic data for crustal magnetization. In general, the polarity boundary dips away from the ridge axis along the Kane TF scarp, with a west-dipping angle of ~45° in the shallow (<1 km) crust and <20° in the deeper crust. The existence of the magnetic polarity boundary (C2r.2r/C2An.1n, ~2.581 Ma) indicates that the lower crust (gabbros) and upper mantle (peridotites) are able to record a coherent magnetic signal. There is not a convincing correlation between the magnetization structures and the lithological distribution, thus we rule out the possibility that the magnetic reversal boundary is exclusively caused by lithological changes. Our results support the conclusion of *Williams* [2007] that lower crust (gabbros) cool through their Curie temperature to become magnetic, with the polarity boundary representing both a frozen isotherm and an isochron. We also test the effects of the rotation of this isotherm structure and/or footwall rotation, and find that the magnetic polarity boundary geometry interpretations are not sensitive to these directional changes.

5.1. INTRODUCTION

Oceanic core complexes (OCCs) are sections of oceanic lithosphere exhumed at the seafloor by long-lived normal faults also referred to as "detachment" faults that initiate at mid-ocean ridges (MORs) [*Cann et al.*, 1997; *MacLeod et al.*, 2002; *Tucholke et al.*, 1996, 1998]. OCCs provide important "tectonic windows" into sections of oceanic lithosphere that are otherwise confined to the deep subsurface. The Kane Megamullion (KMM) is an OCC located between ~30-55 km off-axis on the North American plate, on the western side of the Mid-Atlantic Ridge (MAR) axis, immediately south of the ~150 km long, left stepping Kane transform fault, between ~23°20'N and ~23°40'N (Figure 5-1). KMM formed between 3.3 Ma and 2.1 Ma based on sea surface magnetic anomaly data, during a period marked by strongly asymmetrical spreading of the MOR spreading center (i.e., 17.9 mm/a on the OCC side on the west, and 7.9 mm/a on the conjugate (east) side between chrons C2 and C2A) (Figure 5-2) [*Williams et al.*, 2006]. The seafloor morphology of KMM shows characteristic smooth surfaces and spreading-parallel corrugations typical of megamullions formed by major oceanic detachment faults [*Tucholke et al.*, 1998].

Long-term movement of the footwall on the detachment fault uplifted and exposed lower crust and upper mantle rocks to the seafloor and can potentially accommodate a significant component of plate motion by extension, even in the absence of magmatism [*Escartín et al.*, 2008; *Tucholke et al.*, 2008]. The abundance of gabbros and altered peridotites exposed along the northern edge of the KMM [*Auzende et al.*, 1994; *Dick et*

al., 2008] is consistent with a positive residual mantle Bouguer gravity anomaly [*Ballu et al.*, 1998; *Maia and Gente*, 1998; *Morris and Detrick*, 1991] and large lateral variations in seismic velocity [*Canales et al.*, 2008; *Xu et al.*, 2009]. These observations indicate that the KMM may be not only an ideal tectonic window where the geological record of mantle flow and melt generation and migration can be studied [*Dick et al.*, 2010], but also an ideal location to define the contribution of gabbro and peridotite to the magnetic anomaly signal [*Williams et al.*, 2006]. A well-defined magnetic anomaly reversal (C2r.2r/C2An.1n, ~2.581 Ma) crosses the KMM from south to north, parallel to the strike of the MOR [*Williams*, 2007], indicating that the lithospheric section at this location has been able to record and preserve magnetic field polarity signals consistent with a seafloor spreading process [*Morley and Larochelle*, 1964; *Vine and Matthews*, 1963]. The presence of this polarity reversal is remarkable because the underlying lithology has been documented to be dominated by gabbro and peridotite [*Dick et al.*, 2008]. The KMM is terminated on its northern boundary by the Kane fracture zone. The relatively steep scarp along the southern wall of the Kane fracture zone provides a good opportunity to measure *in situ* vertical magnetic structure and to define the nature of the polarity reversal that intersects the Kane transform wall at the KMM. The symmetric distribution of marine magnetic lineations about the axes of MOR provide key evidence for seafloor spreading processes and the theory of plate tectonics [*Morley and Larochelle*, 1964; *Vine and Matthews*, 1963], which states that coherent marine magnetic anomalies are a record of the recurring polarity reversals of the Earth's magnetic field preserved in oceanic crust by seafloor spreading at MORs. However, the geometry and even the existence of polarity

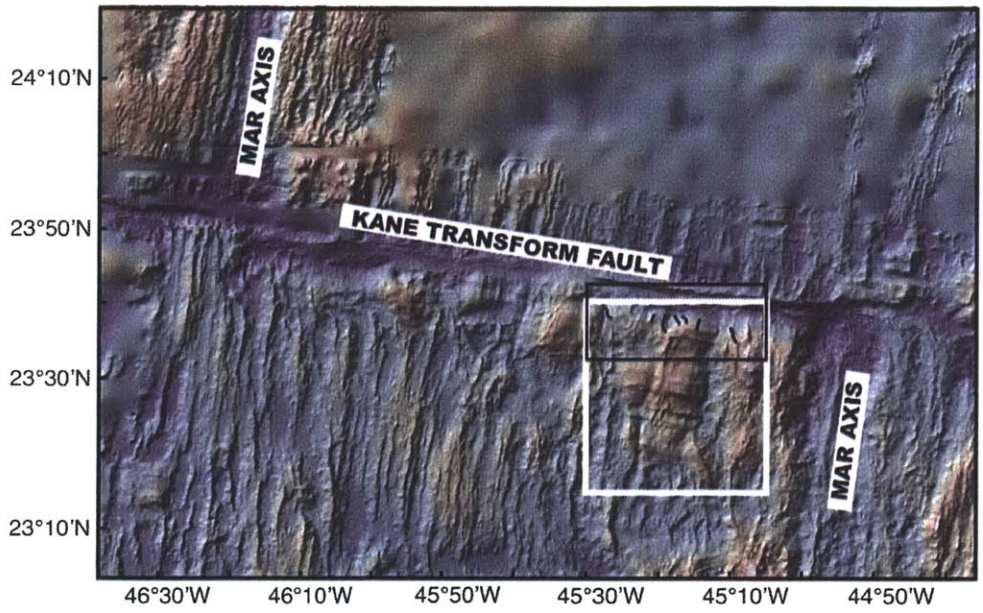

Figure 5-1. Shaded relief bathymetry of the Mid-Atlantic Ridge (MAR) around the Kane fracture zone from the Marine Geoscience Data System (http://www.geomapapp.org). The black box outlines the study area (Figures 5-2 and 5-3), the white box outlines the Kane OCC, and black lines represent seven magnetic survey profiles that were obtained during the 1992 *Kanaut Expedition* [*Auzende et al.*, 1992].

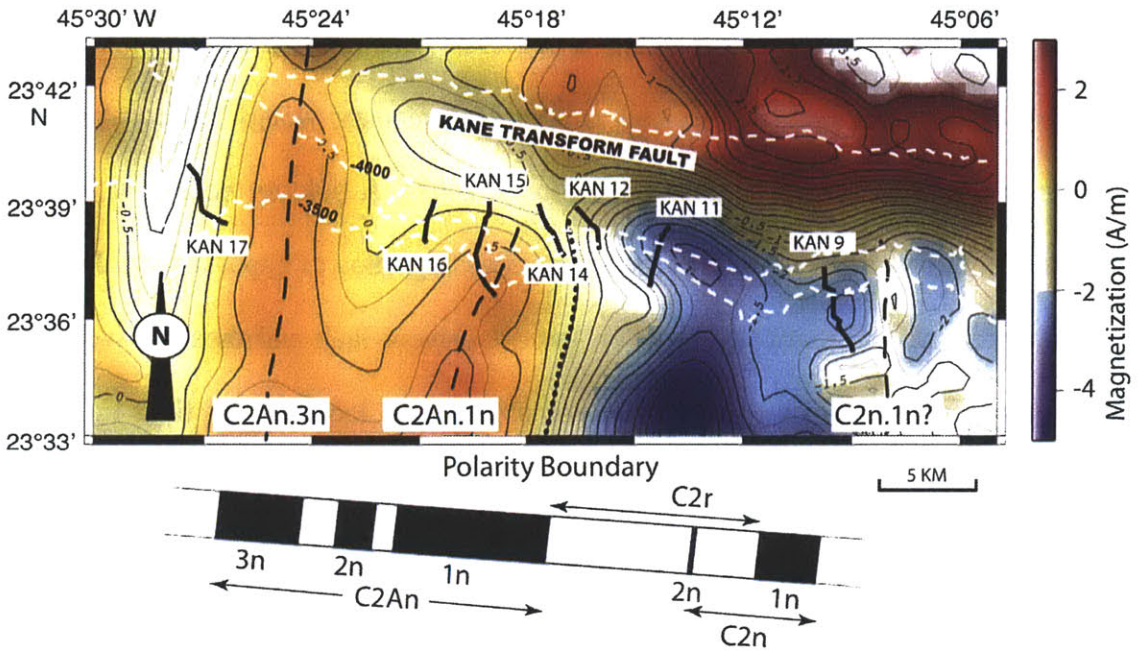

Figure 5-2. Contoured inversion result of the sea surface magnetic anomaly data around the Kane fracture zone (adapted from *Williams* [2007]) overlain with near-bottom magnetic survey profiles (shown in solid black lines). The contour interval is 0.25 A/m, and every 0.5 A/m is labeled. The Kane transform valley is outlined by two iso-bathymetry contours (shown in white dashed lines), at 3500 m and 4000 m. The Geomagnetic Polarity Time Scale (GPTS) of *Ogg and Smith* [2004] is projected to the direction perpendicular to the MAR at the bottom of the figure. Chrons C2n and C2An are made up of several subchrons. The black dotted line marks the C2r.2r/C2An.1n polarity boundary, while the black dashed lines locate the possible locations of subchrons C2An.3n, C2An.1n and C2n.1n. The question mark indicates that the location of subchron C2n.1n is not well resolved by the sea surface magnetic anomaly data.

boundaries within lower crustal and upper mantle rocks is a subject of debate, speculation and inference with very little direct information available to test the various models. The prevailing hypothesis suggests that the lower crust (gabbros) cools through its Curie isotherm to become magnetic so that a polarity boundary would represent a frozen isotherm as well as an isochron [e.g., *Williams*, 2007]. A polarity boundary in altered peridotite could be either a result of the progressive migration of upper mantle through an alteration zone as the footwall moves on the detachment fault and thus behaves like an isochron or the upper mantle could become altered at a location and time that has no isochronal relevance. *Williams* [2007] finds that both the gabbro and peridotite lithologies have the potential to preserve remanent magnetic signals, i.e., they could contribute to the source of the observed magnetic anomaly signal. Thus the presence and geometry of a polarity boundary at KMM and the Kane transform wall provides an important opportunity to investigate the history and structure of oceanic crust and upper mantle exposed on a detachment fault and to investigate how crustal magnetization may be preserved in these lithospheric sections.

In this paper, we analyze a series of magnetic profiles collected by the submersible *Nautile* vertically up the southern wall of the Kane fracture zone and present the calculated magnetization structure to determine the geometry of a magnetic polarity reversal boundary exposed in cross-section on the northern boundary of KMM on the flanks of the MAR near 23°40'N. The final results present obvious magnetization contrasts that vary in position and depth across the scarp face. These magnetization

contrasts could arise either from lithological variations (i.e., gabbro versus altered peridotite magnetization intensity) or they could represent true magnetic polarity reversals. We discuss these two possibilities but conclude that the polarity interpretation is the most likely explanation for the observed variation and correlate these magnetization variations to produce a map of the geometry of the polarity boundary in cross-section. Finally, we investigate the impact of footwall and/or isotherm rotation on both the inverted magnetization vector and the geometry of polarity boundaries that we interpret from the data.

5.2. DATA COLLECTION

The magnetic data used in this study were acquired during the 1992 *Kanaut Expedition* [*Auzende et al.*, 1993, 1994]. This expedition used the submersible *Nautile* to study the southern wall of the Kane fracture zone from its eastern intersection with the MAR to 5 Myr in age [*Auzende et al.*, 1994]. A total of 20 *Nautile* dives were conducted, including ten at the eastern ridge-transform intersection and the inside corner massif and ten along the southern wall of the Kane fracture zone between 45°08'W and 45°28'W. Here, we present results from seven *Nautile* dives (KAN 9, 11, 12, 14-17) conducted where the transform wall forms the northern boundary of the KMM [*Auzende et al.*, 1993, 1994; *Ghose et al.*, 1996] (Figures 5-1 and 5-3). Magnetic field data were obtained using a three-axis fluxgate magnetometer mounted to the front sample basket of *Nautile.* Data were recorded inside the submersible on a laptop computer and later combined with depth, heading, and altitude, which were simultaneously recorded by the *Nautile* data

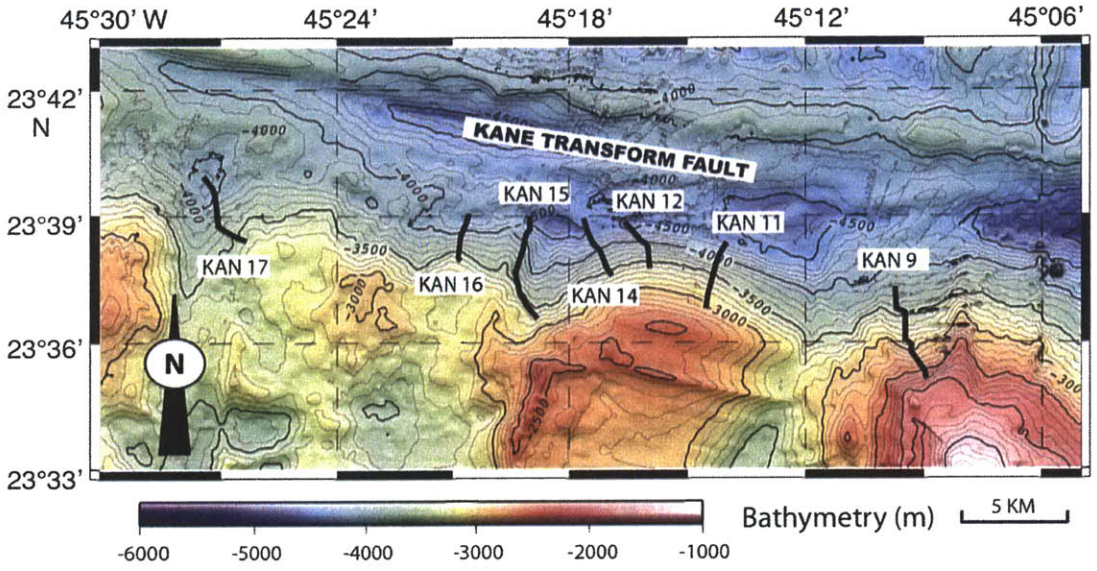

Figure 5-3. Detailed SeaBeam bathymetry map obtained from *R/V Knorr* Cruise 180-2 (adapted from *Dick et al.* [2008]). The contour interval is 100 m, and every 500 m is labeled. The black lines show positions of the seven near-bottom magnetic survey lines employed in this study.

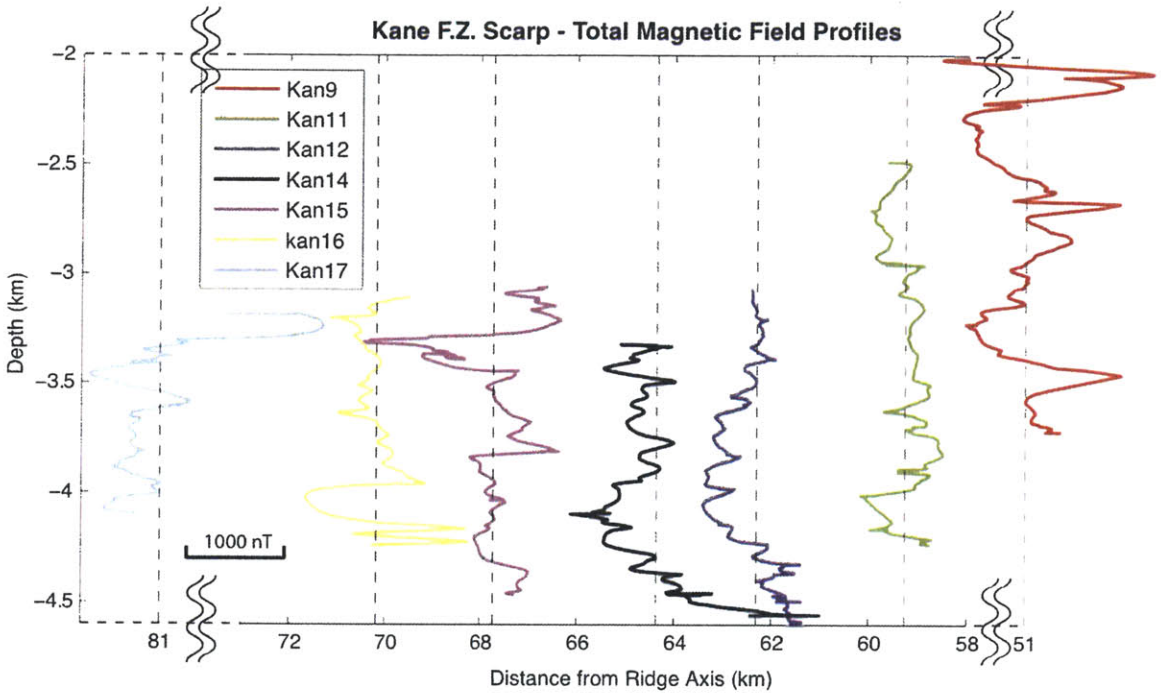

Figure 5-4. Observed total magnetic field anomaly (nT) profiles plotted versus depth below the sea surface at the approximate lateral distance from the MAR axis. Profiles Kan 9 and Kan 17 are plotted offset from their true location as shown by dashed lines to better compare all the profiles.

system. Submersible navigation used a ship-based acoustic transponder net with an estimated XY accuracy of ±10 m. The measured three-axis magnetic field components were vector summed for total field, because no independent orientation data were available for vector analysis. The near-bottom measurements along the relatively steep Kane scarp allow us to record vertical magnetic profiles (Figure 5-4) that were used in magnetic inverse modeling. Magnetic field data were corrected for the permanent and induced magnetic fields of the submersible by using a Nelder-Meade algorithm [*Press et al.*, 1986] to minimize the total magnetic field variations measured during spins of the submersible on the descent and ascent of each dive. The residual noise levels were generally below 200 nT in amplitude and insignificant compared to the geophysical signals of several thousands of nanoteslas. Finally, the 10^{th} generation International Geomagnetic Reference Field (IGRF) [*Maus et al.*, 2005] for year 1992 was removed from the magnetic data. Magnetic field measurements, obtained at a 1 Hz sampling rate, were typically obtained at a variable altitude from a few meters to a few hundred meters above the Kane scarp because of the local scarp topography and the overall convex-shaped scarp face. Short wavelength magnetic anomalies arise during the rock sampling process. The sample basket at the submersible swings out to allow samples to be stored and the manipulators come close to the magnetic sensor during these operations, which imparts magnetic field distortions. To eliminate these short wavelength anomalies we deleted these sampling periods from the magnetic record (Figure 5-4).

5.3. METHODS

5.3.1. Vertical Magnetic Profile Analysis

The vertical magnetic profiling (VMP) approach [*Tivey*, 1996; *Tivey et al.*, 1998] is used to analyze the magnetic field data collected along transects up the Kane transform scarp where exposures of oceanic upper lithosphere are found. The relatively steep geometry of these escarpments provides an excellent tectonic window to map the vertical magnetic structure and stratigraphy of oceanic lithosphere [e.g., *Karson et al.*, 1992; *Tivey*, 1996; *Tivey et al.*, 1998]. To demonstrate the vertical magnetic profile analysis approach, we assume the simplest geometry of a single fault with a monotonic slope and calculate the predicted anomaly that would arise for the north-facing Kane transform wall measurements.

Conventional analysis of marine magnetic field data collected over the seafloor assumes the magnetic source region is composed of crustal prisms of finite thickness and of infinite length perpendicular to the profile [e.g., *Parker*, 1973; *Schouten and McCamy*, 1972; *Vacquier*, 1962]. This layered model is a good approximation of normal oceanic crustal structure, but the nonuniqueness of the magnetic inversion method means that either the source layer thickness or magnetization can be determined, but not both. Typically, a constant thickness source layer is assumed to obtain a vertically averaged crustal magnetization for the layer [*Parker and Huestis*, 1974]. This approach has worked well within the overall framework of oceanic crustal structure that has been derived from ophiolite, crustal drilling and seismic studies [e.g., *Granot et al.*, 2006; *Henstock et al.*,

1995; *Schouten and Denham*, 1979]. In the vertical magnetic profile case, the geometry of layered oceanic crust can be used to advantage in order to calculate the magnetic response of the source layer. Magnetic measurements adjacent to a vertical scarp face (Figure 5-5a) can be viewed in a new, rotated reference frame, where the scarp face is rotated into the horizontal (Figure 5-5b). The original geomagnetic field and magnetization vectors are also rotated within this new reference frame. In this rotated coordinate system, a reasonable and realistic approximation can be made that the oceanic crust is composed of a series of thin tabular bodies, perpendicular to the profile and extending to infinite depth. If we assume that the magnetic anomalies are two-dimensional and strike along the scarp perpendicular to profile (Figure 5-5b), we can use analytical and Fourier transform solutions [*Gay*, 1963; *Pedersen*, 1978; *Tivey*, 1996] to calculate the resultant magnetic field. We can also carry out an inversion of the magnetic field for crustal magnetization using the same reference frame. In general, the zero level of the magnetization contrast can be fixed by using the contrast of nonmagnetic seawater with the top of the scarp. The direction of magnetization remains unknown so that a geocentric dipole direction must be assumed, as in conventional analysis. As with other nonlinear inversion techniques, however, solutions are nonunique so that any number of magnetization solutions may exist.

For the more realistic case of a non-vertical scarp face, e.g., with a slope of 23° (the same value as the averaged slope of all seven dive profiles used in this study) (Figure 5-5c), the scarp face is rotated into the horizontal by an amount equal to the slope angle

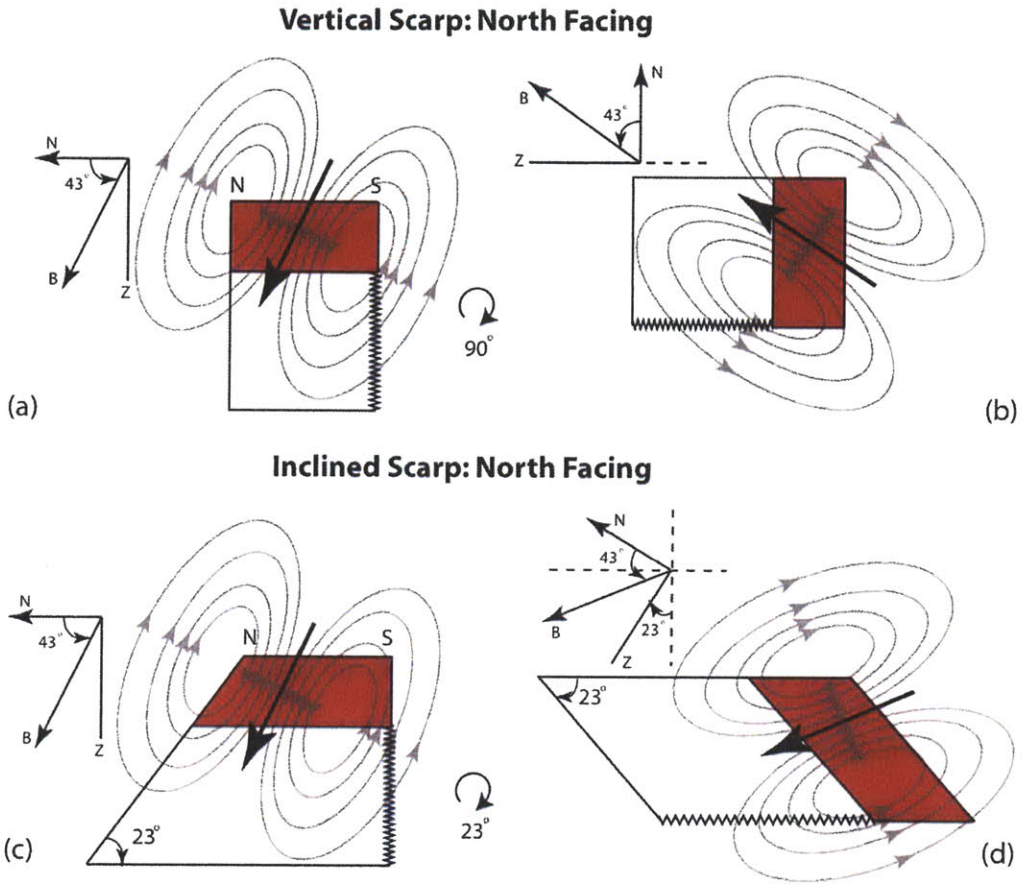

Figure 5-5. A cartoon showing the rotation of the coordinate systems used in the analysis of the vertically oriented magnetic data (modified from *Tivey* [1996]). (**a**) The conventional coordinate orientation showing a north facing vertical scarp face oriented east-west with a magnetized layer (shaded in red color) extending to the south. (**b**) The vertical scarp face shown in (**a**) has been rotated into the horizontal so that the magnetization layer now extends to infinite depth. In this orientation vertical boundaries indicate that the phase shift is due to field and magnetization inclinations. (**c**) A scarp face with a 23° slope and a magnetized layer (shaded in red color) in the conventional orientation. (**d**) The sloping scarp face shown in (**c**) has been rotated into the horizontal with an angle equal to the slope angle. Note the magnetized layer now dips with an angle equal to the slope angle, which adds to the phase shift due to the field and magnetization inclinations.

(Figure 5-5d). In this case, instead of vertically oriented tabular bodies, source bodies are dipping with an angle equivalent to the slope in the new coordinate system (Figure 5-5d), which introduces an additional phase shift into the anomaly. This rotation is merely to facilitate the mathematical analysis and has no physical meaning for crustal rotation.

5.3.2. A Test Case Example of Forward and Inverse Modeling

To demonstrate the feasibility of magnetic measurements along a scarp we construct two forward models in which we make no inferences about crustal structure, but merely show what we expect from a single horizontally layered magnetized body (Figure 5-6). For the vertical scarp (Figure 5-6a), the combination of scarp slope angle (90°) and geomagnetic field inclination +43°, means that the effective magnetic field has a new inclination direction of -47° (i.e., equivalent to being in the southern hemisphere), and it provides a sufficiently large contrast to generate anomalies on the order of 10000 nT at 5 m distance from the scarp for a 10 A/m magnetization contrast (Figure 5-6a). For the non-vertical scarp face (Figure 5-6b), the combination of scarp slope angle (23°) and geomagnetic field inclination +43°, indicates that the effective magnetic field has a shallow inclination of +20°, which is enough to generate somewhat weaker anomalies on the order of 4000 nT at 5 m distance from the scarp for a 10 A/m magnetization contrast (Figure 5-6b). Remember also that in this case the source body dips at an angle of 23° rather than being vertically oriented thus imparting an additional phase shift.

Inversion for crustal magnetization can be obtained from the observed magnetic field

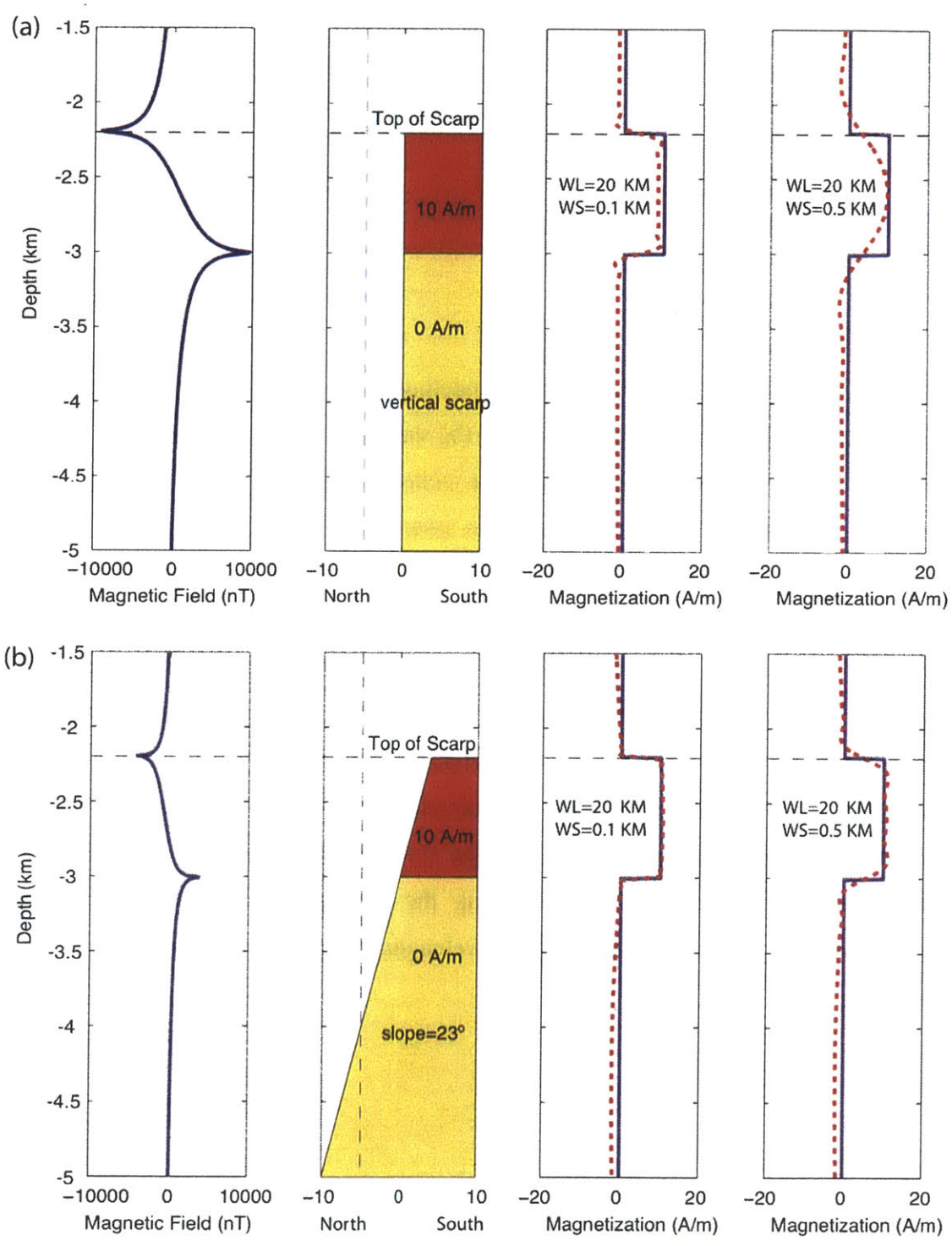
(a)
(b)
Depth (km)
-1.5
-2
-2.5
-3
-3.5
-4
-4.5
-5
−10000
0
10000
Magnetic Field (nT)
Top of Scarp
10 A/m
0 A/m
vertical scarp
slope=23°
−10
0
10
North
South
WL=20 KM
WS=0.1 KM
WS=0.5 KM
−20
0
20
Magnetization (A/m)

Figure 5-6. Forward and inverse magnetic modeling to demonstrate the vertical magnetic profile analysis of (**a**) vertical scarp face and (**b**) sloping scarp face with an angle of 23°. The rotated magnetic field and magnetization inclinations are 47°, and declinations are -17° and 0°, respectively. The survey height is assumed to be 5 m over the scarp and the magnetization of the crust is assumed to be 10 A/m for the upper 800 m and nonmagnetic for the lower crustal section. In each case, (**Left**) computed magnetic field, the resultant asymmetric magnetic field has a magnetic low at the top indicating reversed polarity and a magnetic high at the transition from the magnetic layer to the nonmagnetic layer; (**Middle Left**) scarp face model and magnetized layer (shaded in red color); (**Middle Right**) the blue line shows the input magnetization, and the red dashed line shows the inverted magnetization using a band-pass filter for wavelengths from 0.1 km to 20 km; (**Right**) the same as middle right, showing the comparison of input and inverted magnetization using a band-pass filter for wavelengths from 0.5 km to 20 km.

data assuming that the dipping bodies extend to effectively infinite depth. Note that both the forward and inverse models assume a level topography and observation plane. The inversion assumes that all the layers dip with the same angle and that the layers extend to infinity with constant magnetization within the layers. The inverted magnetization profiles can be compared with the input models (Figures 5-6). As with any potential field measurement, the depth that the VMP technique effectively "samples into the wall" is wavelength dependent, with longer wavelengths representing greater penetration of the wall, and shorter wavelength features representing surficial and topographic signals. Figure 5-6 shows two inversions with different wavelength band-pass filters: 0.1-20 km and 0.5-20 km. The 0.5 km cut-off, compared with 0.1 km, smoothes the inversion result as predicted so that it cannot fully resolve the sharp change between the two different magnetic layers. We also note that for the inversions with the same filter (0.1-20 km or 0.5-20 km), the non-vertical scarp case (with a slope angle of 23°) appears to fit the input magnetization much better than the vertical scarp case. This is caused by the different geometry of the two model scarps. For the sloping scarp model, rotation results in an effectively wider source body that separates the two edge effects of the magnetized body and reduces their interference. As in all near-bottom survey techniques, the short averaged length of the profile of ~3.5 km in this study limits the longest wavelengths that can be reliably sampled.

The magnetic effect of a single magnetized block while useful is perhaps too simple. Thus we constructed a more complicated model attempting to model a series of slipped

fault blocks akin to a "slipped deck of cards" [*Francheteau et al.*, 1979]. This may be particularly important for scarps that are composed of repeated crustal sections (Figure 5-7). We compute the magnetic field for a conceptual model, where an upper, highly magnetized crustal section is faulted three times, producing three slipped blocks. The resultant magnetic field is shown for the upper magnetized unit alone and then for all the units (Figure 5-7). As can be seen from the forward model, each slipped block produces a short wavelength magnetic anomaly with anomaly highs at the toe of each block and anomaly lows at the top of each block. The intact block at the top gives an overall longer wavelength signature. The forward modeled magnetic field was inverted for crustal magnetization to simulate our data analysis steps using two different wavelength band-pass filter, 0.1-20 km and 0.5-20 km (Figure 5-7). Both inversions show that the overall positive magnetization of the upper block is recognizable as a long wavelength positive zone, while the slipped blocks give a less intuitive result. The short wavelength magnetization highs reflect the variable thickness of the source layers due to the overlapping of the blocks, rather than any amplitude difference in magnetization. Note also that the profile shows zones of reversely magnetized crust where there are normal polarity blocks (e.g., ~4 km deep in Figure 5-7) for both filters. These models (Figures 5-6 and 5-7) are meant to serve as a guide to interpreting our observed magnetic profiles rather than to explicitly fit them. The submersible observations on the southern Kane transform wall find, however, that the wall has an overall convex morphology with no evidence of any repeated lithologic sections [*Auzende et al.*, 1992; *Auzende et al.*, 1994; *Dick et al.*, 2008]. It is unlikely that we have this type of crustal structure.

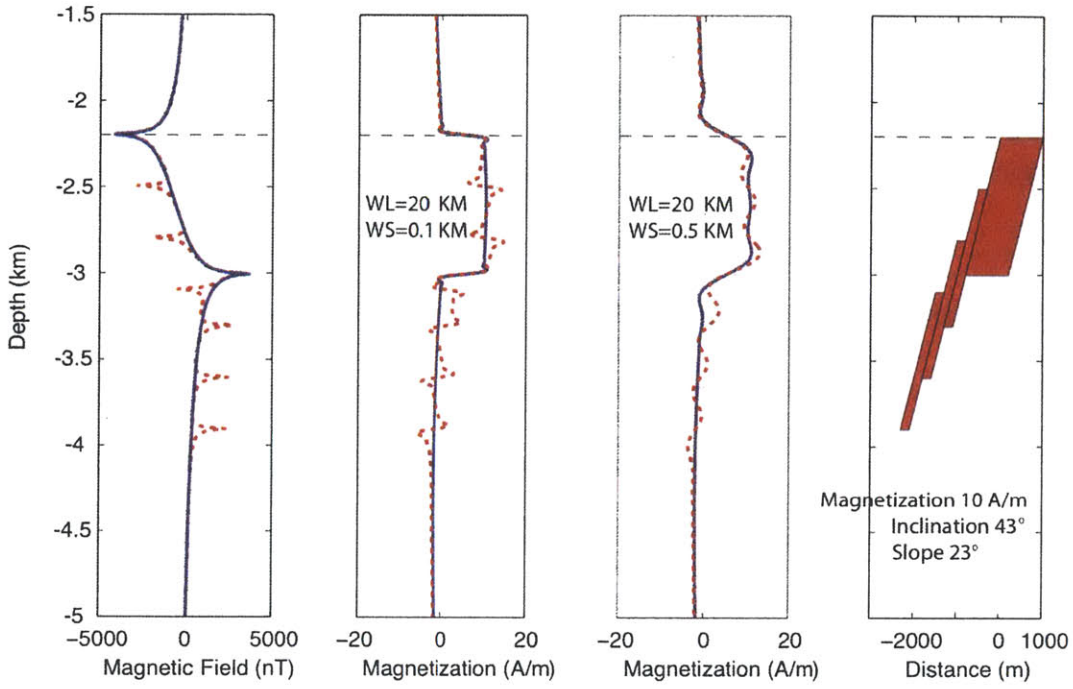

Figure 5-7. Forward magnetic model showing the effect of faulted blocks upon the magnetic signal. (**Right**) A model with an upper intact block and three slipped blocks, all with a 10 A/m normal polarity magnetization and a slope angle of 23°; (**Left**) calculated magnetic field: solid line represents the field due to a single intact block without the slipped blocks, and the red dashed line represents the field due to the integrated effect of all blocks. Note that magnetic lows align with the top of blocks and magnetic highs with the toe of blocks; (**Middle Left**) inversion of the calculated magnetic field for crustal magnetization using a band-pass filter of wavelength range from 0.1 km to 20 km: solid line is inversion for the single intact block, while the red dashed line is for the integrated inversion of all the blocks; (**Middle Right**) the same as middle left, but using a different band-pass filter of wavelength range from 0.5 km to 20 km for inversion. Note that there is a complex relationship between magnetization and the blocks. Magnetization highs correlated to where the fault blocks overlap reacting to the effective thickness of the magnetized layer.

5.4. DATA PROCESSING AND RESULTS

We applied the VMP approach described above to the magnetic profiles measured on the Kane transform wall in the KMM area. For the seven *Nautile* magnetic lines used in this paper, we first edited out bad data points at rock sampling stations (as described in section 5.2) and then smoothed the data using a 100-point moving average window (~100 m) after equal-spaced interpolation. The magnetic profiles were then projected into the direction parallel to the strike of the MAR axis, perpendicular to the general strike of the scarp. An average slope of 23° was used to represent the slope angle of the Kane scarp. Because the magnetic data were obtained along an uneven surface just above the convex-shaped scarp, we must upward continue the observed magnetic field data to a level plane above the seafloor topography. We use an iterative Fast Fourier Transform approach to obtain this upward continued field [*Guspi*, 1987; *Pilkington and Urquhart*, 1990]. Figure 5-8 shows the geometry necessary to reduce the magnetic measurements made on an uneven surface to a level plane. First of all, the observed level (i.e., dive track) is rotated clockwise to a horizontal plane with an angle of 23° that is equivalent to the average scarp slope. The resultant magnetic field data were then downward continued to a constant water-depth plane to remove the effects of variations in submersible altitude. The choice of this water-depth leads to better convergence of the Fourier transform method [*Guspi*, 1987]. Finally, the magnetic field data were upward continued to another constant water-depth that is also referred to as guspi level, since all bathymetry of the survey lies below this water depth. The resultant upward continued magnetic profiles are shown in Figure 5-9, and all the profiles, in general, exhibit clear variations up the scarp.

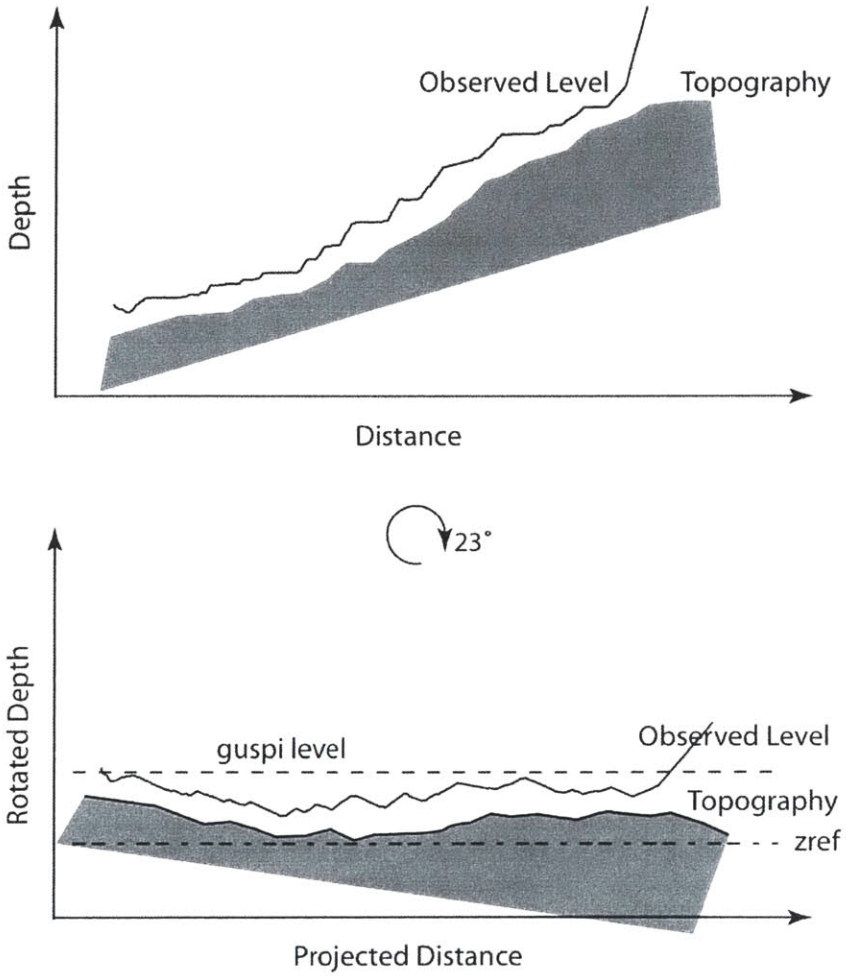

Figure 5-8. A cartoon shows the guspi-upcon transform procedure to reduce magnetic measurements made on an uneven surface to a level plane [*Guspi*, 1987]. First of all, the observed level is rotated clockwise to a horizontal plane, i.e., with an average scarp angle 23° in this paper. The resultant magnetic field data are then downward continued to a constant water-depth plane (zref), i.e., an equivalent plane, to remove the effects of variations in vehicle altitude. Finally, the magnetic field data are upward continued to a water depth (guspi level), such that all of the bathymetry in the survey lies below this depth.

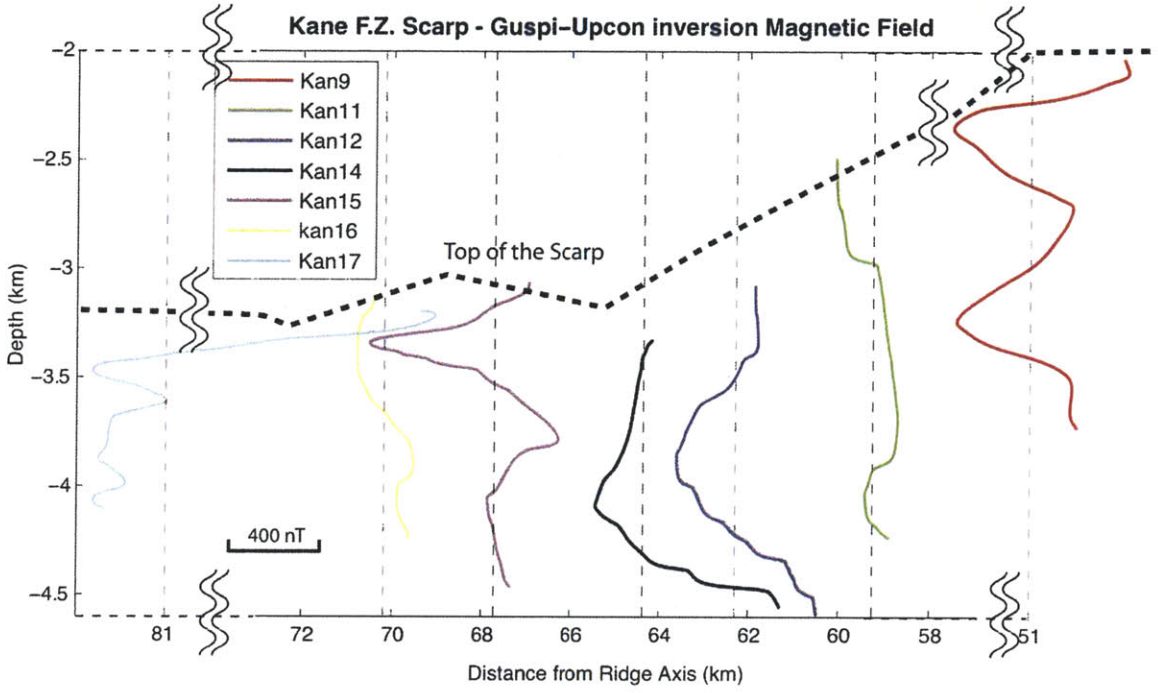

Figure 5-9. The computed guspi-upcon magnetic profiles plotted versus depth at the approximate lateral distance from the MAR axis. The magnetic profiles are calculated using an iterative Fast Fourier Transform based on the method of *Guspi* [1987]. The required upward continuation levels are set to four data points spacing above the minimum depth of each profile.

The profiles were then inverted for magnetization using a modified Fourier transform approach for the analysis of dipping tabular bodies, assuming the semi-infinite source [*Tivey*, 1996; *Tivey et al.*, 1998]. A band-pass wavelength filter from 0.5 km to 20 km was used to filter out short wavelength anomalies that presumably arise from local bathymetric sources and submersible motion and which do not affect the main magnetic signal that we seek. The filtering also helps in the convergence of the inversion solution [*Tivey*, 1994].

A summary of the inverted crustal magnetization profiles for the Kane scarp study area is shown in Figure 5-10. The nonuniqueness of the inversion solution is represented by the annihilator function, which is a magnetization that produces no external field. An infinite amount of annihilator may be added to the solution without affecting the resultant magnetic field. In our result, unfortunately, we cannot locate the accurate positions of the magnetization contrast between the top of the scarp and the overlying nonmagnetic seawater, thus we only adjusted the solution profiles so that the maximum and minimum magnetization values of each profile were balanced. These magnetization inversions show alternating zones of magnetization intensity that appear to correlate laterally between profiles (Figure 5-10). The magnetization of all the profiles ranges from approximately -4 A/m to 4 A/m which is roughly consistent with the magnetization values obtained from sea surface data (Figure 5-2) and paleomagnetic analysis of representative rock samples [*Williams*, 2007; *Williams et al.*, 2006].

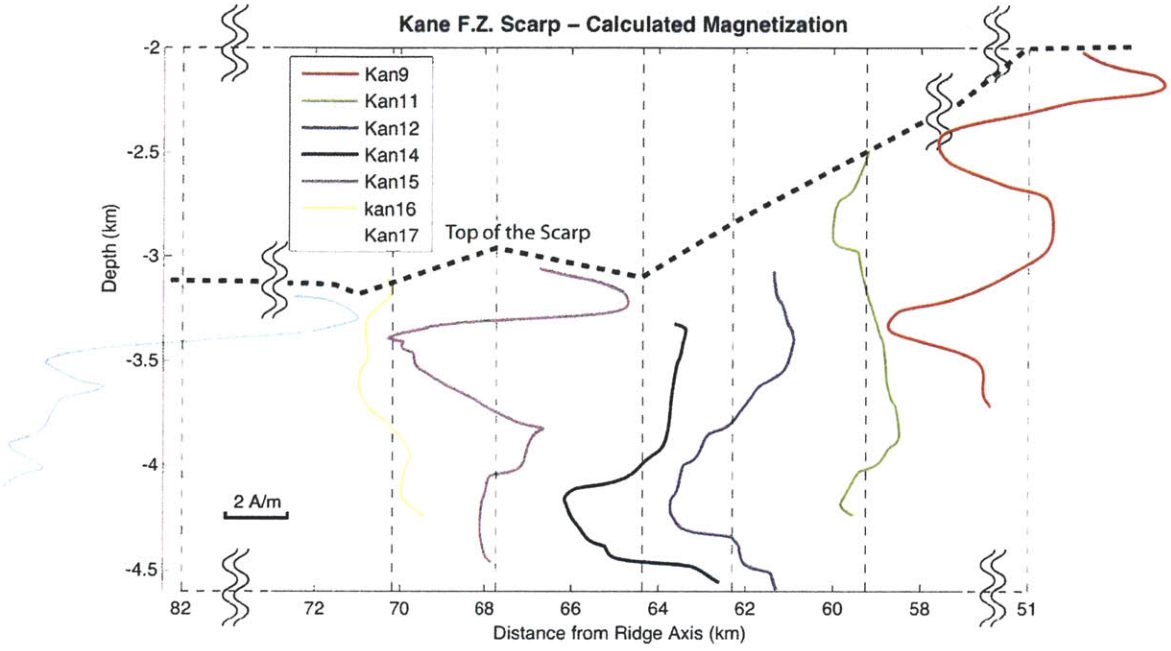

Figure 5-10. Inverted magnetization profiles plotted versus depth at the approximate lateral distance from the MAR axis. Note that the strong vertical variations in magnetization are required to fit the observed magnetic data (Figure 5-4) and are not just simply consistent with the observed data.

5.5. DISCUSSION

The computed magnetization profiles from the northern scarp of the KMM (Figure 5-10) show variations that appear to correlate laterally among the profiles. However, because there is an ambiguity in the actual magnitude of the magnetization (i.e., the zero magnetization level), we must address two potential end member explanations for the source of these observed variations. The first explanation is that these magnetization variations simply represent lithological variations, specifically that we are documenting weakly magnetized formations in contrast to more strongly magnetized formations, i.e., there is no polarity information contained in these profiles. If on the other hand the observed magnetization variations represent true polarity differences then the lateral correlation of these units have some isochronal significance. Below we discuss the relative merits of these two cases.

5.5.1. The Case for a Lithological Source

Here we discuss the possibility that the magnetization variations we find are the result of lithological variations. We concentrate our correlation analysis on four dives (Kan 11, 12, 14 and 15) that form relatively complete transects up the south wall of the Kane transform located on the northern part of KMM (Figure 5-3). The four dives together provide a relatively continuous transect over the interpreted magnetic polarity boundary C2r.2r/C2An.1n (Figure 5-2). In situ submersible observations and rock samples suggest that the Kane scarp is composed primarily of gabbros and serpentinized peridotites (Figure 5-11) [*Auzende et al.*, 1994; *Dick et al.*, 2008].

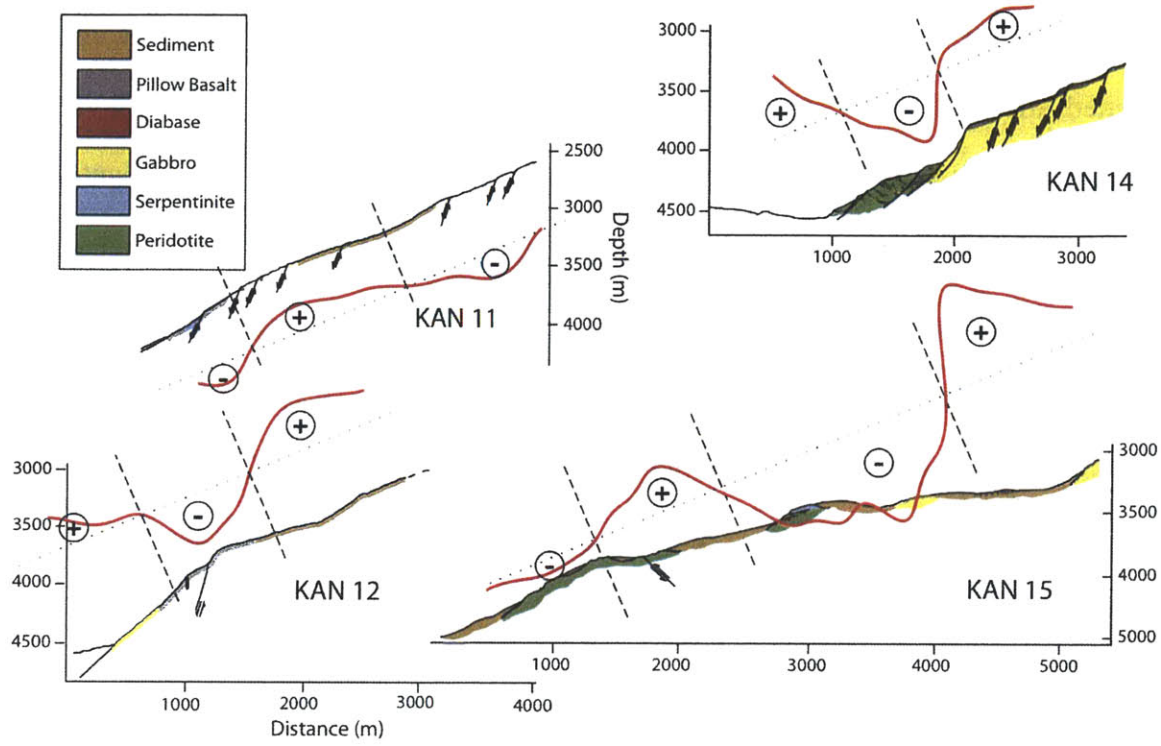

Figure 5-11. Comparison of projected inverted magnetization structures and lithologies of four dive profiles, Kan 11, 12 14 and 15. The lithological distribution map is adopted from *Dick et al.* [2008]. The dotted lines mark the 0 A/m in inverted magnetization, or translated magnitude 4 A/m. The dashed lines represent the interpreted strongly (labeled as circled "+") and weakly (labeled as circled "-") magnetized boundaries. Note that there is no basic correlation between magnetization structures and lithologies and/or between magnetized boundaries and lithological transitions.

We create a magnetization-lithology correlation by mapping the magnetization solution profiles and the interpreted lithological distributions [*Dick et al.*, 2008] along the dive tracks (Figure 5-11). However, because we cannot unambiguously define the magnetization polarity (zero magnetization level), we may only discuss the correlation with relatively weak and strong magnetization instead of positive and negative magnetization. If we take -4 to +4 A/m as the range in inverted magnetization then this translates to 0 to +8 A/m, with 0 A/m indicating the weakest magnetization and +8 A/m indicating the strongest magnetization. The magnetization profiles are projected on the top of the scarp face to compare with the lithological distributions in Figure 5-11. At the bottom of profile Kan 11, serpentinized peridotites correlate with weak magnetization. Along profile Kan 12, the serpentinized peridotite section correlates with weak magnetization while the gabbro section at the bottom of the profile shows somewhat stronger magnetization. Gabbros along the upper section of profile Kan 14 correlate with strong magnetization while a peridotite section at the bottom of the profile shows magnetization increasing downwards. Profile Kan 15 shows a more complicated lithological distribution and magnetization structure, and our data resolution does not allow us to infer a clear correlation. Peridotite sections correlate mostly with weak magnetization, however, a small gabbro section at the top of the profile shows strong magnetization while a gabbro section near the middle of the profile shows weak magnetization. A clear correlation cannot be deduced between the magnetization and lithology and/or between strongly and weakly magnetized boundaries and the positions that show lithological transitions (Figure 5-11). However, it is still interesting to notice

that most gabbro sections are showing stronger magnetizations (e.g., on the top of profile Kan 14 and bottom of profile Kan 12), except the middle gabbro section of profile Kan 15, while most (serpentinized) peridotites are showing weaker magnetizations (e.g., on the bottom of profiles Kan 11 and 15, and in the middle section of profile Kan 12 and Kan 14).

The range in translated magnetization from 0 to +8 A/m is greater than the paleomagnetic results of *Williams*' [2007] work. Also, the relatively weak and strong magnetization of gabbro and peridotite shown in Figure 5-11 is not consistent with previous rock magnetic and paleomagnetic results from the KMM which indicate that serpentinized peridotites have higher mean natural remanent magnetizations (NRM) (4.7 ± 5.8 A/m) compared to the gabbros (1.5 ± 2.5 A/m), although both are capable carrying a remanent magnetization of geomagnetic origin and the gabbros are more stable and have a higher koenigsberger ratio than the peridotites [*Williams*, 2007].

The magnetization-lithology correlation investigated here is strongly based on the seafloor surficial geological interpretation [*Auzende et al.*, 1994; *Dick et al.*, 2008]. Thus it is not necessarily indicative of deeper phases of more major lithology variations. We should also note that we used a short wavelength cut-off (0.5 km) during the magnetization inversion, which means that the high frequency magnetic signal resulting from shallower lithologic units is filtered out and that only broad scale changes are

effectively imaged. If lithological distributions do influence the magnetization structure, it most likely is closely linked to a magnetic polarity source described as follows.

5.5.2 The Case for a Polarity Source

We now describe the calculated magnetization variations in terms of polarity variation and discuss the arguments that support and perhaps refute this interpretation. If we assume that the magnetization variations are representative of polarity variations then the first observation we can make is that all the magnetization profiles show alternatively positive and negative magnetizations that are consistent with the GPTS subchrons [*Ogg and Smith*, 2004] projected from the sea surface magnetic interpretation framework (Figure 5-12). The magnetization structures of the middle five profiles were used to simulate the polarity boundary geometry according to the sequence of the GPTS subchrons [*Ogg and Smith*, 2004]. The boundary of chrons C2An and C2r (~2.581 Ma) appears to be well defined underneath the fault scarp with a shallow west-dipping angle, roughly estimated, to be ~ 45° in the shallow crust and < 20° in the deeper crust (Figures 5-12 and 5-13). Question marks in Figures 5-12 and 5-13 indicate the location where we are not fully confident interpreting the geometry because of the broad spacing of the profiles and the corresponding potential subchron interpretations. Another two magnetic profiles were obtained a little further from the northern margin of KMM. The eastern profile Kan 9 was obtained near the normal subchron C2n.1n and the western profile Kan 17 was measured near the normal subchron C2An.2n, determined on the basis of the GPTS of *Ogg and Smith* [2004].

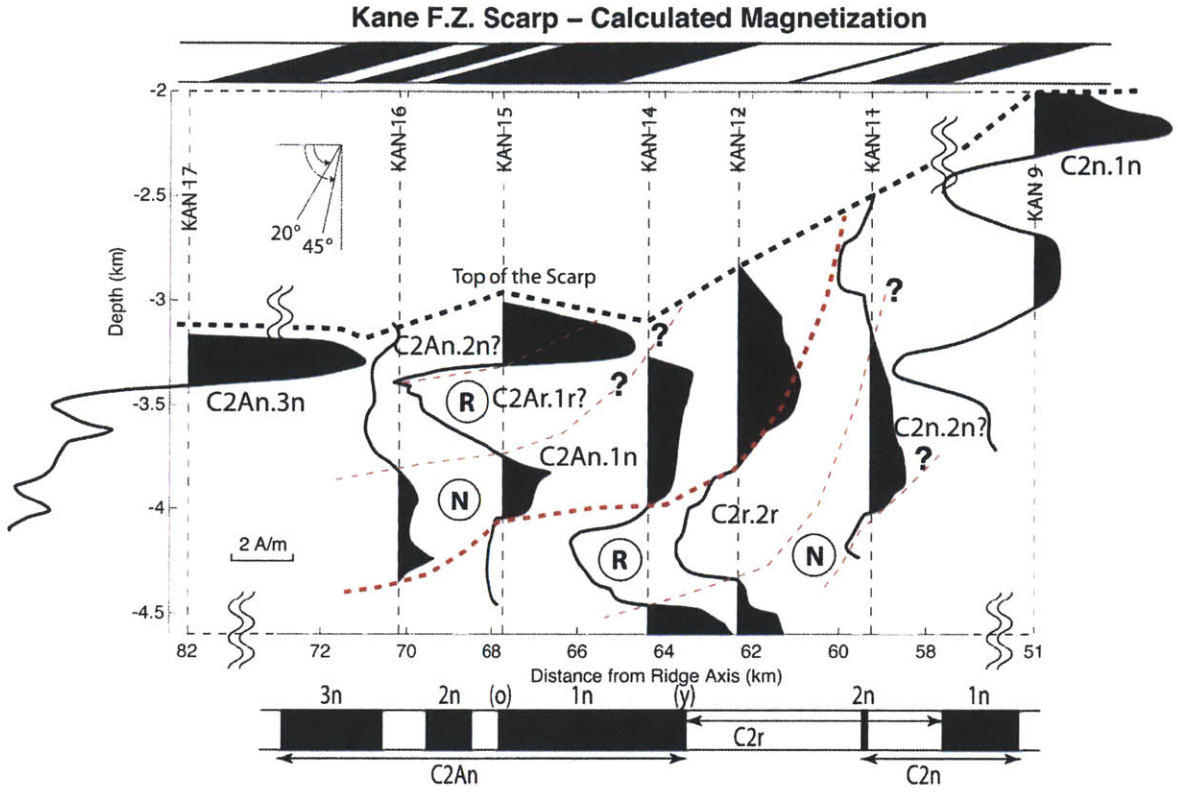

Figure 5-12. Summary diagram of the inverted magnetization profiles plotted versus depth for the Kane scarp study area at approximately the horizontal distance from the MAR axis. Kan 9 and Kan 17 are plotted offset from their true location as shown by dashed lines to better compare all the profiles. Dive numbers are labeled on the top of each profile. Positive magnetized sections are filled in black. A conceptual dipping GPTS of *Ogg and Smith* [2004] is projected on the top of the figure and another normal GPTS is projected at the bottom of the figure. Label (o) on bottom GPTS represents old side, while (y) represents young side. The black dashed line roughly outlines the top of the scarp. The thick red dashed line outlines the main polarity boundary of chrons C2r.2r/C2An.1n while the thin red lines represent other subchron boundaries. All of the possible corresponding subchrons are labeled along each magnetization profile. Question marks indicate that the local interpretation was made without full confidence.

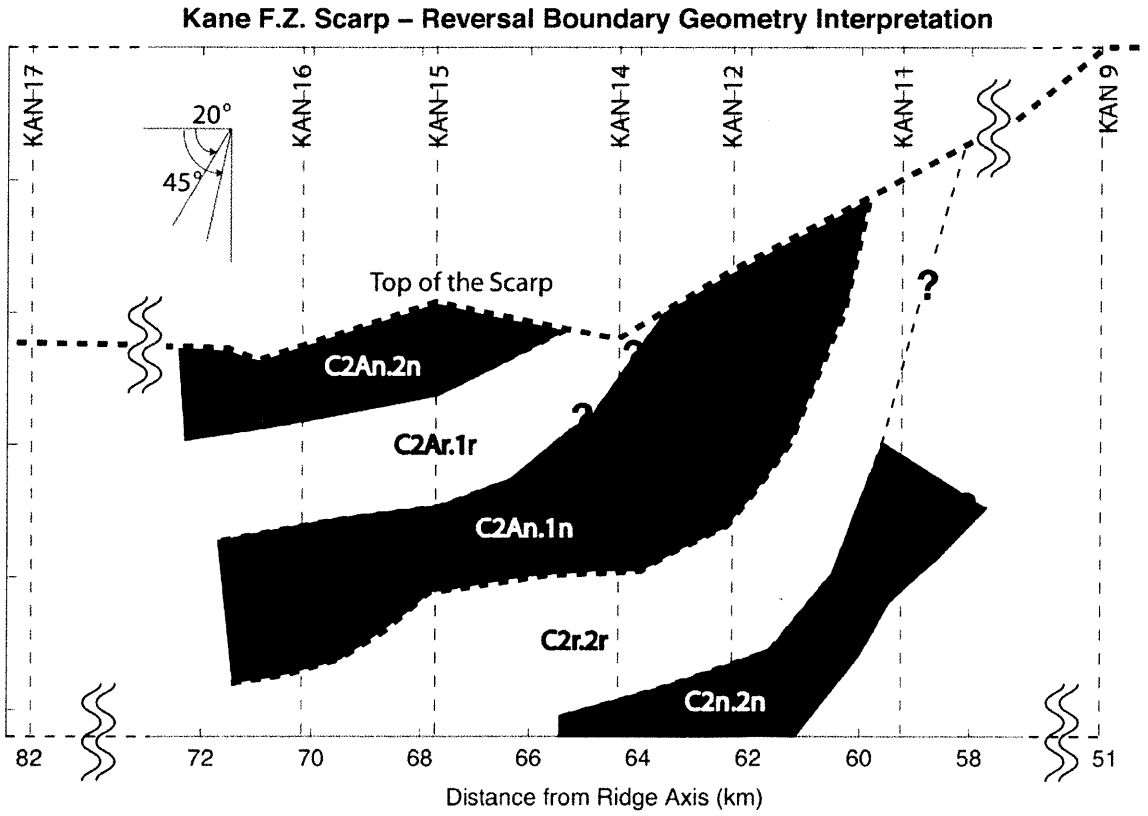

Figure 5-13. Simplified reversal boundary geometry interpretation along the Kane scarp on the basis of Figure 5-12. Other features are as described in Figure 5-12. The interpreted polarity boundary dips away from the ridge axis, with a west-dipping angle ~45° in the shallow crust and <20° in the deeper crust.

The sea surface inversion results over the KMM [*Williams*, 2007] clearly show the lineated anomalies formed at the MAR (Figure 5-2). Based on the regional magnetic lineations, the interpreted magnetic reversal boundaries in Figure 5-13 represent the period between subchrons C2An.1n and C2r.2r (~2.581 Ma). Chron C2An is composed of three normal subchrons, C2An.1n, C2An.2n and C2An.3n, but the sea surface inversion results indicate that only two subchrons, possibly the two longer ones, C2An.1n (2.581-3.032 Ma) and C2An.3n (3.33-3.596 Ma), are clearly resolved by the sea surface data. From sea surface data, the C2An.1n (young) boundary (Figure 5-12) is linear in appearance at the southern wall of the Kane transform fault, but it is not well defined north of 23°40'N (Figure 5-2), indicating that the lineated anomalies are truncated by the Kane fracture zone. Chron C2n (1.778-1.945 Ma) is composed of two normal subchrons, C2n.1n and C2n.2n, and only the former subchron is resolved by the sea surface data (Figure 5-2). However, in general, our vertical magnetization models resolve all of the subchrons within the chrons C2An and C2n (Figure 5-12), including those represented by subchron C2An.3n shown in profile Kan 17; subchron C2An.1n shown in profiles Kan 12, 14, 15 and 16; the relative short subchron C2An.2n shown along the top of profile Kan 15 with some uncertainty; subchron C2n.2n in profiles Kan 11 and Kan 12 with some uncertainty; and subchron C2n.1n at the top of profile Kan 9. We also attempt to interpret the short subchrons C2An.2n and C2n.2n that represented by subchron names with question marks in Figure 5-12 based on the inverse magnetization models.

The crustal magnetization inversion solution across the magnetic reversal boundary calculated from the sea surface data varies from about -3 to 1 A/m in the direction of increasing age, assuming a nominal 1 km thick source layer and geocentric axial dipole direction (inclination is 40°, declination is 0°) (Figure 5-2) [*Williams*, 2007]. However, because our magnetization solution along each profile was obtained only by balancing the maximum and minimum magnetization amplitude, our results cannot resolve the absolute magnetization values across the polarity boundary without an accurate zero magnetization level. Note that the magnetization profile of dive Kan 12, showing positive magnetization on the top of the scarp, is shifted some distance from the subchron C2n.1n. This discrepancy can be caused by the dipping geometry of the polarity boundary underneath the scarp. Furthermore, the sea surface data inversion solution (Figure 5-2) and GPTS subchrons (Figure 5-12) only represent the average magnetization structure beneath the scarp although a nominal 1 km thick source layer was assumed for inversion. Thus we would also not expect a good comparison between the shallow magnetization amplitudes and the surface data inversion solution and GPTS.

5.5.3. Magnetic Polarity Reversal Boundary

The interpreted geometry of the polarity reversal boundary of chrons C2An/C2r (Figure 5-13) shows that both the normal section of subchron C2A.1n and the reversal section of subchron C2r.2r are recorded along the middle five profiles. The polarity boundary dips west away from the ridge axis with an angle of ~45° in the shallow (<1 km) crust and <20° in the deeper crust. The interpretation of how the reversal boundary

formed is important for understanding the history and structure of oceanic crust and upper mantle.

Because there is not a solid correlation between the magnetization structure and the lithology (see section 5.5.1), it is easy to rule out the possibility that the geomagnetic reversal boundary was exclusively formed by the lithological changes even though gabbros and serpentinized peridotites show different magnetic characteristics. Rock magnetic and paleomagnetic data analyzed by *Williams* [2007] has determined that the polarity boundary dips to the west in the northern dome of KMM, which is consistent with the frozen cooling isotherm hypothesis for the source of polarity boundaries in gabbro. *Williams*' analysis resolves the dipping angle of the boundary using an analytic signal technique applied to the near-bottom ABE (The Autonomous Benthic Explorer) profiles and suggests a dip of 46°W±14° for the northern region of KMM. This is roughly consistent with our shallow interpretation (~45°) along the Kane scarp.

The cartoon in Figure 5-14 shows a conceptual model explaining how the frozen cooling isotherm is formed as the gabbros cool through the magnetite curie temperature at 580°C. The footwall rotates when exposed by the detachment faulting, and the rotation results in a more steepened magnetization vector and frozen polarity boundary. According to the temperature structure calculation of *Williams* [2007], the isotherm of 580°C has an initial dip angle of 13°, but after footwall rotation, the dip angle becomes 57°, indicating a 44° of rotation. Rotation angles have also been estimated in other OCCs

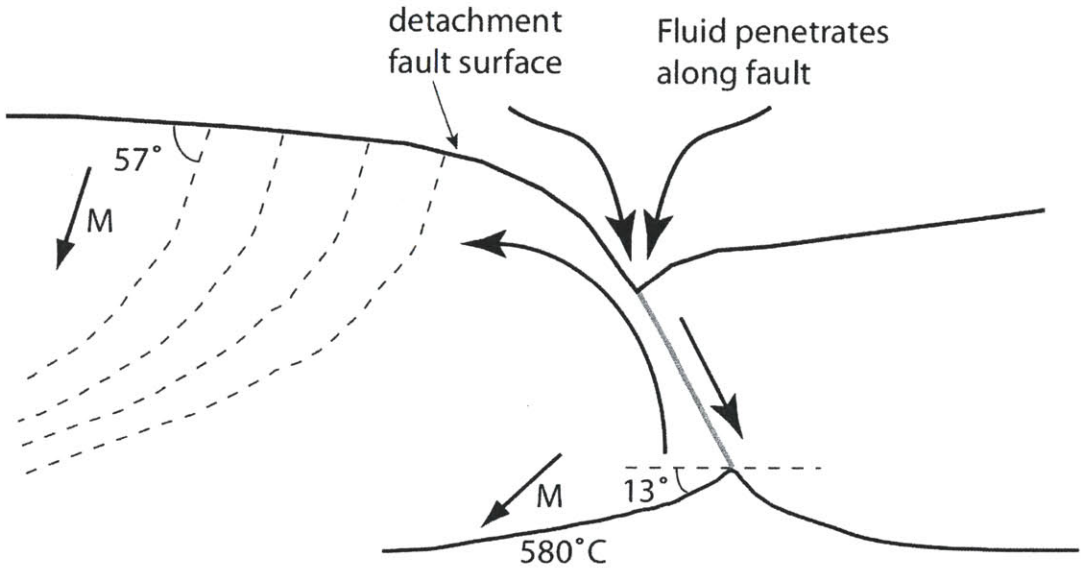

Figure 5-14. A conceptual model explaining how the frozen cooling isotherm formed as the source of polarity boundaries following the rotation of the footwall. The angles of isotherms are taken from the calculation of a two dimensional thermal model perpendicular to the ridge axis [*Williams*, 2007]. The angle of the frozen isotherm increases from ~13° at 0.5 Ma to ~57° at 3 Ma. The rotation of magnetization M is also shown in the figure. The fluid penetrates the seafloor along the detachment fault, creating serpentinized alternation zones in the peridotites.

using paleomagnetic vectors from drill cores. *Garcés and Gee* [2007] used the remanence vector in core complex gabbros from the 15°20'N region as a measure of the rotation, assuming that the samples acquired their magnetization prior to deformation and their vectors remained as passive markers during subsequent rotation of the footwall. Their results suggest rotations of 50°-80° in 1 Ma old crust. A similar study conducted by *Carlut et al.* [2006] from footwall samples at 15°45'N shows rotations of ~40°. Estimates from the limited paleomagnetic data suggest that the KMM has only experienced approximately 15° of counterclockwise rotation [*Williams*, 2007].

For our analysis we assumed a geocentric axial dipole (GAD) direction for magnetization in the absence of any other information. We can, however, calculate the effect of such footwall rotations of a GAD direction. The initial recorded magnetization was assumed to have a GAD inclination of 43° and declination of 0°. The rotated inclination and declination can be calculated following the method of *Verosub et al.* [1981] for footwall rotation about an axis parallel to the strike of the MAR. Inverted magnetization profiles of dives Kan 12 and Kan 15 using the new parameters after a 15° rotation (calculated from the paleomagnetic data, [*Williams*, 2007]) and a 44° rotation (calculated from the temperature structure) are compared with the original inverted profiles in Figure 5-15. The three sets of magnetization profiles share the same shape although with some amplitude variations. After footwall rotation of 44°, the inverted magnetizations are exaggerated more than twice of their original value (Figure 5-15). However, while the amplitude changes, the location of the magnetization contrasts does

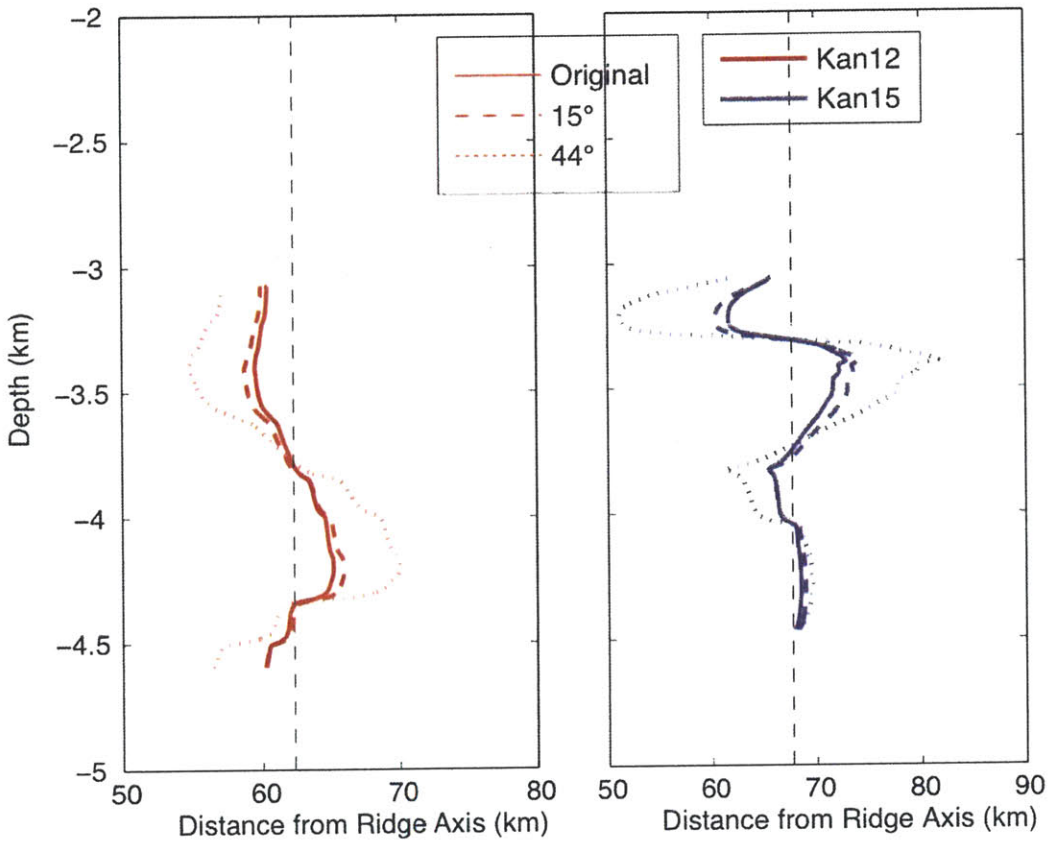

Figure 5-15. Comparison of inverted magnetization profiles after 15° and 44° rotations with the original inverted magnetization for two dive profiles, Kan 12 and Kan 15. All of the calculations assumed that the samples acquired their magnetization prior to the footwall rotation and with the initial inclination of 43° and declination of 0°. Note that all of the three sets of magnetization profiles share the same shape although with exaggerated amplitudes.

not change. Therefore our polarity reversal interpretation is not sensitive to these directional changes. Nevertheless, the magnetic vector direction is an important aspect of this work; in order to achieve the accurate inclination and declination required to resolve the footwall rotation angles oriented drill hole samples would be necessary.

5.6. CONCLUSIONS

Our detailed study of submersible magnetic profiles from the exposed crustal section of the Kane scarp shows that the horizontal variation in crustal magnetization as a function of depth can be mapped and directly related to the overlying lineated anomaly signal measured at the sea surface. This variation suggests that the contributions of gabbros and (serpentinized) peridotites to the magnetic source layer are significant, but our data cannot resolve the relative contributions. A dipping magnetic polarity boundary can be interpreted from the magnetization variations within the crustal sequence and it is compatible with the location of boundary of subchrons C2An.1n and C2r.2r (~2.581 Ma). The interpreted polarity boundary has a ~45° dipping angle in the shallow crust which is consistent with the estimates from the rock magnetic and paleomagnetic solutions while there is a relatively shallow dipping angle (<20°) in the deeper crustal section. Our result is consistent with the prevailing hypothesis that lower crust (gabbros) cool through magnetite Curie isotherm to become magnetic so that a magnetic polarity boundary would represent both a frozen isotherm and an isochron. Our polarity reversal boundary interpretation does not depend on the rotation angle of the KMM footwall.

Acknowledgement

We thank the captain, crew and scientific party of *R/V Kanaut Expedition* Cruise for their efforts in making the *Nautile* magnetic surveys a success. We thank H. Dick and B. Tucholke for generously sharing the geologic sample data on KMM with us. M. Tivey participated in the *Kanaut Expedition*, and we particularly thank chief scientist J. M. Auzende and the *Kanaut* scientific party for the well-documented cruise report.

References

Auzende, J.-M., M. Cannat, P. Gent, J.-P. Henriet, T. Juteau, J. Karson, Y. Lagabrielle, and M. Tivey (1992), Rapport de la Campagne Kanaut du Nautille sur le N/O Nadir, *science report*, 426.

Auzende, J.-M., M. Cannat, P. Gente, J.-P. Henriet, T. Juteau, J. A. Karson, Y. Lagabrielle, C. Mével, and M. A. Tivey (1993), Affleurements des roches profondes de la croûte océanique et du manteau sur le mur sud de la fracture Kane (Atlantique central) : observations par submersible, *C. R. Acad. Sci. Paris*, *317*, 1641-1648.

Auzende, J.-M., M. Cannat, P. Gente, J.-P. Henriet, T. Juteau, J. A. Karson, Y. Lagabrielle, C. Mével, and M. A. Tivey (1994), Observation of sections of oceanic crust and mantle cropping out on the southern wall of Kane FZ (N. Atlantic), *Terra Nova*, *6*, 143-148, doi:10.1111/j.1365-3121.1994.tb00647.x.

Ballu, V., J. Dubois, C. Deplus, M. Diament, and S. Bonvalot (1998), Crustal structure of the Mid-Atlantic Ridge south of the Kane fracture zone from seafloor and sea surface gravity data, *J. Geophys. Res.*, *103*, 2615-2631, doi:10.1029/97JB02542.

Canales, J. P., B. E. Tucholke, M. Xu, J. A. Collins, and D. L. Dubois (2008), Seismic evidence for large-scale compositional heterogeneity of oceanic core complexes, *Geochem. Geophys. Geosyst.*, *9*(Q08002), doi:10.1029/2008GC002009.

Cann, J. R., D. K. Blackman, D. K. Smith, E. McAllister, B. Janssen, S. Mello, E. Avgerinos, A. R. Pascoe, and J. Escartín (1997), Corrugated slip surfaces formed at

ridge-transform intersections on the Mid-Atlantic Ridge, *Nature*, *385*, 329-332, doi:10.1038/385329a0.

Carlut, J., C. J. MacLeod, H. Horen, and J. Escartin (2006), Paleomagnetic results from a mid-ocean ridge detachment at the Mid-Atlantic Ridge, 15°45'N, *EGU Meeting, Vienna.*

Dick, H. J. B., M. A. Tivey, and B. E. Tucholke (2008), Plutonic foundation of a slow-spread ridge segment: The oceanic core complex at Kane Megamullion, 23°30'N, 45°20'W, *Geochem. Geophys. Geosyst.*, *9*, Q05014, doi:10.1029/2007GC001645.

Dick, H. J. B., C. J. Lissenberg, and J. M. Warren (2010), Mantle Melting, Melt Transport, and Delivery Beneath a Slow-Spreading Ridge: The Paleo-MAR from 23°15'N to 23°45'N, *Journal of Petrology*, *51*(1-2), 425-467; doi:10.1093/petrology/egp088

Escartín, J., D. K. Smith, J. Cann, H. Schouten, C. H. Langmuir, and S. Escrig (2008), Central role of detachment faults in accretion of slow-spreading oceanic lithosphere, *Nature*, *455*, 790-794, doi:10.1038/nature07333.

Francheteau, J., P. Choukroune, R. Hekinina, X. Le Pichon, and H. D. Needham (1979), Oceanic fracture zones do not provide deep sections in the crust, *Canadian J. Earth Sci.*

Garcés, M., and J. Gee (2007), Paleomagnetic evidence of large footwall rotations associated with low-angle faults at the Mid-Atlantic Ridge, *Geology*, *35*(3), 279-282.

Gay, S. P. J. (1963), Standard curves for interpretation of magnetic anomalies over long tabular bodies, *Geophysics*, *28*, 161-200.

Ghose, I., M. Cannat, and M. Seyler (1996), Transform fault effect on mantle melting in the MARK area (Mid-Atlantic Ridge south of the Kane Transform), *Geology*, *24*, 1139-1142.

Granot, R., M. Abelson, H. Ron, and A. Agnon (2006), The oceanic crust in 3D: Paleomagnetic reconstruction in the Troodos ophiolite gabbro, *Earth and Planet. Sci. Lett.*, *251*, 280-292.

Guspi, F. (1987), Frequency-Domain Reduction of Potential Field Measurements to a Horizontal Plane, *Geoexploration*, *24*, 87-98.

Henstock, T. J., R. S. White, and J. H. McBride (1995), The OCEAN study area: tectonic history from magnetic anomaly data and seismic reflectivity, *J. Geophys. Res.*, *100*(B10), 20059-20078.

Karson, J. A., J. R. Delaney, F. N. Spiess, S. D. Hurst, B. Lawhead, S. Bigger, D. D. Naidoo, and P. Gente (1992), Deep-tow operations at the eastern intersection of the Mid-Atlantic Ridge and the Kane fracture zone, *EOS Trans. Am. Geophys. Union*, *73*(43), Fall Meet. Suppl., 552.

MacLeod, C. J., et al. (2002), Direct geological evidence for oceanic detachment faulting: The Mid-Atlantic Ridge, 15°45N, *Geology*, *30*(10), 879-882.

Maia, M., and P. Gente (1998), Three-dimensional gravity and bathymetry analysis of the Mid-Atlantic Ridge between 20°N and 24°N: Flow geometry and temporal evolution of the segmentation, *J. Geophys. Res.*, *103*, 951-974, doi:10.1029/97JB01635.

Maus, S., et al. (2005), The 10th generation international geomagnetic reference field, *Phys. Earth. Planet. Int.*, *151*(3-4), 320-322.

Morley, L. W., and A. Larochelle (1964), Paleomagnetism as a means of dating geological events, *Roy. Soc. Can. Spec. Publ.*, *8*, 39-50.

Morris, E., and R. S. Detrick (1991), Three-dimensional analysis of gravity anomalies in the MARK area, Mid-Atlantic Ridge 23°N, *J. Geophys. Res.*, *96*, 4355-4366, doi:10.1029/90JB02173.

Ogg, J. G., and A. G. Smith (2004), A geomagnetic polarity time scale, in *A Geologic Time Scale 2004*, edited by F. M. Gradstein, J. G. Ogg and A. G. Smith, pp. 63-86, Cambridge Univ. Press, Cambridge, UK.

Parker, R. L. (1973), The rapid calculation of potential anomalies, *Geophys. J. R. Astron. Soc.*, *31*, 447-455.

Parker, R. L., and S. P. Huestis (1974), The inversion of magnetic anomalies in the presence of topography, *J. Geophys. Res.*, *79*, 1587-1593.

Pedersen, L. B. (1978), A statistical analysis of potential fields using a vertical cylinder and a dike, *Geophysics*, *43*, 943-953.

Pilkington, M., and W. E. S. Urquhart (1990), Reduction of potential field data to a horizontal plane, *Geophysics*, *55*(5), 549-555.

Press, W. H., B. P. Flannery, S.A.Teukolsky, and W. T. Vetterling (1986), Numerical recipes: The art of scientific computing, *Cambridge University Press, Cambridge, UK*, 818.

Schouten, H., and K. McCamy (1972), Filtering marine magnetic anomalies, *J. Geophys. Res.*, *77*, 7089-7099.

Schouten, H., and C. Denham (1979), Modeling the oceanic magnetic source layer, paper presented at Deep drilling results in the Atlantic Ocean: Ocean crust: Maurice Ewing Series.

Tivey, M. (1996), Vertical magnetic structure of ocean crust determined from near-bottom magnetic field measurements, *J. Geophys. Res.*, *101*, 20275-20296.

Tivey, M. A. (1994), Fine-scale magnetic anomaly field over the southern Juan de Fuca Ridge: axial magnetization low and implications for crustal structure, *J. Geophys. Res.*, *99*(B3), 4833-4855.

Tivey, M. A., H. P. Johnson, C. Fleutelot, S. Hussenoeder, R. Lawrence, C. Waters, and B. Wooding (1998), Direct measurement of magnetic reversal polarity boundaries in a cross-section of oceanic crust, *Geophys. Res. Lett.*, *25*(19), 3631-3634.

Tucholke, B. E., J. Lin, and M. C. Kleinrock (1996), Mullions, megamullions, and metamorphic core complexes on the Mid-Atlantic Ridge, *Eos Trans. AGU, 77, Fall Meet. Suppl.*, F724.

Tucholke, B. E., J. Lin, and M. C. Kleinrock (1998), Megamullions and mullion structure defining oceanic metamorphic core complexes on the Mid-Atlantic Ridge, *J. Geophys. Res.*, *103*, 9857-9866, doi:10.1029/98JB00167.

Tucholke, B. E., M. D. Behn, R. Buck, and J. Lin (2008), The role of melt supply in detachment faulting and the formation of oceanic core complexes, *Geology*, *36*(6), 455-458; doi:10.1130/G24639A.

Vacquier, V. (1962), A machine method for computing the magnetization of a uniformly magnetized body from its shape and a magnetic survey, *Benedum Earth Magnetism Symposium, Univ. of Pittsburgh Press, Pittsburgh*, 123-127.

Verosub, K. L., and E. M. Moores (1981), Tectonic rotations in extensional regimes and their paleomagnetic consequences for oceanic basalts, *J. Geophys. Res.*, *86*, 6335-6349.

Vine, F. J., and D. H. Matthews (1963), Magnetic anomalies over oceanic ridges, *Nature*, *199*, 947-949.

Williams, C. M., M. A. Tivey, and M. D. Behn (2006), The magnetic structure of Kane megamullion: Results from marine magnetic anomalies, paleomagnetic data and thermal modeling, *Eos Trans. AGU, 87(52)*, Fall Meet. Suppl., Abstract T42A-03.

Williams, C. M. (2007), Oceanic lithosphere magnetization: marine magnetic investigations of crustal accretion and tectonic processes in mid-ocean ridge environments, Ph.D. thesis, 254 pp, Woods Hole Oceanographic Institution, Woods Hole.

Xu, M., J. P. Canales, B. E. Tucholke, and D. L. DuBois (2009), Heterogeneous seismic velocity structure of the upper lithosphere at Kane oceanic core complex, Mid-Atlantic Ridge, *Geochem. Geophys. Geosyst.*, *10*(Q10001), doi:10.1029/2009GC002586.